

**NANO-MODIFIED BASALT FIBER-REINFORCED CEMENTITIOUS
COMPOSITES FOR STRUCTURAL APPLICATIONS**

by

Ahmed Gaber Mohamed Rashwan Bediwy

A Thesis submitted to the Faculty of Graduate Studies of
The University of Manitoba

in partial fulfilment of the requirements of the degree of
DOCTOR OF PHILOSOPHY

Department of Civil Engineering
University of Manitoba
Winnipeg, MB, Canada

Copyright © 2021 by Ahmed Gaber Bediwy

ABSTRACT

The use of fiber-reinforced concrete (FRC) has been proposed to develop high performance cementitious composites to strengthen and rehabilitate concrete infrastructure, particularly those in harsh environment. A pioneer research program is conducted to investigate; (1) the behaviour of basalt fiber reinforced cementitious composites (BFRCC) incorporating 40% slag, 6% nano-silica and reinforced with basalt fiber pellets (BP) under ambient and severe environmental conditions, and (2) the feasibility of implementing the BFRCC in large-scale structural elements. The program consists of three phases. Phase *I* is devoted to study the mechanical properties of the BFRCC on small-scale specimens, Phase *II* focuses on assessing the bond of GFRP bars embedded in such composite under ambient and harsh conditions to confirm its potential for structural applications. Phase *III* consists of two stages, experimental and analytical. The experimental stage involves the construction and testing of eleven simply supported deep beams under one-point loading. As for the analytical stage, it involves the assessment of current shear design models for FRP-FRC deep beams and the introduction of new models.

The results show that the nano-modified slag-based cementitious composites reinforced with 4.5% or 6.9% BP are suitable for new construction and rehabilitation applications vulnerable to freeze–thaw and wet-dry environments, as the presence of BP in the cementitious composites effectively discounted the rate of deterioration. Moreover, the partial replacement of cement with 40% of slag, in addition to 6% of nano silica, significantly increases the failure load, and the addition of BP is capable of retaining approximately 90% of the pullout capacity for specimens exposed to harsh conditions. Furthermore, the inclusion of BFRCC in the whole depth of the deep beams is an effective substitution to conventional transverse reinforcement in deep beams. However, from the direct cost perspective, adding the BP as a layer in the tie zone reduces costs and achieves an

acceptable level of performance in terms of strength and ductility. The strut-and-tie models in most of the design codes, such as North American, European and Japanese, do not provide proper prediction of the capacity of deep beams. Therefore, a new model is proposed to account for the effect of incorporating different types of discrete fibers into the beam either as a layer in the tie zone or entirely over the whole depth

CO-AUTHORSHIP

This thesis has been prepared in accordance with the regulation of integrated-article format stipulated by the Faculty of Graduate Studies at the University of Manitoba. Substantial parts of this thesis were either published in or submitted for publication to peer-reviewed technical journals and international conferences.

Journal Papers

1. **Bediwy, A.**, Bassuoni, M., and El-Salakawy, E. “Residual Mechanical Properties of BPRCC under Cyclic Environmental Conditions.” *Journal of Materials in Civil Engineering*, ASCE, in press.
2. **Bediwy, A.**, and El-Salakawy, E. “Bond Behaviour of Straight and Headed-end GFRP Bars Embedded in Basalt Fiber Pellets Cementitious Composites.” *Journal of Composites for Construction*, ASCE, in press.
3. **Bediwy, A.**, and El-Salakawy, E. “Bond Degradation of GFRP Bars Embedded in BFRCC under Harsh Conditions.” *ACI Materials Journal*, submitted.
4. **Bediwy, A.**, and El-Salakawy, E. “Assessment of bond strength of GFRP bars embedded in FRCC.” *Cement and Concrete Composites*, submitted.
5. **Bediwy, A.**, Mahmoud, K., and El-Salakawy, E. “Structural Behaviour of FRCC Layered Deep Beams Reinforced with GFRP Headed-End Bars.” *Engineering Structures*, in press.
6. **Bediwy, A.**, and El-Salakawy, E. “Ductility and Performance Assessment of GFRP-RC deep beams incorporating BFRCC.” *ACI Structural Journal*, in press.
7. **Bediwy, A.**, and El-Salakawy, E. “Assessment of Shear Strength Design Models for Fiber-Reinforced Concrete Deep Beams.” in “Development and Applications of FRP Reinforcements”, *ACI Special Publication*, submitted.

Conference Papers

1. **Bediwy, A. G.** Bassuoni, M. T. and El-Salakawy E. (2018). “Post-Cracking Behaviour of Cementitious Composite Incorporating Nano-Silica and Basalt Fiber Pellets” *Sixth International Conference on the Durability of Concrete Structures*, University of Leeds, Leeds, West Yorkshire, United Kingdom.
2. **Bediwy, A. G.** and El-Salakawy E. (2019). “Behaviour of BFRCC Layered System Exposed to Harsh Environment” *CSCE Annual Conference, Laval (Greater Montreal)*, QC, Canada. June 12-15.
3. Shang, C. Mahmoud, K. **Bediwy, A. G.** and El-Salakawy E. (2019). “Evaluation of the Bond-Dependent Coefficient for Ribbed-Deformed GFRP Bars in Concrete Beams” *CSCE Annual Conference, Laval (Greater Montreal)*, QC, Canada. June 12-15.
4. **Bediwy, A. G.** Mahmoud, K. A. and El-Salakawy E. (2021). “Structural Behaviour of BFRCC Layered Deep Beams Reinforced with GFRP Headed-End Bars” *Tenth International Conference on FRP Composites in Civil Engineering*, Virtual Conference, Istanbul, Turkey, December 8-10.
5. **Bediwy, A. G.** and El-Salakawy E. (2021). “Pull-out Behaviour of Headed-End Bars Embedded in Basalt Fiber Cementitious Composites” *Eighth International Conference on Advanced Composite Materials in Bridges and Structures*, Virtual Conference, Sherbrooke, QC, Canada, August 5-7.
6. **Bediwy, A. G.** and El-Salakawy E. (2021). “Effect of Longitudinal Reinforcement Ratio on the Behaviour of GFRC-RC Deep Beams without Web Reinforcement” *CSCE Structures Specialty Conference*, Virtual Conference, Canada, May 26-29.

To Mom and Dad,

I hope this achievement gets me “another” step closer to making you proud of me.

To my beloved wife Esraa,

You are the best thing I've done with my life.

To my soul Tamara and Younis,

No work is more important than my love for you, and playing with you is the happiest moment of my day.

To my brother Mohamed,

You are always the backbone of our family.

To my sister Marwa,

You are the source of joy in our family.

ACKNOWLEDGMENTS

In the name of **ALLAH**, the Most Gracious and the Most Merciful.

All praise and thanks are due to almighty **ALLAH (GOD)**, WHO endowed me with strength, guidance and blessings to complete this work. I would like to express my sincere gratitude and appreciation to my supervisor Dr. Ehab El-Salakawy, PEng, FCSCE, Professor of Structural Engineering and Canada Research Chair in Durability and Modernization of Civil Infrastructure (2006-2016), Department of Civil Engineering, University of Manitoba, for his unremitting guidance and cordial support in all stages of this research accomplishment. I do also deeply convey my sincere thanks to him for his encouragement and help to organize my ideas and focus my interests, as well; I express my deep appreciation for what I have learned from him during my study.

I highly appreciate the financial support from the Natural Sciences and Engineering Research Council of Canada (NSERC) and the University of Manitoba Graduate Fellowship (UMGF). The assistance received from the staff of the W. R. McQuade Heavy Structures Laboratory at the University of Manitoba is acknowledged. I would also like to thank my colleagues for their continuous support specially Mohammed El-Gendy, Ahmed Hamed, Ahmed Mostafa (Croc) and Ahmed El-Wali, whose comments and suggestions were remarkable.

Reading countless pages of acknowledgements in countless books, I never realized how difficult a task it would be to say “thank you” for all the help, support, understanding, prayers given by my Dad “Gaber” and my Mom “Farida” over the time it took to complete this work. I wish to thank my wife, Esraa, who has stood by me through all my travails, my absences, my fits of pique and impatience. She gave me support and help, discussed ideas and prevented several wrong turns. She

also supported the family during much of my graduate studies. Thank you for being you! Along with her, I want to send my love to my two kids, Tamara and Younis. They have never known their Dad as anything but a student, it seems. Good girl and good boy, and great sources of love and relief from scholarly endeavour.

I would like to thank my siblings “Mohamed” and “Marwa” and their families for their invaluable love, wishes, prayers and support. In fact, all my family have been steadfast and supportive. Thank you all, without your sincere support, I would not be here to make this achievement.

Ahmed Gaber Bediwy

TABLE OF CONTENTS

ABSTRACT.....	i
CO-AUTHORSHIP	i
ACKNOWLEDGMENTS	iv
TABLE OF CONTENTS.....	vi
LIST OF FIGURES	xii
LIST OF TABLES	xv
CHAPTER 1 : INTRODUCTION	1
1.1 Overview	1
1.2 Problem Statement	3
1.3 Objectives.....	4
1.4 Scope and Work Methodology.....	5
<i>Phase I</i>	5
<i>Phase II</i>	Error! Bookmark not defined.
1.5 Thesis Structure.....	8
CHAPTER 2 : LITERATURE REVIEW	12
2.1 Fiber Reinforced Cementitious Composite	12
2.2 Fiber Reinforced Polymers.....	14
2.2.1 Physical properties.....	15
2.2.1.1 <i>Density</i>	15
2.2.1.2 <i>Coefficient of thermal expansion</i>	15
2.2.2 Mechanical properties.....	16
2.2.2.1 <i>Tensile strength</i>	16
2.2.2.2 <i>Compressive strength</i>	17
2.3 Bond of FRP Bars	17
2.3.1 General.....	17
2.3.2 Research on bond behaviour of FRP bars	18
2.4 Behaviour of Deep Beams.....	21
2.4.1 Overview	21
2.4.2 Deep members	21
2.4.3 Strut-and-tie model.....	23
2.4.4 Previous research on FRP reinforced concrete deep beams	26

2.7 Closure	29
CHAPTER 3 : RESIDUAL MECHANICAL PROPERTIES OF BPRCC UNDER CYCLIC ENVIROMENTAL CONDITIONS	30
3.1 Introduction	32
3.2 Research Significance	34
3.3 Experimental Program.....	34
3.3.1 Materials	34
3.3.2 Proportions and mixing procedures	36
3.3.3 Exposure	38
3.3.4 Tests.....	39
3.4 Results and Discussion.....	41
3.4.1 Mechanical performance of composites	41
3.4.1.1 <i>Compressive capacity</i>	41
3.4.1.2 <i>Flexural performance</i>	44
3.4.2 Resistance of composites to frost action.....	50
3.4.3 Compatibility with substrate concrete	51
3.5 Conclusions	56
CHAPTER 4 : BOND BEHAVIOUR OF STRAIGHT AND HEADED-END GFRP BARS EMBEDDED IN BASALT FIBER PELLETS CEMENTITIOUS COMPOSITES	58
4.1 Introduction	60
4.2 Experimental Program.....	62
4.2.1 Materials	62
4.2.1.1 <i>Cementitious composite</i>	62
4.2.1.2 <i>Fibers</i>	63
4.2.1.3 <i>GFRP reinforcement</i>	64
4.2.2 Proportions and mixing procedures	65
4.2.3 Test specimens.....	66
4.2.4 Test setup and instrumentation	68
4.3 Results and Discussions	69
4.3.1 Compressive strength	69
4.3.2 Pullout load-slip response.....	71
4.3.3 Modes of failure.....	75
4.3.4 Factors affecting the pullout load and bond strength	78

4.3.4.1 <i>Effect of cementitious matrix type</i>	78
4.3.4.2 <i>Effect of bar diameter</i>	79
4.3.4.3 <i>Effect of GFRP bar end type (straight vs headed-end bars)</i>	82
4.3.4.4 <i>Effect of adding discrete fibers</i>	83
4.3.5 Evaluation of code provisions for bond strength.....	85
4.4 Conclusions	88
CHAPTER 5 : BOND DEGRADATION OF GFRP BARS EMBEDDED IN BFRCC UNDER HARSH CONDITIONS	90
5.1 Introduction	92
5.2 Research Significance	95
5.3 Experimental Procedure	95
5.3.1 Materials	95
5.3.1.1 <i>Cementitious composite</i>	95
5.3.1.2 <i>Fibers</i>	96
5.3.1.3 <i>GFRP reinforcement</i>	97
5.3.2 Proportions of mixtures	98
5.3.3 Test specimens and conditioning procedure.....	98
5.3.4 Test setup and instrumentation	102
5.4 Experimental Results and Discussion	103
5.4.1 Internal damage assessment.....	103
5.4.1.1 <i>Visual analysis</i>	103
5.4.1.2 <i>Residual compressive strength</i>	105
5.4.1.3 <i>Relative dynamic modulus of elasticity</i>	106
5.4.2 Modes of failure.....	107
5.4.3 Effect of environmental conditions on load-slip response	109
5.4.4 Effect of environmental conditions on pullout load	110
5.5 Conclusions	113
CHAPTER 6 : ASSESSMENT OF BOND STRENGTH OF GFRP BARS EMBEDDED IN FRCC	115
6.1 Introduction	117
6.2 Summary of Experimental Results.....	120
6.3 Experimental Database.....	124
6.4 Review of Bond Provisions in Current Codes	125

6.4.1 CSA building code provisions (CSA/S806-12).....	133
6.4.2 CSA bridge code provisions (CSA/S6-19).....	134
6.4.3 ACI provisions (ACI 440.1R-15).....	135
6.4.4 JSCE code provisions (JSCE 2007).....	135
6.5 Review of Bond Strength Equations Proposed in the Literature	137
6.5.1 Model <i>I</i> (Krem 2013).....	137
6.5.2 Model <i>II</i> (Quayyum and Rteil 2011)	138
6.5.3 Model <i>III</i> (Newman et al. 2010).....	139
6.5.4 Model <i>IV</i> (Basaran and Kalkan 2020)	140
6.5.5 Model <i>V</i> (Islam et al. 2015)	140
6.6 Assessment of Current Code Provisions	141
6.7 Proposed Model and Verification	144
6.8 Conclusions	156
 CHAPTER 7 : STRUCTURAL BEHAVIOUR OF FRCC LAYERED DEEP BEAMS REINFORCED WITH GFRP HEADED-END BARS.....	
7.1 Introduction	160
7.2 Experimental Program.....	164
7.2.1 Test specimens.....	164
7.2.2 Materials	165
7.2.3 Test setup.....	170
7.3 Test Results and Discussion.....	170
7.3.1 Crack pattern and mode of failure	170
7.3.2 Cracking load and ultimate capacity	174
7.3.3 Load-deflection response.....	177
7.3.4 Crack width.....	179
7.3.5 Strain in reinforcement and strain profile.....	181
7.3.6 Comparison between experimental and code predicted load	186
7.4 Conclusions	187
 CHAPTER 8 : DUCTILITY AND PERFORMANCE ASSESSMENT OF GFRP-RC DEEP BEAMS INCORPORATING BFRCC	
8.1 Introduction	191
8.2 Research Significance	195
8.3 Experimental Procedure	195

8.3.1 Test specimens.....	195
7.3.2 Materials	197
7.3.3 Test setup.....	200
8.4 Experimental Results and Discussion	201
8.4.1 Modes of failure and crack pattern	201
8.4.2 Cracking load and ultimate capacity	205
8.4.3 Load-deflection response.....	207
8.4.4 Ductility	210
8.4.5 Load-longitudinal reinforcement strain relationship	212
8.4.6 Evaluation of code provisions for strut and tie models	218
8.5 Conclusions	221
CHAPTER 9 : ASSESSMENT OF SHEAR STRENGTH DESIGN MODELS FOR FIBER- REINFORCED CONCRETE DEEP BEAMS.....	223
9.1 Introduction	225
9.2 Research Significance	228
9.3 Summary of Experimental Results.....	228
9.4 Experimental Database.....	232
9.5 Review of Current Code Provisions for STM.....	239
9.5.1 The CSA codes provisions (CSA S806-12 and CSA S6-19) for STM	239
9.5.2 AASHTO-LRFD code provisions (AASHTO LRFD-14) for STM.....	240
9.5.3 ACI code provisions (ACI 318-19) for STM	240
9.5.4 Eurocode 2 code provisions (BS EN 1992-1-1-2004) for STM.....	241
9.5.5 JSCE code provisions (JSCE 2007) for STM.....	241
9.6 Review of Models Proposed in the Literature.....	242
9.6.1 Model <i>I</i> (Mohamed et al. 2017).....	242
9.6.2 Model <i>II</i> (Dharir 2017).....	243
9.6.3 Model <i>III</i> (Ashour et al. 1992).....	243
9.6.4 Model <i>IV</i> (Shahnewaz and Alam 2014)	244
9.7 Assessment of Current Design Models	245
9.8 Proposed Equation and Verification	248
9.9 Conclusions	251
CHAPTER 10 : CONCLUSIONS AND FUTURE WORK.....	253
10.1 Summary	253

10.2 Conclusions	254
10.2.1 Conclusions from phase <i>I</i>	254
10.2.2 Conclusions from phase <i>II</i>	255
10.2.2.1 <i>For unexposed specimens</i>	255
10.2.2.2 <i>For exposed specimens</i>	257
10.2.3 Conclusions from phase <i>III</i>	258
10.2.3.1 <i>For the experimental part</i>	258
10.2.3.2 <i>For the analytical part</i>	260
10.3 Recommendations for Future Work.....	261
REFERENCES	263

LIST OF FIGURES

Figure 1.1: Flow chart showing the connections between the three phases	7
Figure 2.1: Stress-strain relationship for steel and FRP bars.....	16
Figure 2.2: Failure surface showing the internal forces (Reproduced from Wight and MacGregor 2009)	22
Figure 2.3: B-regions and D-regions (Reproduced from Wight and MacGregor 2009)	24
Figure 2.4: Strut and tie model of a simply supported deep beam containing no web reinforcement (Reproduced from Wight and MacGregor 2009)	25
Figure 2.5: Nodal zones (Reproduced from Mohamed 2015)	26
Figure 3.1: Reinforcing fibers, (a) basalt fiber pellets, and (b) steel fibers	36
Figure 3.2: Flexural test set-up showing a layered prism	39
Figure 3.3: Locations of Demec points for relative shrinkage test (all dimensions in mm).....	41
Figure 3.4: Exemplar failure plane of a layered prism from mixture H-B-2.5.....	45
Figure 3.5: Representative load-deflection (P- δ) curves for specimens after the combined exposure, (a) N, and (b) H composites	47
Figure 3.6: SEM images for the BP and SF, (a) hydration products depositing in the BP grooves, and (b) smooth surface of SF	49
Figure 3.7: Exemplar layered slabs after the relative shrinkage test, (a) N-X-0.0, and (b) N-B-6.9 after 148 days	53
Figure 3.8: Bond strength of all composites from the pull-off test before and after the combined exposure	55
Figure 3.9: Mode of failure of exemplar layered slabs obtained from the pull-off test after the combined exposure, (a) H-X-0.0, and (b) H-B-2.5	56
Figure 4.1: Reinforcing fibers: (a) basalt fibers pellets, and (b) steel fibers	63
Figure 4.2: GFRP bars and configuration of the head	64
Figure 4.3: Test specimens, a) schematic drawings of the specimens, b) and c) GFRP bar in the form work showing the bond breaker for headed-end and straight bars, and d) specimens after casting in the curing room (dimensions are in mm)	67
Figure 4.4: Pullout test setup and instrumentation.....	69
Figure 4.5: The average compressive strength for all mixtures.....	70

Figure 4.6 : Load–slip relationship at the loaded end for No. 15 GFRP straight and head-end bars	73
Figure 4.7: Load–slip relationship at the loaded end for No. 20 GFRP straight and head-end bars	74
Figure 4.8: Mode of failure for all specimens: (a) PO, (b) PPO, (c) SC, (d) CSH, (e) CC, and (f) CCSB	77
Figure 4.9: Distribution of BP in specimens: (a) BF-2.5-19-H, and (b) BF-4.5-19-H.....	84
Figure 5.1: Reinforcing fibers (a) basalt fibers pellets, and (b) steel fibers.....	96
Figure 5.2: GFRP bars and configuration of the head	97
Figure 5.3: Test specimens, (a) schematic drawing of the specimens, (b) specimens after casting in the curing room, and (c) specimens in the environmental chamber (all dimensions in mm). 100	
Figure 5.4: Pullout test setup and instrumentation.....	103
Figure 5.5: Appearance of specimens after combined exposure (Visual rating [VR]).....	104
Figure 5.6: Mode of failure for all specimens, (a) PO, (b) PPO, (c) SCH, (d) SC, and (e) CC..	109
Figure 5.7: Load–slip relationship at the loaded end, (a) unconditioned specimens, and (b) conditioned specimens	111
Figure 6.1: Configuration of the head of GFRP bars.....	120
Figure 6.2: Schematic drawing of the specimen (All dimensions in mm).....	121
Figure 6.3: Typical modes of failure: (a) Pullout for straight GFRP bar, (b) Splitting of concrete, (c) Cracking of concrete.....	123
Figure 6.4: Exemplar load–slip relationship for No.15 GFRP straight and head-end bars	124
Figure 6.5: Prediction of available models for straight FRP bars embedded in normal concrete	152
Figure 6.6: Prediction of available models for headed-end FRP bars embedded in FRC.	154
Figure 7.1: Details of specimens (all dimensions in mm)	166
Figure 7.2: Reinforcing fibers: (a) basalt fibers pellets, and (b) steel fibers	167
Figure 7.3: Pull-off test, (a) slab specimens, and (b) mode of failure	168
Figure 7.4: Configuration of the head.....	169
Figure 7.5: Schematic drawing of the test setup (dimensions are in mm).....	171
Figure 7.6: Cracking pattern at failure of beams	173
Figure 7.7: Mode of failure of test beams.....	175

Figure 7.8: Effect of reinforcement ratio on the ultimate load capacity	176
Figure 7.9: Load-deflection relationship for beams.....	178
Figure 7.10: Crack width for a) the flexural crack, and b) the diagonal crack	180
Figure 7.11: Strains at mid-span section in tested deep beams.....	183
Figure 7.12: Strain profile in deep beams without FRRC layer	184
Figure 7.13: Strain profile in deep beams with FRRC layer.....	185
Figure 7.14: Strut-and-tie model (STM) for simply supported deep beams.....	186
Figure 8.1:Details of specimens (all dimensions in mm)	197
Figure 8.2: Reinforcing fibers, (a) basalt fiber pellets, and (b) steel fibers	199
Figure 8.3:Configuration of the head of GFRP bar	200
Figure 8.4: Schematic drawing of the test setup (all dimensions in mm).....	201
Figure 8.5: Mode of failure of test beams.....	204
Figure 8.6: Cracking patterns at failure	206
Figure 8.7: Ultimate capacity of test beams.....	208
Figure 8.8: Load-deflection relationship for beams.....	209
Figure 8.9: Definition of ductility index and line S	212
Figure 8.10: Strains at mid-span section in tested deep beams.....	214
Figure 8.11: Strain profile in deep beams	216
Figure 8.12: Strut-and-tie model (STM) for simply supported deep beams.....	220
Figure 9.1: Strut-and-tie model (STM) for simply supported deep beams.....	226
Figure 9.2: Details of specimens (all dimensions in mm)	229
Figure 9.3: Schematic drawing of the test setup (all dimensions in mm).....	230
Figure 9.4: Typical crushing of strut failure mode (A-B-4.5-1.0).....	231
Figure 9.5: Typical Strain profile in deep beams (L-B-2.5-1.0).....	232
Figure 9.6: Prediction of available models for FRP-RC deep beams	246
Figure 9.7: Prediction of available models for FRP-FRC deep beams.....	251

LIST OF TABLES

Table 2.1: Comparison of physical and chemical properties of fibers used in concrete (ACI 1996)	13
Table 2.2: Typical densities of reinforcing bars (ACI 2015).....	15
Table 2.3: Typical coefficients of thermal expansion (ACI 2015).....	15
Table 2.4: Typical tensile properties of reinforcing bars (ACI 2015).....	17
Table 3.1: Chemical and physical properties of GU cement and slag.....	35
Table 3.2: Properties of fibers.....	36
Table 3.3: Proportions of the mixtures per cubic meter.....	38
Table 3.4: Mechanical properties of the reference cementitious composites tested at 28 days....	42
Table 3.5: Residual mechanical properties of the cementitious composites after F/T and W/D cycles.....	42
Table 3.6: Summary of relative shrinkage at different ages of cementitious composites	52
Table 4.1: Chemical and physical properties of GU cement and slag.....	63
Table 4.2: Properties of fibers.....	63
Table 4.3: Mechanical properties of GFRP	64
Table 4.4: Proportions of the mixtures per cubic meter.....	66
Table 4.5: Details of test specimens for pullout	68
Table 4.6: ANOVA for the results of compressive strength at 28 days	71
Table 4.7: Pullout test results.....	79
Table 4.8: ANOVA for the results of pullout test.....	80
Table 4.9: Bond toughness indices for the test specimens.....	86
Table 4.10: Comparison between the experimental and predicted bond strength	88
Table 5.1: Chemical and physical properties of GU cement and slag.....	96
Table 5.2: Properties of fibers.....	96
Table 5.3: Mechanical properties of GFRP	97
Table 5.4: Proportions of the mixtures per cubic meter.....	99
Table 5.5: Details of test specimens for pullout	102
Table 5.6: Air content, RE_n , and compressive strength of the cementitious composites.....	106

Table 5.7: Pullout test results.....	108
Table 6.1: Mechanical properties of GFRP bars.....	120
Table 6.2: Properties of discrete fibers	121
Table 6.3: Characteristics of test specimens for pullout.....	122
Table 6.4: Test data for straight FRP bars embedded in normal concrete.....	126
Table 6.5: Test data for straight FRP bars embedded in FRC	128
Table 6.6: Test data for headed-end FRP bars embedded in normal concrete	130
Table 6.7: Test data for headed-end FRP bars embedded in FRC.....	132
Table 6.8: Model comparisons for straight FRP bars embedded in normal concrete.....	145
Table 6.9: Model comparisons for straight FRP bars embedded in FRC	147
Table 6.10: Model comparisons for headed-end FRP bars embedded in normal concrete	149
Table 6.11: Model comparisons for headed-end FRP bars embedded in FRC.....	151
Table 7.1: Design code provisions for STM.....	163
Table 7.2: Details of test beams	165
Table 7.3: Properties of fibers.....	167
Table 7.4: GFRP Reinforcement properties.....	169
Table 7.5: Summary of test results	179
Table 7.6: Comparison between the experimental and predicted failure loads	187
Table 8.1: Details of test beams	197
Table 8.2: Properties of fibers.....	199
Table 8.3: GFRP reinforcement properties.....	200
Table 8.4: Summary of test results	203
Table 8.5: Code design provisions for STM.....	219
Table 8.6: Comparison between the experimental and predicted failure loads	220
Table 9.1: Details of test beams	229
Table 9.2: Properties of fibers.....	230
Table 9.3: GFRP reinforcement properties.....	230
Table 9.4: Test data for FRP-RC deep beams.....	234
Table 9.5: Test data for steel-FRC deep beams	237
Table 9.6: Test data for FRP-FRC deep beams	249

CHAPTER 1: INTRODUCTION

1.1 Overview

Concrete often cracks due to its limited tensile and deformational capacities. Since the presence of cracks may not only affect the aesthetics of structures, but also its durability by allowing infiltration of moisture and oxygen causing corrosion of reinforcing steel accompanied by a deterioration of concrete (Vasanelli et al. 2013). In addition, the presence of de-icing salts and repeated freezing-thawing cycles, in cold regions, will aggravate the damage of concrete. Therefore, to expand the possibilities of using concrete in such harsh environments, developing high performance cementitious composites to rehabilitate concrete infrastructure (e.g., bridge decks, pavements, parking structures) is much needed (Nes and Øverli 2015). In this context, the use of fiber-reinforced concrete (FRC) has been suggested by many researchers to enhance the short-term structural performance. Incorporating discrete fibers into any cementitious composite is capable of reducing bleeding, controlling shrinkage cracking, and improving impact resistance. Furthermore, the most pronounced advantages of using fibers in cementitious composites are increasing their energy absorbing capacity/toughness, deformation capability, and load bearing capacity after cracking (Bentur and Mindess 2007).

Various types of fibers can be used to produce fiber-reinforced cementitious composites (FRCC), such as steel, synthetic, organic and inorganic fibers. However, a relatively new type of fiber manufactured from basalt rocks is progressively immersing in civil engineering research, including a special type of basalt fiber pellets [BP], which is made of basalt fibers coated by polyamide or other resins. The production process of basalt fibers is more environment friendly, and it is cheaper with respect to the other types of fibers such as glass fibers. In addition, basalt

fibers have high tensile strength, and they are not vulnerable to corrosion contrary to the case of steel fibers that corrode resulting in irregular/rough surfaces, e.g. slab on ground, bridge decks and pavements (Iyer et al. 2015; Arslan 2016; Ayub et al. 2016; Ghazy et al. 2016; Mahmoud et al. 2017).

Despite the advantages of fibers, it was reported that adding fibers in mortar/concrete may increase its permeability due to the formation of numerous weak interfacial transition zones (ITZ) between the fibers and the cementitious matrix; in addition, the efficacy of fiber reinforcement depends upon the matrix composition (Bentur and Mindess 2007; Banthia et al. 2014; Soylev and Ozturan 2014; Afroughsabet and Ozbakkaloglu 2015; Zheng et al. 2015; Ghazy et al. 2016). Therefore, it is crucial to produce a cementitious composite with superior properties, which can be obtained by incorporating supplementary cementitious materials (SCMs) such as silica fume and/or ground granulated blast-furnace slag. These supplementary materials have the ability to react with calcium hydroxide crystals, the weakest by-product of the cement hydration reaction, to form more calcium-silicate-hydrate (C-S-H), which is the backbone of concrete strength and binding, resulting in refined and denser microstructure and ITZ. Nevertheless, it is worth noting that slag is a latent hydraulic binder that mainly contributes to improving the long-term performance of cementitious systems. Incorporating high dosages of slag usually leads to delay of hardening and strength as well as microstructural development at early ages (Malhotra et al. 2000; Zhang et al. 2012). In addition, it is well-documented that adding a small dosage of innovative materials, such as nanoparticles [e.g., nano-silica (NS)], can vigorously speed up the kinetics of cement hydration and improve the microstructural development of cement-based materials (Said et al. 2012; Kong et al. 2012; Madani et al. 2012; Zhang et al. 2012; Ghazy et al. 2016).

1.2 Problem Statement

This research presents a part of an extensive ongoing program at the University of Manitoba. The first phase of this program was undertaken by Mahmoud et al. (2017), who investigated the behaviour of BFRCC incorporating 6% NS with 40% slag and reinforced with BP in terms of flexural strength, toughness and pull-out strength relative to reinforcing bars with different end shapes. It was concluded that this BFRCC has high performance and potential to be applied in structural applications. For example, the bond strength of BFRCC to sand-coated glass fiber reinforced polymer (GFRP) bars was determined, and it showed superior bond to both straight and headed end GFRP bars compared to normal strength concrete (NSC). In addition, it is worth emphasizing that the use of BFRCC can be effective and more economical in practice, if it is particularly cast as a layer in the tension side of structural members to enhance their bond and post-cracking characteristics, which can presumably prolong the service life of structures and discount their maintenance and repair costs.

Yet, some research gaps and limitations still exist and need to be addressed in order to fully exploit this innovative composite (BFRCC) in infrastructure applications. For instance, only one dosage of BP was used in the previous study by Mahmoud et al. (2017). All tests were conducted in ambient conditions, and the results were not compared with composites incorporating steel fibers, which are currently the most commonly used fibers in the construction industry. Moreover, it is imperative to implement this new composite in large-scale concrete elements. In North America, structures in aggressive environments, such as bridges and parking structures, are deemed as prime examples for the use of FRC. In such structures, it is common to use deep beams as transfer girders, pile caps, and foundation walls. Thus, deep beams have been selected to be investigated for the incorporation of BFRCC as a layer in the tie zone. Reinforced concrete deep beams are structural

members with a relatively small shear span-to-depth ratio ($a/d < 2.5$) and higher load capacity compared to slender beams. It is worth mentioning that the arch action is the load transfer mechanism in deep beams unlike the beam action in slender beams (CSA 2019c). The arching action mechanism involves the transmission of vertical loads to the support through the concrete compression struts, while the longitudinal reinforcement acts as a tie for the arch. In addition, the strength of deep beams is strongly affected by the reinforcement detailing of their support zones, as the longitudinal bars carry high tension over the entire shear span (the distance from the point of application of concentrated load to its respective reaction force), which requires longer anchorage/development length at the region adjacent to the support (over-hang part) compared to slender beams. Therefore, using BFRCC at this location, where the tie should be formed would shorten the anchorage length considerably. Also, it should be emphasized that delaying the initiation of cracks and increasing the tensile strength of the concrete matrix in deep beams may enhance the load carrying capacity of the inclined strut. Since the BP showed a significant effect in improving the post-cracking behaviour, the presence of BP may considerably enhance the flexural toughness of the cementitious composites, resulting in enhancing the capacity of deep beams. However, these trends have not been substantiated by large-scale testing and in-depth research work. In general, conducting research in the aforementioned aspects shall provide much better understanding for achieving an improved performance of structural concrete elements incorporating BFRCC.

1.3 Objectives

Based on the aforementioned problem statement, the specific objectives of this doctoral research are to:

- Study the effect of varying BP dosages on the flexural strength and toughness of BFRCC under ambient and severe environmental conditions;
- Investigate the effectiveness of adding a BFRCC layer on the tension face of normal concrete elements, conduct a comparison of the performance of this novel composite with steel fiber reinforced cementitious composite (SFRCC), and evaluate the bond strength of the developed BFRCC layer as well as its dimensional stability relative to base/substrate concrete;
- Assess the potential of implementing BFRCC in large-scale structural elements, in terms of the residual bond (pull out bond strengths) properties and behaviour of GFRP bars embedded in this composite (BFRCC) after being subjected to: dual effects of freeze-thaw and wet-dry cycles; and
- Evaluate the behaviour of simply-supported concrete deep beams reinforced with GFRP bars incorporating BFRCC as a layer in the tie zone.

1.4 Scope and Work Methodology

To achieve the objectives of this research, the research work is described in the following three phases, as shown in Fig 1.1.

Phase I

Phase I focused on investigating the behaviour of BFRCC incorporating 40% slag and reinforced with BP under ambient and severe environmental conditions. The effect of varying the dosage of BP on the flexural strength and toughness of small-scale specimens was evaluated. In addition, to evaluate its potential for structural applications, the pull-off bond strength of the developed BFRCC layer and the dimensional stability of BFRCC relative to the base concrete was determined. Ten different mixtures were cast and tested for the following: (1) compressive strength

using triplicate cylinders (100×200 mm) according to ASTM C39 (2020a), (2) flexural performance of triplicate prism specimens (350 × 100 × 100 mm) following the general guidelines of ASTM C1609 (ASTM 2019d), (3) pull-off strength using duplicate concrete slabs of 250×250 mm surface area and 100-mm thickness according to ASTM C1583 (2020c), and (4) dimensional stability using concrete slabs similar to those of the pull-off test.

Phase II

a- Experimental work

For reinforced concrete structures, the quality of bond between concrete and reinforcement is considered a crucial parameter so that stresses are transferred efficiently. However, it might be adversely affected by severe exposure conditions such as freeze-thaw cycles, and wet-dry cycles. Therefore, to evaluate the potential of the new composite for structural applications, Phase *II* focused on evaluating the bond characteristics between the BFRCC and GFRP bars under both ambient and harsh environmental conditions. The experimental program for this phase was composed of two series: (I) control pullout tests, and (II) combined environmental conditions. A total of 180 specimens consisting of 200-mm concrete cubes were cast and tested according to the guidelines of Annex G of the CSA/S806-12 (CSA 2017). In addition to the cementitious matrix type, the test variables included the size of the GFRP bar, and the type of the GFRP bar end (straight or headed-end bars), the type and the dosage of discrete fibers in the matrix.

b- Analytical work

In this part, test results of 413 pullout specimens, divided into four groups based on the type of the FRP bar or the cementitious matrix, were used to evaluate the available models in the codes and literature to predict the bond strength. In addition, a proposed model to predict the bond performance of headed-end FRP bars with FRC pullout specimens was introduced.

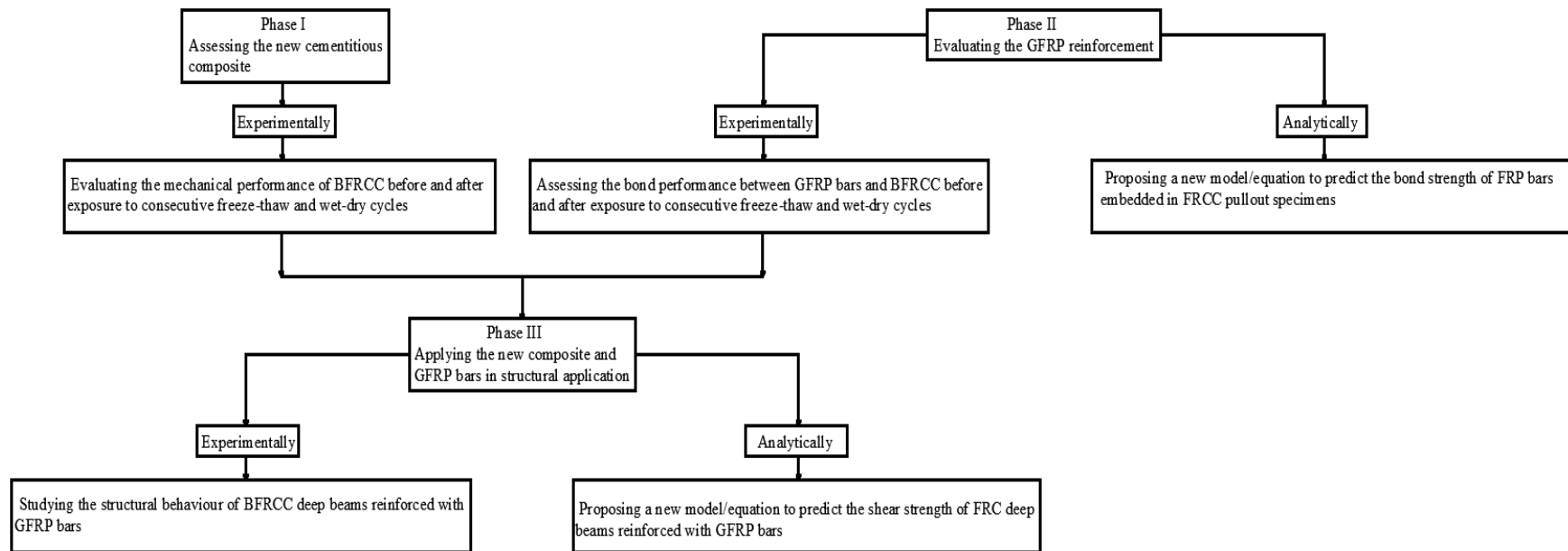


Figure 1.1: Flow chart showing the connections between the three phases

Phase III

a- Experimental work

Phase *III* focused on investigating the feasibility of implementing the BFRCC in large-scale structural elements. Deep beams have been selected based on the aforementioned rationale (Section 1.2). A total of eleven simply-supported deep beams were constructed and tested under one-point loading. All beams had a rectangular cross section measuring 250-mm width by 590-mm height, and a length of 2,100 mm. The test parameters included the type of the fibers (steel or BP), the dosage of the BP, the web reinforcement, and the longitudinal reinforcement ratio.

b- Analytical work

In the analytical part, different models predicting the shear capacity of FRP-RC deep beams incorporated in the current standards and guidelines or proposed in the literature were reviewed. In addition to the FRP-FRC deep beams tested in the experimental phase under gravity load, a database comprising fifty-four FRP-RC and thirty-one steel/FRP-FRC deep beams subjected to gravity loads from the literature was compiled and used to assess the different models. Based on the assessment, a model capable of accurately predicting the shear capacity of FRP-FRC deep beams was proposed.

1.5 Thesis Structure

The thesis consists of ten chapters as described below:

- Chapter 1 presents a brief background of the research topic, identifies the problem definition and scope of work, states the main objectives of the work, and provides a general description of the followed methodology.

- Chapter 2 provides an essential theoretical background regarding the properties of fiber reinforced cementitious composites, FRP reinforcement, bond transferring mechanisms between FRP and concrete, the behaviour of deep beams. In addition, it reviews previous research on FRP-RC deep beams subjected to gravity load.

The following six chapters (Chapters 3 to 9) are presented in journal article format, where they were in-press or under review.

- Chapter 3 (Article 1, in press) presents the results and discussion on evaluating the behaviour of the nano-modified BFRCC compared to SFRCC in terms of the compressive strength, flexural performance, pull-off bond strength, and dimensional stability relative to the base concrete.

Bediwy, A., Bassuoni, M. and El-Salakawy, E. “Residual mechanical properties of BPRCC under cyclic environmental conditions.” *Journal of Materials in Civil Engineering.*, ASCE, in press.

- Chapter 4 (Article 2, in press) investigates the effect of various parameters on the bond of straight and headed-end FRP bars embedded in BFRCC and SFRCC using the pullout approach under ambient conditions. The load-slip response of pull-out specimens containing BP are discussed providing evidence that BFRCC enhanced the failure pullout load compared to counterpart specimens comprising SF.

Bediwy, A. and El-Salakawy, E. “Bond behaviour of straight and headed-end GFRP bars embedded in basalt fiber pellets cementitious composites.” *Journal of Composites for Construction*, ASCE, in press.

- Chapter 5 (Article 3, under review) addresses the effect of different environmental exposure on the residual bond strength of GFRP bars embedded in BFRCC and SFRCC. The efficiency of two different GFRP bars (straight and headed-end bars) embedded in cementitious composites reinforced with different dosages of BP on resisting dual effect of consecutive cycles of freeze-thaw and wet-dry is discussed in detail.

Bediwy, A. and El-Salakawy, E. “Bond degradation of GFRP bars embedded in BFRCC under harsh conditions.” *ACI Materials Journal*, submitted.

- Chapter 6 (Article 4, under review) assesses the available bond strength equations incorporated in different design codes and guidelines as well as those available in the literature, and propose a new model to predict the bond strength of headed-end GFRP bars embedded in FRC.

Bediwy, A. and El-Salakawy, E. “Assessment of bond strength of GFRP bars embedded in FRCC.” *Cement and Concrete Composites*, submitted.

- Chapter 7 (Article 5, in press) examines the effect of the reinforcement ratio and the addition of basalt FRCC layer in the tie zone on the behaviour and ductility of simply supported GFRP-RC deep beams.

Bediwy, A., Mahmoud, K. and El-Salakawy, E. “Structural behaviour of FRCC layered deep beams reinforced with GFRP headed-end bars.” *Engineering Structures*, in press.

- Chapter 8 (Article 6, in-press) investigates the effect of the addition of different dosages of BP to the cementitious composites on the shear behaviour of deep beams reinforced longitudinally with GFRP headed-end bars. Discussions regarding the ductility evaluation

for the GFRP-RC members and the ability of BP to supplant shear reinforcement are also provided.

Bediwy, A. and El-Salakawy, E. “Ductility and Performance Assessment of GFRP-RC deep beams incorporating BFRCC.” *ACI Structural Journal*, in press.

- Chapter 9 (Article 7, under review) assesses the available empirical models incorporated in different design codes and guidelines and proposed by several researchers. A comprehensive database is established using FRP-RC and steel/FRP-FRC deep beams. The database is then used to evaluate the design models. Based on this assessment, a model capable of accurately predicting the capacity FRP-FRC, is proposed.

Bediwy, A., and El-Salakawy, E. “Assessment of shear strength design models for fiber-reinforced concrete deep beams.” in “Development and Applications of FRP Reinforcements”, *ACI Special Publication*, submitted.

- Chapter 10 provides a summary of the major findings of the experimental and analytical work as well as recommendations for future research.

CHAPTER 2: LITERATURE REVIEW

This chapter provides a focused literature review to topics related to the subject matter of this thesis and its scope of work.

2.1 Fiber Reinforced Cementitious Composite

Cementitious materials usually are brittle in nature, which had low tensile strength and strain capacity. Therefore, fibers have been adopted to reinforce any brittle materials. Short and randomly distributed discrete fibers (three-dimensional reinforcement) are used to alleviate the shortcomings associated with the concrete brittleness and poor resistance to crack initiation and growth, as fiber inclusion in matrix greatly improve the engineering properties such as the tensile strength, flexural strength, impact, fatigue, deformation capability, toughness, and load bearing capacity after cracking.

The fiber reinforced cementitious composite (FRCC) are made of different constituents and proportions such as hydraulic cement, fine aggregate, and discontinuous discrete fibers. There are numerous types of fibers available for commercial and experimental use. Nowadays, the available fibers in the market can be classified into two following categories: I) fibers with low modulus of elasticity and a high elongation property and II) fibers with high modulus of elasticity. Natural and synthetic fibers such as nylon, polypropylene, and polyethylene are of the first category. These fibers normally do not lead to strength improvement; however, they enhance toughness and the plastic shrinkage resistance. High modulus of elasticity fibers such as steel, glass, asbestos, and carbon are added mainly to improve the strength and stiffness of the cementitious matrix. The

physical and chemical properties of fibers used in concrete are listed in Table 2.1, as reported by ACI 544-1R-96 (2002).

Table 2.1: Comparison of physical and chemical properties of fibers used in concrete (ACI 1996)

Properties	Fiber type				
	Steel	Polymeric	Carbon	Glass	Basalt
Filament diameter (μm)	250 - 1000	10 - 1000	8 - 18	6 - 21	9 - 23
Mass density (g/cm^3)	7.8	0.9 - 1.4	1.6 - 2.15	2.46 - 2.74	2.6 - 2.7
Tensile strength (MPa)	1000- 3000	75 - 2900	480 - 4000	2500 - 3500	4150 - 4800
Modulus of elasticity (GPa)	200	3.5-115	27- 480	65-80	90-110
Ultimate elongation (%)	0.5-35	3-150	0.5-2.4	2.5-4.8	2.5-3.15
Adhesiveness in matrix	Low	Low	Low	Good	Good
Chemical stability	Average	High	High	High	High

Steel fibers are usually manufactured with various aspect ratios (the length of the fiber over the diameter; L/D), anchorages, and tensile strengths. Steel fibers are usually added to the concrete matrix to improve crack control and redistribute stresses in the hardened cementitious matrix created by dynamic and static loading conditions. The typical amount of steel fiber used in any mix is estimated to be 0.2% to 0.5% by volume. However, using a fiber content more than 2% by volume generally results in poor workability and poor fiber distribution due to the tendency for steel fibers to ball or clump together (Bentur and Mindess 2007). On the other hand, a relatively new type of fiber is introduced to industry, namely basalt fibers. Basalt fibers are manufactured in a single-stage process by melting crushed volcanic basalt rock. They are environmentally safe, non-toxic, possess high heat stability, and insulating characteristics, and have an elastic structure. Iyer et al. (2015) studied the effect of adding basalt chopped fibers in filament form with different dosages and lengths on the 28-day compressive strength and modulus of rupture. This study found

that the optimum length and optimum amount of basalt fiber are 36 mm and 8 kg/m³, which behaved comparably (modulus of rupture) to counterpart specimens comprising steel fibers.

2.2 Fiber Reinforced Polymers

Fiber reinforced polymers are composite materials essentially made of two basic components, reinforcing fibers and a matrix (resin). The fibers, which are responsible for carrying the load and providing strength, are ideally elastic, brittle and have high strength. The resin basically provides a cohesive environment to transfer stresses between fibers, keep the fibers together, and provide lateral support for the fibers against buckling. The material characteristics of FRP reinforcement are essentially different from those of steel, as the ACI 440.1R-15 (ACI 2015) summarizes the main differences between FRP and steel as follows:

- FRP is linear elastic up to failure whereas steel yields;
- FRP is anisotropic whereas steel is isotropic;
- FRP has lower modulus of elasticity; thus, design for serviceability often controls;
- FRP bars have a low creep-rupture threshold than steel;
- FRP bars have different coefficients of thermal expansion in longitudinal and radial directions;
- FRP has endurance time in fire and elevated temperature applications less than that of steel; and
- Degradation of FRP bars, if present, is benign to the surrounding concrete unlike steel that expands and causes failure of the member.

2.2.1 Physical properties

2.2.1.1 Density

The density of the FRP is significantly lower than that of steel as listed in Table 2.2. It is worth mentioning that the lower the density the lighter the bars are, leading to considerable reduction in the transportation and labor costs.

Table 2.2: Typical densities of reinforcing bars (ACI 2015)

Reinforcement type	Steel	GFRP	Carbon (C)FRP	Aramid (A)FRP
Density (gm/cm ³)	7.9	1.25-2.1	1.5-1.6	1.25-1.4

2.2.1.2 Coefficient of thermal expansion

The longitudinal direction of the FRP bars has a coefficient of thermal expansion that differs from that of transverse direction based on the material itself (fibers and resin), unlike steel bars which exhibit the same coefficient in all direction. The coefficients of thermal expansion of different types of reinforcing bars as given in the ACI 440.1R-15 (ACI 2015) are listed in Table 2.3. it can be noted that the transverse direction of FRP bars has a thermal expansion coefficient much higher than that of hardened concrete which may lead to a concrete cover failure due to splitting cracks in the concrete surrounding the bars under high temperatures. Surprisingly, it can be noted that the thermal coefficient in the longitudinal direction for CFRP bars is almost zero, which indicates that CFRP are not affected by varying the temperature.

Table 2.3: Typical coefficients of thermal expansion (ACI 2015)

Reinforcement type	Steel	GFRP	CFRP	AFRP
Coefficient (×10 ⁶ /°C)	11.7	6 to 10	-9 to 0	-6 to -2
	11.7	21 to 23	74 to 104	60 to 80

2.2.2 Mechanical properties

2.2.2.1 Tensile strength

FRP tensile behaviour is generally characterized by its unidirectional nature, as the fibers, which are mainly responsible for strength are positioned in the longitudinal direction only. FRP bars behaviour is linear elastic up to failure as shown in Figure 2.1. They do not undergo a yielding plateau prior to rupture when they loaded in tension. FRP bars have higher strengths and lower stiffness with respect to the conventional steel as listed in Table 2.4. The tensile strength and modulus of an FRP bar can be affected by many parameters; the type of fibers and resin, the fiber-volume fraction, and the bar diameter. In addition, the quality control of the fabrication process may considerably affect such properties. For example, having two bars with the same characteristics (the same diameter, made of the same constituents material and with the same fiber-volume fraction) does not mean that they have the same tensile properties.

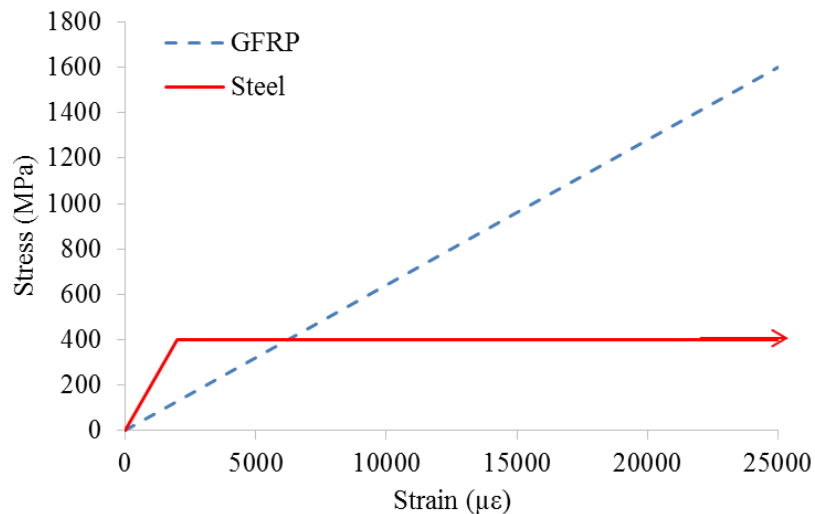


Figure 2.1: Stress-strain relationship for steel and FRP bars

Table 2.4: Typical tensile properties of reinforcing bars (ACI 2015)

Reinforcement type	Steel	GFRP	CFRP	AFRP
Ultimate tensile strength (MPa)	276-517*	483-1,690	600-3,690	1,720-2,540
Tensile modulus (GPa)	200	35-51	120-580	41-125
Ultimate tensile strain ($\mu\epsilon$)	1,400-2,500 ^a	12,000-31,000	5,000-17,000	19,000-44,000

* at yielding

2.2.2.2 Compressive strength

The compressive strength of FRP bars are less than the tensile ones of the same product as FRP materials are vulnerable to buckling under compression. Some recent studies suggested reducing the value of compressive strength of FRP materials to 50% of its tensile strength, while the modulus of elasticity is the same under both cases of loading (Deitz et al. 2003).

2.3 Bond of FRP Bars

2.3.1 General

Despite the attractive properties of FRP, FRP reinforcing bars have a relatively weak bond with concrete besides being elastic brittle, thus studying the structural performance of concrete structures reinforced with FRP has attracted huge interest, especially the bond–slip behaviour. The fundamental understanding of the bond stress is how to transfer the tensile stresses from the concrete to the reinforcing bars through the bond strength at the bar/concrete interface safely. Chemical adhesion, friction, and interlock/bearing are the three mechanisms to transfer the force between the concrete and reinforcing bar. The chemical bond (adhesion) is responsible for transfer the stress at the very beginning during the pullout test; however, it is low and lost rapidly. Consequently, the stress transfer is developed through interlocking and friction mechanisms

(Cosenza et al. 1997). Such mechanisms depend mainly on some parameters such as the resin type, bar shape, surface pattern, etc.

Unlike steel reinforcement, FRP bars present different modes of failure. As reported by Tastani et al. (1984), the following types of failure were observed in pullout specimens under monotonic load:

- **Pullout failure:** the bar is pulled out of the concrete, with little to no damage in the concrete matrix.
- **Splitting failure:** Splitting of the concrete element or concrete cover leading to loss of bond resistance.
- **Failure with cone detachment:** The bar is pulled out of the concrete bringing along a concrete cone. In this case the concrete element dimensions are not enough to provide the necessary anchorage.
- **Bar rupture (FRP):** The bar achieves its tensile strength, and bar rupture is achieved without bond failure. In this case, the embedment length is equal or greater than the development length. No slip is recorded at the free-end.

2.3.2 Research on bond behaviour of FRP bars

Larger size bars produce smaller bond stress, and it loses its adhesive bond earlier than small size bars (in the case of sand-coated GFRP bars). Benmokrane et al. (1996), and Larralde and Silva-Rodriguez (1993) studied the effect of bar diameter in the bond resistance of GFRP bars with different surface patterns. The results revealed an increase in the bond stress with decreasing bar diameter. It is worth noting that such findings were obtained when the tests conducted under ambient conditions.

Alves et al. (2011) investigated the residual bond properties and behaviour of GFRP embedded in concrete after being subjected to simultaneous effects of freeze-thaw cycles and sustained loads, fatigue loading, and combined effect of freeze-thaw cycles and sustained loading and then fatigue loading. Thirty-six specimens were constructed and tested. The test parameters/variables included bar diameter (No.16 and No.19), concrete cover thickness, loading scheme, and environmental conditioning. The specimens adopted in this study were conditioned to 1,000,000 cycles in a sinusoidal wave with minimum and maximum stress levels of 2.5 and 25% of the ultimate guaranteed tensile strength. In addition, the specimens were exposed to 200 freezing and thawing cycles in accordance with ASTM C666 (2019c). It was reported that unconditioned specimens presented very stiff behaviour with no slip up to failure. Smaller- diameter No. 16 GFRP bars showed approximately 30–50% higher bond strength than larger No. 19 bars. In addition, it was observed that freeze-thaw cycles along with the sustained load conditioning increased the bond strength for No. 16 bars with the three concrete covers used. This observation is valid for No. 19 bars with concrete cover of $2.5d_b$ only. Such conditioning resulted in significant increase in the peak slip (decrease in bond stiffness) for No. 19 bars, while for No. 16 bars, only specimens with a clear concrete cover of $2.5 d_b$ showed increase in slip.

Belarbi and Wang (2012) studied the bond durability of FRP bars embedded in fiber-reinforced concrete (FRC) and compared with that of FRP bars in plain concrete. Thirty-six specimens (200-mm side length concrete cubes) were constructed and subjected to pullout bond test. A combined environmental cycle consisted of 20 freeze-thaw cycles and 20 high temperature cycles. The same cycles were repeated 10 times. Thus, a total of 200 freeze-thaw cycles and 200 high temperature cycles were conducted to simulate the seasonal weather changes, while submerged in the salt solution (a solution of sodium chloride, 5% by weight). The FRC specimens were cast using a

polypropylene fiber, which is fibrillated and commercially available in 57-mm length. The investigated parameters were the concrete type (plain and fiber reinforced concrete), the bar diameter (No. 13 and No. 25), and the reinforcement type (GFRP and CFRP). It was observed that adding the polypropylene fibers significantly improved the bond durability owing to the restriction of the crack development at the interface, as the loss of ultimate bond strength of FRP bars in plain concrete owing to aging effects was found to be 28% on average, whereas only a 6% reduction was observed in the FRC specimens. In addition, it was noticed that degradation of bond is tightly correlated with the degradation of FRP bar, as substantiated by the findings in this study. Thus, CFRP specimens had superior long-term bond durability compared with GFRP specimens due to the more durable characteristics of the CFRP bar.

Altalmas et al. (2015) investigated the bond durability of sand-coated basalt fiber-reinforced polymer (BFRP). Sixty-two sand-coated BFRP and ribbed GFRP were tested under direct tensile load after being exposed to accelerated conditioning environments. The test parameters included the bar material (basalt and glass), the conditioning environment (acid, saline, and alkaline), and the duration of exposure (30, 60, and 90 days). The bond behaviour of the tested specimens was reported in terms of stress–slip response, bond strength, bar slip, adhesion, and failure mechanism. The BFRP bars showed higher adhesion and bond strengths to concrete than the ribbed glass fiber-reinforced polymer (GFRP) bars irrespective of the fiber type and the exposure condition.

Yan and Lin (2017) studied the bond durability of GFRP bars to fiber-reinforced concrete (FRC) exposed to saline solutions. One hundred and five pullout specimens reinforced with steel and polyvinyl alcohol (PVA) fibers were prepared and immersed in the saline solutions at 50 and 70 °C under 30, 45, and 60 days, respectively. Their durability was quantified in terms of failure mode, adhesion stress as well as the bond strength. Test results revealed that the steel FRC samples

exhibited the better bond durability than that of PVA-FRC ones, when the same fiber volume fraction was used, as the reduction of bond strength due to weathering was about 10% for the steel FRC specimens with fiber contents of 1.0% as compared to 16% for the plain concrete specimens.

2.4 Behaviour of Deep Beams

2.4.1 Overview

Generally, deep beams are the main load transfer element in many structures such as bridges, pile caps and in high-rise buildings. There are many successful trials to investigate the behaviour of steel-reinforced concrete (RC) simply-supported deep beams. The results were conclusive, demonstrating that the strut-and-tie model (STM) is a rational method to design and analysis deep beams. Consequently, strut-and-tie model (STM) has been adopted by several codes and guidelines, including the Canadian code (CSA/S806-17, CSA/A23.3-19 and CSA/S6-19) and the USA codes and guidelines (AASHTO LRFD 2014 and ACI 318-19).

2.4.2 Deep members

Shear failure of reinforced concrete members (without web reinforcement) takes place after the formation of diagonal tension cracks. The shear stresses are transmitted by combination mechanisms which identified by the joint ASCE-ACI Committee 445 (1998), as shown in Figure 2.2:

- 1) Shear stresses in un-cracked concrete, that is, the flexural compression zone (V_{cz});
- 2) Interface shear transfer, often-called aggregate interlock or crack friction (V_a);
- 3) Dowel action of the longitudinal reinforcing bars (V_d);
- 4) Arch action; and
- 5) Residual tensile stresses transmitted directly across cracks.

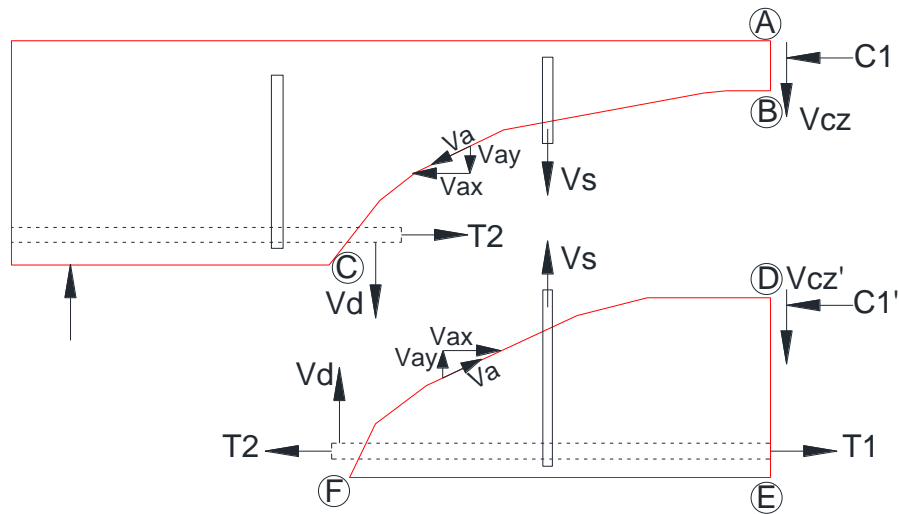


Figure 2.2: Failure surface showing the internal forces (Reproduced from Wight and MacGregor 2009)

Accordingly, the joint ASCE-ACI committee 445 (1998) explained the preceding mechanisms as follows:

Before the initiation of cracks in beam, the shear force is transmitted by inclined principal tensile and compressive stresses. After the occurrence of cracks, such statement will be valid in the uncracked compressive zone.

Aggregate interlock, in normal strength concrete, takes place due to the resistance to relative slip between two rough interlocking surfaces of the crack. In high strength concrete, the cracks pass through the aggregate; hence, the aggregate interlock contribution to the shear strength is lower for beams made of high strength concrete.

The contribution of dowel action is deemed insignificant in member without transverse reinforcement. This can be attributed to that the maximum shear in a dowel is limited by the tensile strength of the concrete cover supporting the dowel. Dowel action may be significant in members

with large amounts of longitudinal reinforcement, particularly when the longitudinal reinforcement is distributed in more than one layer.

The residual tensile stresses can be illustrated as follows: when the crack in a concrete beam initiates, a full break does not take place; however, small pieces of concrete will bridge the crack and continue to transfer tensile force up to crack width in the range of .05 to .15 mm.

The arching action mechanism occurs in deep beams, which are defined by Wight and MacGregor (2009) in which a significant amount of load is carried to the supports by a compression thrust linking the load and the reaction. This phenomenon takes place if a concentrated load acts closer than about $2d$ to the support, or for uniformly loaded beams with a span-depth ratio, l_n/d less than about 4 to 5; where: d is the depth of the member, l_n is the total span of the member, and a is the distance between a concentrated load and the support. In deep members, the assumptions of plane sections remain plane and uniform shear stress distribution used in the design and analysis of slender members are not valid. If sectional shear design approaches are used for deep members, the true shear capacity can be much higher. A nonlinear strain distribution dominates the deep member behaviour. Therefore, empirically derived design methods, truss models, or finite element analysis are some of the techniques used in analysis and design of non-slender members. One common method is the strut and tie model (STM) which is the method of interest in this research project and is described in section 2.4.3.

2.4.3 Strut-and-tie model

Strut and tie modeling is a technique used to analyze regions of nonlinear strain distributions. Nonlinear strain distributions in concrete members are caused by changes in geometry or loading and are commonly referred to as disturbed regions or D-regions. The remaining portions of the

member that are not subjected to disturbances are referred to as B-regions, as illustrated in Figure 2.3.

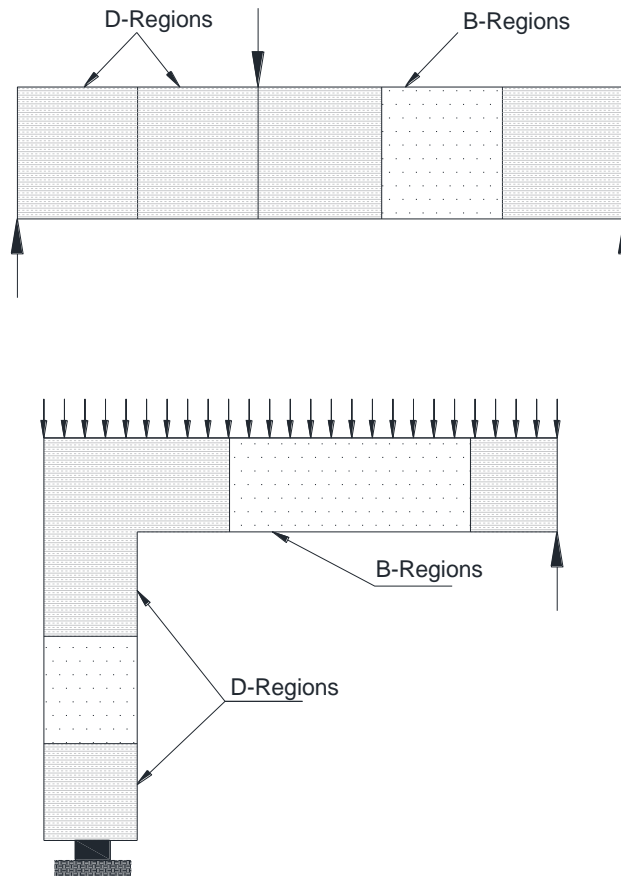


Figure 2.3: B-regions and D-regions (Reproduced from Wight and MacGregor 2009)

For the strut and tie modelling technique, the flow of forces in a simply supported deep member after cracking is idealized using a pin-jointed truss model consisting of compression struts and tension ties. The struts and ties intersect at nodes. Therefore, STMs consist of three main elements: struts, ties, and nodes. Struts are used to represent the assumed compressive stress fields in the concrete after cracking. Ties represent the primary tension reinforcement with the tie location made to correspond to the centroid of the reinforcement. An example of a STM for a beam under

four-point loading is shown in Figure 2.4. The nodes are the points where struts and ties meet in STM. They are idealized as pinned joints. Nodal zones are the concrete surrounding the nodes as shown in Figure 2.4. There are three or four forces acting on the node to achieve node equilibrium. Accordingly, nodal zones are classified as C-C-C, C-C-T or C-T-T depending on the type of forces acting on the node as shown in Figure 2.5 where “C” and “T” stands for compression and tension, respectively.

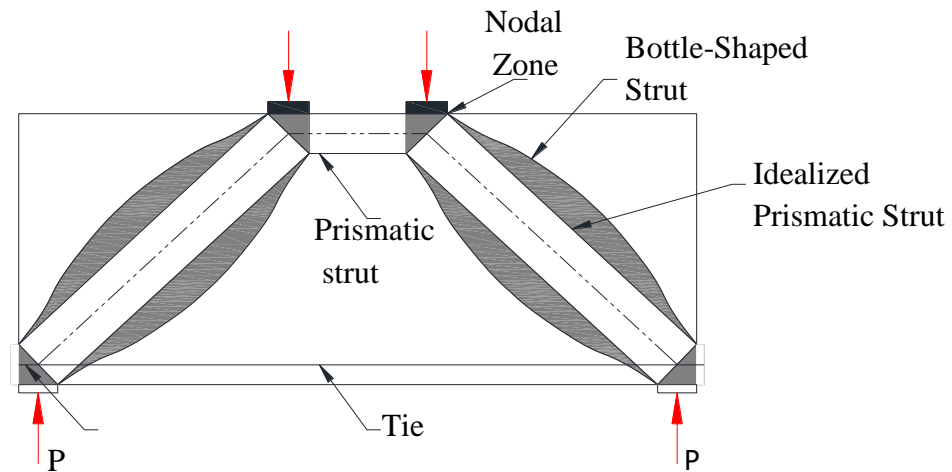


Figure 2.4: Strut and tie model of a simply supported deep beam containing no web reinforcement (Reproduced from Wight and MacGregor 2009)

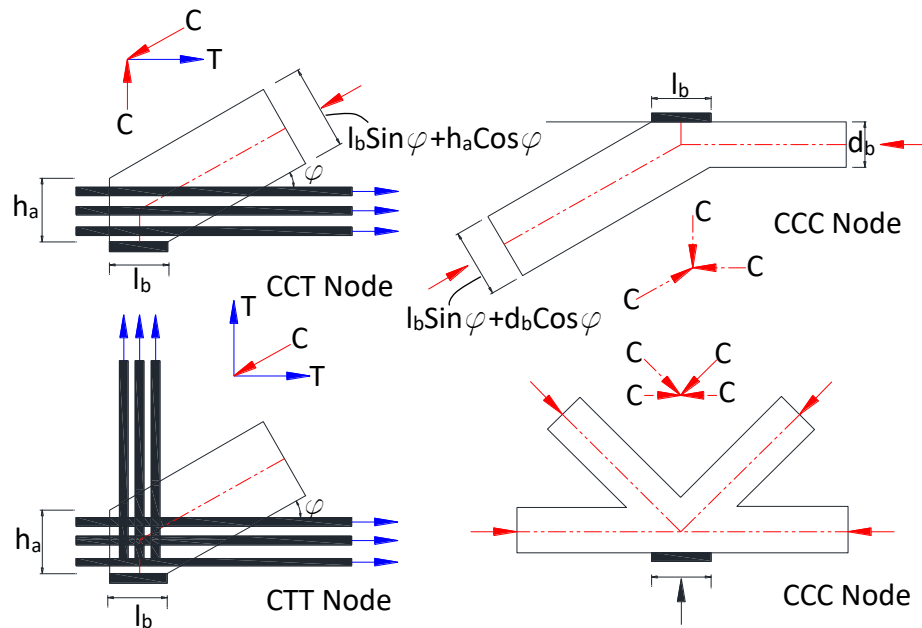


Figure 2.5: Nodal zones (Reproduced from Mohamed 2015)

2.4.4 Previous research on FRP reinforced concrete deep beams

Brown and Bayrak (2007) tested 10 deep beams to examine the impact of load distribution and shear reinforcement on the behaviour of the beams. The specimens were 686-mm in depth and 3048-mm in effective span but with different amount of vertical-only or horizontal-only web reinforcement. They observed that the two specimens with only horizontal web reinforcement carried less shear than the counterpart specimens with no shear reinforcement of any kind. They explained that this counterintuitive result was likely due to the large amounts of scatter associated with the shear strength of reinforced concrete beams. On the other hand, a small amount of vertical reinforcement increased strength much more effectively than a large amount of horizontal reinforcement. However, additional vertical reinforcement did not seem to produce any additional increase in shear strength.

Omeman et al. (2008) presented the experimental results of eight CFRP reinforced, seven GFRP reinforced, and four steel reinforced concrete deep beams. The main variables in the test program were the a/d ratio, effective depth, axial stiffness of the reinforcement, and the concrete strength. The majority of the specimens had an effective depth, d , of 150 mm. Specimens having an effective depth of 250 and 350 mm were also tested. The a/d ratio ranged from 1.4 to 2.3 and the reinforcement ratio varied between 1.13 and 2.33%. Normal strength concrete (target $f_c' = 35$ MPa) and high strength concrete (target $f_c' = 60$ MPa) mixes were used but the final normal concrete strength varied from 35 MPa to 48 MPa and the high strength concrete achieved 63 MPa. The beams were tested in a four-point bending configuration using load control. It was observed that the shear strength increased as the reinforcement ratio increased. The shear capacity of the CFRP reinforced specimens was reported to be higher than the shear capacity of the steel reinforced specimens having the same effective depths, a/d ratios and similar reinforcement ratios and concrete strengths. It was found that the shear strength of the CFRP-reinforced short beams was proportional to the cubic root of the reinforcement ratio, $(\rho)^{1/3}$.

El-Sayed et al. (2012) studied the shear strength and behaviour of concrete deep beams reinforced with fiber-reinforced polymer (FRP) bars. Ten full-scale reinforced concrete beams without web reinforcement were constructed and tested in four-point bending. Five beams were reinforced with CFRP bars, and five beams were reinforced with GFRP bars. The tested beams were 2,600-mm long, 250-mm wide and 400-mm deep. The test variables were the reinforcement ratio and the modulus of elasticity of the longitudinal reinforcing bars as well as the shear span to depth ratio. All ten beams showed significant reserve strength after the inclined cracking was fully developed. The test results also indicated that the ultimate shear strength of the tested beams considerably increased with the decrease of the shear span to depth ratio. It was concluded that the shear strength

of the reinforced concrete deep beams without web reinforcement was proportional to the amount of FRP longitudinal reinforcing bars. As the amount of longitudinal reinforcement was increased, the obtained shear strength increased. This behaviour was observed for the two different types of FRP reinforcing bars employed in this study.

Campione (2012) conducted an experimental research to evaluate the flexural behaviour of deep beams cast with plain and fibrous concrete with hooked steel fibers and subjected to monotonic vertical loads. Four deep fiber-reinforced concrete beams were cast. Two of them were made of plain concrete, where the main and web reinforcements were steel, and two were made of hooked steel fiber-reinforced concrete (SFRC) with main steel reinforcements. Hooked steel fibers having a length of 30 mm and a diameter of 0.5 mm were utilized in a percentage of $v_f = 1.0\%$ by volume, corresponding to 80 kg/m^3 of fibers. Steel fibers, according to the manufacturer, had a tensile yielding stress of 1,115 MPa. Using SFRC showed an increase in the maximum strength and ductility compared to RC deep beams. It also has to be noted that although the strength of an RC beam can always be increased by using higher-strength concrete or different dimensions or increasing the amount of bars, etc., an increase in ductility is more difficult to achieve, and the use of fibers is a simple way to achieve this objective. The author observed that using steel fibers is deemed as a viable alternative to web reinforcement.

Andermatt and Lubell (2013) investigated the behaviour of concrete deep beams reinforced internally with GFRP. Twelve deep beams with heights ranged from 306 mm to 1,005 mm were tested to failure under 4-point bending. The specimens contained longitudinal GFRP reinforcement but no stirrups or distributed web reinforcement. The primary test variables included the a/d ratio, which varied from 1.1 to 2.1 and the longitudinal reinforcement ratio. The results indicated that the load carrying capacity of the specimens decreased as the a/d ratio increased. Increasing the

reinforcement ratio resulted in a slight increase in capacity. Beam with lower a/d ratio showed extremely ductile behaviour after concrete crushing in the flexural compression region was detected.

2.7 Closure

Demands for using new innovative high strength/high ductility cementitious composites incorporating non-metallic fibers for field applications have been growing to alleviate/diminish the shortcomings associated with the concrete brittleness and the corrosion of metallic fibers. Thus, the use of an innovative composite incorporating BP that behave comparably to the most commonly used metallic-fiber (e.g. steel fibers) is imperative. In addition, there is dearth of research data on the application of non-metallic fibers in structural application. Hence, further investigations in the short/long term performance under ambient and harsh conditions of this composite are required, as it might be affected by a multitude of parameters including the cementitious matrix, the dosage of fiber, and the exposure regime.

In particular, no published work has focused on investigating the effect of incorporating non-metallic fibers as layer in the tension tie in deep beams. In addition, the general notion that discrete fibers can replace the web reinforcement and increase the ductility of deep beams was substantiated based on the results steel fibrous reinforced concrete deep beams. Hence, phase II and III tend to challenge this notion, as Phase II will start at identifying the interaction and bond between the new composite and the reinforcing bar, and then Phase III will explore the performance of simply-supported layered deep beams to gauge the reliability and practicality of this composite for structural application

CHAPTER 3: RESIDUAL MECHANICAL PROPERTIES OF BPRCC UNDER CYCLIC ENVIRONMENTAL CONDITIONS

Authors and Affiliation:

- Ahmed G. Bediwy, PhD Candidate, Department of Civil Engineering, University of Manitoba.
- Mohamed T. Bassuoni, Professor, Department of Civil Engineering, University of Manitoba.
- Ehab F. El-Salakawy, Professor, Department of Civil Engineering, University of Manitoba.

Journal and Status:

American Society of Civil Engineers (ASCE) Journal of Materials in Civil Engineering, accepted for publication on February 11, 2021.

Reference:

Bediwy, A., Bassuoni, M., and El-Salakawy, E. (forthcoming a). “Residual mechanical properties of BPRCC under cyclic environmental conditions.” *Journal of Materials in Civil Engineering.*, ASCE, in press.

Note:

The manuscript had been slightly altered from the original paper by renumbering the tables and figures to include the chapter number. In addition, the reference list and list of notations have been moved to the appropriate sections in the thesis as indicated in the table of contents.

Abstract

In this study, the performance of basalt pellet-reinforced cementitious composites (BPRCC) was evaluated after exposure to harsh conditions. The exposure consisted of consecutive 300 freeze-thaw cycles followed by 75 wet-dry cycles simulating successive winter and summer seasons. The mixtures, incorporated general-use cement, slag, and nano-silica, and reinforced with either the recently developed basalt fiber pellets (BP) - basalt fiber strands coated by a polymeric resin - or steel fibers. The resilience of composites was assessed by internal damage, residual compressive and flexural strengths, as well as their compatibility with base/parent concrete, when used in a layered system with normal concrete. The incorporation of 40% slag, as a partial replacement of cement, and 6% of nano-silica with the presence of BP, significantly enhanced the residual mechanical properties of composites exposed to aggravated environmental conditions, which makes them a promising candidate for construction of exposed infrastructural elements.

Keywords: Environmental exposures, nano-silica, basalt pellets, fiber-reinforced cementitious composites, residual mechanical properties, dimensional stability.

3.1 Introduction

The early-age limitations [e.g. delay in hardening and strength development] associated with concrete comprising high-volume of supplementary cementitious materials (SCMs) such as slag (latent hydraulic binder) can be mitigated by incorporating small dosages of reactive nanoparticles. In particular, ultrafine nano-silica (Ns) [size scale of 1-100 nm with high content of amorphous silica $\geq 99\%$] has been widely used in cementitious materials research. Several studies reported that incorporating controlled dosages (2 to 6%) of well-dispersed Ns along with SCMs shortened the setting time and enhanced the early-age strength of cement pastes, mortars and concretes (Li et al. 2004; Qing et al. 2007; Ghazy et al. 2016). The ultrafine nature of Ns vigorously accelerates the kinetics of cement hydration by creating additional surfaces for early precipitation of hydration product and the early pozzolanic reactivity of Ns (within the first day of cement hydration) are among the key reasons behind the improvement of the microstructure of concrete with SCMs at early-age (Said et al. 2012; Madani et al. 2012).

Plain (non-reinforced) mortar/concrete has low tensile/deformational capacity and resistance to cracking. When micro-cracks connect together to form a continuous network, this will lead to permeable concrete, which in turn may increase the possibility of ingress of chloride ions, oxygen and moisture causing corrosion of reinforcing steel and deterioration of concrete infrastructure (Vasanelli et al. 2013; Muhammad et al. 2015). In cold regions (e.g. North America), concrete is subjected to de-icing salt and repetitive freeze-thaw cycles. This will allow water to enter the cracks during the thawing period of the cycle to freeze again later, which causes a progressive deterioration of the concrete with each freeze-thaw cycle. Therefore, the use of fiber-reinforced concrete (FRC) has been proposed to expand the applications of concrete in such harsh environments, especially for developing high performance mortars/composites to strengthen and

rehabilitate concrete infrastructure [e.g. bridge elements, pavements, parking structures] (Nes and Øverli 2015). Incorporating discrete fibers into cementitious composites may significantly improve their engineering properties such as the tensile strength as well as resistance to impact, fatigue and abrasion. The most pronounced advantages of fibers in cementitious composites are providing the composite with pseudo strain-hardening behaviour, increasing the energy absorbing capacity/toughness and transforming the mode of failure from brittle to ductile (Wille et al. 2012). This has been attributed to the fibers' ability to bridge cracks and to transfer tensile stresses across crack openings (Bentur and Mindess 2007).

Different types of fibers, such as steel, synthetic, organic and inorganic, have been used to make fiber-reinforced cementitious composites (FRCC). Basalt fibers are a relatively new type of inorganic fibers manufactured by the extrusion of melted basalt rocks. The basalt fibers are gaining momentum in the construction market since the production process of basalt fibers is more environment friendly, and it is cheaper with respect to other types of fibers such as glass fibers. Basalt fibers have high tensile strength (3,000 - 4,000 MPa), reasonable modulus of elasticity (93 - 110 GPa), and they are not vulnerable to surface corrosion contrary to the case of metallic (e.g. steel) fibers (Iyer et al. 2015; Mahmoud et al. 2017). Nevertheless, basalt fibers are prone to severe degradation when incorporated in high alkaline media (e.g. concrete); thereby, a special type of basalt fiber pellets (BP), which are made of basalt fiber strands coated by alkali resistant polymeric resins (e.g. epoxy or polyamide) was adopted in recent studies (Mahmoud et al. 2017; Bediwy et al. 2018; Azzam et al. 2019). However, research on this topic is still at early stages.

3.2 Research Significance

In a previous study at the University of Manitoba, Mahmoud et al. (2017) evaluated the behaviour of high-strength nano-modified cementitious composites incorporating 6% NS with 40% slag and reinforced with BP (BPRCC) in terms of compressive strength, flexural strength, and toughness. It was concluded that BPRCC had an acceptable rate of hardening and improved mechanical properties and ductility. However, this work used only one dosage of BP (2.5%) and the results were not compared with those of the commonly used fibers in the concrete industry (e.g. steel fibers). In addition, those tests were conducted under ambient laboratory conditions after curing and did not involve harsh environments (e.g. freeze-thaw and wet-dry cycles), which are customarily encountered in the field. In addition, the concept of using such novel composites in layered-systems was not tested. These layered systems can be economically used to improve the efficiency of concrete members. For example, if the composite is cast as a layer in the tension side of new structural members, it would enhance their bond and post-cracking characteristics, which may presumably prolong the service life of such members and discount their maintenance costs. Hence, this study aimed at experimentally assessing the mechanical performance of BPRCC before and after exposure to consecutive freeze-thaw and wet-dry cycles simulating consecutive winter and summer seasons in cold regions. Furthermore, these composites were used in a layered system with parent concrete and their compatibility were tested before and after the same combined exposure.

3.3 Experimental Program

3.3.1 Materials

General Use (GU) cement (ASTM Type I) was used in the present study. Grade 100 ground granulated blast furnace slag was used at 40% replacement of cement. Both cementitious materials,

complying with the requirements of CSA-A3001 standard (2018), were used for producing the base binder of the composite. Table 3.1 summarizes the chemical and physical properties of the cement and slag used in this study.

Table 3.1: Chemical and physical properties of GU cement and slag

Binder	Chemical composition (%)							Physical properties	
	SiO ₂	Al ₂ O ₃	Fe ₂ O ₃	CaO	MgO	SO ₃	Na ₂ O _{eq}	Blaine (m ² /kg)	Specific Gravity
Cement	19.21	5.01	2.33	63.22	3.31	3.01	0.12	390	3.15
Slag	33.40	13.4	0.76	42.70	5.30	2.40	0.30	492	2.87

In addition, a commercial Ns sol - aqueous solution with 50% solid content of SiO₂ particles - was added to the binder at a dosage of 6% by mass of the base binder. The mean particle size of the Ns is 35 nm, and the specific surface, viscosity, density and pH values were 80 m²/g, 8 cP, 1.1 g/cm³ and 9.5, respectively - as provided by the manufacturer. Locally available fine aggregate, with a fineness modulus of 2.9 and a gradation of 0 to 600 μm, according to ASTM C136 (2019a), was used to prepare the mixtures. The specific gravity and absorption of the fine aggregate were 2.6 and 1.5%, respectively, according to ASTM C128 (2015). A high-range water-reducing admixture (HRWRA) based on polycarboxylic acid and complying with ASTM C494 Type F (2019b) was added to maintain a target flow of 200±15 mm for all the mortar mixtures. The cementitious composites were reinforced with either BP or steel fibers (SF), as shown in Figure 3.1. The 36-mm long and 1.8-mm diameter BP were made of 16-micron basalt roving coated by polyamide resin with the BF represented 60% of the pellet by weight. Hooked-end SF of diameter 0.5 and 30-mm length were also used. The properties of the BP and the SF are listed in Table 3.2.

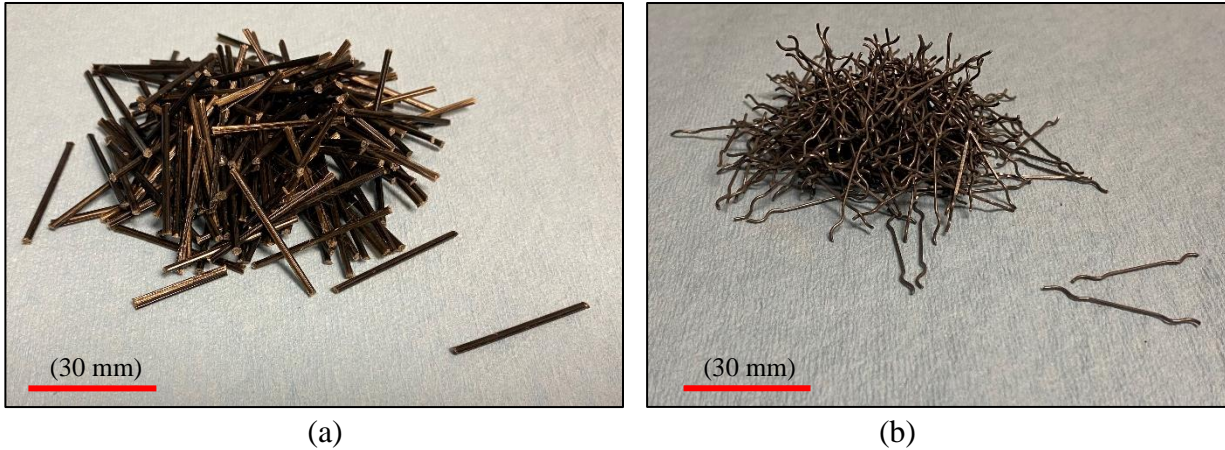


Figure 3.1: Reinforcing fibers, (a) basalt fiber pellets, and (b) steel fibers

Table 3.2: Properties of fibers

Properties	Properties of fibers	
	BP	Hooked steel
Length (mm)	36	30
Diameter/dimensions (mm)	1.80	0.65
Aspect ratio	20	45
Specific gravity	1.74	7.70
Tensile strength (MPa)	2,300	1,200
Elastic modulus (GPa)	65	200

3.3.2 Proportions and mixing procedures

For the composites, two different mixtures were produced in this study: normal cementitious composite (designated as N), and high-performance cementitious composite (designated as H). The N mixture was prepared with GU cement (700 kg/m^3), while the H one was prepared with GU cement and a constant dosage of slag (280 kg/m^3), representing 40% replacement by mass of the binder (700 kg/m^3 comprising GU cement and slag); in addition, Ns was added at a dosage of 6% by mass of the binder. The water-to-binder ratio (w/b) was kept constant at 0.30 for both mixtures. The mixtures were reinforced with either BP or SF. Two approaches were adopted to select the range of dosages of BP, when compared to SF: maintaining either the same volume or the same stiffness (multiplier of the fiber volume by the modular ratio defined as the ratio of modulus of

elasticity of SF to that of BP). The BP was added to the mixtures at different dosages of 2.5%, 4.5% and 6.9% by volume, corresponding to 1%, 2% and 3%, respectively, of basalt fibers, whereas in the case of SF, it was 1%. It is worth mentioning that the composites with 6.9% BP and 1% SF had the same stiffness, as defined earlier.

The control mixtures were made with the same constituents but without fibers. The proportions of all the cementitious composites are listed in Table 3.3. For the mixture coding, the first part refers to the type of the cementitious composite (“N” for normal composite and “H” for high-performance composite), whereas the second part denotes the fiber type (“B” for basalt fiber pellet and “S” for steel fiber). The third part represents the fiber dosage used. As for the normal concrete used with the composites in the layered system, only one mixture was used, which met the requirements stipulated by the City of Winnipeg (COW), Manitoba, Canada, for structural concrete works of bridge decks. These specifications require a 28-day concrete compressive strength of 35 MPa that meets a C-1 class of exposure (this class of exposure specified for structurally-reinforced concrete exposed to chlorides with freezing and thawing conditions) and comprising synthetic fibers (100% virgin polypropylene) to meet the requirements for residual post-cracking index of 0.15 at 7 days.

For each mixture, triplicate prisms (100×100×350 mm), triplicate cylinders (100×200 mm), and duplicate slabs (250×250×100 mm) were prepared and tested before and after exposure to consecutive freeze-thaw (F/T) and wet-dry (W/D) cycles. The prisms and slabs were cast using the FRCC and normal concrete layers (layered specimens), whereas the cylinders were fully cast using the FRCC. The mixing procedures introduced by Mahmoud et al. (2017) was followed herein. In the layered specimens, the FRCC layer was cast first (bottom/tension face) with a thickness of 40 mm, and within one hour, the normal concrete layer was cast above it to improve the integrity of

the bond between the two layers. After casting, all specimens were covered with plastic sheets for the first day, then demolded and cured in standard curing room for 27 days.

Table 3.3: Proportions of the mixtures per cubic meter

Mixture ID.	Cement (kg)	Slag (kg)	Water ^a (kg)	Nano-silica (Ns, kg)	Fine aggregate (kg)	HRWRA (L)	Fibers (kg)		Air content (%)	RE_n^* (%)
							BP	Hooked steel		
N-X-0.0	700	-	210	-	1,471	5.7	-	-	5.9	71.4
H-X-0.0	420	280	180	84	1,328	7.4	-	-	5.4	79.5
N-B-2.5	700	-	210	-	1,406	5.7	43.3	-	6.7	83.2
N-B-4.5	700	-	210	-	1,354	5.7	78.3	-	7.3	88.6
N-B-6.9	700	-	210	-	1,293	5.7	119.2	-	7.8	90.2
N-S-1.0	700	-	210	-	1,445	5.7	-	77	6.8	85.4
H-B-2.5	420	280	180	84	1,268	7.4	43.3	-	6.4	87.6
H-B-4.5	420	280	180	84	1,211	7.4	78.3	-	6.9	93.8
H-B-6.9	420	280	180	84	1,150	7.4	119.2	-	7.5	94.6
H-S-1.0	420	280	180	84	1,302	7.4	-	77	6.2	88.5

^aAdjusted amount of mixing water considering the water content of nano-silica (aqueous solution with 50% solid content of SiO₂).

* RE_n denotes the relative dynamic modulus of elasticity after the freeze-thaw portion of the combined exposure.

3.3.3 Exposure

For exposed specimens, the combined cyclic regime consisted of 300 F/T and 75 W/D cycles. This exposure simulated consecutive winter and summer seasons, which correlates to in-service conditions in cold regions. The F/T cycles were applied in accordance with ASTM C666, procedure A (2019c) that requires alternately lowering the temperature from +4 to -18°C for freezing and raising it from -18 to +4°C for thawing. For each cycle, the peak temperature at freezing (-18°C) and thawing (+4°C) was kept for 2 hrs. It should be noted that there are no standard test methods for the W/D exposure of concrete. The cyclic regime in this study was selected similar to that adopted by Bassuoni and Rahman (2015) to achieve significant moisture changes and aggravated test conditions. The exposure continued for 75 days, where each cycle (24

hrs) consisted of two consecutive stages: an 8-hr hot/dry stage ($40\pm 2^{\circ}\text{C}$ and $35\pm 5\%$ RH) followed by a 16-hr temperate/humid stage ($20 \pm 2^{\circ}\text{C}$ and $90\pm 5\%$ RH).

3.3.4 Tests

To determine the residual compressive strength of the mixtures, triplicate cylinders were tested before and after the exposure according to ASTM C39 (ASTM 2020a). Following the guidelines of ASTM C1609 (ASTM 2019d), four-point bending tests were carried before and after exposing the layered prisms to the aforementioned exposure regime to evaluate the residual flexural performance of the mixtures using triplicate standard prisms. A closed loop servo-controlled testing machine (Figure 3.2) was used to apply the load, where the displacement rate was governed by the measured net mid-span deflection of the prism.

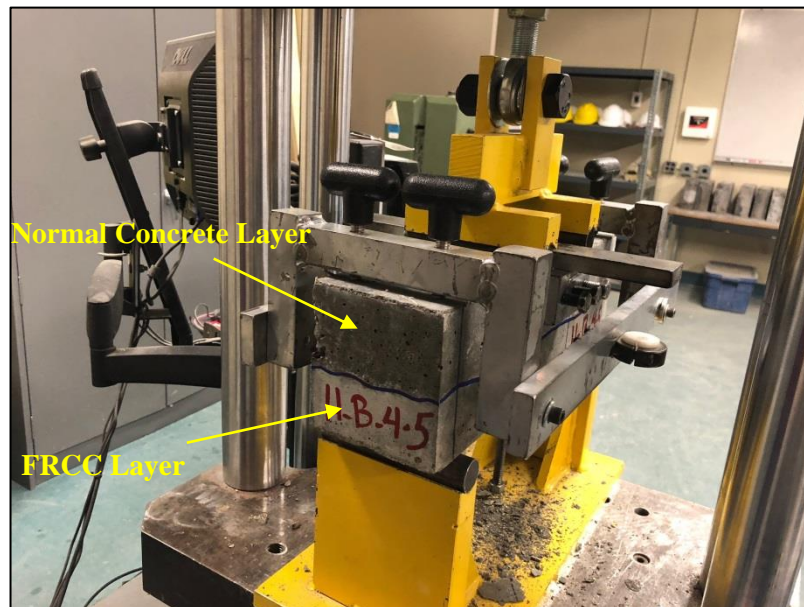


Figure 3.2: Flexural test set-up showing a layered prism

The residual strength at net deflection of $(\text{span}/600)$ and $(\text{span}/150)$ was calculated based on Equation 3.1:

$$f = \frac{P\ell}{bd^2} \quad \text{Equation 3.1}$$

where, f is the strength (MPa), P is the load (N), ℓ is the span length (mm), b is the average width of the specimen at the fracture, as oriented for testing (mm), and d is the average depth of the specimen at the fracture, as oriented for testing (mm). The flexural toughness is commonly defined as the area under the load-deflection curve (P - δ), and it is also referred to as the total energy to fracture (Bentur and Mindess 2007). However, in this study, the toughness was calculated according to ASTM C1609 (ASTM 2019d) as the area under the P - δ curve up to a deflection equals to span/150 (i.e. 2 mm for the prism size used).

The air content of the freshly mixed composites was measured according to ASTM C231 (2017). To evaluate the frost resistance of cementitious composites, the relative dynamic modulus of elasticity was evaluated during the cyclic exposure using the resonance frequency method on the layered prisms (transverse mode) according to ASTM C215 (2019e). The relative dynamic modulus was calculated as per ASTM C666 (2019c) by the following equation:

$$RE_n = \left(\frac{F_n^2}{F_o^2} \right) \times 100 \quad \text{Equation 3.2}$$

where, RE_n is the relative dynamic modulus at n cycles of exposure (%), F_n is the fundamental transverse frequency at n cycles (kHz), and F_o is the initial fundamental transverse frequency (kHz).

To assess the dimensional stability and compatibility between the two layers, concrete slabs were cast. After demolding, four pairs of demec points were attached to the surface and sides of each slab across a length of 200 mm (Figure 3.3). The length change was measured by a dial gauge extensometer to record the average deformation of two slabs for each mixture. The relative shrinkage of the cementitious composites was measured under moist curing (21°C and > 95% RH)

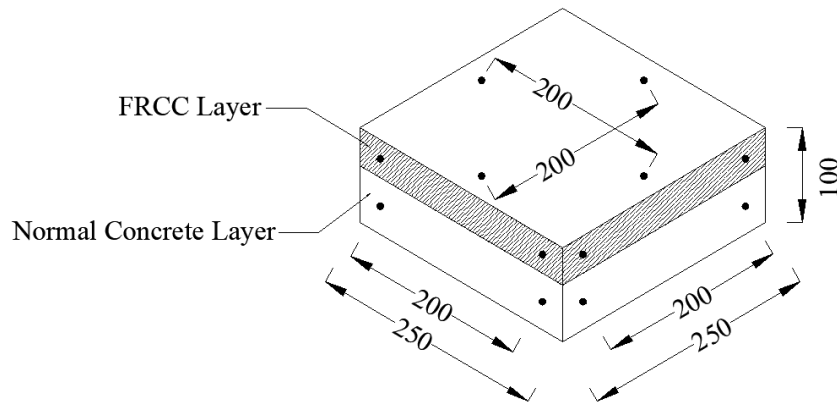


Figure 3.3: Locations of Demec points for relative shrinkage test (all dimensions in mm)

up to 28 days. The specimens were then moved to a hot/dry exposure of $40\pm 1^\circ\text{C}$ and $35\pm 5\%$ RH and the cumulative shrinkage of the fibrous composite layer was monitored for up to 148 days. In addition, duplicate layered slabs were partially cored to determine the pull-off strength before and after the exposure according to ASTM C1583 (ASTM 2020c).

3.4 Results and Discussion

3.4.1 Mechanical performance of composites

3.4.1.1 Compressive capacity

A summary of the results for the reference/unexposed specimens tested at 28 days and after the cyclic F/T and W/D exposure is given in Tables 3.4 and 3.5. Irrespective of the type and dosage of fibers used, the composites comprising Ns and high-volume slag yielded higher compressive strength than that of composites with plain cement. For example, the compressive strength of the control H composite (H-X-0.0) was markedly increased by 33 and 45% before and after the combined exposure relative to that of the control composite (N-X-0.0), which was 71 MPa and 49 MPa, respectively. This might be attributed to the reported synergistic effects of Ns and slag at

refining and densifying the pore structure of the matrix and thus increasing its compressive strength after curing for 28 days. This was confirmed by thermogravimetry analysis conducted

Table 3.4: Mechanical properties of the reference cementitious composites tested at 28 days

Mixture ID	Compressive strength (MPa)	Flexural test results at 28 days			
		First-peak strength (MPa)	Residual strength L/600 (MPa)	Residual strength L/150 (MPa)	Toughness (J)
N-X-0.0	71.3 (4.2)	5.8 (0.3)	0.6	0.5	8.20 (0.2)
H-X-0.0	94.5 (6.3)	7.1 (0.1)	1.2	1.8	13.1 (1.1)
N-B-2.5	64.1 (1.2)	6.8 (0.2)	3.6	4.0	26.8 (2.3)
N-B-4.5	59.1 (2.6)	5.8 (0.4)	4.9	4.6	32.0 (0.8)
N-B-6.9	53.8 (1.9)	5.6 (0.1)	5.4	4.5	33.4 (1.9)
N-S-1.0	78.7 (5.8)	7.1 (0.2)	4.6	1.8	23.5 (0.2)
H-B-2.5	81.3 (2.5)	6.8 (0.2)	5.2	5.0	33.8 (0.8)
H-B-4.5	70.3 (3.1)	6.6 (0.3)	7.8	7.6	47.4 (1.7)
H-B-6.9	63.8 (0.9)	6.1 (0.1)	7.8	7.4	45.2 (2.1)
H-S-1.0	98.8 (9.2)	7.4 (0.1)	7.3	4.6	39.4 (0.6)

Note: numbers in parentheses represent standard deviations.

Table 3.5: Residual mechanical properties of the cementitious composites after F/T and W/D cycles

Mixture ID	Compressive strength (MPa)	Flexural test results			
		First-peak strength (MPa)	Residual strength L/600 (MPa)	Residual strength L/150 (MPa)	Toughness (J)
N-X-0.0	49.3 (1.3)	4.0 (0.1)	0.8	0.6	6.1 (0.1)
H-X-0.0	71.3 (2.1)	4.7 (0.1)	1.8	0.5	8.1 (0.1)
N-B-2.5	54.2 (1.6)	5.1 (0.3)	2.5	2.9	25.2 (1.3)
N-B-4.5	52.1 (1.5)	4.7 (0.2)	4.2	4.5	28.2 (1.6)
N-B-6.9	49.7 (2.1)	4.8 (0.3)	3.7	3.8	28.9 (0.8)
N-S-1.0	58.5 (1.8)	6.3 (0.1)	4.2	1.7	19.3 (0.2)
H-B-2.5	73.4 (2.2)	5.4 (0.2)	3.1	3.7	30.7 (2.5)
H-B-4.5	67.4 (3.6)	5.3 (0.4)	7.8	5.4	39.5 (1.5)
H-B-6.9	58.4 (0.9)	5.6 (0.6)	7.7	4.8	40.3 (2.2)
H-S-1.0	81.2 (4.8)	6.7 (0.3)	5.2	2.1	29.5 (0.7)

Note: numbers in parentheses represent standard deviations.

by Mahmoud et al. (2017) at the University of Manitoba to quantify the relative amount of portlandite (CH amount). It was found out that significant consumption of CH in the mixture containing 40% slag and 6% Ns at 28 days relative to the reference mixture (without SCMs). This highlighted that the presence of Ns catalyzed the reactivity of slag in concrete, resulting in an improved level of hydration and evolution of microstructure. However, both types of composites (N and H) had lower compressive strength after the combined exposure, likely due to the formation of micro-cracks in the matrix. For instance, irrespective of the dosage and type of fibers added, exposing the N and H composites to the combined cyclic regime decreased the average compressive strength by 19 and 10%, respectively. The less degradation of the H composites conformed to the densified nano-modified slag-based matrix, which originally had higher mechanical capacity (Table 3.4).

The effect of including fibers into the cementitious composites on the compressive strength had mixed trends. As the addition of BP and SF in the N and H cementitious composites showed decrease and increase, respectively, in the compressive strength values compared to counterpart specimens without fibers. Similar mixed trends were reported in the literature (Puertas et al. 2003; Zhang et al. 2009; Branston et al. 2016). For example, at 28 days, the incorporation of BP in the N composites at dosages of 2.5, 4.5 and 6.9% led to a reduction of 11, 17 and 25%, respectively. For H composites, these reductions were 14, 26 and 33%, respectively. It can be noted that the reduction consistently increased with the dosage of pellets, which can be ascribed to the increase in air content (Table 3.3) and interfacial transition zones (ITZs) in the matrix. On the other hand, adding 1% of SF in the N and H composites showed marginal increase in the compressive strength by 10 and 4%, respectively, likely due to the higher stiffness of SF.

After the cyclic exposure, the presence of BP, irrespective of the dosage or the type of the cementitious composite, effectively controlled the rate of deterioration and reduction in the compressive strength. For example, after the consecutive F/T and W/D cycles, the compressive strength of the control mixtures N-X-0.0 and H-X-0.0 decreased by 31 and 25%, respectively, while the inclusion of BP in specimens N-B-2.5, N-B-4.5, N-B-6.9, H-B-2.5, H-B-4.5 and H-B-6.9 yielded much less reduction in compressive strength of approximately 15, 12, 8, 10, 4 and 8%, respectively. This might be ascribed to the ability of the BP to control micro-cracks and maintain the integrity of the matrix during the entire combined exposure.

When the SF was added to the cementitious composites (either N or H), they showed more reduction in residual compressive strength compared with that of counterpart composites reinforced with BP. For example, exposing the N and H composites reinforced with 1% SF (N-S-1.0 and H-S-1.0) to the combined cyclic exposure reduced the compressive strength by 25 and 18%, respectively. These reductions were only 15 and 9%, respectively, when incorporating 2.5% BP in the similar composites (i.e. N-B-2.5 and H-B-2.5). This alluded to higher efficiency of BP at controlling micro-cracking in the cementitious matrix, likely due better interfacial bonding relative to SF, as discussed in the flexural performance section.

3.4.1.2 Flexural performance

The flexural strength of the layered prisms can be divided into two stages: pre-cracking and post-cracking. The first one defines the flexural capacity of the prism, while the second determines its ductility. It is worth mentioning that the highest tensile stress was carried by the nano-modified cementitious composite and no debonding was noticed at the interface between the nano-modified cementitious composite (bottom layer) and the normal concrete (top layer), as for example shown in Figure 3.4.

Regarding the pre-cracking stage, all the N and H mixtures after the combined exposure adopted in this study, showed a reduction in the first-crack/peak flexural strength (Table 3.5), compared with the initial one before exposure (Table 3.4). For example, the average residual first-crack strength for the N and H composites after the cyclic regime were 4.8 and 5.5 MPa, which corresponded to a reduction of 23 and 19% respectively, when it was compared with their counterpart unexposed composites. During the pre-cracking stage, the quality and properties of the cementitious matrix affected the capacity of the composite, i.e. up to reaching the first-crack/peak

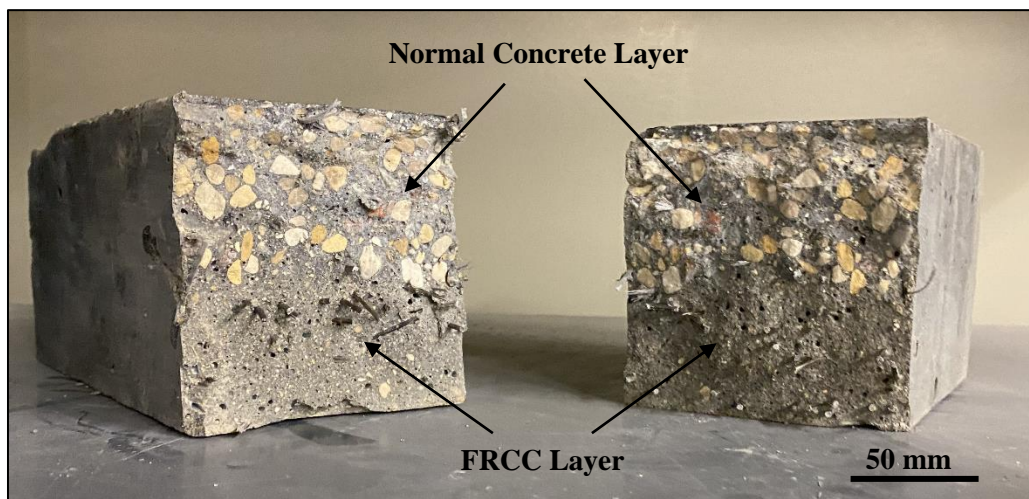
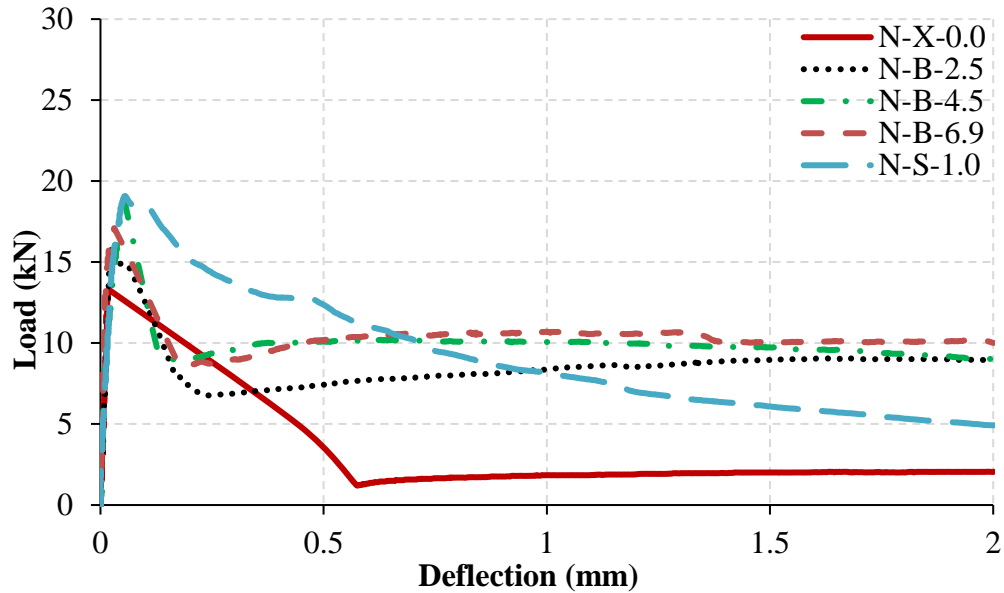


Figure 3.4: Exemplar failure plane of a layered prism from mixture H-B-2.5

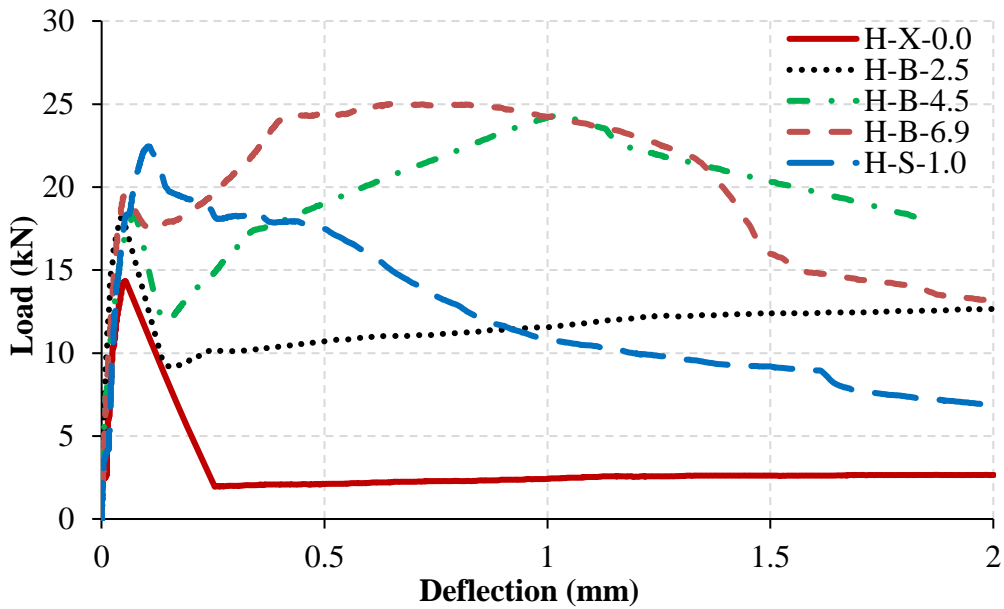
load. Micro-cracks induced by the cyclic regime, at the least by the tensile stresses generated during the F/T portion of the exposure as discussed in the next section, led to weakening the strength of the matrix. For instance, the average reduction in the first-crack/peak flexural strength for the N and H composites was 20 and 18%, respectively. The reason behind such a comparable trend was the progression of the hydration process for the N and H composites, especially with the high volume of cement and slag, respectively especially during the wetting portion of the combined exposure.

The presence of BP in the matrix contributed to delaying the propagation of these cracks during the first stage, as highlighted by maintaining higher residual flexural strength, with increasing the dosage of BP. For example, exposing the control composites (N-X-0.0 and H-X-0.0) to consecutive F/T and W/D cycles led to a 31 and 34% reduction in the first-crack/peak flexural strength, respectively. Comparatively, adding 2.5, 4.5 and 6.9% BP in both the N composites led to a reduction of 25, 19 and 15%, respectively in the first-crack flexural strength. For H composites, these reductions were 20, 18 and 7%, respectively. Analogously, the addition of SF had a noticeable effect in controlling the reduction of the first-crack flexural strength, since exposing the N and H composites that contained 1% of SF (N-S-1.0 and H-S-1.0) to cyclic environments led to a reduction of 11 and 10%, respectively, compared to that of their initial values before exposure. Representative $P-\delta$ curves for the layered prisms exposed to the F/T and W/D cycles are shown in Figure 3.5. All specimens exhibited comparable elastic behaviour before the appearance of the first-crack corresponding to small deflection values (maximum of 0.1 mm). Therefore, the moduli of elasticity were in the narrow range of 30 and 27 GPa for the N and H composites, respectively. After first-cracking, three different post-peak behaviours were observed in this study. The first one was an abrupt drop in the load (approximately 95% reduction in the peak load), which occurred in the control specimens (H-X-0.0 and N-X-0.0). The insignificant post-cracking behaviour for the latter composites was attributed to the presence of synthetic fibers (100% virgin polypropylene) in the top normal concrete layer. In addition, when slag and Ns were incorporated in the cementitious matrix, it showed higher resistance to the combined exposure and improved post-cracking behaviour. For example, the average residual toughness for the H composites was 30 J, which was 37% higher than that of the corresponding N composites (22 J) due to the synergistic effects of slag and Ns as discussed earlier. The second trend was deflection-softening behaviour

characterized by a descending branch in the load-deflection response; this behaviour was observed for the majority of the reinforced specimens (N-B-2.5, N-B-4.5, N-B-6.9, N-S-1.0, H-B-2.5 and H-S-1.0). The third trend was deflection hardening behaviour characterized



(a)



(b)

Figure 3.5: Representative load-deflection ($P-\delta$) curves for specimens after the combined exposure, (a) N, and (b) H composites

by an ascending branch in the load-deflection response up to a second peak load; this trend was exhibited by the H composites with higher dosages of BP (4.5 and 6.9%). Therefore, specimens H-B-4.5 and H-B-6.9 using H composites, achieved superior post-cracking behaviour after the combined exposure, as their residual strengths at a deflection of 0.5 mm (span/600) were approximately 32 and 27%, respectively, higher than their first-crack strengths, which were 7.8 and 7.7 MPa, respectively.

Irrespective of the cementitious composite type, the incorporation of BP at different dosages significantly enhanced the post-cracking behaviour of layered prisms before exposure, as adding 2.5, 4.5 and 6.9% of BP to the N and H composites, N-B-2.5, N-B-4.5, N-B-6.9, H-B-2.5, H-B-4.5 and H-B-6.9, yielded toughness values of 27, 32, 33, 34, 47 and 45 J, respectively. Comparatively, the control layered specimens cast without fibers (N-X-0.0 and H-X-0.0) had toughness values of 8 and 13 J. Consistently, exposing the fiber-reinforced specimens to consecutive F/T and W/D cycles yielded similar trends. For instance, relative to the plain N and H composites after the combined exposure, incorporating BP in N-B-2.5, N-B-4.5, N-B-6.9, H-B-2.5, H-B-4.5 and H-B-6.9, showed a noticeable increase in the energy-absorbing capacity (toughness) of 317, 381, 370, 279, 381 and 398%, respectively. In comparison with the initial properties of composites comprising BP (Table 3.4), exposing such composites to repetitive F/T and W/D cycles did not significantly affect their post-cracking properties, especially for the composites reinforced with high volumes of BP. For example, incorporating BP in N-B-2.5, N-B-4.5, N-B-6.9, H-B-2.5, H-B-4.5 and H-B-6.9 had a 28-day toughness of 27, 32, 34, 33.8, 48 and 45 J, respectively, while after the cyclic regime, it showed a less toughness of 25, 28, 29, 31, 40 and 41 J, respectively.

Interestingly, specimens reinforced with BP were found to have the least reduction in toughness after the combined exposure. Albeit the BP had lower modulus of elasticity and aspect ratio with respect to the SF, a superior post-cracking behaviour was observed for the N and H composites, in terms of residual strength at both deflections (span/600 and span/150) and energy absorption (toughness). In case of using BP specimens with the same stiffness as that of the SF specimens, the toughness was markedly increased. For instance, after exposure, replacing 1% of SF with 6.9% BP in both cementitious composites (N-B-6.9 and H-B-6.9) led to a significant increase of 55 and 37%, respectively, in the toughness of specimens. Interestingly, when the volume of both fibers was kept constant, taking into consideration the superior properties of SF with respect to the BP, the post-cracking behaviour was quite comparable. To explain this trend, scanning electron microscopy (SEM) was employed on fracture pieces. It was found out that the improved post-cracking performance of specimens reinforced with BP over those reinforced with SF was due to the enhanced bonding of the cementitious matrix within the textured grooves in the longitudinal direction of the BP. These grooves provided a host for the deposition of the hydration products, unlike the smooth surface in the longitudinal direction of SF, as for example shown in Figure 3.6.

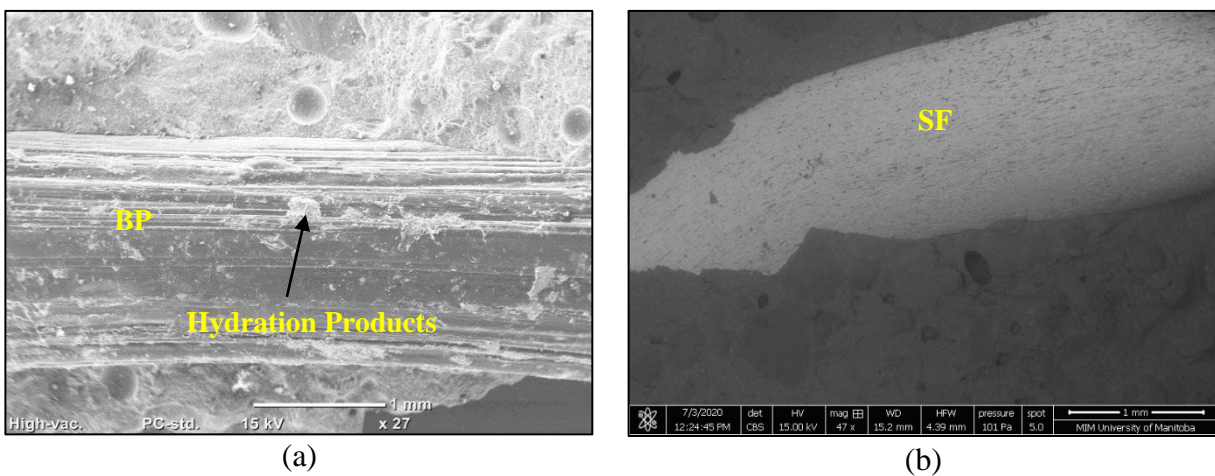


Figure 3.6: SEM images for the BP and SF, (a) hydration products depositing in the BP grooves, and (b) smooth surface of SF

3.4.2 Resistance of composites to frost action

To evaluate the potential of the developed BPCC in resisting the F/T portion of the cyclic exposure, no air-entraining agents were added deliberately into the mixtures. In general, the air content in the matrix increased with the incorporation of fibers (Table 3.3), complying with previous studies (Cavadar 2014; Alsaif et al. 2018 & 2019). Irrespective of the type of binder, an incremental increase in the air content was associated with increasing the dosage of BP. For example, incorporating the BP at dosages of 2.5 and 6.9% in N-B-2.5, N-B-6.9, H-B-2.5 and H-B-6.9, showed an increase in the air content by 14, 32, 19 and 39%, respectively, with respect to their counterpart specimens cast without fibers (N-X-0.0 and H-X-0.0). This might be attributed to the internal friction between the mortar and prismatic BP surfaces that created a foaming action, which accordingly increased the amount of air in the matrix.

The relative dynamic modulus of elasticity (RE_n) after 300 F/T cycles for the N and H composites are listed in Table 3.3. The RE_n of the cementitious composites cast without any SCMs and fibers (N-X-0.0), showed a good frost resistance, as it survived 300 cycles and its RE_n value remained above the threshold value of 60% as specified by the ASTM C666 (ASTM 2019c). This may be attributed to the low w/b of the paste and thus less vulnerability to critical saturation. Compared to the N composites, all the H counterparts, comprising slag and Ns, exhibited better resistance to frost action. The average RE_n for the N and H composites were 84 and 90, respectively, owing to the pronounced role of slag and Ns in refining the pore structure of the cementitious matrix, thus further reducing the potential of critical saturation and consequently frost damage (Özbay et al. 2013; Salemi and Behfarnia 2013). This links to the improved residual mechanical performance of these nano-modified composites after the combined exposure, as discussed in the previous sections.

In comparison to the control composites (N-X-0.0 and H-X-0.0), all the BPRCC specimens yielded less reduction of RE_n , particularly those containing higher volumes of BP (N-B-4.5, N-B-6.9, H-B-4.5, and H-B-6.9). Similarly, the incorporation of SF adequately controlled the rate of internal damage, as reflected by the RE_n values. For instance, adding 1% of SF to the N and H composite (N-S-1.0 and H-S-1.0) showed an enhancement in the dynamic modulus of elasticity by 20 and 11%, respectively, when compared to that of the control specimens cast without fibers (N-X-0.0 and H-X-0.0). Maintaining the same volume of BP or SF in either the N or H composite showed comparable values of RE_n , taking into account the superior properties of SF in terms of the modulus of elasticity and aspect ratio. In addition, the superior performance for all fiber-reinforced composites could be linked to the higher air content (Table 3.3), which relieved pressures from F/T cycles and the restraining action of fibers along with the superior residual mechanical capacity that led to maintaining intactness of specimens.

3.4.3 Compatibility with substrate concrete

In a layered system, due to the high rate of differential shrinkage after casting, incompatibility between FRCC and base concrete (normal concrete layer) may lead to debonding and premature failure of the assembly. Therefore, to prove the concept of implementing the nano-modified BPRCC as a layer in concrete members, a relative shrinkage test was conducted. The relative shrinkage up to 148 days, including 28 days in moist curing and 120 days in hot/arid conditions, representing a severe scenario that might be encountered in practice, is listed in Table 3.6.

After 1 and 7 days of moist curing, the H composites, whether it was reinforced with BP or SF, yielded higher rate of shrinkage in comparison to the corresponding N composites. For example, after 1 and 7 days of curing, the average relative shrinkage for the H composites were 83 and 176 micro-strain, which were 63 and 66% higher than the average shrinkage of N composites (51

Table 3.6: Summary of relative shrinkage at different ages of cementitious composites

Mixture ID	Relative shrinkage (micro-strain)			
	1 day	7 days	28 days	148 days
N-X-0.0	60 (4.9)	122 (11)	255 (21)	521 (42)
H-X-0.0	92 (5.6)	191 (14)	264 (29)	562 (32)
N-B-2.5	58 (3.6)	118 (10)	252 (15)	460 (51)
N-B-4.5	49 (1.2)	102 (09)	230 (16)	412 (22)
N-B-6.9	40 (2.3)	88 (08)	216 (22)	398 (18)
N-S-1.0	48 (2.6)	97 (12)	234 (33)	452 (29)
H-B-2.5	87 (3.1)	185 (07)	258 (18)	480 (35)
H-B-4.5	80 (1.9)	171 (09)	244 (23)	388 (11)
H-B-6.9	74 (3.9)	162 (06)	236 (12)	354 (27)
H-S-1.0	81 (4.2)	168 (15)	247 (28)	451 (37)

Note: numbers in parentheses represent standard deviations.

and 106 micro-strain), respectively. This behaviour is attributed to the role of Ns in accelerating the reactivity of the blended cement/slag binder at early age; however, this trend diminished between 7 and 28 days, according to the thermogravimetry results reported in a previous study (Mahmoud et al. 2017). On the other hand, after 28 days of curing, the N and H composites showed comparable rates of shrinkage, and the total shrinkage of all composites was in the narrow range of 236 to 264 micro-strain. The higher rate of shrinkage for the N composites, at 28 days, can be ascribed to the continual moist and hence hydration development, especially with the high cement content used.

No composite showed signs of surface cracking up to 28 days. Irrespective of the composite type, the shrinkage behaviour was significantly affected by the coexistence of fibers in the composite. According to Table 6, all the composites comprising fibers, either BP or SF, showed lower shrinkage values at different curing ages. For instance, irrespective of the fiber type, adding fibers to N-B-2.5, N-B-4.5, N-B-6.9, H-B-2.5, H-B-4.5 and H-B-6.9 reduced the average shrinkage values by 18, 17.9, 13, 10 and 7%, with respect to the control N and H composites at 1, 7 and 28 days, respectively. This effect was more pronounced in composites reinforced with high dosage of

BP. For instance, in comparison to the control N and H composites without fibers (N-X-0.0 and H-X-0.0), specimens N-B-6.9 and H-B-6.9 showed notable reduction in the shrinkage with 33, 28 and 15% and 19, 15 and 10% after 1, 7, and 28 days of moist curing, respectively, which highlighted the vital contribution of BP in restraining differential shrinkage relative to the base concrete.

After exposing the composites to drying conditions at $40\pm 1^\circ\text{C}$ and $35\pm 5\%$ RH for additional 120 days, the shrinkage deformation was amplified. At the end of the drying exposure, the control composites showed minor cracking on the surface, while even the lowest dosage of BP or SF were capable of completely eliminating shrinkage cracking, as shown in Figure 7. After exposing the composites to the hot environment, the shrinkage values for the control composites (N-X-0.0 and H-X-0.0) were markedly increased by 104 and 112%, respectively, compared to the shrinkage values after 28 days of moist curing.

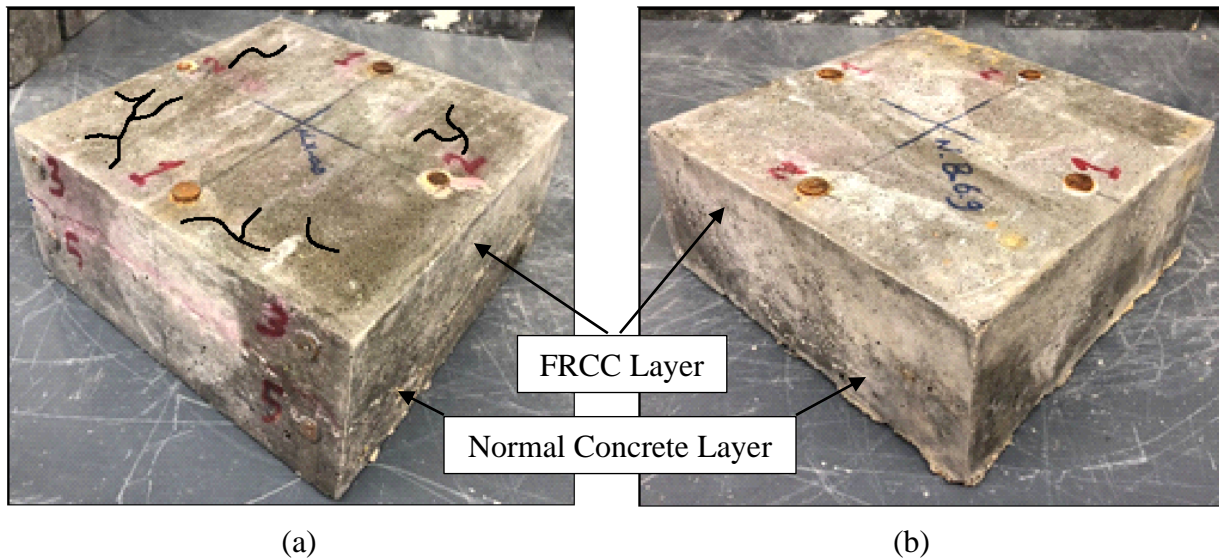


Figure 3.7: Exemplar layered slabs after the relative shrinkage test, (a) N-X-0.0, and (b) N-B-6.9 after 148 days

This was mainly attributed to the absence of either large coarse aggregates or fibers to provide adequate resistance arising from volume change due to loss of moisture. For instance, with respect to the shrinkage values of the control N-X-0.0 and H-X-0.0 composites (521 and 562 micro-strain), incorporating 2.5% BP and further increasing the dosage to 4.5 and 6.9% in N-B-2.5, N-B-4.5, N-B-6.9, H-B-2.5, H-B-4.5 and H-B-6.9 showed 12, 21 and 24% and 15, 31 and 37% reduction in the cumulative relative shrinkage values at 148 days, respectively. Hence, with higher dosage of BP, there was more reduction in the cumulative relative shrinkage, which was attributed to the abundance and random distribution of the BP in the matrix, thus controlling and bridging micro-cracks in the matrix and discounting its volumetric change. In addition, it was observed that there was more reduction in the cumulative shrinkage values at 148 days for the H composites with respect to the N composite counterparts at the same dosage of BP. This can be explained by the effectiveness of the nano-modified ternary binder (cement, slag and Ns) at providing better fiber/matrix interaction and continual increase in microstructural development and thus stiffness, complying with the results of mechanical performance.

The residual bond strength between the nano-modified slag based cementitious composites and the base concrete after the combined exposure is a key factor affecting the concept of layered elements. If the two layers are not compatible with each other, they will deform differently resulting in failure at the interface. Therefore, the bond strength between either BPRCC or SFRCC and the base concrete was evaluated using a direct tension test (pull-off) to mimic the worst-case loading configuration after the combined cyclic exposure. The average bond strength values before and after the combined exposure is shown in Figure 3.8.

The average pull-off strength results showed that the bond strength of the control N and H composites (N-X-0.0 and H-X-0.0) decreased significantly after the combined exposure by 38 and

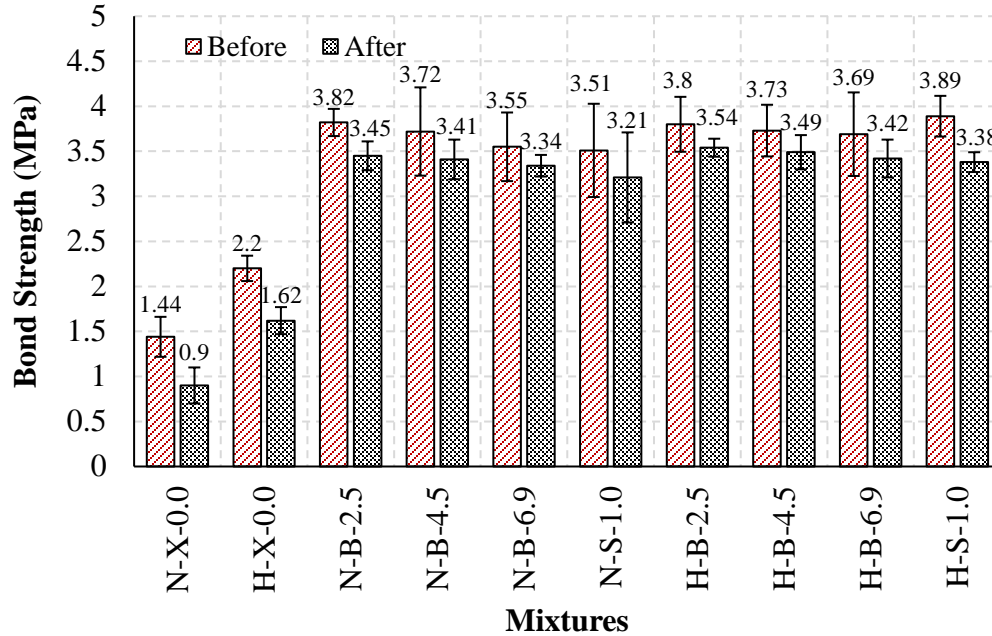


Figure 3.8: Bond strength of all composites from the pull-off test before and after the combined exposure

26%, respectively, compared to the initial values obtained at 28 days. In addition, the failure of these specimens occurred in the N and H composites without fibers, which reflected the degradation of the composites, as shown in Figure 3.9. Conforming to the previous trends obtained from the compressive strength and flexural performance, the composites comprising fibers showed much less reduction in the bond strength after the combined exposure. For instance, exposing the N and H composites in N-B-2.5, N-B-4.5, N-B-6.9, H-B-2.5, H-B-4.5, and H-B-6.9 to consecutive F/T and W/D cycles slightly reduced the bond strength by 6 to 10%, in comparison to the initial values (Fig. 8). Failure of the assembly mostly occurred in the substrate layer (30 to 50 mm below the interface), which indicated high compatibility between the two layers and soundness of the proposed BPRCC (see Figure 3.9).

The incorporation of SF in N and H composites yielded quite comparable bond strength results with those obtained from specimens reinforced with BP and tested before or after exposure. For

example, after the combined exposure, keeping the volume of fibers or maintaining the stiffness of the composites constant by comparing 1% of SF with 2.5% or 6.9% of BP, respectively, in the N and H composites (N-B-2.5, N-B-6.9, N-S-1.0, H-B-2.5, H-B-6.9 and H-S-1.0) yielded bond strength within a relatively narrow range of about 3.2 to 3.5 MPa. The adequate compatibility of BPRCC with substrate concrete after the combined F/T and W/D cycles can be linked to the preceding findings of the previous tests (compressive capacity, flexural performance, relative shrinkage), since the BP significantly improved the volume stability of the composites and prevented considerable deformations/deterioration that may be triggered by the combined exposure.

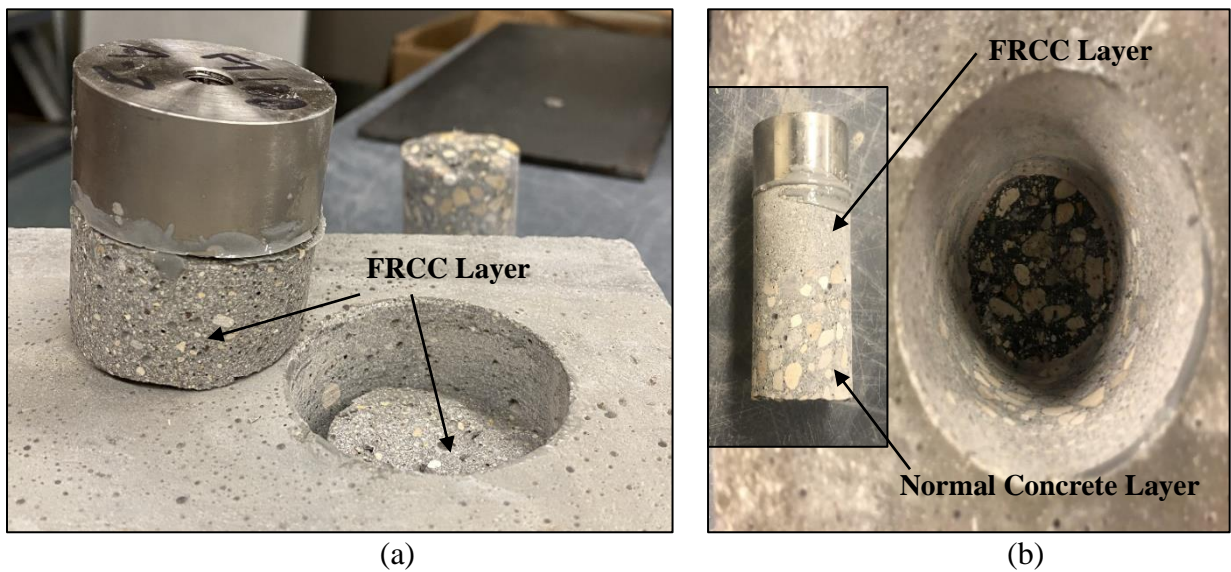


Figure 3.9: Mode of failure of exemplar layered slabs obtained from the pull-off test after the combined exposure, (a) H-X-0.0, and (b) H-B-2.5

3.5 Conclusions

Based on the experimental investigations, the following conclusions can be drawn:

- The synergistic effects of Ns and slag in refining and densifying the pore structure of the matrix in the H composites led to higher residual compressive and flexural strengths as

well as relative dynamic modulus of elasticity, compared to that of counterpart N composites without SCMs.

- The presence of BP in the cementitious composites effectively discounted the rate of deterioration, resulting in lower reductions in compressive and flexural capacity as well as toughness. The presence of BP impeded the damage imparted by the tensile stress induced by the combined exposure, especially due to the efficient bonding with matrix (deposition of hydration products in microgrooves).
- The layered prisms cast with the H composite comprising high dosages of BP (H-B-4.5 and H-B-6.9) achieved superior post-cracking (deflection-hardening) behaviour after the combined exposure, as the residual strengths at a deflection of 0.5 mm (span/600) were approximately 32 and 27%, respectively higher than their first-crack strengths, and their residual toughness was comparable to that of their initial values before exposure. In addition, BPRCC specimens containing high volume (4.5% and 6.9%) of BP yielded the lowest reduction in stiffness after the F/T portion of the exposure, due to the increased air content associated with the foaming action during mixing.
- All the N and H composites, reinforced with either BP or SF, showed high compatibility with the base concrete. There was no relative shrinkage cracking during curing and exposure to hot/arid conditions. Correspondingly, the substrate failure was the dominant mode of failure in the pull-off bond test, with marginal reductions of the bond strength after exposure to consecutive F/T and W/D cycles. This implies that all the BPRCC and SFRCC produced herein has enhanced dimensional stability relative to normal concrete, when they are cast within a short period of time (one hour) forming a layered system.

CHAPTER 4: BOND BEHAVIOUR OF STRAIGHT AND HEADED-END GFRP BARS EMBEDDED IN BASALT FIBER PELLETS CEMENTITIOUS COMPOSITES

Authors and Affiliation:

- Ahmed G. Bediwy, PhD Candidate, Department of Civil Engineering, University of Manitoba
- Ehab F. El-Salakawy, Professor, Department of Civil Engineering, University of Manitoba

Journal and Status:

American Society of Civil Engineers (ASCE) Journal of Composites for Construction, accepted for publication on April 30, 2021.

Reference:

Bediwy, A., and El-Salakawy, E. “Bond behaviour of straight and headed-end GFRP bars embedded in basalt fiber pellets cementitious composites.” *Journal of Composites for Construction, ASCE*, in press.

Note:

The manuscript had been slightly altered from the original paper by renumbering the tables and figures to include the chapter number. In addition, the reference list and list of notations have been moved to the appropriate sections in the thesis as indicated in the table of contents.

Abstract:

In this study, the bond behaviour of sand-coated glass fiber-reinforced polymer (GFRP) bars embedded in a novel type of cementitious composite, containing nano-silica, slag, and reinforced with the recently developed basalt fiber (BF) pellets, was evaluated. Steel fibers (SF) were incorporated in control mixes for comparison purposes. A total of 95 cubic pullout specimens were prepared and tested according to the Canadian standards. The test parameters were the type of cementitious composite, the bar diameter, the type of fibers, the dosage of BP, and the type of GFRP bar end. The bond performance was elucidated through compressive strength of the composite and load-slip response of GFRP bars. In addition, the fiber bridging mechanism was determined by evaluating the residual bond strength and toughness indices. The provisions for bond strength in the Canadian and American codes were also assessed. The test results showed the effectiveness of the BP in enhancing the failure pullout load compared to counterpart specimens comprising SF, which makes them a good candidate for infrastructural applications including rehabilitation.

Keywords: glass fibers reinforced polymer, headed-end bars, basalt fiber pellets, pullout, bond strength.

4.1 Introduction

Despite their attractive properties, glass fiber-reinforced polymer (GFRP) reinforcing bars have different bond characteristics with concrete. Therefore, numerous research and development efforts around the world have been conducted to evolve new technologies in the GFRP manufacturing process to widespread their use in the construction industry. As a result, GFRP bars are produced with different types and surface textures to overcome the problems associated with bond failure. Recently, the development of a GFRP bar with a headed end has proven to be remarkably useful and robust in providing the required anchorage and controlling the premature bond failure. Benmokrane et al. (2016) and Mahmoud et al. (2017) conducted an experimental study to characterize and evaluate the performance of GFRP bars with straight and headed-ends, and concluded that headed-end bars had higher (approximately 90% more) pull-out capacity with respect to straight counterpart bars in concrete specimens. This makes these bars a good candidate as internal reinforcement for structural applications that require a long development length (e.g. deep beams and corbels).

On the other hand, the quality of the cementitious composite material (or concrete) largely affects the reinforcement-matrix bond properties. Accordingly, the development of a high-performance cementitious composite became imperative; a common form of such material is the high-strength concrete. This can be achieved by incorporating supplementary cementitious materials (SCMs), such as silica fume and/or ground granulated blast-furnace slag. In addition, adding a small dosage of nanoparticles (e.g. nano-silica, Ns) had the ability to boost the strength of concrete and the overall performance of a cementitious matrix by accelerating the kinetics of cement hydration and their contribution in improving the microstructural development of cement-based materials (Zhang et al. 2012; Said et al. 2012).

However, the increased strength of concrete is usually associated with increased brittleness (Dancygier et al. 2010). Therefore, many studies have employed discrete fibers into cementitious materials/concrete aiming at enhancing the flexural toughness of the cementitious composites, which in turn, contributed to improving the ductility of structural elements (Song and Hwang 2004; Xu et al. 2012; Corinaldesi and Nardinocchi 2016). Different types of fibers are available to produce fiber-reinforced cementitious composites (FRCC), such as steel, synthetic, organic and inorganic fibers. In this context, steel fiber-reinforced concrete (SFRC) has gained increased popularity in the construction industry in recent years, as these fibers had the capability to enhance the bond-slip behaviour. Kim et al. (2013) and Yan and Lin (2017) conducted an extensive experimental work to evaluate the pull-out strength of sand-coated and helically-wrapped GFRP bars embedded in concrete reinforced with hooked-end steel and polypropylene fibers. Both studied observed a notable enhancement and better bond behaviour and ductility with the presence of steel fibers (SF) compared to plain concrete due to fiber bridging action. However, the main drawback of using steel in the form of bars or discrete fibers still exists, as they are vulnerable to corrosion, which in turn would negatively affect the durability and functionality of concrete structures.

As such, a new non-corrosive type of basalt fiber (BF), made of basalt rocks, is introduced to the construction market. This BF has high mechanical properties (tensile strength between 3,000 and 4,000 MPa and reasonable modulus of elasticity between 93 and 110 GPa) and lower cost with respect to other types of fibers such as glass fibers (Iyer et al. 2016; Ghazy et al. 2016). A special form of BF is basalt fiber pellets, which is made of basalt fibers encapsulated by polyamide or other resins to alleviate the low alkaline resistance. This makes it a strong candidate for FRCC, as proved by previous studies (Mahmoud et al. 2017).

Numerous research have been carried out to investigate the bond characteristics of FRP bars embedded in plain concrete; however, to the authors' knowledge, there is a dearth of research data on the bond behaviour of the hybrid system consisting of FRP bars and discontinuous non-metallic fibers such as BP. This study presents the second phase of an ongoing research program at the University of Manitoba. The first phase of this program was undertaken by Mahmoud et al. (2017), who investigated the behaviour of basalt fiber-reinforced cementitious composite (BFRCC) that consisted of nano-modified cementitious composites incorporating 6% Ns with 40% slag and BP in terms of compressive strength, flexural strength, toughness, and pull-out strength for GFRP reinforcing bars with different end shapes. It was concluded that this BFRCC has high performance and potential to be applied in structural applications. In this second phase of the program, the effect of various parameters including different dosages of BP, type of fibers, type of cementitious composite, bar diameter, and the type of GFRP bar end on the bond performance between GFRP bars and FRCC is evaluated.

4.2 Experimental Program

4.2.1 Materials

4.2.1.1 Cementitious composite

General use (GU) cement and slag were used as the main components of the binder complying with the requirements of CSA A3001 standard (2018). Table 4.1 shows the chemical and physical properties of these components. In this study, an Ns solution was added to the binder. Fine sand, with a fineness modulus of 2.9 and a gradation less than 600 μm according to ASTM C136 (2019a), was adopted to cast the composites. A high-range water-reducing admixture (HRWRA) complying with ASTM C494 Type F (2019b) was used to target a flow between 185 and 215 mm for all composites.

Table 4.1: Chemical and physical properties of GU cement and slag

Binder	Chemical composition (%)							Physical properties	
	SiO ₂	Al ₂ O ₃	Fe ₂ O ₃	CaO	MgO	SO ₃	Na ₂ O _{eq}	Blaine (m ² /kg)	Specific Gravity
Cement	19.21	5.01	2.33	63.22	3.31	3.01	0.12	390	3.15
Slag	33.40	13.4	0.76	42.70	5.30	2.40	0.30	492	2.87

4.2.1.2 Fibers

The cementitious composites were reinforced with either BP or SF (Figure 4.1). The BF represented 60% of the pellet by weight. The BP were 36 mm long with a diameter of 1.8 mm. Hooked-end SF of 0.5-mm diameter and 30-mm length were also used. The properties of the BP and the SF are listed in Table 4.2.

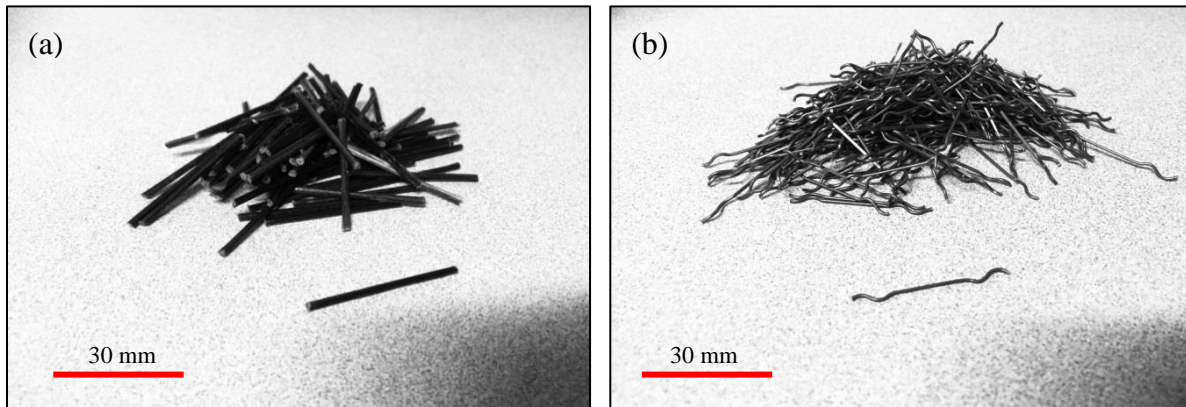


Figure 4.1: Reinforcing fibers: (a) basalt fibers pellets, and (b) steel fibers

Table 4.2: Properties of fibers

Properties	Properties of fibers	
	BP	Hooked steel
Length (mm)	36	30
Diameter/dimensions (mm)	1.80	0.65
Aspect ratio	20	45
Specific gravity	1.74	7.70
Tensile strength (MPa)	2,300	1,200
Elastic modulus (GPa)	65	200

4.2.1.3 GFRP reinforcement

Sizes No.15 and No.20 sand-coated, GFRP bars with either straight or headed ends were used. The headed-ends were made of thermoplastic matrix reinforced with short glass fibers, cast on the end of the bar at high temperature. Irrespective of the bar size, the 100-mm long head had a stepped surface with a maximum outer diameter of 50 mm at the end as shown in Figure 4.2. The mechanical properties of the GFRP bars were obtained through standard tests carried out according to ASTM D7205-06 (2016), as listed in Table 4.3.



Figure 4.2: GFRP bars and configuration of the head

Table 4.34: Mechanical properties of GFRP

Bar Type	Bar size	Nominal diameter (mm)	Area (mm ²)		Tensile strength (MPa)	Modulus of elasticity (GPa)	Ultimate strain (%)
			Nominal	CSA/S806-12 Annex A			
GFRP	No. 15	15.9	198	291	1,184	62.6	1.89
	No. 20	19.0	285	394	1,105	63.7	1.73
GFRP Head	-	-	-	-	552*	68.0	0.80*

Note: Properties are the same for straight and headed-end bar

* Usable design stress/strain provided by the manufacturer (corresponds to a pull-out load capacity of 70 kN)

4.2.2 Proportions and mixing procedures

Two different mixtures were produced in this study: normal cementitious composite (designated as NP), and high-performance cementitious composite (designated as HP). The NP mixture was prepared with GU cement content of 700 kg/m^3 , while the HS one was cast with GU cement and a constant dosage of slag of 280 kg/m^3 , representing 40% replacement of cement content. In addition, Ns, at a dosage of 6% by mass of the binder, was added to the HP mixtures. The water-to-binder ratio (w/b) was kept constant at 0.30 for both mixtures. The mixtures were reinforced with either BP or SF. The BP were added to the mixtures at different dosages of 2.5 and 4.5% by volume, corresponding to 1.0 and 2.0%, respectively, by volume of basalt fibers, as the fibers represents 40% of the pellets by volume. Whereas, in the case of SF, this dosage was 1.0%. The proportions of all the cementitious composites are listed in Table 4.4. Further description of the components and the mixing procedures can be found elsewhere (Mahmoud et al. 2017). For the mixture nomenclature, the first part stands for the type of the cementitious composite (“NP” for a composite cast without SCMs and “HP” for a composite cast with slag and Ns), whereas the second part refers to the fiber type (“B” for basalt fiber pellet and “S” for steel fiber). The third part represents the fiber dosage used (2.5 and 4.5 for BP, and 1.0 for SF).

Additional two reference mixtures were cast, namely, normal strength concrete (NSC) and normal strength mortar (NSM) to evaluate the effect of changing the cementitious composite from mortar to concrete. A ready-mix concrete with a target 28-day compressive strength (f'_c) of 40 MPa and a target slump of 130 mm was used to prepare the NSC, while the NSM was cast with only GU cement (400 kg/m^3) and a w/c ratio of 0.50 with a target f'_c of 40 MPa and a slump of 120 mm. The actual compressive strength of cementitious composites was determined by testing standard

cylinders (100 × 200 mm) on the day of testing according to CSA A23.1-19/A23.2-19 (CSA 2019b).

Table 4.4: Proportions of the mixtures per cubic meter

Mixture ID	Cement (kg)	Slag (kg)	Water ^a (kg)	Nano-silica (Ns, kg)	Fine aggregate (kg)	HRWRA (L)	Fibers (kg)	
							BP	Hooked steel
NSC	Ready mix concrete with a target $f_c = 40$ MPa							
NSM	400	-	200	-	1,745	4.5	-	-
NP-X-0.0	700	-	210	-	1,471	5.7	-	-
HP-X-0.0	420	280	180	84	1,328	7.4	-	-
HP-B-2.5	420	280	180	84	1,268	7.4	43.3	-
HP-B-4.5	420	280	180	84	1,211	7.4	78.3	-
HP-S-1.0	420	280	180	84	1,302	7.4	-	77

^a Adjusted amount of mixing water considering the water content of nano-silica (aqueous solution with 50% solid content of SiO₂).

4.2.3 Test specimens

A total of 95 specimens were fabricated following the guidelines of Annex G of the CSA/S806-12 (CSA 2017). The pullout specimens consisted of a 200-mm side length cube with concentric placement of the bar. The dimensions of the specimen were chosen to avoid splitting of the cube. The embedded length was four times the bar diameter ($4 d_b$) in bars with straight ends, whereas it was equal to the head length (100 mm) in headed-end bars. The unbonded length was wrapped with a smooth surface tape to ensure that no bond exists between the cementitious matrix and the bar over this length. The other end of the GFRP bar was sheathed with thick-wall steel pipe, then the pipe was filled with a commercial expansive grout to anchor the bar to the pipe. After casting, the cubes were demolded and the specimens were kept inside a curing room (21°C and > 95% RH) until testing. Details of the specimens are presented in Figure 4.3.

The test parameters include the cementitious composite type, the type and dosage of fiber added to the cementitious matrix, and the diameter and end type of the reinforcing bar. The nomenclature

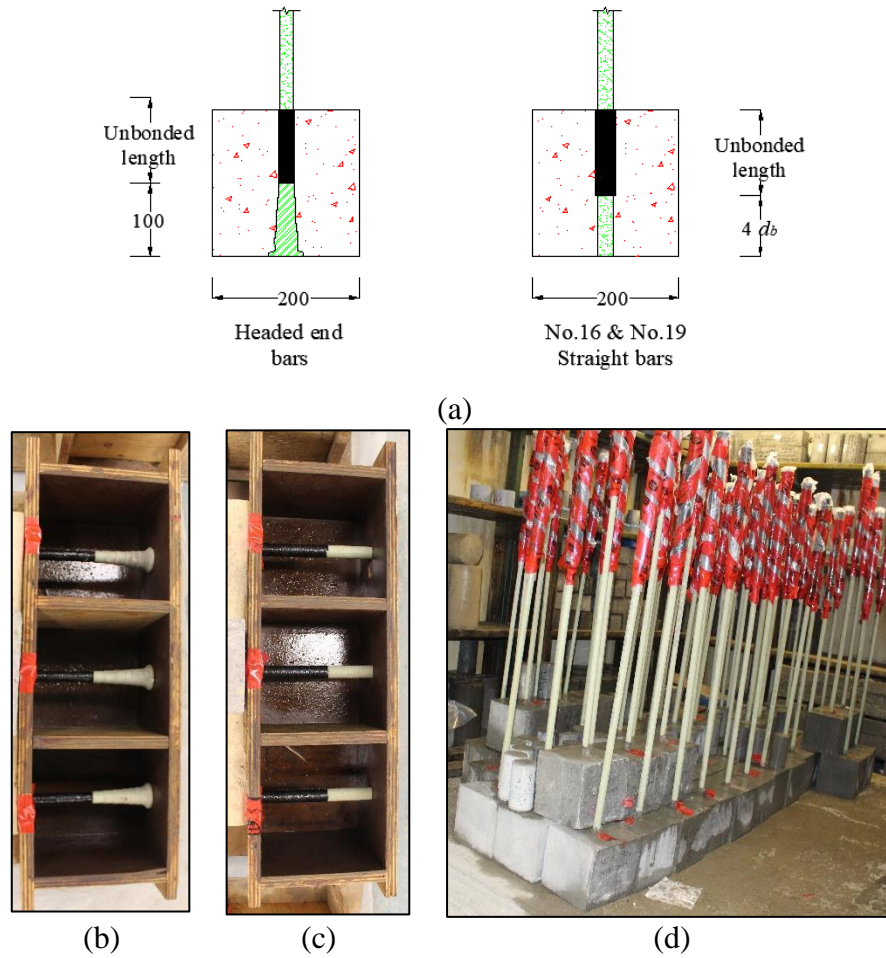


Figure 4.3: Test specimens, a) schematic drawings of the specimens, b) and c) GFRP bar in the form work showing the bond breaker for headed-end and straight bars, and d) specimens after casting in the curing room (dimensions are in mm)

of the specimens consisted of four parts; the first part is referring to the composite type (“HP” for a composite with SCMs and without any fibers, “BF” for a composite with SCMs and basalt fiber pellets, “SF” for a composite with SCMs and steel fibers, “NP” for a mortar (cement content 700 kg/m^3) without SCMs or fibers, “NSM” for a normal strength mortar (cement content 400 kg/m^3) without SCMs or fibers, and “NSC” for a normal strength concrete without SCMs or fibers). The second part described the dosage of fibers added, if any (2.5% and 4.5% for BP, and 1.0% for SF). The third part indicated the bar diameter (15 and 20 mm), and the last part indicates the bar end

type (“S” for straight bars, and “H” for headed-end bars. The details of the specimens are listed in Table 4.5.

Table 4.5: Details of test specimens for pullout

Specimens	Composite type	Fiber type	Fiber dosage (%)	Bar diameter (mm)	Bar end
NSC-X-15-S	Normal strength concrete*	-	-	15	Straight
NSM-X-15-S	Mortar with cement 400 kg/m ³ *	-	-	15	Straight
NP-X-15-S	Mortar with cement 700 kg/m ³ *	-	-	15	Straight
HP-X-15-S	Composite with SCMs and without fibers	-	-	15	Straight
HP-X-20-S		-	-	20	Straight
HP-X-15-H		-	-	15	Headed
HP-X-20-H		-	-	20	Headed
BF-2.5-15-S	Composite with SCMs and BP	Basalt	2.5	15	Straight
BF-2.5-20-S		Basalt	2.5	20	Straight
BF-2.5-15-H		Basalt	2.5	15	Headed
BF-2.5-20-H		Basalt	2.5	20	Headed
BF-4.5-15-S	Composite with SCMs and BP	Basalt	4.5	15	Straight
BF-4.5-20-S		Basalt	4.5	20	Straight
BF-4.5-15-H		Basalt	4.5	15	Headed
BF-4.5-20-H		Basalt	4.5	20	Headed
SF-1.0-15-S	Composite with SCMs and SF	Steel	1.0	15	Straight
SF-1.0-20-S		Steel	1.0	20	Straight
SF-1.0-15-H		Steel	1.0	15	Headed
SF-1.0-20-H		Steel	1.0	20	Headed

*NSC and NSM were cast without SCMs or fibers

4.2.4 Test setup and instrumentation

The pullout testing of the samples was conducted using an MTS machine. A monotonically increasing load at a rate of 10 kN/min, which is less than the 22 kN/min maximum rate specified in the CSA/S806-12, was applied. A total of three linear variable displacement transducers (LVDTs) were attached to each specimen; two at the loaded-end and one at the free-end to measure the slip of the GFRP bar. A data-acquisition system monitored by a computer was used to record the readings of the machine load and the LVDTs. Figure 4.4 depicts the test setup details.

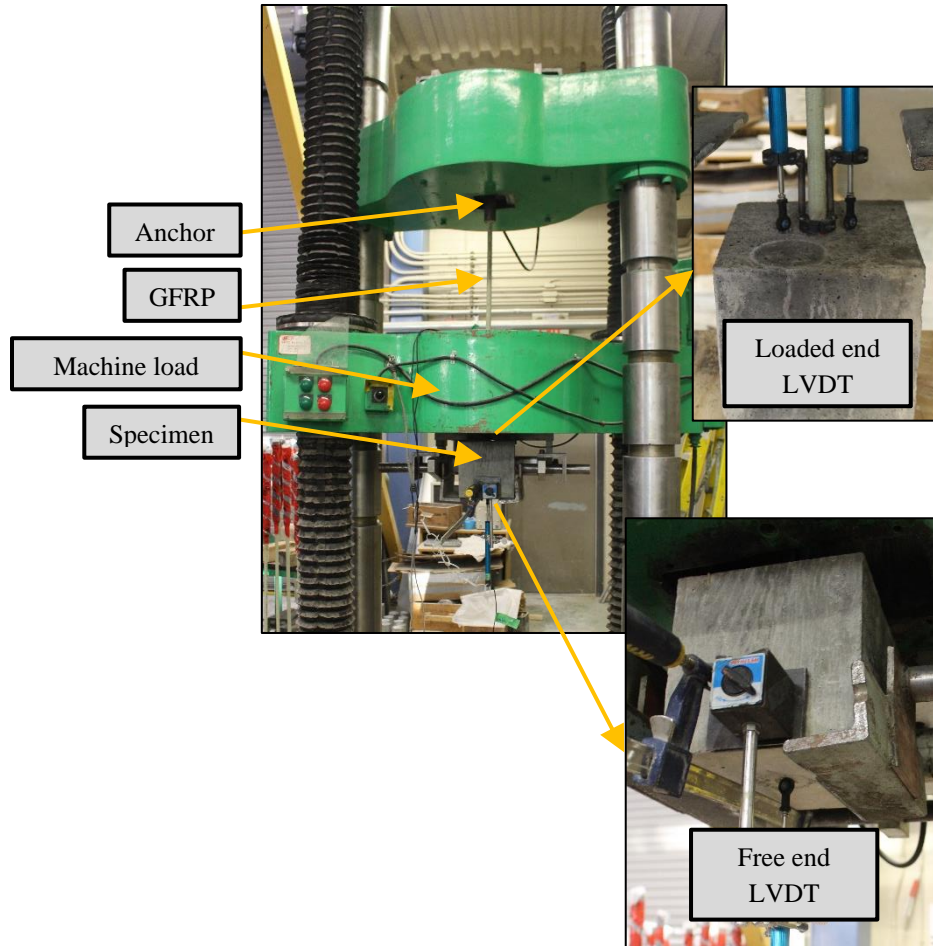


Figure 4.4: Pullout test setup and instrumentation

4.3 Results and Discussions

4.3.1 Compressive strength

Figure 4.5 shows the average compressive strength for all mixtures, obtained from cylinders. Compared to control normal strength concrete (NSC), excluding the coarse aggregate, SCMs and fibers (i.e. specimens with mortar), showed a slight reduction of 6% in the compressive strength. This may be attributed to the formation of interfacial transitional zones (ITZs) around the coarse aggregate, which negatively affected the strength of the matrix. The results were assessed by the analysis of variance (ANOVA) to determine whether there are any statistically significant differences between the means of compressive strength, as listed in Table 4.6. According to

Montgomery (2017), exceeding the F_{cr} value of an F distribution density function indicates that the variable tested has a significant effect on the average results. The insignificant effect of changing the cementitious matrix composition from concrete to mortar to target the same compressive strength was statistically supported by ANVOA for the compressive strength results at 28 days, since adding coarse aggregate yielded F value of 0.2, which was less than the F_{cr} of 4.4. In addition, increasing the cement content from 400 kg/m³ in mixture NSM to 700 kg/m³ (NP-X-0.0) showed an increase in the compressive strength from 44 to 61.3 MPa, respectively. This was due to the progression of the hydration process, especially with the high volume cement adopted herein along with the continual moist curing up to 28 days. As evident by the compressive strength results, the addition of Ns along with slag showed more significant effect on the strength development, when it was compared to the corresponding reference mixture cast with cement only. For example, the compressive strength of the nano-modified slag-based composite (HP-X-0.0) was significantly increased by 19% compared to that of the reference cement-based specimen (NP-X-0.0), as listed in Table 4.6.

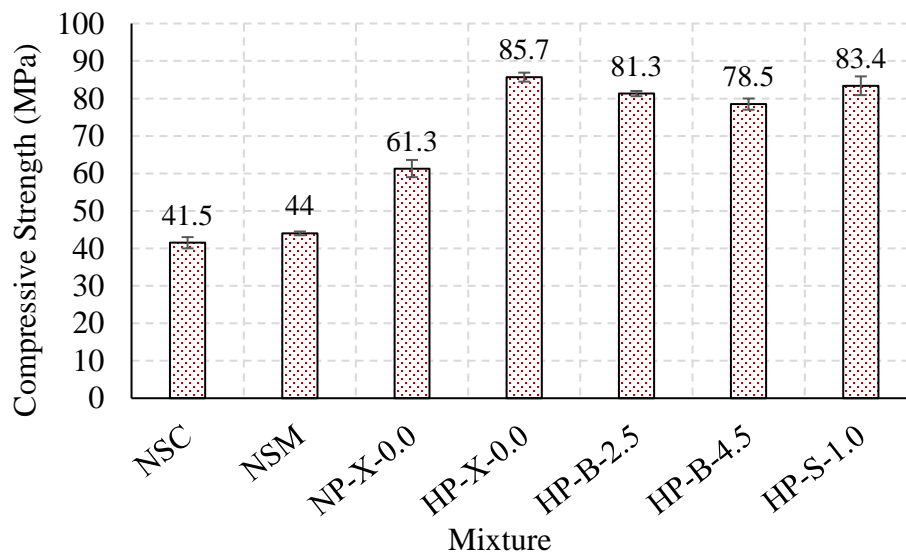


Figure 4.5: The average compressive strength for all mixtures

On the other hand, the inclusion of fibers, irrespective of fiber type, did not show any improvement in terms of the compressive strength; however, the mode of failure of the cylinder samples considerably altered from sudden to confined failure, as the bridging effect of the fibers maintained the integrity of the specimen. For instance, the compressive strength was slightly reduced by 5 and 8% with the incorporation of BP at dosages of 2.5 and 4.5%, respectively, with statistical insignificance (Table 4.6). In the same context, it is worth noting that the compressive strength was marginally affected by the properties of fibers. For example, replacing 2.5 % of BP with 1% steel fiber yielded F value of 0.1, which was less than the F_{cr} value of 4.4. Similar values were observed when BP was incorporated at a dosage of 4.5% (Table 4.6).

Table 4.6: ANOVA for the results of compressive strength at 28 days

Parameter	Compressive strength		
	F	F_{cr}	Effect
<u>Effect of the cementitious matrix type</u>			
NSM vs. NSC	0.20	7.7	Insignificant
NP-X-0.0 vs. NSM	10.2	7.7	Significant
NP-X-0.0 vs. HP-X-0.0	15.2	7.7	Significant
<u>Effect of adding fibers</u>			
HP-B-2.5 vs HP-X-0.0	1.10	7.7	Insignificant
HP-B-4.5 vs HP-X-0.0	2.70	7.7	Insignificant
HP-S-1.0 vs HP-X-0.0	0.80	7.7	Insignificant
<u>Effect of fiber type</u>			
HP-B-2.5 vs HP-S-1.0	0.10	7.7	Insignificant
HP-B-4.5 vs HP-S-1.0	2.40	7.7	Insignificant
<u>Effect of the dosage of BP</u>			
HP-B-2.5 vs HP-B-4.5	3.10	7.7	Insignificant

4.3.2 Pullout load-slip response

Figures 4.6 and 4.7 show the typical load-slip relationship at the loaded end of both No.15 and No.20 GFRP bars, straight and headed-end, embedded in different types of cementitious matrices.

The main load transfer mechanism between the bar and the cementitious matrix for non-deformed

(e.g. sand-coated) bars is well established to be provided by friction, which depends mainly on the transverse pressure (Baena et al. 2009; Kim et al. 2013). It is worth noting that the recorded slip at the loaded end was much higher than the measured slip at the unloaded end. In general, in the pre-cracking stage, the load-slip behaviour is characterized by a stiff linear increase of the load with a little range of slip. During this stage, internal circumferential tensile cracks initiated in the cementitious matrix at the fiber-matrix interface until the peak pullout load was reached. After the peak load, the residual load-slip response (the descending stage) showed different responses with varying the type of fibers and cementitious composites. Irrespective of the bar diameter, the straight GFRP bar that was embedded in plain cementitious matrix cast without any fibers exhibited an abrupt decay in the load accompanied with small slip values. This behaviour may be attributed to the delamination of the coating layer off the GFRP bars. Nevertheless, the post peak behaviour for the headed-end GFRP bar embedded in the same composite was not recorded due to the splitting of the block into pieces and detaching of the LVDTs.

On the other hand, the post-peak load-slip response of the GFRP bar in the cementitious matrix, containing 2.5 and 4.5% BP, mainly relied on the fiber dosage. For example, the behaviour of the GFRP bar (No. 20) in the matrix reinforced with 2.5 % BP showed a sharp drop in the load after the bond strength was attained; whereas, increasing the dosage to 4.5% yielded a gradually decayed slope reaching higher slip values due to the gradual propagation of internal cracks along with the predominant role of fibers in bridging such cracks. Similar experimental findings were previously reported for deformed steel bars (Ezeldin and Balaguru 1989) and sand-coated GFRP bar (Kim et al. 2013) embedded in concrete reinforced with hooked-end steel and PVA fibers.

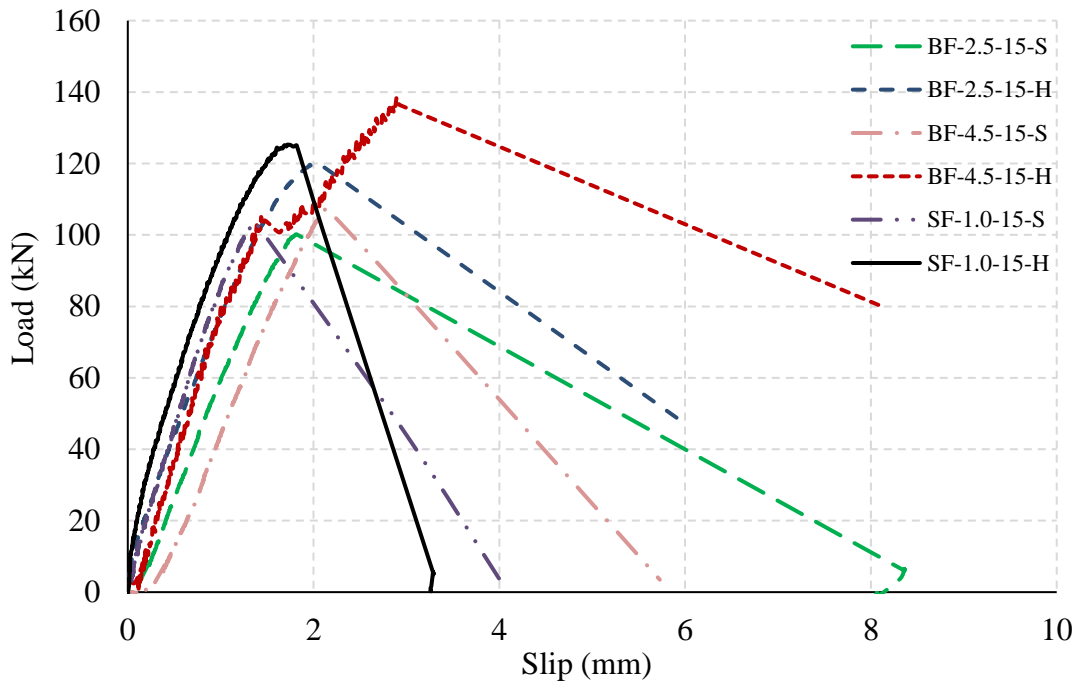
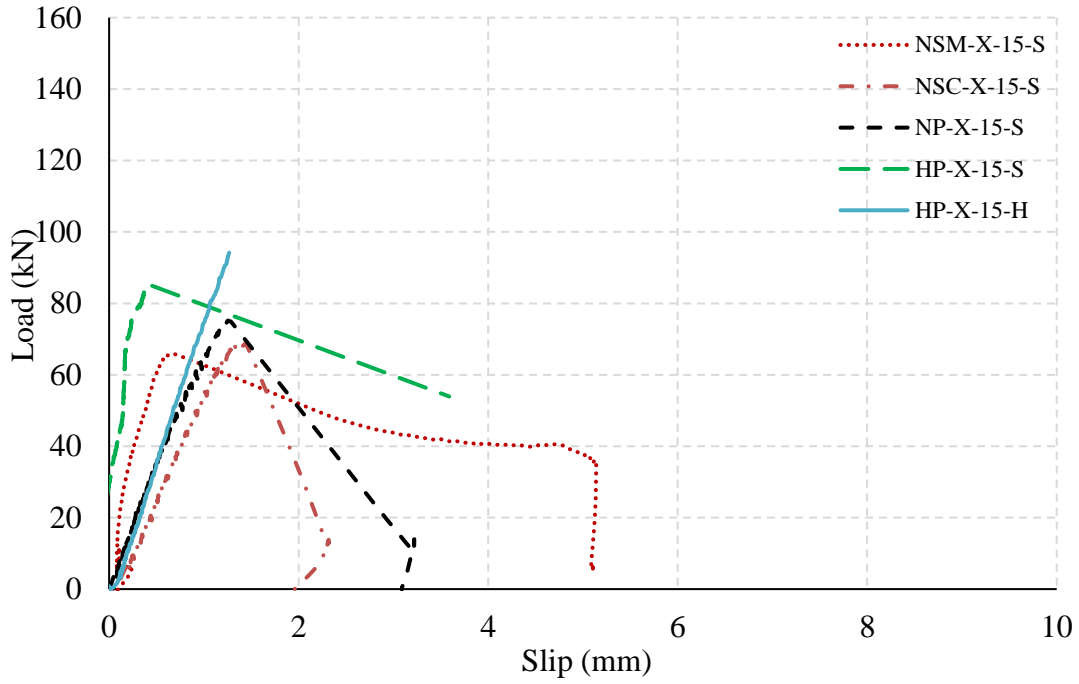


Figure 4.6 : Load–slip relationship at the loaded end for No. 15 GFRP straight and head-end bars

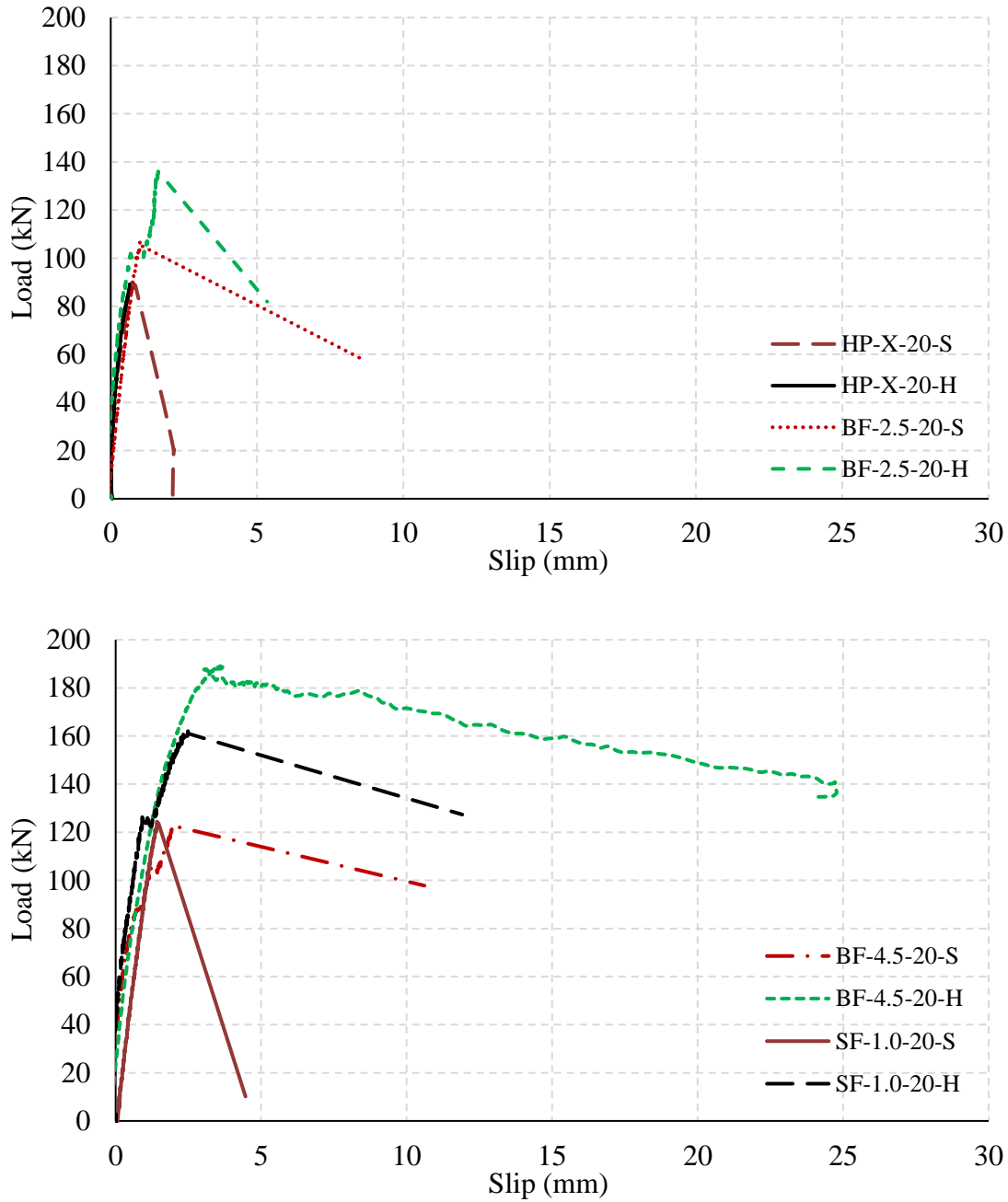


Figure 4.7: Load–slip relationship at the loaded end for No. 20 GFRP straight and head-end bars

4.3.3 Modes of failure

The ACI 440.1R-15 (ACI 2015) and numerous studies in the literature reported that there are two major modes of failure for GFRP bars in concrete: pull-out and concrete splitting (Yan et al. 2016; Gravina et al. 2020). In this paper, several modes of failure were observed for the tested GFRP bars embedded in plain and fibrous cementitious composites. Pure pullout (PO) and partial pullout (PPO) of the GFRP bar were observed for specimens with straight GFRP bar and cast without fibers. However, all other plain composites with headed-end bars showed splitting of concrete (SC), or crushing of concrete followed by splitting of the head (CSH). It is worth mentioning that the later modes of failure for the specimens with headed bars and without fibers were brittle in nature and were associated with sudden drop in the load capacity. Similar observations were reported by Benmokrane et al. (2016) for GFRP headed-end bars embedded in concrete. A description of the preceding modes of failure is presented as follows:

- PO: this failure is characterized by a full pullout of the bar from the specimen without any cracking in the cube. After testing, the cube was split into two halves to assess the surface of the bar and its surrounding cementitious composite. From Figure 4.8(a), full stripping of the sand coating on the outer surface of the bar and white residue on the dent of the embedment length were observed.
- PPO: this type of failure is characterized by a partial pullout of the GFRP bar from the cube, as shown in Figure 4.8(b). This might be imparted by the residual friction between the GFRP bar and the cementitious composite from the remaining sand coating on the outer surface of the bar after reaching the peak load.
- SC: this failure is violent and characterized by splitting of the concrete into three or four pieces as shown in Figure 4.8(c); however, in this failure, the head of the bar remained

undamaged. This type of failure took place when the head leaned against the cementitious composite, and the splitting resistance of the composite was less than the bond between the GFRP bar and the head leading to crushing of the cube.

- CSH: this failure is similar to SC failure in terms of crushing of the cube into three or four pieces; however, the head of the GFRP bar was damaged or broken (see Figure 4.8(d)) since the head's strength was exceeded. This failure was accompanied by partial slippage of the bar from the head.

On the other hand, the specimens, reinforced with either BP or SF, showed three modes of failure: PPO of the GFRP bar for the specimens with straight bars, while the specimens with headed-end GFRP bars showed either cracking of concrete (CC) or cracking of cementitious composite followed by bar slippage from the head (CCSB)

- CC: this type of failure was the dominant failure in most of the specimens with fibers, irrespective of the fiber type. This failure is characterized by the formation of several cracks that initiated at the bar and propagated toward the corners of the block; however, the bridging effect of fibers kept the block as one unit as depicted in Figure 4.8(e). In addition, the head of the bar remained undamaged, and no sign of bar slippage from the head was observed.
- CCSB: this type of failure is similar to the CC failure in terms of the major cracks developed in the block without splitting the block into pieces due to the presence of fibers (BP or SF). However, there was a partial slippage of the bar from the head, as shown in Figure 4.8(f).

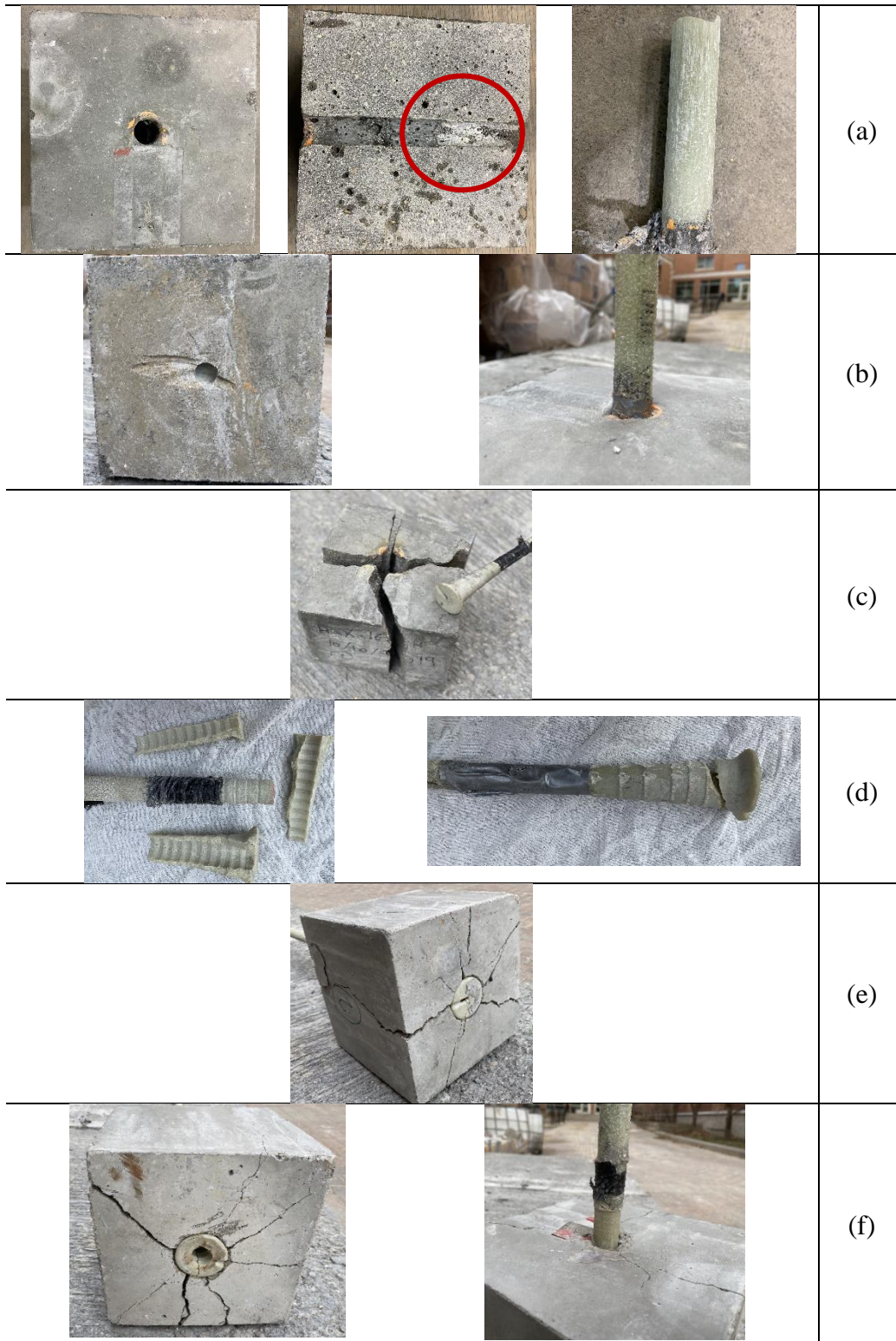


Figure 4.8: Mode of failure for all specimens: (a) PO, (b) PPO, (c) SC, (d) CSH, (e) CC, and (f) CCSB

4.3.4 Factors affecting the pullout load and bond strength

The experimental results for the pullout peak load, bond strength, and the mode of failure of the straight and headed-end bars are listed in Table 4.7. In addition, the pullout load results were statistically substantiated by ANOVA, as listed in Table 4.8.

4.3.4.1 Effect of cementitious matrix type

The results showed that specimen NSM-X-15-S yielded the lowest pullout load with 66 kN. This may be attributed to the absence of coarse aggregate and discrete fibers, which created a smooth crack surface during the pullout process of the straight bar. On the other hand, the incorporation of coarse aggregate contributed to improving the bond between the GFRP bar and the cementitious matrix that results from the resistance to relative slip between two rough interlocking surfaces of the crack. For example, with respect to the control mortar specimen (NSM-X-15-S), adding gravel to cast concrete approximately having the same compressive strength of 40 MPa, slightly increased the pullout load by 6%. However, such effect was statistically assessed by ANOVA, and the results indicated that the coarse aggregate had insignificant effect on the pullout maximum load ($F = 1.2$ was less than $F_{cr} = 7.7$). Moreover, despite the considerable increase in the compressive strength, increasing the cement content from 400 to 700 kg/m³ showed a negligible improvement in the failure load (only 3% increase), with statistical insignificance (Table 4.8).

On the contrary, it was well documented that the SCMs are usually added to any cementitious matrix to exhibit outstanding mechanical and durability properties. Similar observation was reported in this study, as adding 40% of slag as a partial replacement of cement in addition to 6% of nano silica (HP-X-15-S vs NP-X-15-S) significantly increased the failure load by 19.1%. This could be attributed to the interactive effect of both slag and Ns in densifying the cementitious

matrix providing higher compressive strength and better bond to the GFRP bar, as discussed earlier.

Table 4.7: Pullout test results

Specimens	Embedment length (mm)	Average failure load (kN)	Average bond strength (MPa)	Mode of failure
NSC-X-15-S	64	70	22.00	PO
NSM-X-15-S	64	66	20.70	PO
NP-X-15-S	64	72	22.60	PO
HP-X-15-S	64	86	27.10	PPO
HP-X-20-S	76	89	19.70	PPO
HP-X-15-H	100	94	475.8	SC
HP-X-20-H	100	89	313.0	CSH
BF-2.5-15-S	64	100	31.30	PPO
BF-2.5-20-S	76	107	23.60	PPO
BF-2.5-15-H	100	120	606.1	CCSB
BF-2.5-20-H	100	136	477.2	CCSB
BF-4.5-15-S	64	111	34.60	PPO
BF-4.5-20-S	76	123	27.10	PPO
BF-4.5-15-H	100	139	699.5	CC
BF-4.5-20-H	100	189	662.8	CC
SF-1.0-15-S	64	103	32.30	PPO
SF-1.0-20-S	76	124	27.50	PPO
SF-1.0-15-H	100	125	632.8	CC
SF-1.0-20-H	100	162	569.1	CCSB

Note: PO is pullout, PPO is partial pullout, SC is splitting of concrete, CSH, is crushing of concrete followed by splitting of the head, CC is cracking of cementitious composite, CCSB is cracking of concrete followed by slippage of the bar.

4.3.4.2 Effect of bar diameter

For specimens with headed-end GFRP bars, the effect of bar diameter was controversial. In plain cementitious composite without fibers, increasing the bar diameter from 15.9 to 19 mm in specimens HP-X-15-H and HP-X-20-H, respectively, showed a reduction in the failure load by 7%. This can be explained by the fact that the peak load largely depends on the projected bearing area of the head on the surrounding matrix. Since both the 15.9- and 19-mm diameter bars have the same overall head size (same outer dimensions), the larger bar diameter reduces that bearing area, leading to less failure load. The same observation was introduced and reported by

Table 4.8: ANOVA for the results of pullout test

Parameter	Average pullout load		
	F	F_{cr}	Effect
<u>Effect of cementitious matrix type</u>			
NSM-X-15-S vs. NSC-X-15-S	1.20	7.7	Insignificant
NP-X-15-S vs. NSX-15-S	0.80	7.7	Insignificant
NP-X-15-S vs. HP-X-15-S	72.9	7.7	Significant
<u>Effect of bar diameter</u>			
All No. 15 specimens vs. No. 20 specimens	15.2	4.3	Significant
BF-4.5-20-H vs. BF-4.5-15-H	30.0	7.7	Significant
SF-1.0-20-H vs. SF-1.0-15-H	22.1	7.7	Significant
<u>Effect of GFRP bar end type</u>			
HP-X-15-S vs. HP-X-15-H	0.54	7.7	Insignificant
HP-X-20-S vs. HP-X-20-H	0.04	7.7	Insignificant
All fibrous specimens with No. 15 straight-end vs. No.15	44.2	4.3	Significant
All fibrous specimens with No. 20 straight-end vs. No.20	51.6	4.3	Significant
<u>Effect of adding fibers</u>			
BF-2.5-15-S vs. HP-X-15-S	11.4	7.7	Significant
BF-2.5-15-H vs. HP-X-15-H	32.3	7.7	Significant
BF-2.5-15-S vs. BF-4.5-15-S	9.40	7.7	Significant
BF-2.5-20-S vs. BF-4.5-20-S	12.3	7.7	Significant
BF-2.5-15-H vs. BF-4.5-15-H	15.6	7.7	Significant
BF-2.5-20-H vs. BF-4.5-20-H	22.8	7.7	Significant
SF-1.0-15-H vs. BF-4.5-15-H	8.40	7.7	Significant
SF-1.0-20-H vs. BF-4.5-20-H	10.9	7.7	Significant
All specimens with 2.5 BP vs. specimens with 1.0% SF	2.90	4.3	Insignificant

Benmokrane et al. (2016) for headed-end GFRP bars embedded in normal strength concrete (35 MPa). As for the headed bars embedded in fibrous matrix, irrespective of the type or dosage of fibers, increasing the bar diameter showed a noticeable improvement in the average peak load specifically the blocks reinforced with high dosage of BP or SF. For instance, using No.20 headed-end GFRP bar in specimens BF-4.5-20-H and SF-1.0-20-H increased the pullout load significantly by 37 and 30%, respectively, compared to their counterpart specimens with No.15 headed-end

GFRP bars (see Table 4.8). This may be attributed to the preponderant effect of the fibers in enhancing the bond performance among other parameters (e.g. bar diameter).

For the straight-end bars, the average bond strength (τ) was computed based on the following equation:

$$\tau = \frac{F}{\pi d_b h_e} \quad \text{Equation 4.1}$$

where F is the peak load; d_b is the nominal bar diameter; and h_e is the embedment length; however, the average bond strength for the headed-end bars was calculated using the nominal cross-sectional area of the bar.

Compared to smaller diameter bars, using larger diameter bars develops less bond strength. Many researchers previously reported similar conclusions for both straight and headed-end GFRP bars (Cosenza et al. 1997; Alves et al. 2011; Benmokrane et al. 2016). For instance, in cementitious composites without fibers, increasing the bar diameter from 15.9 to 19 mm for straight and headed-end bars in specimens HP-X-15-S and HP-X-15-H, HP-X-20-S and HP-X-20-H led to a considerable reduction in the bond strength by 30 and 34%, respectively (with statistical significance, Table 4.8). Three factors are responsible for the lower bond strength: the embedment length, transverse contraction strain, and shear lag. Larger bar diameter requires longer embedment length, and it was found that the distribution of bond stresses is nonlinear along the bar; therefore, this nonlinearity is more pronounced in longer embedment length, resulting in lower bond strength. The contraction of bar diameter, when the GFRP bar is under direct tension, also known as “Poisson effect”, reduces the frictional stresses with the surrounding matrix. The non-uniform distribution of normal stresses through the cross section of the bar leads to a difference between the actual stresses exerted on the surface and the calculated average bond stress. Such difference

is more pronounced in larger diameter and might lead to less bond stress (Achillides and Pilakoutas 2004; Saleh et al. 2019).

4.3.4.3 Effect of GFRP bar end type (straight vs headed-end bars)

Limited research was conducted to investigate the interaction between the relatively new GFRP bar with headed-end and cementitious matrix. Islam et al. (2015) and Benmokrane et al. (2016) indicated that the pullout failure load was significantly increased for headed-end GFRP bars embedded in concrete with respect to straight bars. However, in this study, there was an insignificant enhancement in the pullout failure load when the straight bars were replaced with headed-end bars in plain composite (mortar) without fibers. For example, compared to HP-X-15-S and HP-X-20-S with straight bars (failure loads of 86.3 and 88.9 kN, respectively), specimens HP-X-15-H and HP-X-20-H with headed-end (failure loads of 94.2 and 89.2 kN, respectively) did not result in a considerable additional capacity (no statistical significance, Table 4.8). As mentioned earlier, the capacity of the headed bars was governed largely by the head bearing against the cementitious matrix causing the early break down of the block before the head reaches its full pullout capacity.

On the contrary, for fibrous specimens using headed-end bars, irrespective of the bar diameter, showed a sizable increase in the failure pullout load compared to counterpart straight bars. For instance, the average failure load for all fibrous specimens with No.15 and No.20 headed-end bars notably increased by 23 and 37%, compared to their counterpart specimens with straight bars, respectively, with statistical significance (Table 4.8). This can be attributed to the role of fibers in maintaining the integrity of the cementitious block through the pullout process up to failure.

4.3.4.4 Effect of adding discrete fibers

During the pullout test, when the induced circumferential tensile stresses at the cementitious matrix-headed-end bar interface exceeded the tensile strength of the matrix, block splitting occurred. Cosenza et al. (2017) concluded that the bond strength was largely relies on concrete confinement. Harajuki and Abouniaj (2010) and Bemokrane et al. (2016) reported that adding steel spirals as confinement reinforcement in the block would lead to tremendous enhancement in the bond strength of GFRP bars. In this study, the presence of discrete fibers, regardless of the type or dosage of fibers, showed drastic improvement in the mode of failure of the concrete block and the pullout failure load of the GFRP bar. For instance, for straight GFRP bars, adding 2.5% of BP in specimens BF-2.5-15-S and BF-2.5-20-S led to 16 and 20% enhancement in the average failure load, respectively, compared with control specimens without any fibers (HP-X-15-S and HP-X-20-S). These percentages were 39 and 53% for specimens with headed-end bars (BF-2.5-15-H and BF-2.5-20-H), respectively. The statistical analysis (ANOVA) confirmed that this increase of failure load was significant (F values of 11.4 and 32.3 versus F_{cr} of 7.7). This may be attributed to the presence of fibers, which played an essential role in controlling the development of cracking, providing better confinement, and dissipating bond energy.

Accordingly, increasing the dosage of BP yielded further improvement in the average failure load, despite the diameter and the end type of GFRP bars. For example, increasing the dosage of BP to 4.5% in specimens BF-4.5-15-S, BF-4.5-20-S, BF-4.5-15-H, and BF-4.5-20-H led to increasing the failure load by 10, 14, 16 and 39%, respectively, compared to the counterpart specimens with 2.5% BP, with statistical significance (Table 4.8). This may allude to the adequate distribution of BP over the cross section of the specimen and the intensity of fibers, which enhanced their efficacy in restraining the cracks in the matrix, as depicted in Figure 4.9.

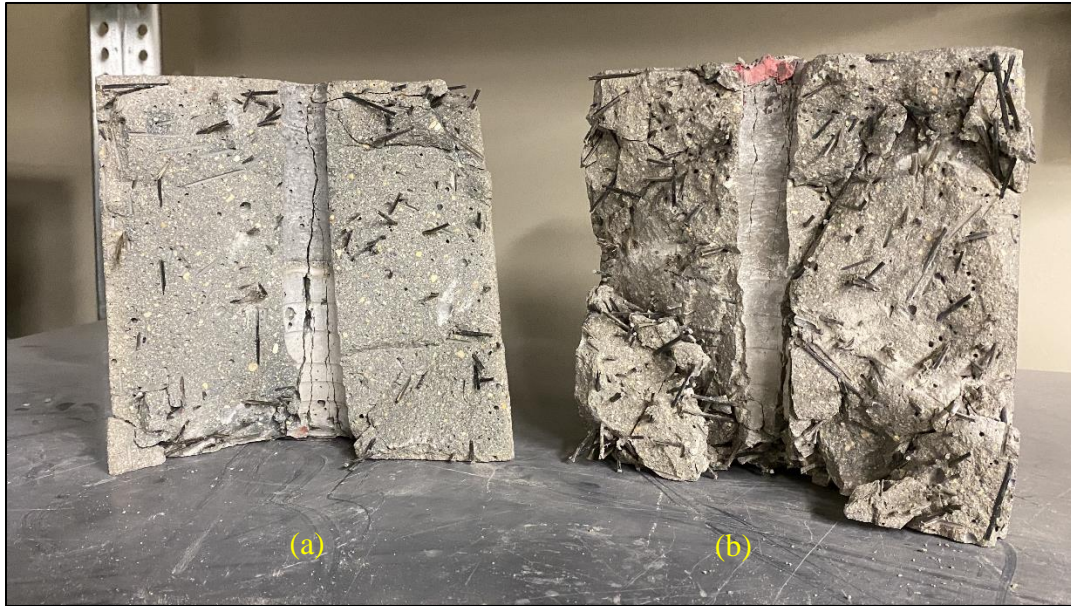


Figure 4.9: Distribution of BP in specimens: (a) BF-2.5-19-H, and (b) BF-4.5-19-H

Albeit the BP had lower modulus of elasticity and aspect ratio with respect to the SF, a comparable, or sometimes superior, performance was observed in terms of failure load and bond strength. For instance, replacing 1.0% of SF with 4.5% BP in specimens with No.15 and No.20 headed-end bars (SF-1.0-15-H and SF-1.0-20-H vs. BF-4.5-15-H and BF-4.5-20-H) led to a significant increase of 11 and 16%, respectively, in the failure load, which was also confirmed by the ANOVA results (see Table 4.8). Interestingly, when the volume of both fibers was kept constant (2.5 % BP and 1.0% SF), taking into consideration the superior properties of SF with respect to the BP, the failure pullout load was comparable. Comparing the two sets of specimens incorporating the same volume of both types (BP and SF) into the matrix yielded F value of 2.9, which was lower than the critical value (F_{cr}) of 4.3. This may be ascribed to the enhanced bonding of the cementitious composite with BP.

Based on the aforementioned discussion, the addition of fibers generally enhanced the ductility and bond strength of all fibrous specimens; thus, the residual bond strength “bond toughness” was

evaluated. Several approaches were reported in the literature to compute the energy dissipation during the load-slip (Kim et al. 2013; Hou et al. 2017). However, bond toughness adopted in this study was proposed by Chu and Kwan (2019), where two toughness indices were obtained: T_{peak} – the area under the load-slip graph up to the peak bond strength, and T_{post} – the area under the bond load-slip graph up to failure. The failure was defined to be either the peak load or 80% of the maximum load on the descending branch of the load-slip response. Table 9 summarizes the computed toughness indices of control and fibrous specimens. Conforming to the previous results, the specimens with higher fiber volume (4.5% of BP) exhibited the highest toughness indices (T_{peak} and T_{post}), irrespective of the bar diameter or the type of bar end. For example, for straight and headed-end bars, incorporating 4.5% of BP in specimens BF-4.5-15-S, BF-4.5-20-S, BF-4.5-15-H, and BF-4.5-20-H drastically increased the T_{post} by 16, 1100, 780, and 8000%, respectively, compared to their counterpart specimens without fibers. In addition, the bond toughness confirmed the authors' notion that adding low dosage of BP was as effective as SF in improving the residual bond strength. The toughness indices (T_{peak} and T_{post}) for the two sets of specimens having 2.5% of BP and 1% SF were quite comparable (see Table 4.9, except for specimen SF-1.0-20-H).

4.3.5 Evaluation of code provisions for bond strength

In this section, an analysis of the bond strength adopted by the ACI 440.1R-15 (ACI 2015), CSA/S806-12 (CSA 2017), and CSA/S6-19 (CSA 2019a) was conducted to examine their applicability to predict the ultimate bond strength of specimens containing fibers. It is worth mentioning that the bond strength was calculated based on the bar geometry, and the obtained mechanical properties.

The ACI 440.1R-15 (2015) recommends the following equation for the bond strength:

Table 4.9: Bond toughness indices for the test specimens

Specimens	Bond toughness up to peak load T_{peak} (kN.mm)	Bond toughness up to 80% of failure load T_{post} (kN.mm)
HP-X-15-S	29.10	189.40
HP-X-20-S	57.70	57.700
HP-X-15-H	59.50	89.300
HP-X-20-H	39.40	39.400
BF-2.5-15-S	94.00	279.30
BF-2.5-20-S	155.1	288.00
BF-2.5-15-H	67.20	336.80
BF-2.5-20-H	156.0	460.20
BF-4.5-15-S	105.6	220.80
BF-4.5-20-S	248.7	507.00
BF-4.5-15-H	187.0	1075.0
BF-4.5-20-H	504.6	3196.8
SF-1.0-15-S	98.10	154.70
SF-1.0-20-S	150.4	195.40
SF-1.0-15-H	95.10	176.00
SF-1.0-20-H	308.4	1671.4

$$\tau_{max} = 0.083\sqrt{f'_c} \left(4 + 0.3 \frac{c}{d_b} + 100 \frac{d_b}{\ell_e} \right) \quad \text{Equation 4.2}$$

where τ_{max} is the bond strength (MPa), f'_c is the compressive strength (MPa), c is the lesser of the cover to the center of the bar or one-half of the center-to-center spacing of the bars being developed (mm), ℓ_e is the embedment length, and c/d_b should be less than 3.5.

The bond strength suggested by CSA/S806-12 (CSA 2017) is given by:

$$\tau_{max} = \frac{d_{cs} \sqrt{f'_c}}{1.15 K_1 K_2 K_3 K_4 K_5 \pi d_b} \quad \text{Equation 4.3}$$

where τ_{max} , f'_c , and d_b are as defined above, d_{cs} is spacing factor and shall not be greater than 2.5 d_b . K_1 , K_2 , K_3 , K_4 , K_5 are the factors that take into account the bar location, concrete density, bar size, bar fiber, and bar surface, respectively, and $\sqrt{f'_c}$ shall not be greater than 5 MPa.

The CSA/S6-19 (CSA 2019a) gave the bond strength using the following equation:

$$\tau_{\max} = \frac{\left(d_{cs} + K_{tr} \frac{E_{frp}}{E_s} \right) f_{cr}}{0.45 K_1 K_6 \pi d_b} \quad \text{Equation 4.4}$$

where $f_{cr} = 0.4\sqrt{f'_c}$ is the cracking strength of concrete (MPa), K_1 is the bar location factor, K_6 is the factor that takes into account the bar surface relative to deformed steel and should be taken as 0.8 in the absence of experimental data, k_{tr} is the transverse reinforcement index and should be less than $2.5 d_b$, and the square root of concrete compressive strength should be less than 8 MPa.

Table 4.10 shows comparisons between the experimental bond strength and the code predicted strength of the tested specimens. The results showed that the tested three codes underestimated the bond strength for all test specimens with the Canadian ones being more conservative. For example, following the ACI guidelines, the mean experimental-to-predicted, P_{exp}/P_{pre} , ratio of 1.25 and 33.2 and CoV of 0.16 and 0.27 respectively, were obtained for straight and headed-end GFRP bars. This might be attributed to the limit of 3.5 stipulated by the code for c/d_b , which led to neglecting the effect of bar diameter. In the Canadian codes (CSA/S806-12 and CSA/S6-19) this can be linked to the limitation of d_{sc} and ignoring the effect of embedded length. However, all codes adopted in this study did not consider the effect of adding discrete fibers to the cementitious matrix and using GFRP bars with different anchorage (e.g. headed-end bars); thus, the current codes need to be revised to obtain better prediction.

Table 4.10: Comparison between the experimental and predicted bond strength

	Specimens	τ_{exp} (kN)	Bond strength					
			ACI 440.1R-15			CSA/S806-12		CSA/S6-19
			τ_{ACI} (kN)	$\tau_{exp/ACI}$	τ_{CSA} (kN)	$\tau_{exp/CSA}$	τ_{CSA} (kN)	$\tau_{exp/CSA}$
Straight-end bars	NSC-X-15-S	22.0	15.98	1.37	4.33	5.06	6.00	3.65
	NSM-X-15-S	20.7	16.46	1.25	4.33	4.77	6.17	3.35
	NP-X-15-S	22.6	19.43	1.16	4.33	5.22	7.29	3.10
	HP-X-15-S	27.1	22.97	1.18	4.33	6.24	7.45	3.63
	HP-X-20-S	19.7	23.09	0.85	4.33	4.53	7.45	2.63
	BF-2.5-15-S	31.3	22.37	1.40	4.33	7.23	7.45	4.20
	BF-2.5-20-S	23.6	22.49	1.05	4.33	5.45	7.45	3.17
	BF-4.5-16-S	34.6	21.98	1.57	4.33	7.99	7.45	4.64
	BF-4.5-19-S	27.1	22.10	1.22	4.33	6.24	7.45	3.63
	SF-1.0-16-S	32.3	22.66	1.42	4.33	7.44	7.45	4.33
	SF-1.0-19-S	27.5	22.78	1.20	4.33	6.34	7.45	3.68
	Mean			1.25		6.10		3.60
	*CoV			0.16		0.19		0.16
Headed-end bars	HP-X-15-H	475.8	16.10	29.55	4.33	109.87	7.45	63.86
	HP-X-20-H	313.0	18.48	16.94	4.33	72.290	7.45	42.02
	BF-2.5-15-H	606.1	15.68	38.65	4.33	139.97	7.45	81.35
	BF-2.5-20-H	477.2	18.00	26.51	4.33	110.21	7.45	64.05
	BF-4.5-16-H	699.5	15.41	45.39	4.33	161.55	7.45	93.89
	BF-4.5-19-H	662.8	17.69	37.47	4.33	153.07	7.45	88.97
	SF-1.0-16-H	632.8	15.88	39.85	4.33	146.15	7.45	84.94
	SF-1.0-19-H	569.1	18.23	31.22	4.33	131.44	7.45	76.39
	Mean			33.2		128.1		74.4
	*CoV			0.27		0.230		0.23

*CoV = coefficient of variation

4.4 Conclusions

Based on the experimental investigations, the following conclusions can be drawn:

- Compared to the control mixtures, mixtures with fibers yielded lower compressive strength, especially with higher dosages of BP with statistical insignificance; however, the mode of failure considerably changed from brittle to ductile.

- Four modes of failure for specimens cast without fibers were observed; pure pullout, partial pullout, splitting of concrete, and concrete crushing followed by splitting of the head. On the other hand, three modes of failure were noticed for fibrous specimens; partial pullout, cracking of concrete, and cracking of concrete followed by bar slippage. It is worth mentioning that the presence of fibers, in general, managed to keep the concrete block as one unit, even for specimens with headed-end bars.
- Adding 40% of slag as a partial replacement of cement in addition to 6% of nano silica (HP-X-15-S vs NP-X-15-S) significantly increased the failure load by approximately 19% due to the synergistic effects of nano-silica and slag resulting in densification of microstructure.
- The embedment length, transverse contraction strain (Poisson effect), and shear lag are the main reasons behind the lower bond strength for larger bar diameter. In addition, using headed-end bar in fibrous specimens, irrespective of the bar diameter, showed a tremendous increase in the failure pullout load compared to straight bars.
- The Canadian standards (CSA 2017 and 2019) and the American guidelines (ACI 2015) for GFRP bars were too conservative in predicting the ultimate bond strength. Therefore, the provisions of bond strength in current FRP design codes and guidelines need to be revised to better predict the bond strength of fibrous concrete reinforced with straight or headed-end GFRP bars.

CHAPTER 5: BOND DEGRADATION OF GFRP BARS EMBEDDED IN BFRCC UNDER HARSH CONDITIONS

Authors and Affiliation:

- Ahmed G. Bediwy, PhD Candidate, Department of Civil Engineering, University of Manitoba
- Ehab F. El-Salakawy, Professor, Department of Civil Engineering, University of Manitoba

Journal and Status:

American Concrete Institute (ACI) Materials Journal, submitted on December 15, 2020.

Reference:

Bediwy, A., and El-Salakawy, E. “Bond degradation of GFRP bars embedded in BFRCC under harsh conditions.” *ACI Materials Journal*, under review.

Note:

The manuscript had been slightly altered from the original paper by renumbering the tables and figures to include the chapter number. In addition, the reference list and list of notations have been moved to the appropriate sections in the thesis as indicated in the table of contents.

Abstract:

This study aims at assessing the long-term bond behaviour of headed-end glass fiber-reinforced polymer (GFRP) bar to fiber reinforced cementitious composite (FRCC) exposed to 300 consecutive freezing-thawing cycles followed by 75 cycles of wetting-drying mimicking successive winter and summer seasons. A total of 85 pullout specimens reinforced with the recently developed basalt fiber pellets and steel fibers were tested. The durability of the specimens was quantified in terms of visual analysis, residual compressive strength, relative dynamic modulus of elasticity as well as the residual pullout capacity. The addition of fibers was capable of retaining approximately 90% of the pullout capacity for specimens exposed to harsh conditions owing to the restriction of cracks in the FRCC. Therefore, the results confirmed the suitability of steel-free reinforcement system for long-term application under severe freeze–thaw and wet-dry environments.

Keywords: glass fiber-reinforced polymer; pullout; basalt fiber pellets; headed-end bars; residual bond strength.

5.1 Introduction

The use of concrete structures reinforced with glass fiber-reinforced polymer (GFRP) has gained significant ground in the construction field to overcome the problems caused by corrosion of steel reinforcement. The non-corrodible nature of GFRP bars along with their high tensile strength, light weight and ease of installation made it a realistic and cost-effective reinforcing alternative to steel especially for concrete structures under aggressive environment. GFRP bars are produced with different shapes and surface textures including the recently developed GFRP bars with anchor head to reduce the required development length and avoid premature anchorage and bond failures, as reported by several researchers (Maranan et al. 2015; Benmokrane et al. 2016; Mahmoud et al. 2017).

However, GFRP reinforcement has relatively low elastic modulus and linear-elastic stress-strain relationship up to failure, which cause GFRP-RC flexural members exhibit less ductility (Naaman and Jeong 1995). In addition, GFRP bars might be vulnerable to significant degradation when exposed to severe conditions, such as freezing-thawing cycles and wetting-drying cycles, which include high humidity and high temperature. Therefore, it is necessary to develop durable and ductile cementitious composite in order to improve the longevity and serviceability of GFRP reinforcement serving in cold regions.

The use of fiber-reinforced concrete (FRC) has been suggested by many researchers to expand the possibilities of using concrete in such harsh environments and developing high performance composites to rehabilitate concrete infrastructure (e.g. bridge decks, pavements, parking structures) (Nes and Øverli 2015). Incorporating discrete fibers into any cementitious composite can provide the composite with strain hardening behaviour, increasing the energy absorbing capacity (toughness), and transforming the brittle behaviour to ductile failure (Wille et al. 2012).

This improvement was attributed to the ability of fibers to bridge cracks and to transfer tensile stress across crack interface (Bentur and Mindess 2007).

Various types of fibers, such as steel, organic and inorganic, have been used to make fiber-reinforced cementitious composites (FRCC). However, basalt fiber (BF) is a new kind of inorganic fibers manufactured by the extrusion of melted basalt rocks. The basalt fibers are gaining momentum in the construction market since the production process of basalt fibers is more environment friendly, and it is cheaper with respect to the other types of fibers such as glass fibers. Basalt fibers have high tensile strength (3,000 - 4,000 MPa) [435000 - 580000 psi], reasonable modulus of elasticity (93 - 110 GPa) [13.5 - 16 ksi], and they are not vulnerable to surface corrosion contrary to steel fibers (SF) that corrode (Arslan 2016; Mahmoud et al. 2017). Nevertheless, basalt fibers are prone to sever degradation when incorporated in high alkaline media (e.g. concrete); therefore, a special type of BP, which was made of basalt fibers coated with polyamide or other resins, has been adopted in this study.

It is well documented that the bond characteristics of GFRP reinforcement are among the vital parameters that control the design of FRP-reinforced concrete (RC) members (Cosenza et al. 1997; Alves et al. 2011). As such, the evaluation and clear understanding of the long-term bond performance and bond degradation mechanisms of a nonferrous reinforcement system, which includes GFRP reinforcement and FRCC as a cementitious matrix, is in high demand. This will help increasing the acceptance and widespread of GFRP reinforcement in civil engineering applications. Abundance of studies have been conducted to evaluate the durability and bond performance of straight-end or headed-end FRP bars embedded in plain concrete (Cosenza et al. 1997; Alves et al. 2011; Islam et al. 2015; Maranan et al. 2015; Benmokrane et al. 2016). However, less research has been devoted to evaluate the bond durability of FRP/FRC as an integral system.

Kim et al. (2013) and Yan and Lin (2017) conducted an extensive experimental work to evaluate the pull-out strength of sand-coated and helically-wrapped GFRP bars embedded in concrete reinforced with hooked-end SF and polypropylene fibers. Both studies observed a notable enhancement in ductility and better bond behaviour with the presence of SF compared to plain concrete due to fiber bridging action. However, the main drawback of using steel, as either reinforcing bars or discrete fibers, still exists since they are vulnerable to corrosion. On the other hand, Belarbi and Wang (2012) studied the bond degradation by exposing GFRP-RC specimens that contained polypropylene fibers to combined environmental conditioning, which included freeze-thaw cycles, high temperature, and deicing salt solution. It was observed that bond durability markedly enhanced, as the presence of polypropylene fibers restrained the propagation of micro cracks. However, the cementitious matrix used in the later study did not provide significant protection to the bar from the ingress of moistures. In addition, the polypropylene fibers were not stiff enough to be used for structural performance, as it is usually used for controlling the plastic shrinkage. To the authors' knowledge, there is no research has been conducted to investigate the bond durability of headed GFRP bars embedded in cementitious matrix reinforced with discrete non-metallic fibers such as BP.

This study presents the second phase of an ongoing program at the University of Manitoba. The first phase of this research project was undertaken by Mahmoud et al. (2017), in which, a pilot investigation on the pullout behaviour of GFRP reinforcing bars with different end shapes cast in nano-modified cementitious composites incorporating 6% Ns with 40% slag and 2.5% BP (basalt fiber reinforced cementitious composite [BFRCC]) by volume of the matrix. This study investigated in more depth the pull-out capacity of GFRP bars embedded in BFRCC with different dosages of BP compared to SF under harsh environmental conditions that include repetitive freeze-

thaw and wet-dry cycles simulating consecutive winter and summer seasons, correlating to in-service conditions.

5.2 Research Significance

FRCC has garnered interest from the civil engineering community due to its significantly improved mechanical properties. Past experimental studies have confirmed that the incorporation of SF into cementitious matrix can significantly enhance the bond performance of GFRP bars. However, SF are vulnerable to corrosion in harsh conditions (e.g. North America), therefore, investigating the effect of using nonferrous fibers on the bond strength of GFRP bars deems necessary. This study is devoted to evaluate the key factors affecting the long-term bond durability of headed-end GFRP bars embedded in cementitious matrix reinforced with a non-structural, non-metallic fibers.

5.3 Experimental Procedure

5.3.1 Materials

5.3.1.1 Cementitious composite

General use (GU) Portland cement and slag were used as the main components of the binder complying with the requirements of CSA A3001 standard (2018). Table 5.1 shows the chemical and physical properties of these components. In this study, a nano-silica (Ns) solution was added to the binder. Fine sand, having a specific properties of fineness modulus of 2.9 and a gradation less than 600 μm according to ASTM C136 (2019a), was adopted to cast the composites. A high-range water-reducing admixture (HRWRA) complying with ASTM C494 Type F (2019b) was used to target a flow between 185 and 215 mm for all composites.

Table 5.1: Chemical and physical properties of GU cement and slag

Binder	Chemical composition (%)							Physical properties	
	SiO ₂	Al ₂ O ₃	Fe ₂ O ₃	CaO	MgO	SO ₃	Na ₂ O _{eq}	Blaine (m ² /kg)	Specific Gravity
Cement	19.21	5.01	2.33	63.22	3.31	3.01	0.12	390	3.15
Slag	33.40	13.4	0.76	42.70	5.30	2.40	0.30	492	2.87

5.3.1.2 Fibers

The cementitious composites were reinforced with either BP or SF (Figure 5.1). The BF represented 60% of the pellet by weight. The BP were 36-mm long with a diameter of 1.8 mm. A 0.5-mm diameter hooked-end SF with a 30-mm length were also used. The properties of the BP and the SF are listed in Table 5.2.

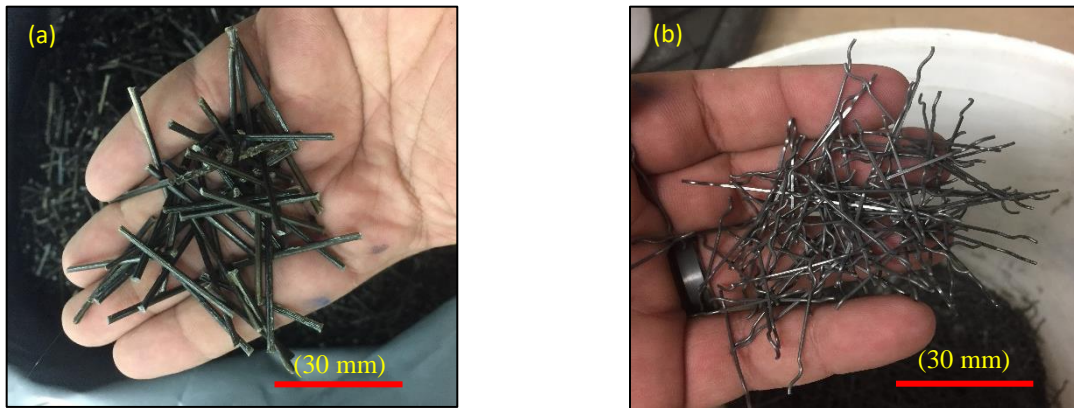


Figure 5.1: Reinforcing fibers (a) basalt fibers pellets, and (b) steel fibers

Table 5.2: Properties of fibers

Properties	Properties of fibers	
	BP	Hooked steel
Length (mm)	36	30
Diameter/dimensions (mm)	1.80	0.65
Aspect ratio	20	45
Specific gravity	1.74	7.70
Tensile strength (MPa)	2,300	1,200
Elastic modulus (GPa)	65	200

5.3.1.3 GFRP reinforcement

Sizes No.15 and No.20 sand-coated, GFRP bars with either straight or headed-ends were used. The headed-ends were made of thermoplastic matrix reinforced with short glass fibers, cast on the end of bars at high temperature. Irrespective of the bar size, the 100-mm long head had a stepped surface with a maximum outer diameter of 50 mm at the end as shown in Figure 5.2. The mechanical properties of the GFRP bars were obtained through standard tests carried out according to ASTM D7205-06 (2016), as listed in Table 5.3.



Figure 5.2: GFRP bars and configuration of the head

Table 5.35: Mechanical properties of GFRP

Bar Type	Bar size	Nominal diameter (mm)	Area (mm ²)		Tensile strength (MPa)	Modulus of elasticity (GPa)	Ultimate strain (%)
			Nominal	CSA/S806-12 Annex A			
GFRP	No. 15	15.9	198	291	1,184	62.6	1.89
	No. 20	19.0	285	394	1,105	63.7	1.73
GFRP Head	-	-	-	-	552*	68.0	0.80*

Note: Properties are the same for straight and headed-end bar

* Usable design stress/strain provided by the manufacturer (corresponds to a pull-out load capacity of 70 kN)

5.3.2 Proportions of mixtures

Two different mixtures were produced in this study: normal cementitious composite (designated as NP), and high-performance cementitious composite (designated as HP). The NP mixture was prepared with a GU cement content of 700 kg/m^3 , while the HP one was cast with 420 kg/m^3 GU cement and a slag content of 280 kg/m^3 , representing 40% replacement of cement content. In addition, Ns, at a dosage of 6% by mass of the binder, was added to the HP mixtures. The water-to-binder ratio (w/b) was kept constant at 0.30 for both mixtures. The mixtures were reinforced with either BP or SF. The BP were added to the mixtures at different dosages of 2.5 and 4.5% by volume, corresponding to 1.0 and 2.0%, respectively, by volume of BF, as the fibers represents 40% of the pellets by volume. Whereas, in the case of SF, this dosage was 1.0%. The proportions of all the cementitious composites are listed in Table 5.4. Further description of the components and the mixing procedures can be found elsewhere (Mahmoud et al. 2017). The mixture nomenclature consists of three parts. The first part stands for the type of the cementitious composite (“NP” for a composite cast without SCMs and “HP” for a composite cast with slag and Ns), whereas the second part refers to the fiber type (“B” for basalt fiber pellet and “S” for steel fiber). The third part represents the fiber dosage percentage used (2.5 and 4.5 for BP, and 1.0 for SF).

5.3.3 Test specimens and conditioning procedure

A total of 85 specimens, five replicates for each mixture, were fabricated following the guidelines of Annex G of the CSA/S806-12 (CSA 2017) to assess the residual bond strength after conditioning the specimens in harsh environment. The pullout specimens consisted of a 200-mm side length cube with concentric placement of the bar. The dimensions of the specimen were chosen to avoid splitting of the cube. The embedded length was four times the bar diameter ($4d_b$)

Table 5.4: Proportions of the mixtures per cubic meter

Mixture ID	Cement (kg)	Slag (kg)	Water ^a (kg)	Nano-silica (Ns, kg)	Fine aggregate (kg)	HRWRA (L)	Fibers (kg)	
							BP	Hooked steel
NP-X-0.0	700	-	210	-	1,471	5.7	-	-
HP-X-0.0	420	280	180	84	1,328	7.4	-	-
HP-B-2.5	420	280	180	84	1,268	7.4	43.3	-
HP-B-4.5	420	280	180	84	1,211	7.4	78.3	-
HP-S-1.0	420	280	180	84	1,302	7.4	-	77

^a Adjusted amount of mixing water considering the water content of nano-silica (aqueous solution with 50% solid content of SiO₂)

in bars with straight ends, whereas it was equal to the head length (100 mm) in headed-end bars. The unbonded length was wrapped with a smooth surface tape to ensure that no bond exists between the cementitious matrix and the bar over this length. The other end of the GFRP bar was sheathed with thick-wall steel pipe, then the pipe was filled with a commercial expansive grout to anchor the bar with the pipe. Details of the specimens are presented in Figure 5.3.

After casting, the specimens were demolded and kept inside the curing room (21°C and >95% RH) for 14 days. All the specimens, then, were subjected to freeze-thaw and wet-dry cycles. This exposure simulated consecutive winter and summer seasons, which correlates to in-service conditions in most of the Canadian cities. The freezing-thawing (F/T) cycles were applied in accordance with ASTM C666 (2019c, procedure A) and it consisted of alternately lowering the temperature from +4 to -18 °C for freezing and raising it from -18 to +4 °C for thawing. The temperature was maintained for 2 hr at each temperature boundary (i.e. -18 and +4 °C). It should be noted that there are no standard test methods for the wetting-drying (W/D) exposure of concrete elements. The cyclic regime in this study was selected similar to that adopted by Bassuoni and Rahman (2015) to achieve significant humidity changes and aggravate test

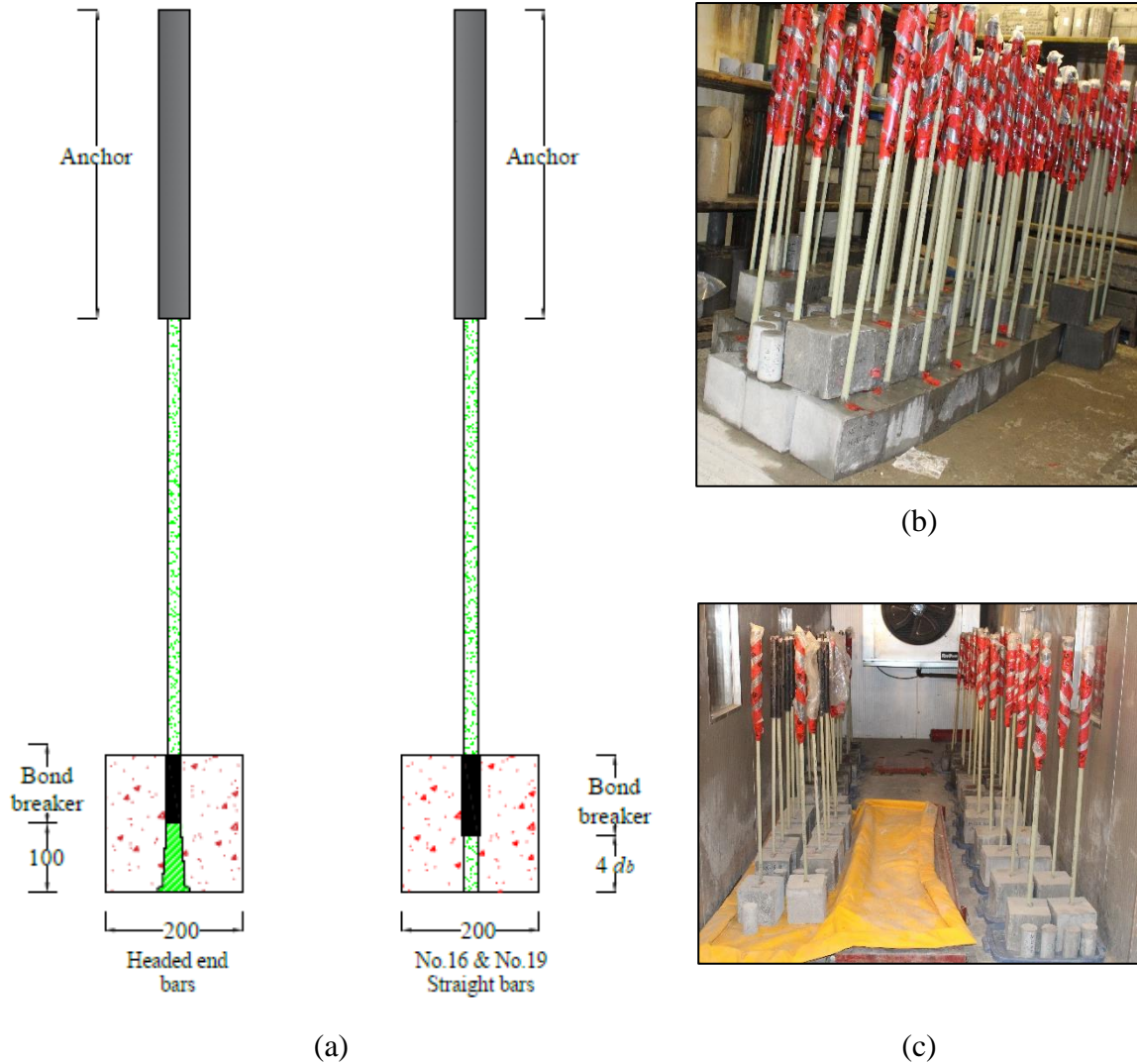


Figure 5.3: Test specimens, (a) schematic drawing of the specimens, (b) specimens after casting in the curing room, and (c) specimens in the environmental chamber (all dimensions in mm)

conditions. The exposure continued for 75 days, where each cycle (24 hr) consisted of two consecutive stages: an 8-hour hot/dry stage ($40 \pm 2^\circ\text{C}$ and $35 \pm 5\%$ RH) followed by a 16-hour temperate/humid stage ($20 \pm 2^\circ\text{C}$ and $90 \pm 5\%$ RH).

It is worth mentioning that companion (un-conditioned/control) specimens were cast and tested at the age of 28 days after moist curing for better interpretation of bond durability of this hybrid system. The combined exposure was assessed based on four criteria. (i) visual analysis. (ii)

residual compressive strength of concrete that was determined by testing standard cylinders (100 × 200 mm) on the day of testing according to CSA A23.1-19/A23.2-19 (CSA 2019b). (iii) the relative dynamic modulus of elasticity that was calculated during the cyclic exposure using the resonance frequency method (transverse mode) on standard prisms (100 × 100 × 350 mm) according to ASTM C215 (2019e). The relative dynamic modulus can be calculated as per ASTM C666 (2019c) by the following equation:

$$RE_n = \left(\frac{N_n^2}{N_0^2} \right) \quad \text{Equation 5.1}$$

where RE_n and N_n are the relative dynamic modulus and the fundamental transverse frequency at n cycles, respectively, while N_0 is fundamental transverse frequency at 0 cycles. Since the wetting and drying exposure have yet been standardized, the authors decided to employ the RE as an indicator to assess the internal damage through the wetting and drying cycles. Finally, (iv) the residual bond strength considering the test parameters that include the type of cementitious composite, the type and dosage of fiber added to the cementitious matrix, the bar diameter, and the reinforcing bar end shape.

It should be noted that the air content of the freshly mixed composites was measured according to ASTM C231 (2017).

The nomenclature of the specimens consists of four parts. The first part is referring to the composite type (“NP” for a composite without SCMs or fibers, “HP” for a composite with SCMs and without any fibers, “BF” for a composite with SCMs and BP, and “SF” a composite with SCMs and steel fibers). The second part describes the dosage of fibers added, if any (2.5% and 4.5% for BP, and 1.0% for SF). The third part indicates the bar diameter (15 and 20 mm), and the

last part indicates the bar end shape (“S” for straight bars, and “H” for headed-end bars. The details of the specimens are listed in Table 5.5.

Table 5.5: Details of test specimens for pullout

Specimens	Composite type	Fiber type	Fiber dosage (%)	Bar diameter (mm)	Bar end
NP-X-15-S	Composite without SCMs and fibers	N/A	N/A	15.9	Straight
HP-X-15-S	Composite with SCMs and without fibers	N/A	N/A	15.9	Straight
HP-X-20-S				19.0	
HP-X-15-H				15.9	Headed
HP-X-20-H				19.0	
BF-2.5-15-S	Composite with SCMs and BP	Basalt	2.5	15.9	Straight
BF-2.5-20-S				19.0	
BF-2.5-15-H				15.9	Headed
BF-2.5-20-H				19.0	
BF-4.5-15-S	Composite with SCMs and BP	Basalt	4.5	15.9	Straight
BF-4.5-20-S				19.0	
BF-4.5-15-H				15.9	Headed
BF-4.5-20-H				19.0	
SF-1.0-15-S	Composite with SCMs and SF	Steel	1.0	15.9	Straight
SF-1.0-20-S				19.0	
SF-1.0-15-H				15.9	Headed
SF-1.0-20-H				19.0	

5.3.4 Test setup and instrumentation

The pullout testing of the samples was conducted using an MTS machine. A monotonically increasing load was applied at a rate of 10 kN/min, which is less than the 22 kN/min maximum rate specified in the CSA/S806-12 (CSA 2017). A total of three linear variable displacement transducers (LVDTs) were attached to each specimen; two at the loaded-end and one at the free-end to measure the slip of the GFRP bar. A data-acquisition system monitored by a computer was used to record the readings of the machine load and the LVDTs. Figure 5.4 depicts the test setup details.

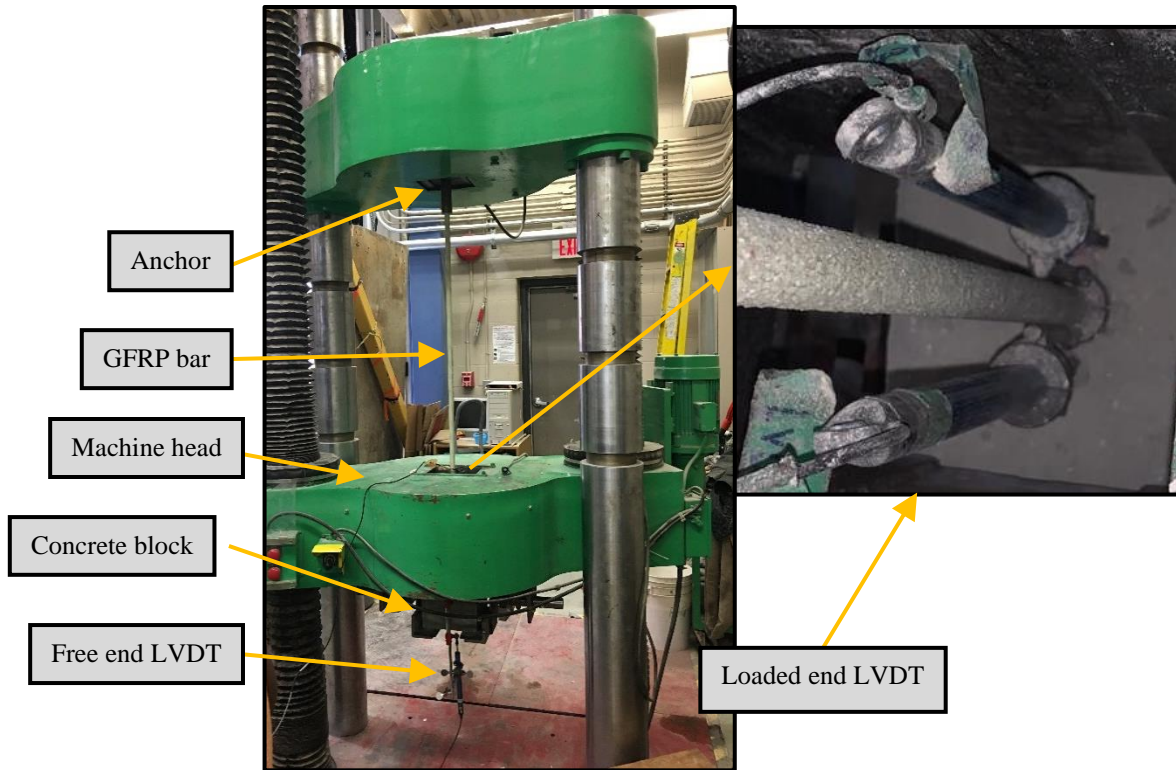


Figure 5.4: Pullout test setup and instrumentation

5.4 Experimental Results and Discussion

5.4.1 Internal damage assessment

5.4.1.1 Visual analysis

Figure 5.5 shows the appearance of the pullout specimens after completing 300 and 75 cycles of F/T and W/D actions. The development and extent of surface cracks were used as a measure for deterioration. To properly assess the status of the specimens, the authors adopted the visual rating category that stipulated by ASTM C672 (2012), where the scale started from 0 (no deterioration/cracks) to (5 severe deterioration/cracks). For the specimens without any fibers, severe damage, characterized by wide web-cracks located at the surface, was observed in specimen NP-X-0.0 (visual rating of 4-5), while moderate deterioration (visual rating of 2-3) was noted for

specimen HP-X-0.0. On the other hand, for fibrous specimens, it seemed that the FRCC specimens were immune to the environmental exposure in comparison with plain cementitious composite specimens. Slight hair-cracks were observed in specimens HP-S-1.0 and HP-B-4.5, these cracks were limited to the edges of the specimens (visual rating of 1), while specimens reinforced with 2.5% BP had no cracks, as the specimens remained completely intact (visual rating of 0). It is worth noting that the visual assessment approach could not accurately capture the performance of all specimens; therefore, a physical indicator (residual compressive strength and relative dynamic modulus of elasticity) reflecting whether the cracks were formed internally and propagated towards the surface should be augmented.



NP-X-0.0 (VR of 4-5)



HP-X-0.0 (VR of 2-3)



HP-B-2.5 (VR of 0)



HP-B-4.5 (VR of 1)



HP-S-1.0 (VR of 1)

Figure 5.5: Appearance of specimens after combined exposure (Visual rating [VR])

5.4.1.2 Residual compressive strength

The average compressive strength obtained from testing three cylinders for each mixture at 28 days under ambient conditions (control mixtures) and after conditioning, are listed in Table 5.6. In general, with respect to the control cement-based, the HP mixtures at 28 days yielded higher compressive strength, irrespective of the type or the dosage of the fibers added. For example, the addition of slag and Ns in HP-X-0.0 markedly improved the compressive strength by 40% with respect to NP-X-0.0. In addition, the compressive strength was decreased for all specimens after the cyclic regime adopted herein due to the formation of internal microcracks that negatively affected the strength; however, the synergistic effect of nano silica and slag in refining and densifying the pore structure of the cementitious matrix effectively controlled the reduction rate in compressive strength. For instance, exposing the NP-X-0.0 and HP-X-0.0 to repetitive F/T and W/D cycles led to 27 and 19% reduction in the compressive strength, respectively. This also can be attributed to the well-documented role of SCMs in improving the properties of the cementitious composite.

On the other hand, the incorporation of discrete fibers yielded an adverse effect on the compressive strength of the specimens when tested under normal conditions (see Table 5.6). This occurred since the fibers increased the interfacial transitional zones (ITZs) in the matrix, in addition to the air that being entrapped in the cementitious matrix after compacting (Table 5.6, as previously reported by Mahmoud et al. (2017).

However, after the cyclic exposure, the presence of fibers, irrespective of their type or dosage, effectively controlled the rate of deterioration and mitigated the reduction in the compressive strength to the extent that it exceeded the compressive strength of their counterpart mixtures cast without fibers. For example, after the F/T and W/D cycles, the compressive strength of the control

mixture HP-X-0.0 was 69.4 MPa, while the inclusion of BP and SF in specimens HP-B-2.5, HP-B-4.5, and HP-S-1.0 yielded a compressive strength of about 72.9, 69.5, and 70.4 MPa, respectively. This was ascribed to the ability of the fibers to control micro-cracks and maintain the integrity of the cylinders up to the end of the exposure period. Interestingly, the incorporation of BP at a dosage of 2.5% (representing 1.0% of BF) showed a reduction rate less than its counterpart specimen cast with 1.0% SF, even though SF has higher modulus of elasticity and better aspect ratio compared with BP. For instance, adding 2.5% of BP and 1.0% of SF in specimens HP-B-2.5 and HP-S-1.0 reduced the compressive strength by 10 and 16%, respectively, after the combined exposure, compared with their counterpart virgin specimens.

Table 5.6: Air content, RE_n , and compressive strength of the cementitious composites

Mixture ID	Air content (%)	*RE_n (%)		Compressive strength (MPa)	
		After F/T	After W/D	Normal conditions	Severe conditions
NP-X-0.0	5.7	67.8	67.6	61.3	44.2
HP-X-0.0	5.5	79.5	79.6	85.7	69.4
HP-B-2.5	7.1	95.5	94.8	81.3	72.9
HP-B-4.5	7.8	91.2	89.6	78.5	69.5
HP-S-1.0	6.2	89.6	87.4	83.4	70.4

5.4.1.3 Relative dynamic modulus of elasticity

The relative dynamic modulus of elasticity was mainly used herein to assess the internal degradation of cementitious composites exposed to F/T and W/D cycles. The total RE_n for the test specimens after 300 cycles of F/T and 75 cycles of W/D are listed in Table 5.6. Conforming to the visual analysis and the residual compressive strength, the specimens cast with HP composites yielded higher relative dynamic modulus of elasticity in comparison with NP composite. Confirming the predominant role of including SCMs (e.g. slag and Ns) in densifying and refining

the pore structure of the cementitious matrix, HP-X-0.0 showed a lower drop (maximum of 20.5%) in RE_n compared to NP-X-0.0 (maximum of 32.2%). In contrary, following 300 freeze-thaw cycles, all FRCC specimens exhibited less deterioration (less than 10% reduction in dynamic modulus), which illustrates that the cracks observed during the visual analysis did not penetrate to the core of the specimen. In addition, these findings should be supplemented by the residual bond strength results. The outstanding RE_n results for fibrous composites may be linked to the high measured air content, which created a pressure release system for F/T cycles (Table 5.6). On the other hand, there was insignificant degradation in stiffness after the W/D cycles indicating that either the relative dynamic modulus of elasticity indicator was not suitable to project the pore structure after such exposure, or the W/D exposure was not harsh as the F/T cycles.

5.4.2 Modes of failure

Following the combined exposure, different modes of failures were identified for the test specimens, as summarized in the last column of Table 5.7. For straight GFRP bars embedded in plain and fibrous cementitious composites, pure pullout (PO) and partial pullout (PPO) were observed. PO failure was identified by a full pullout of the bar from the cementitious matrix, while the cube remained intact. Whereas, PPO failure was the most common mode of failure, which was characterized by a partial pullout of the GFRP bar from the cube due to the residual friction, resulted from the remaining sand coating on the outer surface, between the bar and the cementitious matrix.

On the other hand, for headed-end bars, the modes of failure can be divided into two categories based on the cementitious matrix type. For non-fibrous composites, splitting of the cube associated with the head of the bar (SCH) failure occurred when the head leaned against the cube, leading to

splitting of the cube into three or four pieces; in addition to breaking the head of the GFRP bar. In few specimens, after crushing of the concrete, the head was remained undamaged (full intact) (SC).

Table 5.7: Pullout test results

Specimens	Unconditioned				Conditioned				Mode of failure
	Failure load (kN)	Bond strength (MPa)	T_{peak} (kN.mm)	T_{post} (kN.mm)	Failure load (kN)	Bond strength (MPa)	T_{peak} (kN.mm)	T_{post} (kN.mm)	
NP-X-15-S	72.2	22.60	22.40	30.60	56.20	17.60	32.20	48.90	PO
HP-X-15-S	86.3	27.10	29.10	189.4	75.20	23.30	55.90	98.10	PPO
HP-X-20-S	88.9	19.70	57.70	57.70	79.20	17.50	49.20	99.00	PPO
HP-X-15-H	94.2	475.8	59.50	89.30	83.60	422.2	83.30	83.30	SC
HP-X-20-H	89.2	313.0	39.40	39.40	80.20	281.4	53.30	53.30	SCH
BF-2.5-15-S	100.0	31.30	94.00	279.3	91.60	28.70	72.20	146.4	PPO
BF-2.5-20-S	107.0	23.60	155.1	288	100.8	22.30	83.00	286.1	PPO
BF-2.5-15-H	120.0	606.1	67.20	336.8	113.5	556.6	135.2	302.0	CC
BF-2.5-20-H	136.0	477.2	156.0	460.2	126.1	442.5	243.8	1374	CC
BF-4.5-15-S	110.5	34.60	105.6	220.8	99.80	31.30	78.50	195.4	PPO
BF-4.5-20-S	122.5	27.10	248.7	507	110.0	24.80	93.70	437.2	PPO
BF-4.5-15-H	138.5	699.5	187.0	1075	125.4	633.3	106.6	228.5	CC
BF-4.5-20-H	188.9	662.8	504.6	3197	174.4	612.0	456.2	1022	CC
SF-1.0-15-S	103.0	32.30	98.10	154.7	93.30	29.00	91.40	158.0	PPO
SF-1.0-20-S	124.4	27.50	150.4	195.4	112.0	24.80	87.40	107.6	PPO
SF-1.0-15-H	125.3	632.8	95.10	176	112.2	566.7	121.1	202.0	CC
SF-1.0-20-H	162.2	569.1	308.4	1671	149.2	523.5	293.8	763.8	CC

Note: PO is pullout, PPO is partial pullout, SC is splitting of concrete, SCH, is splitting of concrete followed by splitting of the head, CC is cracking of cementitious composite.

In contrary, the presence of either BP or SF drastically altered the mode of failure for headed GFRP bars to be cracking of the cube (CC), as the bridging effect of fibers maintained the integrity of the cube as one unit. This failure is characterized by the formation of several cracks that initiated at the bar and propagated toward the corners of the block, while the head of the bar remained sound, and no sign of bar slippage from the head. Figure 5.6 shows the mode of failure for all cementitious composite cubes.

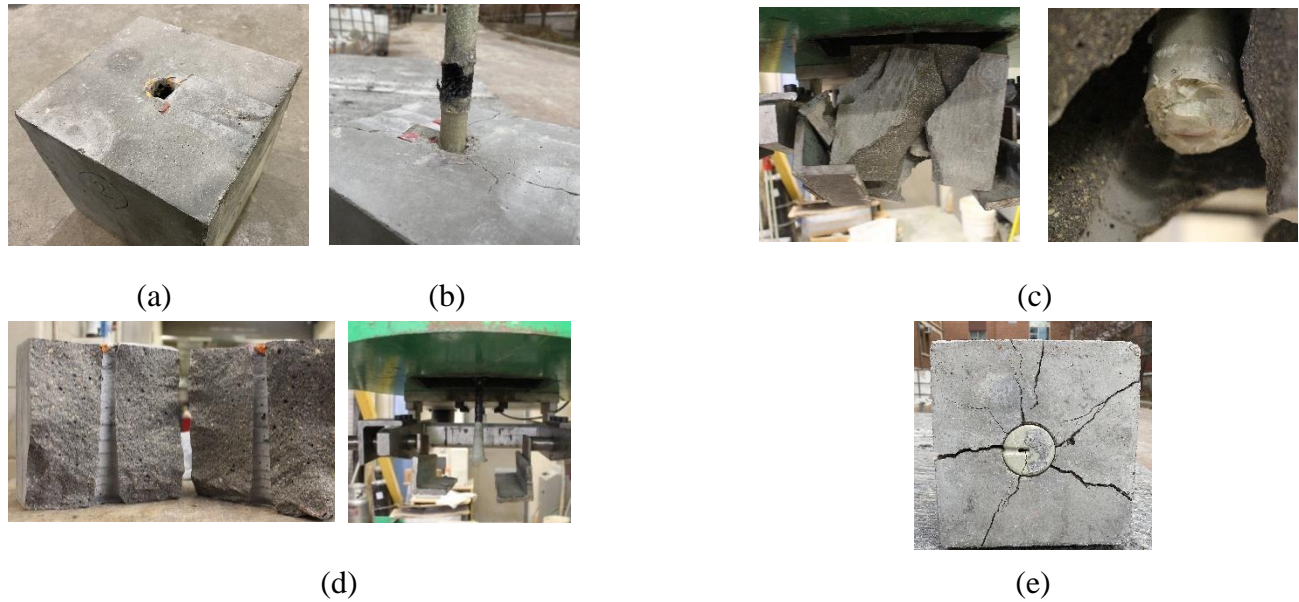


Figure 5.6: Mode of failure for all specimens, (a) PO, (b) PPO, (c) SCH, (d) SC, and (e) CC

5.4.3 Effect of environmental conditions on load-slip response

Figure 5.7 shows the typical load-slip curves at the loaded end of both No.15 and No.20 straight and headed-end GFRP bars embedded in plain and fibrous cementitious composites before and after conditioning. It is worth mentioning that the recorded slip at the loaded end was much greater than the measured slip at the free end. In general, a sharp linear ascending branch of the load-slip curves was observed, defining the pre-cracked stage. Such increase occurred over a small range of slip until the peak load was reached, despite the cementitious composite type, the GFRP bar type, or the bar size. For the post-peak stage, an abrupt drop in the load was observed reaching a maximum slip of 4 to 5 mm for the straight GFRP bar embedded in plain composites, while the behaviour beyond the peak load for the headed-end bars was not recorded due to the splitting of the cube (Figure 5.5). Similar behaviour was noticed for the unconditioned specimens.

Conversely, conditioning the fibrous specimens moderately altered the post-peak behaviour from progressive pullout failure that associated with large slip to a softened behaviour (the descending

branch beyond the first peak), except for specimen BF-2.5-20-H. For example, the unconditioned BF-4.5-20-H had a gradually-decayed slope reaching higher slip values beyond 30 mm, while conditioning such specimen (BF-4.5-20-H) yielded a sharp decrease in the load reaching a slip value of 15 mm. Similar observation was reported by Belarbi and Wang (2012) for a sand coated GFRP bar embedded in fibrous concrete and exposed to the combined effect of F/T cycles, high temperature (60 °C), and deicing salt solution.

5.4.4 Effect of environmental conditions on pullout load

The mean values of the pullout peak load and bond strength obtained from testing five replicates for all conditioned and unconditioned mixtures are listed in Table 5.7. Compared with the reference unconditioned specimens, the conditioned specimens showed degradation in pullout failure load of the GFRP bars. However, the low tensile strength, and the internal cracks induced by the combined exposure degraded the matrix surrounding the bar and led to that NP-X-15-S had the lowest pullout load (56.2 kN) after the exposure. The cementitious matrix had an important role in improving the residual failure load, as adding SCMs to the plain cementitious matrix proved to be highly effective in resisting the combined exposure. For example, exposing NP-X-15-S and HP-X-15-S to 300 F/T and 75 W/D cycles led to 22 and 12% reduction in the average pullout load, respectively, when it is compared to the unconditioned counterpart specimens. This confirms the interactive effect of both slag and Ns in densifying the cementitious matrix and providing a shield to protect the bar from the thermal fluctuations; in addition to controlling the reduction rate of the compressive strength leading to better bond quality to the GFRP bar.

In general, the effect of changing the bar diameter on the pullout capacity for specimens tested under the same conditions is well documented by many researchers (Cosenza et al. 1997; Davalos et al. 2008; Alves et al. 2011; Calvet et al. 2015; Benmokrane et al. 2016). It was concluded that

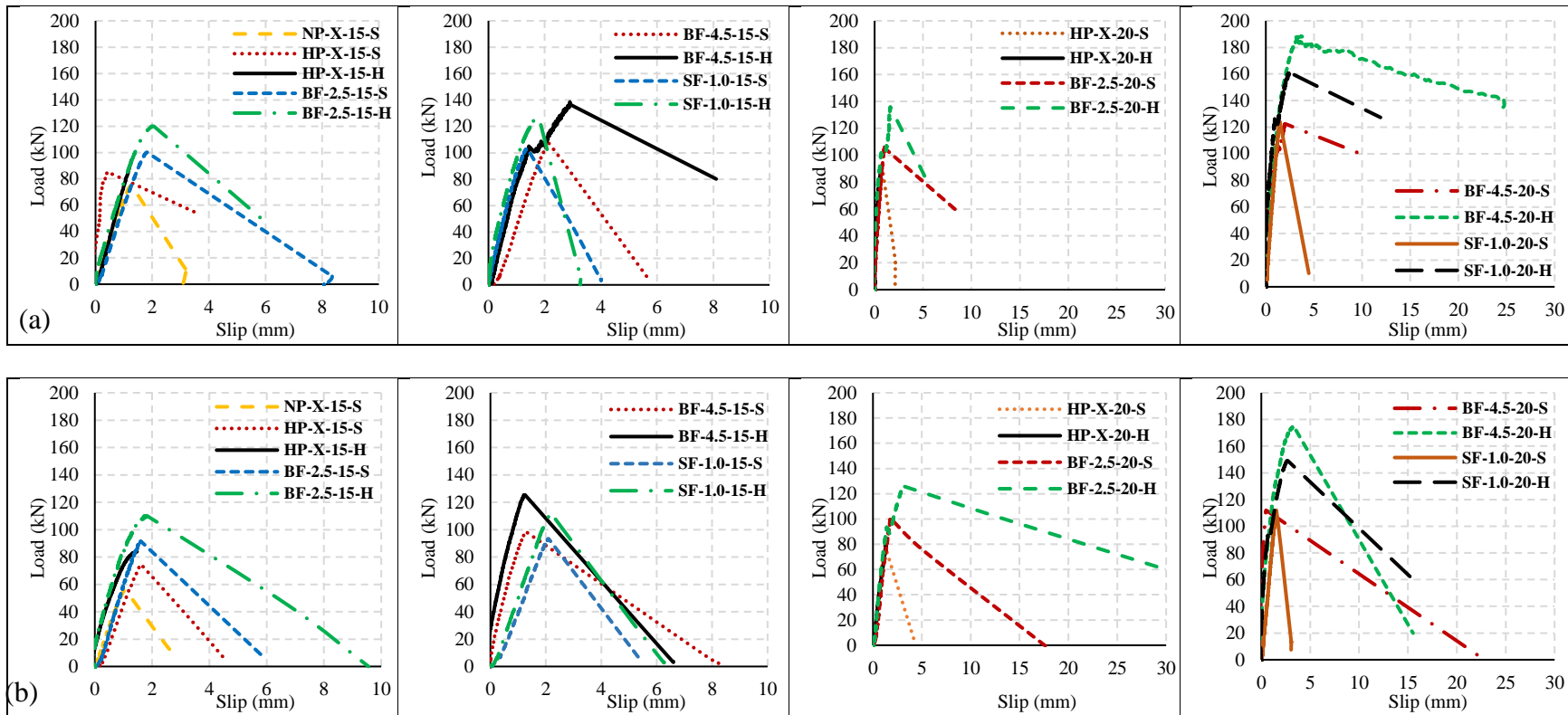


Figure 5.7: Load–slip relationship at the loaded end, (a) unconditioned specimens, and (b) conditioned specimens

increasing the bar diameter led to considerable reduction in bond strength due to different factors such as Poisson effect and shear lag. However, the effect of varying bar diameter on controlling bond degradation of GFRP bars remain contentious and not fully covered. In this study, it was observed that increasing the bar diameter from 15.9 to 19 mm for the exposed specimens was accompanied by a consistent slight increase (in the range of 1-3%) in the failure load retention. Therefore, the authors believe that the efficacy of such parameter in controlling the deterioration of GFRP bar embedded in cementitious block induced by F/T and W/D exposures is insignificant, which conforms to previous studies (Davalos et al. 2008; Calvet et al. 2015; Li et al. 2017). Similarly, the findings of this research revealed that the conditioned specimens with either straight or headed GFRP bars did not affect the rate of deterioration of the cube. Similar, if not identical, reduction in the pullout failure load was observed for the bars having the same diameter and embedded in the same cementitious matrix, yet with different bar end type. This findings in a good agreement with Benmokrane et al. (2016), where the residual pullout capacity was tightly correlated to the exposure type rather than the bar end type.

One of the bond degradation mechanisms is caused by the difference between the longitudinal and the transverse coefficients of thermal expansion (CTEs) for GFRP bars and the cementitious matrix. As a result, thermal fluctuations can lead to mismatch of transverse thermal expansions between GFRP and cementitious matrix, resulting in bond degradation and even concrete cracking. Therefore, the presence of discrete fibers markedly improved the durability of bond. For example, irrespective of the bar diameter and bar end type, an average reduction of 14% in failure load was obtained in the plain specimens, whereas 8% reduction was observed in the FRCC specimens. The addition of either BP or SF significantly mitigated the bond deterioration imparted by environmental exposures, since the fibers restricted the propagation of cracks leading to a

moderate rate of deterioration. In addition, the presence of fibers usually contributed to increase the air bubbles, which acted as receivers of the excess water, thus relieving the pressure created in the cementitious composite (Alsaif et al. 2019).

The post-peak behaviour of all specimens after the combined exposure was assessed by computing the residual bond toughness. As proposed by Chu and Kwan (2019), where two toughness indices were obtained: T_{peak} – the area under the load-slip graph up to the peak bond strength, and T_{post} – the area under the bond load-slip graph up to failure. The failure was defined to be either the peak load or 80% of the maximum load on the descending branch of the load-slip response. From Table 5.7, the bond toughness for the majority of fibrous matrices experienced degradation when exposed to consecutive cycles of F/T and W/D. However, the most notable observation was that adding small dosage of BP retained higher peak and post-peak bond toughness (T_{peak} and T_{post}) than that specimen reinforced with SF. For example, exposing specimens with 2.5% BP, irrespective of the bar diameter or bar end type, showed an average peak and post-peak bond toughness of 134 and 527.2 kN.mm, respectively, which were 10 and 71% higher than that of the counterpart specimens reinforced with SF. These values for the later were 121 and 308 kN.mm, respectively, taking into account the superior properties of SF in terms of the aspect ratio and modulus of elasticity.

5.5 Conclusions

Based on the experimental investigations, the following conclusions can be drawn:

- Based on the visual analysis, the control specimens without any fibers suffered from severe damage that was reflected by wide web cracks located at the surface. On the other hand, fibrous specimens seem to be immune to the environmental exposure.
- The compressive strength was decreased for all specimens after the cyclic conditioning regime adopted in this study due to the formation of internal microcrack. Nevertheless, the

synergistic effect of nano silica and slag refined the pore structure of the matrix, which accordingly controlled the reduction rate in compressive strength. Similarly, the incorporation of fibers effectively mitigated the rate of deterioration to the extent that the fibrous mixtures exceeded the compressive strength of their counterpart mixtures cast without fibers.

- All the FRCC specimens yielded the lowest stiffness degradation, in particular the composites containing BP. This is mainly linked to the increased air content associated with the use of high dosages of BP (e.g. 4.5 %), so it can be said that better F/T and W/D durability was attained without the inclusion of intentional entrained air.
- Four modes of failure for specimens cast without fibers were observed; pure pullout, partial pullout, splitting of concrete, and splitting of both concrete and the head of the bar. On the other hand, the dominant mode of failure for fibrous specimens was partial pullout for straight bars, and cracking of concrete for headed-end bars. It is worth mentioning that the presence of fibers, in general, managed to keep the concrete cube as one unit, even for specimens with headed-end bars.
- The bond durability markedly enhanced for fibrous specimens due to the restriction of the crack propagation at the bar/matrix interface. The loss of pullout capacity of GFRP bar embedded in plain composite was found to be 22%, whereas only 8% reduction, on average, was obtained for the FRCC specimens.

CHAPTER 6: ASSESSMENT OF BOND STRENGTH OF GFRP BARS EMBEDDED IN FRCC

Authors and Affiliation:

- Ahmed G. Bediwy, PhD Candidate, Department of Civil Engineering, University of Manitoba
- Ehab F. El-Salakawy, Professor, Department of Civil Engineering, University of Manitoba

Journal and Status:

Elsevier, *Cement and Concrete Composites* Journal, submitted on February 27, 2021.

Reference:

Bediwy, A., and El-Salakawy, E. “Assessment of bond strength of GFRP bars embedded in FRCC.” *Cement and Concrete Composites*, under review.

Note:

The manuscript had been slightly altered from the original paper by renumbering the tables and figures to include the chapter number. In addition, the reference list and list of notations have been moved to the appropriate sections in the thesis as indicated in the table of contents.

Abstract:

In this study, the bond behavior of sand-coated glass fiber-reinforced polymer (GFRP) bars embedded in cementitious composite matrix reinforced with the recently developed basalt fiber (BF) pellets and steel fibers (SF) was evaluated. Several studies have attempted to introduce empirical models to estimate the bond strength of FRP-reinforced concrete (RC) specimens. In this study, the applicability of these models to predict the bond stress of straight and headed-end FRP bars embedded in normal concrete and fiber-reinforced concrete (FRC) was assessed. Test results of 413 pullout specimens, which were divided into four groups based on the type of the FRP bar or the cementitious matrix, were used to evaluate the available models. In addition, a proposed model to predict the bond performance of headed-end FRP bars with FRC pullout specimens was introduced. The model was calibrated against experiments conducted previously by the authors on FRP-FRC specimens. The model was capable of predicting the maximum bond strength with a mean experimental-to-predicted value of 1.09 and a standard deviation of 0.19.

Keywords: empirical models, headed-end bars, basalt fiber pellets, pullout, bond strength, FRP, database

6.1 Introduction

Exposing reinforced concrete (RC) structures to harsh and aggressive environments stimulates corrosion of typically-used steel reinforcement, impairing the integrity and durability of the whole structure. Therefore, fortunately, fiber reinforced polymer (FRP) reinforcement has been introduced as a viable alternative to steel, eliminating the corrosion-related issues. Moreover, glass FRP (GFRP) has the advantage of high tensile strength, lightweight and ease of installation, relatively low cost and acceptable strain capacity compared to other FRP types. In addition, in order to widespread the use of FRP bars in the construction industry, GFRP bars are produced with different types and surface textures to overcome the problems associated with bond failure. As a result, the development of a GFRP bar with a headed-end has proven to be significantly effective and vigorous in shortening the development length and controlling the premature bond failure, as concluded by several studies (Maranan et al. 2015; Benmokrabe et al. 2016; Mahmoud et al. 2017). The bond behavior between FRP and concrete is essential in all RC structures, as bond failure is not permitted in design. The bond behavior of FRP bars has several similarities to the bond behavior of conventional steel bars. However, it was found that the parameters affecting the interaction between the FRP and concrete were much greater than those affecting the bond between steel and concrete. In this context, several attempts have been made to investigate the factors affecting the bond behaviour based on direct pullout test (Daniali 1992; Cosenza et al. 1997; Lee et al. 2008; Yan et al. 2016). Those factors include, but not limited to, FRP reinforcement type, bar surface treatment, bar diameter, concrete strength, concrete cover thickness, environmental conditions, and concrete confinement provided by transverse reinforcement. Accordingly, design provisions in codes and guidelines pertaining to FRP-RC structures have stipulated

recommendations associated with bond mechanisms in terms of development length and bond strength.

For several decades, fiber-reinforced concrete (FRC) has been increasingly utilized, especially in RC members reinforced with FRP bars due to its favorable properties, as FRP bars had brittle behavior and low modulus of elasticity. Thus, the application of FRP bars induces new structural problems: i.e., unsatisfactory structural ductility and serviceability performance. Those attractive aspects of FRC include, but not limited to, superior toughness, ductility, and resistance to crack growth (Song and Hwang 2004; Xu et al. 2012; Corinaldesi and Nardinocchi 2016). Different types of fibers are available to produce fiber-reinforced cementitious composites (FRCC), such as steel, synthetic, organic and inorganic fibers. In this context, steel FRC (SFRC) has gained significant ground in the construction field, as these fibers had the capability to enhance the bond-slip behaviour (Kim et al. 2013; Yan and Lin 2017). However, the main drawback of using steel in the form of bars or discrete fibers still exists, as they are vulnerable to corrosion, which in turn would negatively affect the durability and functionality of concrete structures.

Accordingly, basalt fiber (BF) is a new kind of inorganic fibers manufactured by the extrusion of melted basalt rocks. The basalt fibers are gaining momentum in the construction market since the production process of basalt fibers is more environment friendly, and it is cheaper with respect to the other types of fibers such as glass fibers. Basalt fibers have high tensile strength (3,000 - 4,000 MPa), reasonable modulus of elasticity (93 - 110 GPa), and they are not vulnerable to surface corrosion (Arslan 2016; Mahmoud et al. 2017). Nevertheless, basalt fibers are prone to sever degradation when incorporated in high alkaline media (e.g. concrete); therefore, a special type of BP (BP), which is made of basalt fibers coated with polyamide or other resins, has been adopted by the authors.

The codes and guidelines, such as JSCE-97 (JSCE 1997), ACI 440.1R (ACI 2015), CSA/S806-12 (CSA 2017), and CSA S6-19 (CSA 2019a), have stipulated equations for development length and bond strength. However, these equations for FRP-RC members are empirical in nature; they are based on statistical fitting of the test results available at the time they were developed, which would result in overly conservative estimates as for the recent experimental results (Hossain et al. 2014; Islam et al. 2015; Velikovic et al. 2017). Consequently, during the last two decades, several empirical equations have been introduced by different researchers to predict the development length and bond strength of FRP-RC members (Wambeke and Shield 2006; Quayyum 2010; Kern 2013; Islam et al. 2015; Basaran and Kalkan 2020). However, the equations introduced in codes or presented in literature do not account for all the parameters that had a direct effect on the FRP-RC bond, such as the effect of incorporating discrete fibers in the cementitious matrix and/or using FRP bars with headed-end.

Therefore, in the present study, the FRP-RC bond strength and development length equations available in current codes and guidelines, as well as the empirical equations developed by different researchers, were evaluated. The applicability of these models on predicting the bond strength of FRC specimens reinforced with FRP bars was investigated, based on the pullout tests. In addition, the models were calibrated against experiments conducted previously by the authors on FRC specimens reinforced with straight and headed-end FRP bars. Refinement of the existing equations to better predicting the bond strength and development length of different types of concrete reinforced with different types of FRP bars was proposed.

6.2 Summary of Experimental Results

A total of 95 pull-out specimens were fabricated based on the guidelines of Annex G of the CSA/S806-12 (2017). Sizes No.15 and No.20 sand-coated, GFRP bars with either straight or headed ends were used. Irrespective of the bar size, the 100-mm long head had a stepped surface with a maximum outer diameter of 50 mm at the end as shown in Figure 6.1. The mechanical properties of the GFRP bars were obtained through standard tests carried out according to ASTM D7205-06 (ASTM 2016), as listed in Table 6.1.

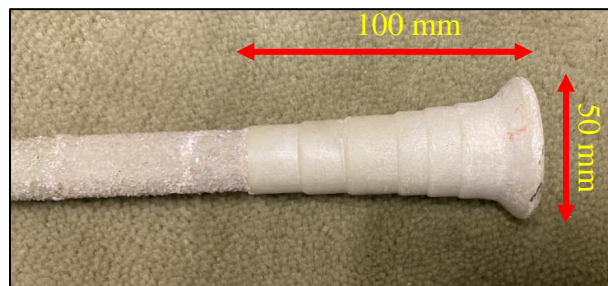


Figure 6.1: Configuration of the head of GFRP bars

Table 6.1: Mechanical properties of GFRP bars

Bar Type	Bar size	Nominal diameter (mm)	Area (mm ²)		Tensile strength (MPa)	Modulus of elasticity (GPa)	Ultimate strain (%)
			Nominal	CSA/S806-12 Annex A			
GFRP	No. 15	15.9	198	291	1,184	62.6	1.89
	No. 20	19.0	285	394	1,105	63.7	1.73
GFRP Head	-	-	-	-	552*	68	0.8*

Note: Properties are the same for straight and headed-end bar

** Usable design stress/strain provided by the manufacturer (corresponds to a pull-out load capacity of 70 kN, despite bar size)*

In addition, two different mixtures were used to produce the cementitious matrix, (1) normal cementitious composite (plain concrete), which was prepared with a general use (GU) cement content of 700 kg/m³, and (2) high-performance cementitious composite, which was cast with 420 kg/m³ GU cement, a slag content of 280 kg/m³ (representing 40% replacement of cement content),

and nano-silica, at a dosage of 6% by mass of the binder. In addition, for the later mixture, few specimens were reinforced with either BP or steel fiber (SF). The properties of the BP and the SF are listed in Table 6.2.

Table 6.2: Properties of discrete fibers

Properties	Type of fiber	
	BP	Hooked steel
Length (mm)	36	30
Diameter/dimensions (mm)	1.80	0.65
Aspect ratio	20	45
Specific gravity	1.74	7.70
Tensile strength (MPa)	2,300	1,200
Elastic modulus (GPa)	65	200

The pullout specimens consisted of a 200-mm side length cube with concentric placement of the bar. The dimensions of the specimen were chosen to avoid splitting of the cube. The embedded length was four times the bar diameter ($4d_b$) in bars with straight ends, whereas it was equal to the head length (100 mm) in headed-end bars. The un-bonded length was wrapped with a smooth surface tape to ensure that no bond exists between the cementitious matrix and the bar over this length. The other end of the GFRP bar was sheathed with thick-wall steel pipe and then the pipe was filled with a commercial expansive grout to anchor the bar with the pipe. Details of the specimens are presented in Figure 6.2.

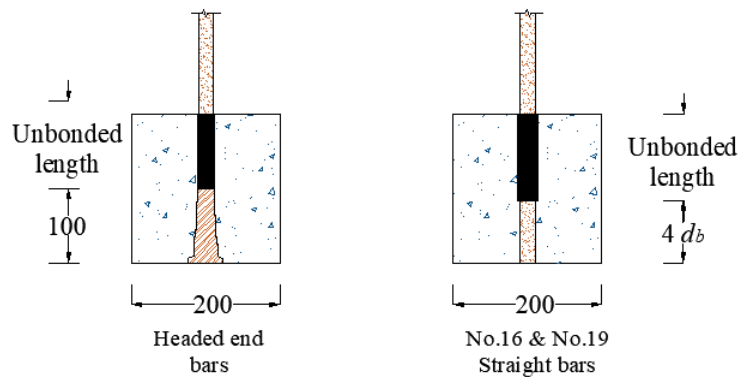


Figure 6.2: Schematic drawing of the specimen (All dimensions in mm)

The test parameters include the cementitious composite type, the type and dosage of discrete fibers added to the cementitious matrix, and the diameter and end type of the reinforcing bar. The details of the test specimens are listed in Table 6.3.

Table 6.3: Characteristics of test specimens for pullout

Specimens	Composite type	Fiber type	Fiber dosage (%)	Bar diameter (mm)	Bar end
NS-X-15-S	Plain concrete without SCMs and fibers	-	-	15.9	Straight
HS-X-15-S	Composite with SCMs and without fibers	-	-	15.9	Straight
HS-X-20-S		-	-	19.0	
HS-X-15-H		-	-	15.9	Headed
HS-X-20-H		-	-	19.0	
BF-2.5-15-S	Composite with SCMs and BP	Basalt	2.5	15.9	Straight
BF-2.5-20-S				19.0	
BF-2.5-15-H				15.9	Headed
BF-2.5-20-H				19.0	
BF-4.5-15-S	Composite with SCMs and BP	Basalt	4.5	15.9	Straight
BF-4.5-20-S				19.0	
BF-4.5-15-H				15.9	Headed
BF-4.5-20-H				19.0	
SF-1.0-15-S	Composite with SCMs and SF	Steel	1.0	15.9	Straight
SF-1.0-20-S				19.0	
SF-1.0-15-H				15.9	Headed
SF-1.0-20-H				19.0	

Pullout of the bar and splitting of concrete were the dominant modes of failure for specimens with straight GFRP bar and cast without fibers (Figure 6.3). However, all other plain concrete with headed-end bars showed splitting of concrete. The later failure was brittle in nature and was associated with a sudden drop in the load capacity. On the other hand, pullout of the GFRP bar, or cracking of concrete were observed for the fibrous specimens (either BP or SF) with straight bars and headed-end GFRP bars, respectively (Figure 6.3).

Despite the bar diameter, the straight GFRP bar that was embedded in plain concrete without any fibers exhibited an abrupt decay in the load accompanied by small slip values, whereas the post peak behaviour for the headed-end GFRP bars embedded in the same composite was not recorded

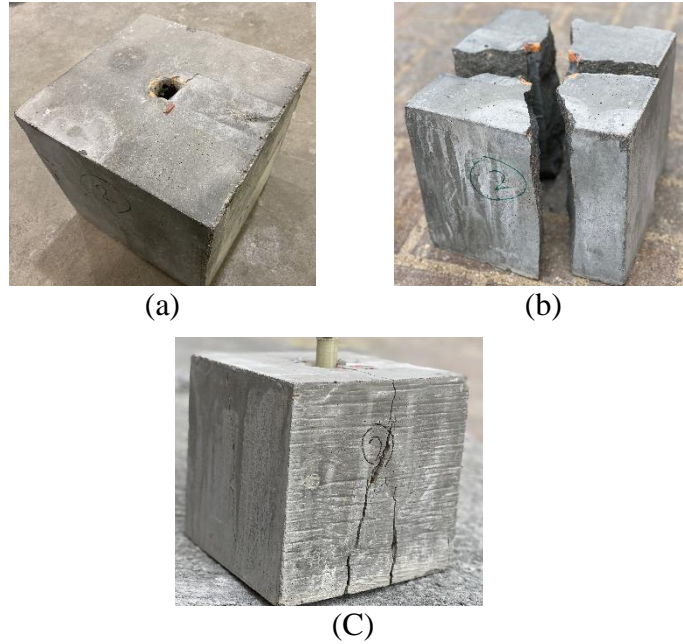


Figure 6.3: Typical modes of failure: (a) Pullout for straight GFRP bar, (b) Splitting of concrete, (c) Cracking of concrete

due to the splitting of the block into pieces. Nevertheless, the addition of fibers generally enhanced the ductility and bond strength of all fibrous specimens, as reflected by the enhanced bond toughness indices. However, the post-peak load-slip response of the GFRP bar in the cementitious matrix, containing BP mainly relied on the fiber dosage. The behaviour of the GFRP bar in the matrix reinforced with 2.5 % BP showed a sharp drop in the load after the peak load was attained; whereas, increasing the dosage to 4.5% yielded a gradually descending slope reaching higher slip values. This was due to the gradual propagation of internal cracks along with the predominant role of fibers in bridging such cracks, as shown in Figure 6.4. More details on this series of tests can be found elsewhere (Bediwy and El-Salakawy forthcoming). The test results were used to assess the bond strength equations in the available codes and guidelines, as well as the proposed equations in the literature.

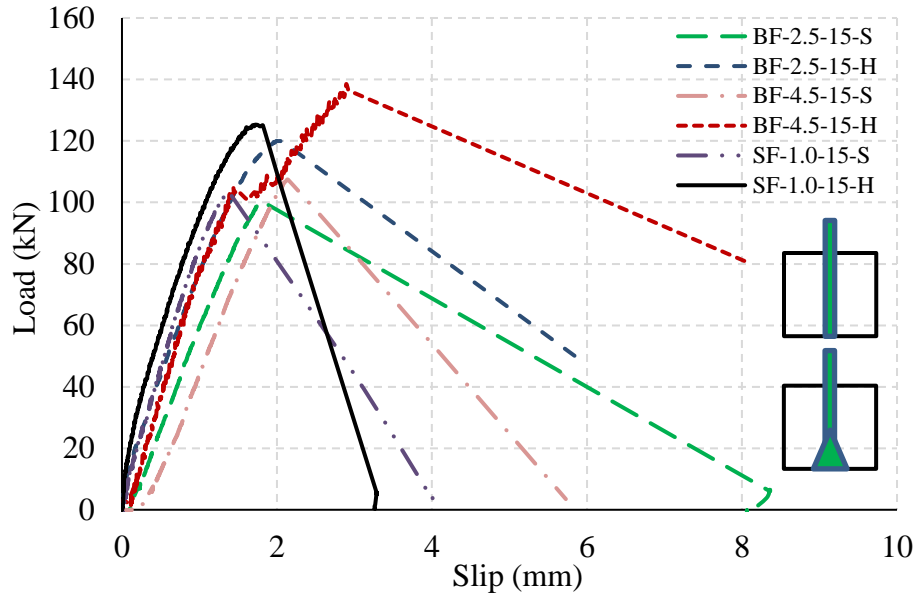


Figure 6.4: Exemplar load–slip relationship for No.15 GFRP straight and head-end bars

6.3 Experimental Database

The bond performance of FRP bars embedded in either normal or high strength concrete has gained considerable attention (Newman et al. 2010; Alves et al. 2011; Quayyum and Rteil 2011; Krem 2013; Islam et al. 2015; Benmokrane et al. 2016; Basaran and Kalkan 2020). A data for 413 pull-out specimens were collected from 7 different investigations available in the literature. The specimens were divided into four groups based on the type of the cementitious matrix (plain concrete or fiber-reinforced concrete) or the FRP reinforcing bar end shape (straight or headed-end), as listed in Tables 6.4-6.7. These specimens covered a large spectrum of materials and geometrical properties with a wide range of specimen width (130 to 300 mm), specimen thickness (100 to 250 mm), concrete strength (35 to 86 MPa), concrete cover thickness (18 to 150 mm), FRP reinforcement type (GFRP and CFRP), modulus of elasticity for FRP reinforcement (40 to 124 GPa), and bar surface finish (sand-coated, ribbed-deformed, helically-wrapped). In addition,

design parameters associated with the properties of discrete fibers such as the length of fibers (30 to 57 mm), the diameter of fibers (0.56 to 1.8 mm), the dosage of fibers (0.5 to 4.5%), and different types of discrete fibers (hooked-end steel fibers, polyvinyl fibers, polypropylene fibers, and basalt fibers).

6.4 Review of Bond Provisions in Current Codes

The bond strength is known as the maximum horizontal shear force per unit area of the bar perimeter. For bond stresses to exist, there must be a variation in the bar stress. The following equation for the force acting on the bar, which was resisted by an average bond stress, can be derived as:

$$\tau_f \pi d_b \ell_e + A_f f_F = A_f (f_F + \Delta f_F) \quad \text{Equation 6.1}$$

where τ_f is the bond stress in MPa, d_b is the diameter of the bar in mm, ℓ_e is the embedment length (mm), A_f is the cross-sectional area of the bar in mm². Thus, the bond stress can be expressed as:

$$\tau_f = \frac{A_f \Delta f_F}{\pi d_b \ell_e} = \frac{d_b \Delta f_F}{4 \ell_e} \quad \text{Equation 6.2}$$

To avoid bond failure, an adequate embedment length, referred to as development length, is required. In the current design codes, the development length required to sustain the design stress in the bar was always specified rather than the bond strength, as it is much easier for practitioners. However, the correlation between development length and bond strength can be obtained using Equation 6.2.

Table 6.4: Test data for straight FRP bars embedded in normal concrete

Specimens ID	Specimen detail						Reinforcement detail					P_{exp} (kN)	τ_{exp} (MPa)
	b (mm)	ℓ (mm)	t (mm)	c (mm)	Replicates	f_c' (MPa)	ℓ_e (mm)	Fiber type	Surface texture	E_{frp} (GPa)	d_b (mm)		
Alves et al. (2011)													
C.16	200	200	200	100	3	50.0	80	GFRP	SC	48.2	15.9	47.1	11.9
C.19	200	200	200	100	3	50.0	95	GFRP	SC	47.6	19.0	58.0	10.2
E.16.15	200	200	200	24	3	50.0	80	GFRP	SC	48.2	15.9	46.2	11.6
E.16.20	200	200	200	32	3	50.0	80	GFRP	SC	48.2	15.9	58.1	14.7
E.16.25	200	200	200	40	3	50.0	80	GFRP	SC	48.2	15.9	55.2	13.9
E.19.15	200	200	200	29	3	50.0	95	GFRP	SC	47.6	19.0	60.2	10.6
E.19.20	200	200	200	38	3	50.0	95	GFRP	SC	47.6	19.0	62.5	11.0
E.19.25	200	200	200	48	3	50.0	95	GFRP	SC	47.6	19.0	59.2	10.4
Belarabi and Wang (2012)													
VP4C	150	150	150	75	3	48.0	65	CFRP	Smooth	124.0	13.0	22.9	8.70
VP4G	150	150	150	75	3	48.0	65	GFRP	HW+SC	41.0	13.0	49.6	18.7
VP8G	250	250	250	125	3	48.0	125	GFRP	HW+SC	41.0	25.0	181.4	18.5
Kim et al. (2013)													
PC0.0GFRP-A	153	102	191	76	5	58.2	64	GFRP	SC	42.0	12.7	41.4	16.3
PC0.0GFRP-B	153	102	191	76	5	58.2	64	GFRP	HW+SC	40.8	12.7	60.1	23.7
Islam et al. (2015)													
12P-C-4d	200	200	98	100	6	68.0	48	GFRP	R	60.0	12.0	19.9	11.0
12P-E1.5d-4d	200	200	98	18	6	68.0	48	GFRP	R	60.0	12.0	19.0	10.5
12P-E2.5d-4d	200	200	98	30	6	68.0	48	GFRP	R	60.0	12.0	21.8	12.1
12P-C-6d	200	200	122	100	6	68.0	72	GFRP	R	60.0	12.0	27.5	10.1
12P-E1.5d-6d	200	200	122	18	6	68.0	72	GFRP	R	60.0	12.0	27.4	10.0

Specimens ID	Specimens details						Reinforcement details					P_{exp} (kN)	τ_{exp} (MPa)
	b (mm)	ℓ (mm)	t (mm)	c (mm)	Replicates	f_c' (MPa)	ℓ_e (mm)	Fiber type	Surface texture	E_{frp} (GPa)	d_b (mm)		
12P-E2.5d-6d	200	200	122	30	6	68.0	72	GFRP	R	60.0	12.0	30.6	11.3
16P-C-4d	200	200	114	100	6	68.0	64	GFRP	R	60.0	16.0	40.7	12.6
16P-E1.5d-4d	200	200	114	24	6	68.0	64	GFRP	R	60.0	16.0	32.4	10.1
16P-E2.5d-4d	200	200	114	40	6	68.0	64	GFRP	R	60.0	16.0	37.6	11.7
16P-C-6d	200	200	146	100	6	68.0	96	GFRP	R	60.0	16.0	56.8	11.8
16P-E1.5d-6d	200	200	146	24	6	68.0	96	GFRP	R	60.0	16.0	48.3	10.0
16P-E2.5d-6d	200	200	146	40	6	68.0	96	GFRP	R	60.0	16.0	49.3	10.2
Yan and Lin (2017)													
PC0.0-Control	127	127	178	64	3	45.3	64	GFRP	HW+SC	46.0	12.7	39.7	15.7
Bediwy and El-Salakawy (forthcoming)													
NS-X-15-S	200	200	200	100	5	61.3	64	GFRP	SC	62.6	15.9	72.2	22.6
HS-X-15-S	200	200	200	100	5	85.7	64	GFRP	SC	62.6	15.9	86.3	27.1
HS-X-20-S	200	200	200	100	5	85.7	76	GFRP	SC	63.7	19.0	88.9	19.7

b = specimen width; ℓ = specimen length; t = specimen thickness; c = concrete cover; f_c' = concrete compressive strength; ℓ_e = development length; E_{frp} = modulus of elasticity of FRP bars; d_b = diameter of the bar; P_{exp} = ultimate pullout load; τ_{exp} = bond strength of specimen
Note: HW = helically-wrapped; SC = Sand-coated; R = ribbed-deformed.

Table 6.5: Test data for straight FRP bars embedded in FRC

Specimens ID	Specimen details					Reinforcement details					Fiber details					P_{exp} (kN)	τ_{exp} (MPa)
	b (mm)	ℓ (mm)	t (mm)	f_c' (MPa)	Replicates	ℓ_e (mm)	Fiber type	Surface texture	E_{frp} (GPa)	d_b (mm)	V_f (%)	L_f (mm)	d_f (mm)	Type	E_{fiber} (GPa)		
Belarabi and Wang (2012)																	
VF4C	150	150	150	37.0	3	65.0	CFRP	Smooth	124.0	13.0	0.5	57	NR	Polypropylene	4	NR	7.10
VF4G	150	150	150	37.0	3	65.0	GFRP	HW+SC	41.0	13.0	0.5	57	NR	Polypropylene	4	NR	16.2
VF8G	250	250	250	37.0	3	125.0	GFRP	HW+SC	41.0	25.0	0.5	57	NR	Polypropylene	4	NR	13.2
Kim et al. (2013)																	
PP0.5GFRP-A	152	102	191	51.5	3	63.5	GFRP	SC	42.0	12.7	0.5	30	NR	Polypropylene	6	28.8	11.4
PP0.5GFRP-B	152	102	191	51.5	3	63.5	GFRP	HW+SC	40.8	12.7	0.5	30	NR	Polypropylene	6	60.5	23.9
PP1.0GFRP-A	152	102	191	56.3	3	63.5	GFRP	SC	42.0	12.7	1.0	30	NR	Polypropylene	6	30.2	11.9
PP1.0GFRP-B	152	102	191	56.3	3	63.5	GFRP	HW+SC	40.8	12.7	1.0	30	NR	Polypropylene	6	55.5	21.9
PVA0.5GFRP-A	152	102	191	54.8	3	63.5	GFRP	SC	42.0	12.7	0.5	30	0.66	Polyvinyl	29	26.0	10.3
PVA0.5GFRP-B	152	102	191	54.8	3	63.5	GFRP	HW+SC	40.8	12.7	0.5	30	0.66	Polyvinyl	29	64.0	25.3
PVA1.0GFRP-A	152	102	191	62.3	3	63.5	GFRP	SC	42.0	12.7	1.0	30	0.66	Polyvinyl	29	26.0	10.3
PVA1.0GFRP-B	152	102	191	62.3	3	63.5	GFRP	HW+SC	40.8	12.7	1.0	30	0.66	Polyvinyl	29	64.0	25.3
Steel0.5GFRP-A	152	102	191	54.8	3	63.5	GFRP	SC	42.0	12.7	0.5	30	0.56	Steel	200	39.1	15.4
Steel0.5GFRP-B	152	102	191	54.8	3	63.5	GFRP	HW+SC	40.8	12.7	0.5	30	0.56	Steel	200	66.1	26.1
Steel1.0GFRP-A	152	102	191	62.3	3	63.5	GFRP	SC	42.0	12.7	1.0	30	0.56	Steel	200	32.7	12.9
Steel1.0GFRP-B	152	102	191	62.3	3	63.5	GFRP	HW+SC	40.8	12.7	1.0	30	0.56	Steel	200	66.5	26.3
Yan and Lin (2017)																	
Steel0.5-Control	127	127	177.8	45.3	3	63.5	GFRP	HW+SC	46.0	12.7	0.5	30	0.56	Steel	200	NR	19.2
Steel1.0-Control	127	127	177.8	46.7	3	63.5	GFRP	HW+SC	46.0	12.7	1.0	30	0.56	Steel	200	NR	21.3
PVA0.5-Control	127	127	177.8	44.9	3	63.5	GFRP	HW+SC	46.0	12.7	0.5	50	0.66	Polyvinyl	29	NR	15.6
PVA1.0-Control	127	127	177.8	45.3	3	63.5	GFRP	HW+SC	46.0	12.7	1.0	50	0.66	Polyvinyl	29.0	NR	16.3
Bediwy and El-Salakawy (forthcoming)																	
BF-2.5-15-S	200	200	200	81.3	5	64.0	GFRP	SC	62.6	15.9	2.5	36	1.80	Basalt	65	100.0	31.3

Specimens ID	Specimen details					Reinforcement details					Fiber details					P_{exp} (kN)	τ_{exp} (MPa)
	b (mm)	ℓ (mm)	t (mm)	f_c' (MPa)	Replicates	ℓ_e (mm)	Fiber type	Surface texture	E_{frp} (GPa)	d_b (mm)	V_f (%)	L_f (mm)	d_f (mm)	Type	E_{fiber} (GPa)		
BF-2.5-20-S	200	200	200	81.3	5	76.0	GFRP	SC	63.7	19.0	2.5	36	1.80	Basalt	65	107.0	23.6
BF-4.5-15-S	200	200	200	78.5	5	64.0	GFRP	SC	62.6	15.9	4.5	36	1.80	basalt	65	110.5	34.6
BF-4.5-20-S	200	200	200	78.5	5	76.0	GFRP	SC	63.7	19.0	4.5	36	1.80	Basalt	65	122.5	27.1
SF-1.0-15-S	200	200	200	83.4	5	64.0	GFRP	SC	62.6	15.9	1.0	30	0.65	Steel	200	103.0	32.3
SF-1.0-20-S	200	200	200	83.4	5	76.0	GFRP	SC	63.7	19.0	1.0	30	0.65	Steel	200	124.4	27.5

b = specimen width; ℓ = specimen length; t = specimen thickness; f_c' = concrete compressive strength; ℓ_e = development length; E_{frp} = modulus of elasticity of FRP bars; d_b = diameter of the bar; V_f = dosage of discrete fibers; L_f = discrete fiber length; d_f = discrete fiber diameter; P_{exp} = ultimate pullout load; τ_{exp} = bond strength of specimen;

Note: HW = helically wrapped; SC = Sand coated; R = ribbed-deformed; NR = not reported

Table 6.6: Test data for headed-end FRP bars embedded in normal concrete

Specimens ID	Specimen details						Reinforcement details					Head details		P_{exp} (kN)	τ_{exp} (MPa)
	b (mm)	ℓ (mm)	t (mm)	c (mm)	Replicates	f_c' (MPa)	ℓ_e (mm)	Fiber type	Surface texture	E_{frp} (GPa)	d_b (mm)	ℓ_h (mm)	D_o (mm)		
Islam et al. (2015)															
12H-C-0d	300	300	125	150	6	68	0	GFRP	R	60.0	12.0	75	30	70.5	25.0
12H-E1.5d-0d	300	300	125	18	6	68	0	GFRP	R	60.0	12.0	75	30	67.0	23.7
12H-E2.5d-0d	300	300	125	30	6	68	0	GFRP	R	60.0	12.0	75	30	70.0	24.8
12H-C-4d	300	300	173	150	6	68	48	GFRP	R	60.0	12.0	75	30	96.0	20.7
12H-E1.5d-4d	300	300	173	18	6	68	48	GFRP	R	60.0	12.0	75	30	71.2	15.4
12H-E2.5d-4d	300	300	173	30	6	68	48	GFRP	R	60.0	12.0	75	30	84.9	18.3
12H-C-6d	300	300	197	150	6	68	72	GFRP	R	60.0	12.0	75	30	98.4	17.8
12H-E1.5d-6d	300	300	197	18	6	68	72	GFRP	R	60.0	12.0	75	30	73.2	13.2
12H-E2.5d-6d	300	300	197	30	6	68	72	GFRP	R	60.0	12.0	75	30	92.8	16.8
16H-C-0d	300	300	150	150	6	68	0	GFRP	R	60.0	16.0	100	40	123.1	24.5
16H-E1.5d-0d	300	300	150	24	6	68	0	GFRP	R	60.0	16.0	100	40	94.2	18.7
16H-E2.5d-0d	300	300	150	40	6	68	0	GFRP	R	60.0	16.0	100	40	113.3	22.6
16H-C-4d	300	300	214	150	6	68	64	GFRP	R	60.0	16.0	100	40	152.2	18.5
16H-E1.5d-4d	300	300	214	24	6	68	64	GFRP	R	60.0	16.0	100	40	106.1	12.9
16H-E2.5d-4d	300	300	214	40	6	68	64	GFRP	R	60.0	16.0	100	40	128.7	15.6
16H-C-6d	300	300	246	150	6	68	96	GFRP	R	60.0	16.0	100	40	145.9	14.8
16H-E1.5d-6d	300	300	246	24	6	68	96	GFRP	R	60.0	16.0	100	40	119.4	12.2
16H-E2.5d-6d	300	300	246	40	6	68	96	GFRP	R	60.0	16.0	100	40	137.3	14.0
Benmokrane et al. (2016)															
A-5-35-N	200	200	200	100	5	35	100	GFRP	SC	62.6	15.9	100	50	123.0	24.6
A-5-35-S	200	200	200	100	10	35	100	GFRP	SC	62.6	15.9	100	50	139.0	27.8
A-5-47-S	200	200	200	100	10	47	100	GFRP	SC	62.6	15.9	100	50	149.0	29.8

Specimens ID	Specimen details						Reinforcement details						Head details		P_{exp} (kN)	τ_{exp} (MPa)
	b (mm)	ℓ (mm)	t (mm)	c (mm)	Replicates	f_c' (MPa)	ℓ_e (mm)	Fiber type	Surface texture	E_{frp} (GPa)	d_b (mm)	ℓ_h (mm)	D_o (mm)			
A-6-35-N	200	200	200	100	5	35	100	GFRP	SC	64.7	19.0	100	50	150.0	25.1	
A-6-35-S	200	200	200	100	5	35	100	GFRP	SC	64.7	19.0	100	50	172.0	28.8	
A-6-47-S	200	200	200	100	10	47	100	GFRP	SC	64.7	19.0	100	50	179.0	30.0	
Bediwy and El-Salakawy (forthcoming)																
HS-X-15-H	200	200	200	100	5	86	100	GFRP	SC	62.6	15.9	100	50	94.2	18.8	
HS-X-20-H	200	200	200	100	5	86	100	GFRP	SC	63.7	19.0	100	50	89.2	15.0	

b = specimen width; ℓ = specimen length; t = specimen thickness; c = concrete cover; f_c' = concrete compressive strength; ℓ_e = development length; E_{frp} = modulus of elasticity of FRP bars; d_b = diameter of the bar; ℓ_h = length of the head; D_o = outer diameter of the head; P_{exp} = ultimate pullout load; τ_{exp} = bond strength of specimen

Note: SC = Sand coated; R = ribbed-deformed.

Table 6.7: Test data for headed-end FRP bars embedded in FRC

Specimens ID	Specimen details					Reinforcement details					Head details		Fiber type					P_{exp} (kN)	τ_{exp} (MPa)				
	b (mm)	ℓ (mm)	t (mm)	c (mm)	Replicates	ℓ_e (mm)	Fiber type	Surface texture	E_{frp} (GPa)	d_b (mm)	ℓ_h (mm)	D_o (mm)	V_f (%)	L_f (mm)	d_f (mm)	Type	E_{fiber} (GPa)						
Bediwy and El-Salakawy (forthcoming)																							
BF-2.5-15-H	200×200×200			81.3	5	GFRP	SC			100	50			2.5	36	1.80	Basalt	65	120	24.0			
BF-2.5-20-H				81.3										76	63.7	19.0			2.5	36	1.80	136	22.8
BF-4.5-15-H				78.5										64	62.6	15.9			4.5	36	1.80	139	27.7
BF-4.5-20-H				78.5										76	63.7	19.0			4.5	36	1.80	189	31.7
SF-1.0-15-H				83.4										64	62.6	15.9	1.0	30	0.65	Steel	200	125	25.1
SF-1.0-20-H				83.4										76	63.7	19.0	1.0	30	0.65			162	27.2

b = specimen width; ℓ = specimen length; t = specimen thickness; c = concrete cover; f_c' = concrete compressive strength; ℓ_e = development length; E_{frp} = modulus of elasticity of FRP bars; d_b = diameter of the bar; ℓ_h = length of the head; D_o = outer diameter of the head; V_f = dosage of discrete fibers; L_f = discrete fiber length; d_f = discrete fiber diameter; P_{exp} = ultimate pullout load; τ_{exp} = bond strength of specimen

Note: SC = Sand coated.

6.4.1 CSA building code provisions (CSA/S806-12)

The Canadian FRP-reinforced concrete standards CSA/S806-12 (CSA 2017) give the following development length equation:

$$\ell_e = 1.15 \frac{K_1 K_2 K_3 K_4 K_5}{d_{cs}} \frac{f_F}{\sqrt{f'_c}} A_b \quad \text{Equation 6.3}$$

where ℓ_e is the development length in mm, A_b is the cross-sectional area of the bar in mm^2 , f_F is the tensile stress in the rebar in MPa, f'_c is the compressive strength of concrete in MPa, d_{cs} is the smallest of the distance from the closest concrete surface to the center of the bar being developed or two-thirds the center to center spacing of the bars being developed in mm, the d_{cs} shall be less than or equal to $2.5 d_b$, where d_b is the diameter of the bar in mm, K_1 is the bar location factors, which is taken 1.3 for horizontal reinforcement placed so that more than 300 mm of fresh concrete is cast in the member below the development length and 1.0 for all other cases, K_2 is the concrete density factor, which is taken as 1.3 for structural low-density concrete, 1.2 for structural semi-low-density concrete and 1.0 for normal density concrete, K_3 is the bar size factor, which is taken 0.8 for the area of reinforcement less than or equal to 300 mm^2 and 1.0 for the area of reinforcement more than 300 mm^2 , K_4 is the bar fiber factor, which is taken equals to 1.0 for CFRP and GFRP and 1.25 for AFRP, K_5 is the bar surface profile factor, which is taken as 1.0 for sand-coated or braided surfaces, 1.05 for spiral pattern or ribbed surfaces and 1.8 for intended surface. It is worth noting that $\sqrt{f'_c}$ shall not be greater than 5 MPa, and the development length shall not be less than 300 mm. From Equations 6.2 and 6.3, the bond strength can be computed as:

$$\tau_f = \frac{d_{cs} \sqrt{f'_c}}{1.15 K_1 K_2 K_3 K_4 K_5 \pi d_b} \quad \text{Equation 6.4}$$

where τ_f is the bond stress in MPa, and d_{cs} , f'_c , d_b , K_1 , K_2 , K_3 , K_4 , K_5 were previously defined.

6.4.2 CSA bridge code provisions (CSA/S6-19)

The Canadian Highway Bridge Design Code, CSA/S6-19 (CSA 2019a) modified the development length equation for steel bar to be suitable for FRP rebar as follows:

$$\ell_e = 0.45 \left[\frac{K_1 K_4}{d_{cs} + K_{tr} \frac{E_{frp}}{E_s}} \right] \left[\frac{f_F}{f_{cr}} \right] A_b \quad \text{Equation 6.5}$$

where ℓ_e , A_b , f_F , d_{sc} were previously defined, K_1 is the bar location factor, which is taken as 1.3 for horizontal reinforcement placed such that more than 300 mm of fresh concrete is cast in the component below the development length and 1.0 for other cases, K_4 is the bar surface factor, which should be computed as the ratio between the bond strength of the FRP bar to that of a steel deformed bar with the same cross-sectional area as the FRP bar, but not greater than 1.0, and in the absence of experimental data, K_4 shall be taken as 0.8, E_{frp} is the modulus of elasticity of FRP bar in MPa, E_s is the modulus of elasticity of steel in MPa, f_{cr} is the cracking strength of concrete in MPa, which is calculated as $0.4\sqrt{f'_c}$, K_{tr} is the transverse reinforcement index, which is calculated as $\frac{A_{tr} f_y}{10.5sn}$, where A_{tr} is the area of transverse reinforcement normal to the plane of splitting through the bars in mm², s is the spacing of the transverse reinforcement in mm, n is the number of bars being developed along the plane of splitting, f_y is the yield strength of transverse reinforcement. It is worth noting that the term $\left[d_{cs} + K_{tr} \frac{E_{frp}}{E_s} \right]$ should be less than 2.5; the development length shall not be less than 250 mm. Substitution of Equation 6.5 in Equation 6.2 was conducted to calculate the bond strength as follow:

$$\tau_f = \frac{\left(d_{cs} + K_{tr} \frac{E_{frp}}{E_s} \right) f_{cr}}{0.45 K_1 K_4 \pi d_b} \quad \text{Equation 6.6}$$

where τ_f is the bond stress in MPa, and d_{cs} , f_{cr} , d_b , K_1 , K_4 , E_{frp} , E_s were previously defined.

6.4.3 ACI provisions (ACI 440.1R-15)

The American design guidelines for concrete reinforced with FRP bars ACI 440.1R-15 (ACI 2015) recommends the use of the following development length equation:

$$\ell_e = \frac{\alpha \frac{f_{frp}}{0.083 \sqrt{f'_c}} - 340}{13.6 + \frac{C}{d_b}} d_b \quad \text{Equation 6.7}$$

where ℓ_e , f'_c , d_b , α is the reinforcement location factor, the default value is 1.0, and can be taken as 1.5 for the bars at a distance higher than 305 mm from the beam soffit, f_{frp} is the tensile stress in the rebar in MPa, C is the lesser of the cover to the centre of the bar or one-half of the centre-to-centre spacing of the bars being developed in mm. C/d_b should not be taken larger than 3.5. The bond strength can be calculated following the approach that previously defined as:

$$\tau_f = 0.083 \sqrt{f'_c} \left(4 + 0.3 \frac{C}{d_b} + 100 \frac{d_b}{\ell_e} \right) \quad \text{Equation 6.8}$$

where τ_f is the bond stress in MPa, f'_c , C , d_b , ℓ_e were previously defined.

6.4.4 JSCE code provisions (JSCE 2007)

The Japanese recommendations for design and construction of concrete structures using continuous fibre reinforcing materials (JSCE 1997) gives the following development length equation:

$$\ell_e = \alpha_1 \frac{f_{frp}}{4f_{bod}} d_b \quad \text{Equation 6.9}$$

where ℓ_e is the development length of a rebar in mm, which it can not be less than $20 d_b$, d_b is the diameter of the bar in mm, f_{frp} is the design tensile strength in the bar in MPa, f_{bod} is the design bond strength of concrete in MPa, and calculated according to the following equation:

$$f_{bod} = \frac{0.28\alpha_2 f_{ck}'^{2/3}}{\gamma_c} \leq 3.2 \text{ MPa} \quad \text{Equation 6.10}$$

where α_2 is a modification factor for bond strength of FRP, which is taken as 1.0 when bond strength is equal or greater than that of deformed steel bars; otherwise α_2 shall be reduced according to test results, f_{ck}' is the compressive strength of concrete in MPa, γ_c equal to 1.3. In Equation 6.9, α_1 is a factor, depending on the parameter k_c :

$$\alpha_1 = \left\{ \begin{array}{ll} 1.0 & k_c \leq 1.0 \\ 0.9 & 1.0 \leq k_c \leq 1.5 \\ 0.8 & 1.5 \leq k_c \leq 2.0 \\ 0.7 & 2.0 \leq k_c \leq 2.5 \\ 0.6 & 2.5 \leq k_c \end{array} \right\} \quad \text{Equation 6.11}$$

where k_c is computed according to the following equation:

$$k_c = \frac{c}{d_b} + \frac{15A_t}{sd_b} \frac{E_t}{E_0} \quad \text{Equation 6.12}$$

where c is the least of the clear cover and half of the bar spacing in mm; E_t is the elastic modulus of transverse reinforcement in MPa and the elastic modulus of steel (E_0) is taken 200 GPa, s is the distance between the centers of the transverse reinforcement, A_t is the area of transverse reinforcement which is vertically arranged to the assumed splitting failure surface. Similarly, from Equation 6.2, the bond strength can be expressed as:

$$\tau_f = \frac{f_{bod}}{\alpha_1} \quad \text{Equation 6.13}$$

where τ_f is the bond stress in MPa, f_{bod} , and α_1 were previously defined.

6.5 Review of Bond Strength Equations Proposed in the Literature

6.5.1 Model I (Krem 2013)

Krem (2013) proposed two models to predict the development length of GFRP and CFRP bars based on the experimental results of forty beams cast with self-consolidating concrete (SCC) and normal vibrated concrete (NVC). These models were developed based on the normalized average bond equations, where the bond stress and concrete cover were normalized to the square root of compressive strength and the diameter of the bar, respectively. So, the minimum required embedment length for GFRP and CFRP can be expressed as;

$$\ell_{e(GFRP)} = \left(\frac{\frac{f_{GFRP}}{\sqrt{f'_c}} - 25.9}{0.652 + 0.288 \frac{C}{d_b}} \right) d_b \quad \text{Equation 6.14a}$$

$$\ell_{e(CFRP)} = \left(\frac{\frac{f_{CFRP}}{\sqrt{f'_c}} - 55.04}{0.36 + 0.48 \frac{C}{d_b}} \right) d_b \quad \text{Equation 6.14b}$$

where ℓ_e is the development length of a rebar in mm, d_b is the diameter of the GFRP bar in mm, f_{GFRP} and f_{CFRP} are the design tensile strengths in the GFRP and CFRP bars, respectively, in MPa, f'_c is concrete compressive strength in MPa, C is the concrete cover thickness to the center of the FRP bar in mm. Then, from Equation 6.2, the bond strength can be expressed as:

$$\tau_{f(GFRP)} = \frac{f_{GFRP}}{4} \left(\frac{0.652 + 0.288 \frac{C}{d_b}}{\frac{f_{GFRP}}{\sqrt{f'_c}} - 25.9} \right) \quad \text{Equation 6.15a}$$

$$\tau_{f(CFRP)} = \frac{f_{CFRP}}{4} \left(\frac{0.36 + 0.48 \frac{C}{d_b}}{\frac{f_{CFRP}}{\sqrt{f'_c}} - 55.04} \right) \quad \text{Equation 6.15b}$$

where τ_f is the bond stress in MPa, d_b, f'_c , and C were previously defined.

6.5.2 Model II (Quayyum and Rteil 2011)

This model was proposed based on the model introduced by Wambeke and Shield (2006) to predict the development length of FRP bars embedded in concrete. Quayyum and Rteil (2011) modified the latter model to include the effect of transverse reinforcement. The authors collected a database to include glass, carbon and aramid FRP bars with different surface textures such as sand-coated, spirally-wrapped and helical-lugs to propose the following equation:

$$l_e = \left(\frac{\frac{f_{frp}}{4\sqrt{f'_c}} - 9}{0.03 + 0.14 \frac{C}{d_b} + 2.9 \frac{A_{tr}}{snd_b}} \right) d_b \quad \text{Equation 6.16a}$$

$$\tau_f = \frac{f_{frp}}{4} \left(\frac{0.03 + 0.14 \frac{C}{d_b} + 2.9 \frac{A_{tr}}{snd_b}}{\frac{f_{frp}}{4\sqrt{f'_c}} - 9} \right) \quad \text{Equation 6.16b}$$

where τ_f, f'_c, d_b, l_e were previously defined, c is the lesser of the cover to the center of the bar or one half of the center-to-center spacing of the bars being developed in mm, A_{tr} is the area of transverse reinforcement normal to the plane of splitting through the bars in mm^2 , s is the spacing

of the transverse reinforcement in mm, n is the number of bars being developed along the plane of splitting.

6.5.3 Model III (Newman et al. 2010)

Newman et al. (2010) conducted an analytical study, which resulted in a refined design equation for the development length of FRP bars. A database of 48 test specimens were collected to investigate the effect of different parameters on the development length through large number of analytical simulations. These parameters include bar type (GFRP, CFRP), bar strength, bar modulus of elasticity, bar diameter, bar surface texture, concrete strength, and confinement. It is worth mentioning that a factor of $(c + K_{tr})$ that accounts for radial stresses acting on the outer concrete surface was adopted and applied towards specimens with additional confinement.

$$\ell_{e(CFRP)} = \frac{f_u \times d_b^2}{14.6\sqrt{f'_c}} \quad \text{Equation 6.17a}$$

$$\ell_{e(GFRP)} = \frac{f_u \times d_b^2}{39\sqrt{f'_c}} \quad \text{Equation 6.17b}$$

$$\ell_{e(CFRP,Confined)} = \frac{f_u \times d_b^2}{3.1\sqrt{f'_c}(c + K_{tr})} \quad \text{Equation 6.17c}$$

$$\ell_{e(GFRP,Confined)} = \frac{f_u \times d_b^2}{8.3\sqrt{f'_c}(c + K_{tr})} \quad \text{Equation 6.17d}$$

$$K_{tr} = \frac{A_{tr}f_{yt}}{260sn} \quad \text{Equation 6.17e}$$

$$\tau_{f(CFRP)} = \frac{14.6\sqrt{f'_c}}{4d_b} \quad \text{Equation 6.17f}$$

$$\tau_{f(GFRP)} = \frac{39\sqrt{f'_c}}{4d_b} \quad \text{Equation 6.17g}$$

$$\tau_{f(CFRP,Confined)} = \frac{3.1\sqrt{f'_c}(c + K_{tr})}{4d_b} \quad \text{Equation 6.17h}$$

$$\tau_{f(GFRP,Confined)} = \frac{8.3\sqrt{f'_c}(c + K_{tr})}{4d_b} \quad \text{Equation 6.17i}$$

where $\tau_f, f'_c, c, d_b, l_e, A_{tr}, s,$ and n were previously defined, f_u is the rupture stress of the bar in MPa,

6.5.4 Model IV (Basaran and Kalkan 2020)

In this model, a development length equation was obtained using multiple regression analysis on a database of 185 hinged-beam experiments, which covered a wide range of design parameters. This equation addressed all kinds of FRP bars and surface textures. It is worth mentioning that this model is the only model, which implicitly considers the effect of adding steel fibers through the term f_{tsp} .

$$\ell_e = \frac{23.81f_{tsp}d_b - 0.89f_{frp}d_b}{f_{tsp}^2 + 0.44f_{tsp}d_{bo} - 3.55f_{tsp}S} \quad \text{Equation 6.18a}$$

$$f_{tsp} = 0.63f_{cu}^{0.5} + 0.288f_{cu}^{0.5}(RI) + 0.052(RI) \quad \text{Equation 6.18b}$$

$$RI = \frac{V_f L_f}{\phi_f} \quad \text{Equation 6.18c}$$

where ℓ_e , d_b , f_{frp} were previously defined, f_{tsp} is the splitting tensile strength of steel-fiber reinforced concrete in MPa, d_{bo} is the reinforcement outer diameters in mm, S is a coefficient for the reinforcement fiber and surface type that is ranged between (5.1 to 9.5), RI is the fiber reinforcing factor, V_f is the volumetric fiber ratio in percent, L_f is the fiber length in mm and ϕ_f is the fiber diameter in mm.

6.5.5 Model V (Islam et al. 2015)

In a recent effort, Islam et al. (2015) proposed an equation to predict the bond strength of headed-end FRP bars based on 18 pullout specimens. A constant B was adopted to increase the bond strength of specimens with headed-end bars.

$$\tau_f = \frac{d_b}{4} f_{frp} \frac{1}{\ell_e} \quad \text{Equation 6.19a}$$

$$\ell_e = B \frac{d_b f_{frp}}{\sqrt{f'_c}} \quad \text{Equation 6.19b}$$

$$B = 0.13 + \frac{\ell_{e2}}{80d_b} \quad \text{Equation 6.19c}$$

where τ_f , ℓ_e , d_b , f_{frp} , and f'_c were previously defined, B is the headed anchorage factor, ℓ'_{e2} is the additional straight part of the bar to the head in mm.

6.6 Assessment of Current Code Provisions

The majority of the studies presented the bond performance in terms of the bond stress (τ) rather than the development length (ℓ_e). Therefore, only the bond strength was calculated and compared against the available equations previously presented. Tables 6.8-6.11 list comparisons between the experimental and predicted bond strength of the straight and headed-end FRP bars embedded in normal and fibrous concrete. The predicted values for all specimens were calculated while all strength and material factors were set to 1.0. As can be noticed in Figure 6.5, in general, the predicted capacities by all codes were scattered either above or below the line of equality, indicating that each provision had shortcomings. It is worth mentioning that the equations presented in codes were developed based on straight FRP bars embedded in normal concrete.

The CSA/S806-12 (CSA 2017), CSA/S6-19 (CSA 2019a), and JSCE-97 (JSCE 1997) highly underestimate the capacity of the specimens. These models predicted the capacity with a mean P_{exp}/P_{pred} , coefficient of variation (CoV) and coefficient of determination (R^2) of 3.65 ± 1.1 , 30% and 0.37, 2.25 ± 0.7 , 29% and 0.41, 3.02 ± 0.8 , 27% and 0.48, respectively, as listed in Table 6.9. For the CSA/S806-12, this was attributed to taking the fiber coefficient as 1.0 for both the CFRP and GFRP neglecting the significant difference in the bond strength between these two types reported in the literature. Despite considering the effect of the surface texture of the bar in the equation proposed by the later code (CSA/S806-12), there was only a difference of 5% between the coefficients stipulated for different surfaces finishes; in addition to, neglecting the intended surface reinforcement. Parameters that directly affect the bond strength of FRP bar such as the reinforcement modulus of elasticity, transverse reinforcement, and the inclusion of discrete fibers

were neglected. For the CSA/S6-19, the conservative estimation of the bond strength might be ascribed to that the equation explicitly neglected the effect of the bar fiber type and surface texture; in addition to the limitation of d_{sc} . For the JSCE-97, the bond strength equation implicitly considered different parameters such as the bar fiber type and surface texture through the term α_2 . However, this parameter needs to be augmented by experimental data of the FRP bar, and in case of the absence of such data, no specific values were stipulated for different bar fiber type or surface finish. On the other hand, the ACI 440.1R-15 equation overestimated the bond stress with a mean P_{exp}/P_{pred} , (CoV) and (R^2) of 0.83 ± 0.26 , 31% and 0.35, respectively.

Similarly, the models collected from literature highly underestimated the bond strength of straight FRP bars embedded in normal concrete (see Table 6.8 and Figure 6.5). For example, *Model I* (krem 2013), *Model II* (Quayyum and Rteil 2011), and *Model III* (Newman et al. 2010) provided highly conservative predictions with a mean P_{exp}/P_{pred} , CoV and R^2 of 4.1 ± 1.3 , 32%, and 0.38, 3.6 ± 1.6 , 45%, and 0.42, and 2.9 ± 1.2 , 42%, and 0.1 respectively. This was attributed to the limited number of specimens used to develop these models, which led to neglecting key parameters. Conversely, *Model IV* provided reasonable predictions for straight FRP bars embedded in plain concrete with a mean P_{exp}/P_{pred} , CoV and R^2 were 1.28 ± 0.42 , 32%, and 0.52. This superior prediction obtained from *Model IV* might be attributed to the wide population of specimens that was used in this study (180 test specimens), which covered all the parameters and mitigated all the deficiencies in the other models. Unlike steel bars, where the interlocking is the main mechanism of stress transfer, the friction is the main bond-resistance mechanism for FRP bars, which is highly dependent on the shape of bar and surface texture. Therefore, including the effect of the fiber type of the bar and the surface textures in *Model IV* implicitly through the parameter S significantly enhanced the

predicted bond strength. In addition, defining boundaries of variables in the bond stress equation led to that the proposed equation from *Model IV* showed realistic estimates.

It was reported that the presence of discrete fibers, regardless of the type or dosage of fibers, showed drastic improvement in the bond strength of the FRP bar. This was attributed to the predominant role in controlling the development of cracking, providing better confinement, and dissipating bond energy. In addition, none of the equations presented herein to predict the bond strength considered the effect of adding fibers on the bond strength of straight FRP bars embedded in FRC. Thus, all previous equations failed in providing reasonable predictions of the bond strength when it was applied to specimens with straight FRP bars embedded in fibrous concrete, as listed in Table 6.9. Out of all models, *Model IV* (Basaran and Kalkan 2020) produced the best estimates with a mean P_{exp}/P_{pred} , CoV and R^2 of 1.22 ± 0.42 , 33% and 0.72, respectively, it provides the least scattered results and best fit for specimens with straight FRP bars embedded in FRC.

Similarly, using headed-end FRP bars instead of straight bars significantly improved the bond stress due to the bearing of the head against the concrete during the pullout process (Islam et al. 2015; Benmokrane et al. 2016). Since the previous models did not include the effect of using bars with anchoring head, the equations presented in the codes or developed in the literature, except for *Model V*, greatly underestimated the bond stress of specimens with headed-end bars embedded in normal concrete, as listed in Table 6.10. For example, the CSA/S806-12 (CSA 2017), JSCE-97 (JSCE 1997), *Model I* (Krem 2013) and *Model III* (Newman et al. 2010) yielded extremely over-conservative bond strength predictions for headed-end FRP bars embedded in plain concrete with a mean P_{exp}/P_{pred} , CoV and R^2 of 5.5 ± 1.43 , 26%, and 0.48, 4.6 ± 1.46 , 31%, and 0.04, 5.8 ± 2.43 , 42%, and 0.12, and 4.3 ± 2.21 , 52%, and 0.20, respectively. On the other hand, *Model V*, which

was particularly developed to predict the bond strength of headed-end FRP bars embedded in plain concrete, yielded better predictions compared to other models reviewed in this study, with a mean P_{exp}/P_{pred} , CoV and R^2 of 1.62 ± 0.44 , 27%, and 0.30, respectively.

6.7 Proposed Model and Verification

As mentioned earlier, *Model IV* and *Model V* provided consistent and reasonable predictions for straight FRP bars (embedded in either plain or fibrous concrete) and headed-end FRP bars embedded in plain concrete without fibers. However, both models are not accurate for specimens with FRP headed-end bars embedded in FRC (see Table 6.11 and Figure 6.6). The mean P_{exp}/P_{pred} and CoV for *Model IV* and *Model V* were 3.1 ± 0.86 and 28%, and 2.9 ± 0.4 and 13%, respectively. Therefore, the authors conducted this research program to test fibrous specimens reinforced with headed-end FRP bars in order to develop a model for accurately capturing the bond strength of such combination.

In this study, modifications were introduced to *Model IV* to make it suitable for all types of bars and cementitious matrices.

In this context, *Model V* considered the effect of using headed-end FRP bars through a coefficient, B . Accordingly, the later coefficient was borrowed from *Model V* (Equation 6.19a) and implemented in *Model IV* (Equation 6.18a); in addition to modifying the factors RI and B' in *Model IV* to include the effect of the modulus of elasticity of discrete fibers (Equations 20a, b, c, d and e). This was conducted through linear regression analysis of the present experimental results of headed-end FRP bars with two different diameters (15.9 and 19.0 mm) embedded in concrete reinforced with BP (dosage of 2.5 and 4.5%) or SF (dosage of 1%).

Table 6.8: Model comparisons for straight FRP bars embedded in normal concrete

Specimens ID	τ_{exp} (MPa)	Models in codes				Models in literature			
		CSA/S806-12	CSA/S6-19	ACI 440.1R-15	JSCE-97	Model I	Model II	Model III	Model IV
		τ_{exp}/τ_{pre}							
Alves et al. (2011)									
C.16	11.9	2.74	1.90	0.81	2.43	2.71	1.83	2.74	1.19
C.19	10.2	2.36	1.64	0.70	2.10	2.66	1.88	2.82	1.24
E.16.15	11.6	4.48	3.10	0.81	3.58	6.05	6.82	2.68	1.17
E.16.20	14.7	4.23	2.93	1.01	4.01	6.72	6.65	3.38	1.47
E.16.25	13.9	3.21	2.22	0.96	3.33	5.71	5.15	3.21	1.40
E.19.15	10.6	4.09	2.83	0.74	3.27	5.52	6.22	2.93	1.29
E.19.20	11.0	3.19	2.20	0.76	3.02	5.06	5.00	3.04	1.34
E.19.25	10.4	2.41	1.67	0.72	2.50	4.29	3.86	2.88	1.27
Belarabi and Wang (2012)									
VP4C	8.70	2.00	1.41	0.60	1.83	1.59	1.49	4.45	1.01
VP4G	18.7	4.32	3.05	1.30	3.94	4.65	3.20	3.60	0.82
VP8G	18.5	5.34	3.02	1.28	3.90	5.08	3.63	6.84	1.14
Kim et al. (2013)									
PC0.0GFRP-A	16.3	3.77	2.42	1.03	3.06	3.58	2.44	2.79	1.34
PC0.0GFRP-B	23.7	5.48	3.52	1.50	4.45	5.20	3.55	4.05	0.96
Islam et al. (2015)									
12P-C-4d	11.0	2.67	1.51	0.53	2.06	1.74	1.11	1.64	0.99
12P-E1.5d-4d	10.5	4.24	2.40	0.52	2.95	4.68	5.28	1.57	0.95
12P-E2.5d-4d	12.1	2.92	1.65	0.59	2.63	4.24	3.82	1.80	1.09
12P-C-6d	10.1	2.46	1.39	0.68	1.90	1.61	1.02	1.51	0.92
12P-E1.5d-6d	10.0	4.08	2.31	0.70	2.84	4.50	5.08	1.51	0.91
12P-E2.5d-6d	11.3	2.74	1.55	0.77	2.47	3.98	3.59	1.69	1.02

Specimens ID	τ_{exp} (MPa)	Models in codes				Models in literature			
		CSA/S806-12	CSA/S6-19	ACI 440.1R-15	JSCE-97	Model I	Model II	Model III	Model IV
		τ_{exp}/τ_{pre}							
16P-C-4d	12.6	3.07	1.73	0.61	2.37	2.49	1.69	2.52	1.49
16P-E1.5d-4d	10.1	4.07	2.30	0.50	2.83	4.49	5.06	2.00	1.18
16P-E2.5d-4d	11.7	2.83	1.60	0.57	2.55	4.11	3.71	2.32	1.37
16P-C-6d	11.8	2.86	1.61	0.79	2.21	2.32	1.57	2.34	1.39
16P-E1.5d-6d	10.0	4.05	2.29	0.69	2.82	4.46	5.03	1.99	1.18
16P-E2.5d-6d	10.2	2.48	1.40	0.70	2.24	3.60	3.25	2.04	1.20
Yan and Lin (2017)									
PC0.0-Control	15.7	3.62	2.63	1.12	3.44	4.44	3.18	3.04	0.70
Bediwy and El-Salakawy (forthcoming)									
NS-X-15-S	22.6	5.22	3.26	1.16	4.24	4.67	3.16	4.71	2.19
HS-X-15-S	27.1	6.26	3.31	1.18	5.08	4.74	3.20	4.77	2.52
HS-X-20-S	19.7	4.55	2.41	0.85	3.69	3.91	2.76	4.15	2.32
Mean		3.65	2.25	0.83	3.03	4.10	3.59	2.93	1.28
SD		1.08	0.66	0.26	0.82	1.32	1.63	1.22	0.42
CoV (%)		29.7	29.4	31.3	27.2	32.2	45.3	41.6	32.7
R ²		0.37	0.41	0.35	0.49	0.38	0.43	0.07	0.52

Table 6.9: Model comparisons for straight FRP bars embedded in FRC

Specimens ID	τ_{exp} (MPa)	Models in codes				Models in literature			
		CSA/S806-12	CSA/S6-19	ACI 440.1R-15	JSCE-97	Model I	Model II	Model III	Model IV
		τ_{exp}/τ_{pre}							
Belarabi and Wang (2012)									
VF4C	7.10	1.65	1.33	0.56	1.79	1.49	1.4	4.17	1.19
VF4G	16.2	3.75	3.01	1.28	4.07	4.59	3.17	3.56	0.46
VF8G	13.2	3.81	2.45	1.04	3.31	4.13	2.95	5.56	0.61
Kim et al. (2013)									
PP0.5GFRP-A	11.4	2.63	1.79	0.76	2.29	2.65	1.81	2.06	0.86
PP0.5GFRP-B	23.9	5.52	3.76	1.78	4.80	5.56	3.80	4.33	0.72
PP1.0GFRP-A	11.9	2.76	1.80	0.76	2.26	2.66	1.82	2.07	1.53
PP1.0GFRP-B	21.9	5.06	3.30	1.40	4.16	4.88	3.33	3.80	0.59
PVA0.5GFRP-A	10.3	2.37	1.57	0.67	1.98	2.32	1.58	1.81	0.82
PVA0.5GFRP-B	25.3	5.84	3.86	1.64	4.88	5.71	3.89	4.44	0.97
PVA1.0GFRP-A	10.3	2.37	1.47	0.63	1.92	2.17	1.48	1.69	0.78
PVA1.0GFRP-B	25.3	5.84	3.62	3.95	4.73	5.35	3.65	4.17	0.88
Steel0.5GFRP-A	15.4	3.56	2.35	4.12	2.98	3.48	2.38	2.71	1.22
Steel0.5GFRP-B	26.1	6.02	3.98	1.69	5.03	5.89	4.02	4.59	0.99
Steel1.0GFRP-A	12.9	2.98	1.85	0.79	2.42	2.73	1.86	2.13	0.97
Steel1.0GFRP-B	26.3	6.07	3.76	1.60	4.92	5.56	3.80	4.33	0.89
Yan and Lin (2017)									
Steel0.5-Control	19.2	4.43	3.22	1.37	4.20	5.42	3.88	3.71	0.82
Steel1.0-Control	21.3	4.91	3.52	1.50	4.57	5.92	4.24	4.05	0.80
PVA0.5-Control	15.6	3.61	2.64	1.12	3.45	4.44	3.18	3.04	0.62
PVA1.0-Control	16.3	3.77	2.74	1.17	3.58	4.62	3.3	3.16	0.58

Specimens ID	τ_{exp} (MPa)	Models in codes				Models in literature			
		CSA/S806-12	CSA/S6-19	ACI 440.1R-15	JSCE-97	Model I	Model II	Model III	Model IV
		τ_{exp}/τ_{pre}							
Bediwy and El-Salakawy (forthcoming)									
BF-2.5-15-S	31.3	7.23	3.92	1.40	5.87	5.62	3.79	5.66	2.10
BF-2.5-20-S	23.6	5.45	2.96	1.05	4.43	4.81	3.4	5.10	2.30
BF-4.5-15-S	34.6	8.00	4.41	1.57	6.49	6.32	4.27	6.37	3.00
BF-4.5-20-S	27.1	6.26	3.46	1.23	5.08	5.62	3.97	5.96	1.69
SF-1.0-15-S	32.3	7.46	4.00	1.43	6.06	5.72	3.86	5.77	1.72
SF-1.0-20-S	27.5	6.36	3.40	1.21	5.16	5.54	3.91	5.87	3.47
Mean		4.71	2.97	1.86	4.02	4.53	3.15	4.00	1.22
SD		1.76	0.92	0.86	1.36	1.42	0.95	1.41	0.42
CoV (%)		37.3	30.9	60.2	33.9	31.29	30.28	35.3	33.4
R ²		0.19	0.69	0.69	0.49	0.53	0.62	0.30	0.72

Table 6.10: Model comparisons for headed-end FRP bars embedded in normal concrete

Specimens ID	τ_{exp} (MPa)	Models in codes				Models in literature				
		CSA/S806-12	CSA/S6-19	ACI 440.1R-15	JSCE-97	Model I	Model II	Model III	Model IV	Model V
		τ_{exp}/τ_{pre}								
Islam et al. (2015)										
12H-C-0d	25.0	6.06	3.42	1.73	4.68	2.84	1.69	3.73	2.25	1.57
12H-E1.5d-0d	23.7	9.59	5.42	1.69	6.67	10.6	11.9	3.54	2.14	1.49
12H-E2.5d-0d	24.8	6.01	3.39	1.74	5.41	8.72	7.86	3.69	2.24	1.56
12H-C-4d	20.7	5.03	2.84	2.04	3.89	2.36	1.40	3.09	1.87	1.81
12H-E1.5d-4d	15.4	6.21	3.51	1.58	4.32	6.85	7.73	2.29	1.39	1.34
12H-E2.5d-4d	18.3	4.44	2.51	1.84	4.01	6.45	5.81	2.73	1.65	1.60
12H-C-6d	17.8	4.31	2.44	1.96	3.33	2.02	1.20	2.65	1.60	1.77
12H-E1.5d-6d	13.2	5.35	3.02	1.53	3.72	5.90	6.65	1.97	1.19	1.31
12H-E2.5d-6d	16.8	4.07	2.30	1.90	3.66	5.90	5.32	2.50	1.51	1.67
16H-C-0d	24.5	5.95	3.36	1.70	4.59	3.53	2.20	4.88	2.88	1.55
16H-E1.5d-0d	18.7	7.58	4.28	1.34	5.27	8.36	9.42	3.73	2.21	1.18
16H-E2.5d-0d	22.6	5.47	3.09	1.59	4.93	7.95	7.16	4.49	2.65	1.42
16H-C-4d	18.5	4.48	2.53	1.82	3.46	2.66	1.66	3.68	2.17	1.61
16H-E1.5d-4d	12.9	5.21	2.94	1.32	3.62	5.74	6.48	2.56	1.52	1.12
16H-E2.5d-4d	15.6	3.79	2.14	1.57	3.42	5.50	4.96	3.11	1.84	1.36
16H-C-6d	14.8	3.60	2.03	1.64	2.78	2.14	1.33	2.95	1.74	1.47
16H-E1.5d-6d	12.2	4.90	2.77	1.40	3.41	5.41	6.10	2.41	1.43	1.21
16H-E2.5d-6d	14.0	3.38	1.91	1.58	3.05	4.91	4.43	2.77	1.64	1.39
Benmokrane et al. (2016)										
A-5-35-N	24.6	5.69	4.71	2.39	6.41	6.75	4.56	6.79	3.21	2.17
A-5-35-S	27.8	6.43	5.32	2.71	7.25	7.62	5.15	7.67	3.63	2.45
A-5-47-S	29.8	6.90	4.92	2.50	6.38	7.05	4.76	7.10	3.65	2.26

Specimens ID	τ_{exp} (MPa)	Models in codes				Models in literature				
		CSA/S806-12	CSA/S6-19	ACI 440.1R-15	JSCE-97	Model I	Model II	Model III	Model IV	Model V
		τ_{exp}/τ_{pre}								
A-6-35-N	25.1	5.81	4.80	2.13	6.55	7.82	5.52	8.28	4.02	2.21
A-6-35-S	28.8	6.66	5.51	2.44	7.51	8.97	6.33	9.50	4.62	2.53
A-6-47-S	30.0	6.93	4.95	2.19	6.42	8.05	5.69	8.53	4.60	2.28
Bediwy and El-Salakawy (forthcoming)										
HS-X-15-H	18.8	4.36	2.30	1.17	3.54	3.30	2.23	3.32	2.20	1.06
HS-X-20-H	15.0	3.46	1.83	0.81	2.80	2.97	2.10	3.15	2.36	0.84
Mean		5.45	3.39	1.78	4.66	5.78	4.99	4.27	2.39	1.62
SD		1.43	1.19	0.43	1.47	2.43	2.72	2.21	0.99	0.45
CoV (%)		26.3	35.2	24.4	31.5	42.0	54.5	51.7	41.3	27.5
R ²		0.48	0.03	0.38	0.04	0.12	0.16	0.20	0.29	0.30

Table 6.11: Model comparisons for headed-end FRP bars embedded in FRC

Specimens ID	τ_{exp} (MPa)	Models in codes				Models in literature					Proposed Model
		CSA/S806-12	CSA/S6-19	ACI 440.1R-15	JSCE-97	Model I	Model II	Model III	Model IV	Model V	
		τ_{exp}/τ_{pre}									
Bediwy and El-Salakawy (forthcoming)											
BF-2.5-15-H		5.55	3.01	1.95	4.51	4.31	2.91	4.35	2.27	2.67	0.93
BF-2.5-20-H		5.27	2.86	1.62	4.27	4.65	3.28	4.93	2.88	2.53	0.98
BF-4.5-15-H		6.41	3.54	2.92	5.20	5.07	3.42	5.11	2.79	3.13	1.11
BF-4.5-20-H		7.32	4.04	2.83	5.94	6.57	4.64	6.96	4.59	3.57	1.45
SF-1.0-15-H		5.80	3.11	4.02	4.71	4.45	3.00	4.48	2.37	2.75	0.96
SF-1.0-20-H		6.28	3.37	3.62	5.10	5.47	3.86	5.80	3.43	2.98	1.15
Mean		6.11	3.32	2.83	4.95	5.09	3.52	5.27	3.06	2.94	1.09
SD		0.73	0.43	0.93	0.60	0.84	0.64	0.98	0.86	0.38	0.19
CoV (%)		12.0	12.9	32.8	12.0	16.6	18.28	18.5	28.2	12.9	0.18
R ²		0.19	0.56	0.25	0.00	0.38	0.35	0.35	0.50	0.56	0.95

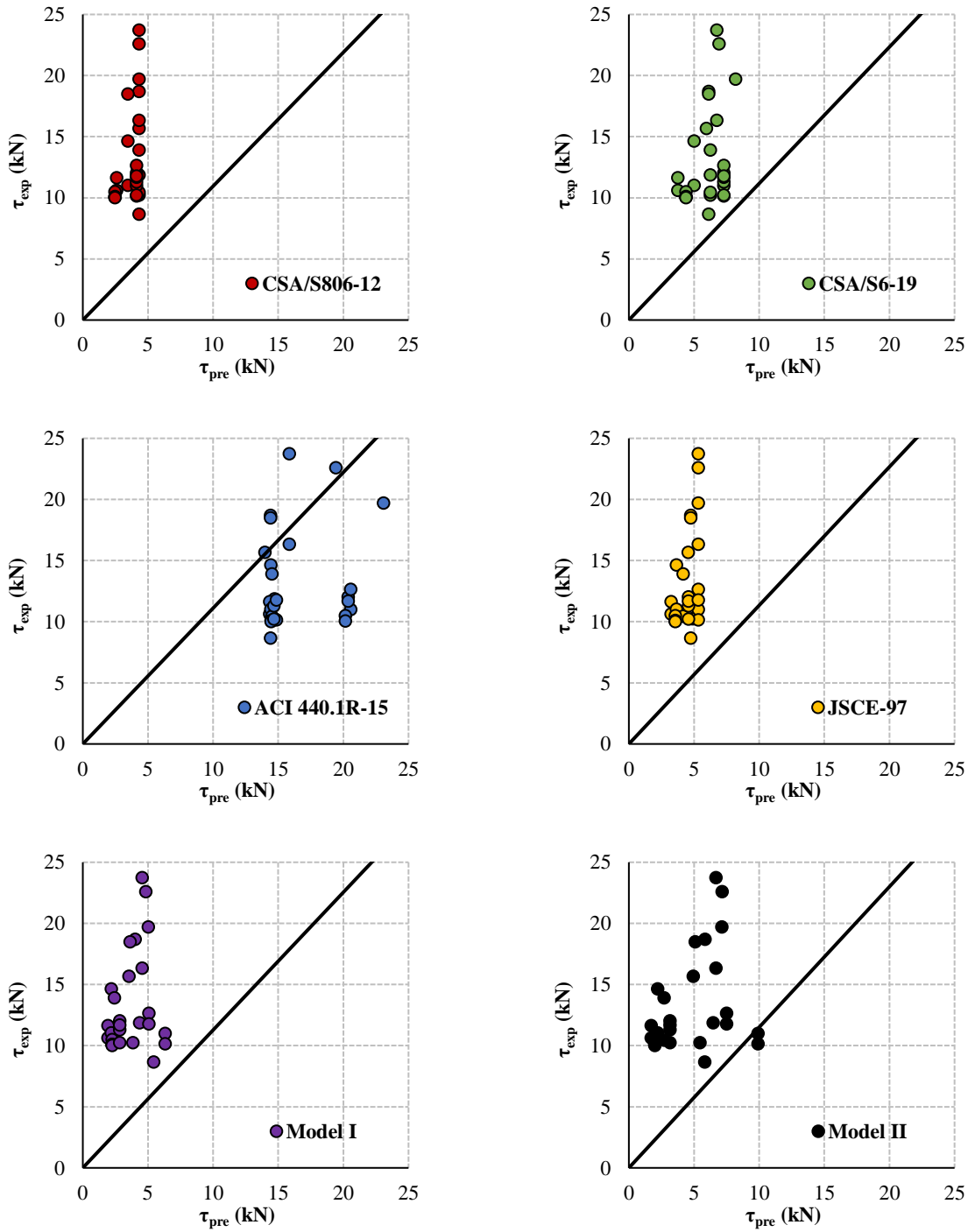


Figure 6.5: Prediction of available models for straight FRP bars embedded in normal concrete

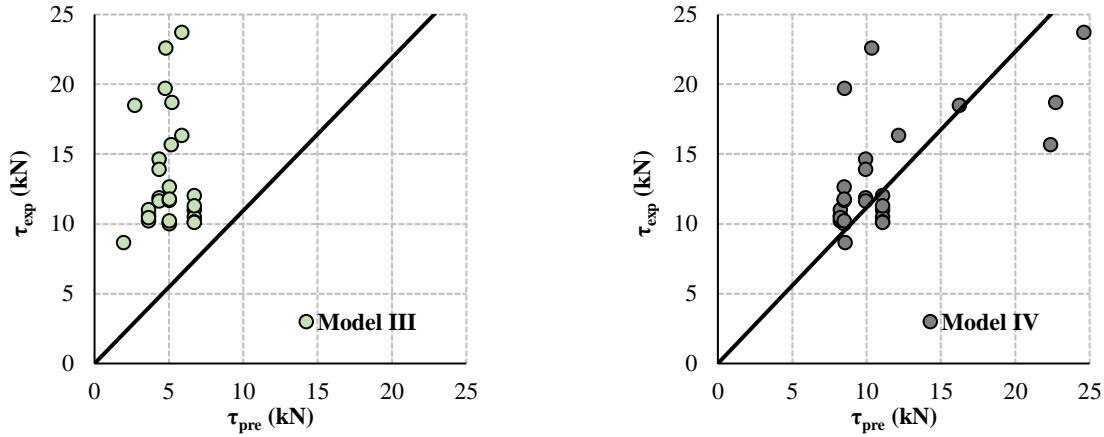


Figure 6.5: Prediction of available models for straight FRP bars embedded in normal concrete (continued).

$$\tau_f = \frac{d_b}{4} f_{frp} \frac{1}{\ell_e} \quad \text{Equation 6.20a}$$

$$\ell_e = \frac{23.8 f_{frc} d_b - 0.9 f_{frc} d_{bo}}{(f_{frc})^2 + 0.44 f_{frc} d_{bo} - 3.55 f_{frc} S - (B')^{1.4}} \quad \text{Equation 6.20b}$$

$$f_{frc} = 0.63 \sqrt{f'_c} + 0.29 \sqrt{f'_c} (RI') + 0.05 (RI') \quad \text{Equation 6.20c}$$

$$RI' = \frac{V_f L_f}{\phi_f} \left(\frac{E_f}{0.25 E_s} \right)^{0.1} \quad \text{Equation 6.20d}$$

$$B' = \frac{\sqrt{f'_c}}{4 \left(0.13 + \frac{\ell'_e}{80 d_b} \right)} \quad \text{Equation 6.20e}$$

where f_{frc} is the splitting tensile strength of FRC in MPa, S is a coefficient for the reinforcement fiber and surface type, detailed description of this parameters can be found in Basaran and Kalkan (2020), RI' is the fiber reinforcing effect, B' is the headed anchorage factor, which it is used only in case of headed-end bars, ℓ'_e is the additional straight part of the bar to the head in mm, if any, τ_f , ℓ_e , d_b , f_{FRP} , d_{bo} , V_f , L_f , ϕ_f , E_f , E_s , f'_c , were previously defined.

The test-to-predicted ratios using the proposed *Model* are listed in Table 6.11 and shown in Figure 6.6. This proposed model produced good predictions with a mean P_{exp}/P_{pred} of 1.09 ± 0.19 , a CoV of 18%, and R^2 of 0.95. Furthermore, the value for the coefficient of determination of 0.96 close

to unity, indicating a strong association between the actual and predicted capacities. In addition, this model explains all variables of the headed-end FRP/FRC bond with a reasonable degree of accuracy.

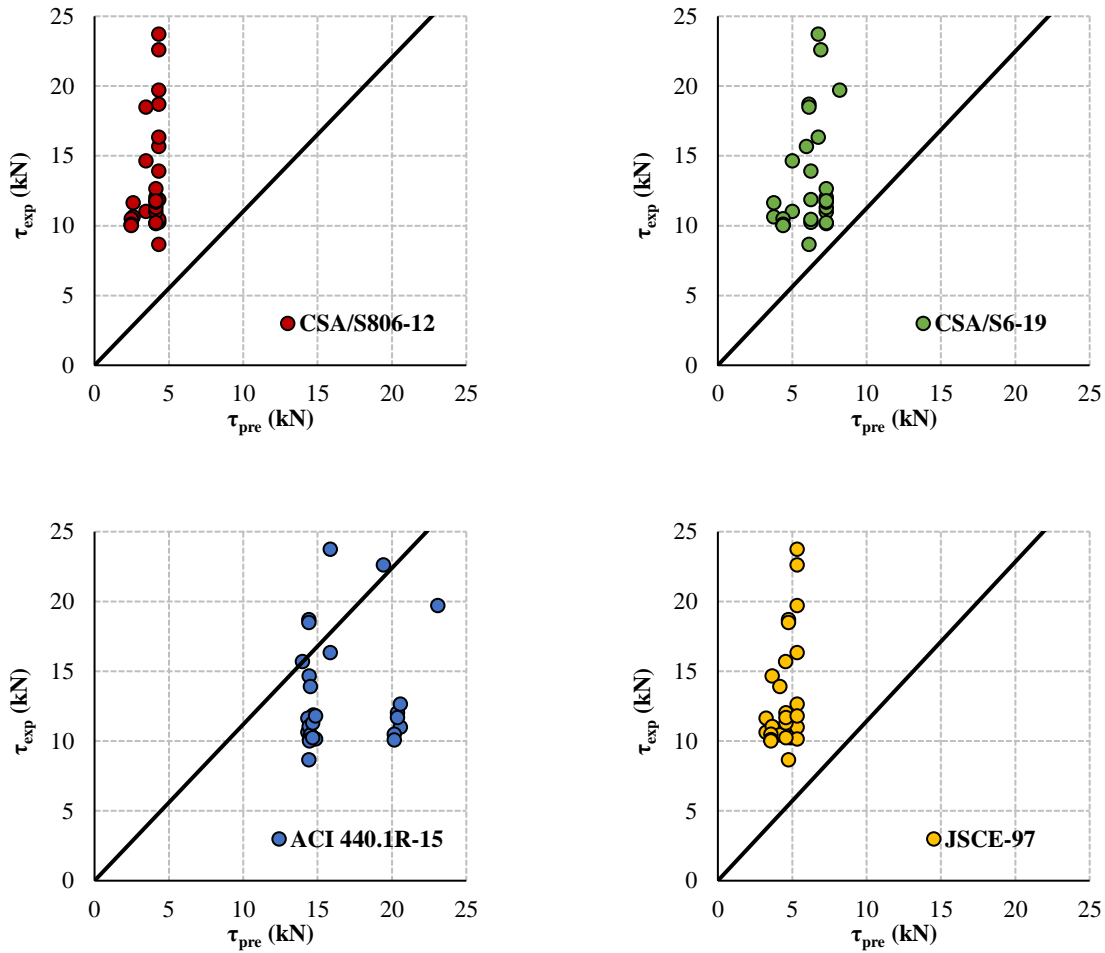


Figure 6.6: Prediction of available models for headed-end FRP bars embedded in FRC.

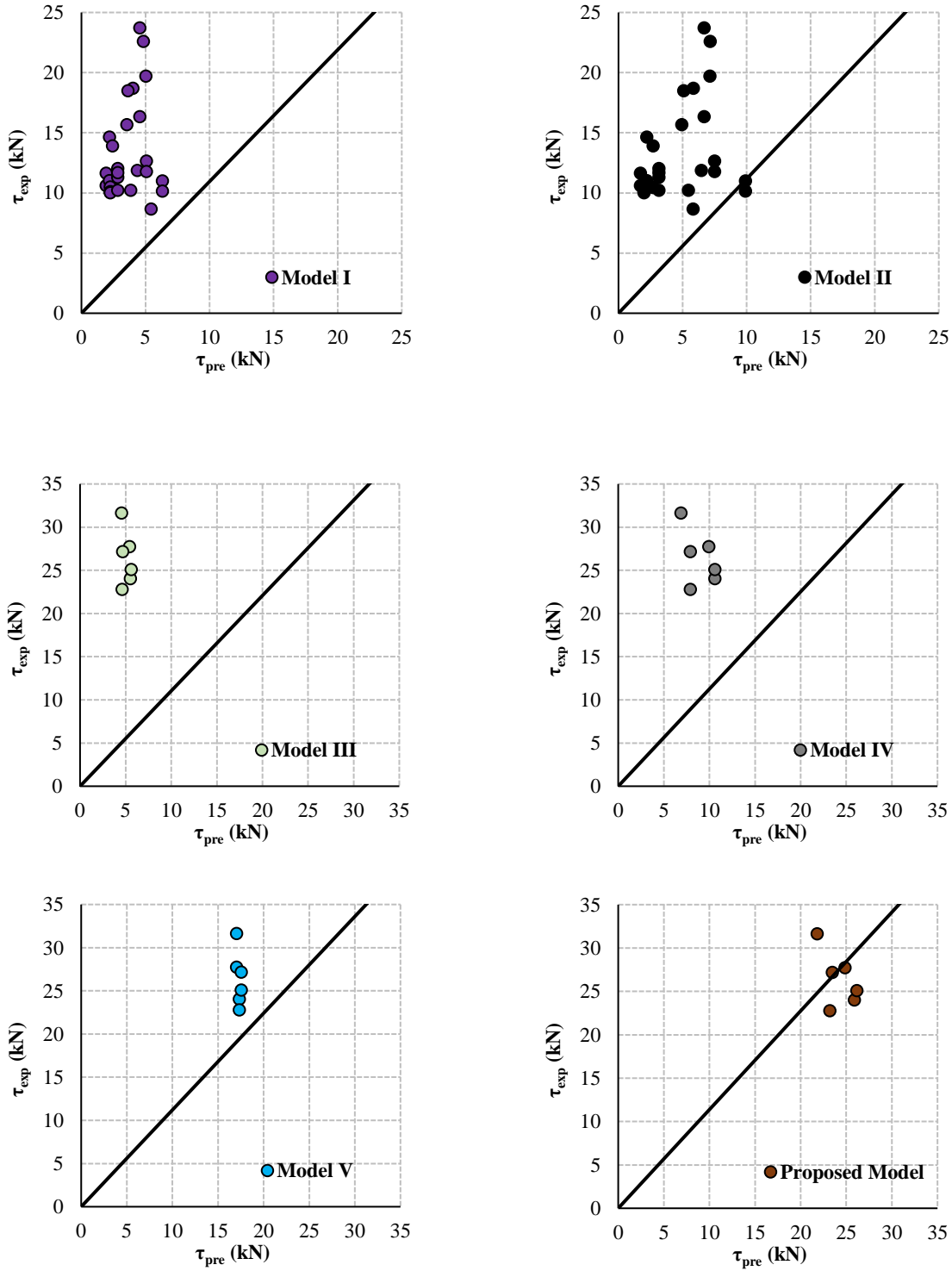


Figure 6.6: Prediction of available models for headed-end FRP bars embedded in FRC (continued).

6.8 Conclusions

Based on the experimental and analytical investigations, the following conclusions can be drawn:

- The bond stress equations in different design provisions were assessed. The CSA/S806-12 (CSA 2017), CSA/S6-19 (CSA 2019), and JSCE-97 (JSCE 1997) highly underestimate the capacity of the specimens reinforced with straight FRP bars embedded in plain concrete without fibers with a mean P_{exp}/P_{pred} , coefficient of variation (CoV) and coefficient of determination (R^2) of 3.65 ± 1.1 , 30% and 0.37, 2.25 ± 0.7 , 29% and 0.41, 3.02 ± 0.8 , 27% and 0.48, respectively. This was attributed to neglecting major factors that directly affect the bond performance. On the other hand, the ACI 440.1R-15 equation overestimated the bond stress with a mean P_{exp}/P_{pred} , (CoV) and (R^2) of 0.83 ± 0.26 , 31% and 0.35, respectively.
- Four models from literature (Krem 2013; Quayyum and Rteil 2011; Newman et al. 2010; Basaran and KalKan 2020) were introduced to mitigate the deficiencies in the bond strength equations stipulated by the design codes. However, all models, except *Model IV*, highly underestimate test results, due to the limited number of specimens used to develop these models. On the other hand, *Model IV* provided better prediction for straight FRP bars embedded in plain concrete with a mean P_{exp}/P_{pred} , CoV and R^2 were 1.28 ± 0.42 , 32%, and 0.52. This prediction of bond strength of straight FRP/plain concrete specimens might be attributed to the wide population of specimens used in that study (180 test specimens), which covered all the parameters and mitigated all the deficiencies in the other models.
- *Model V*, which was particularly developed to predict the bond strength of headed-end FRP bars embedded in plain concrete, yielded reasonable, yet conservative, predictions

compared to other models reviewed in this study, with a mean P_{exp}/P_{pred} , CoV and R^2 were 1.62 ± 0.44 , 27%, and 0.30, respectively.

- Out of all models, *Model IV* (Basaran and Kalkan 2020) produced the best estimates for specimens reinforced with straight FRP bars embedded in fibrous concrete (FRC), with a mean P_{exp}/P_{pred} , CoV and R^2 of 1.27 ± 0.42 , 33% and 0.52, respectively. It provides the least scattered results and best fit for specimens reinforced with straight FRP bars embedded in FRC.
- All current models failed in providing reasonable predictions of the bond strength when it was applied to specimens reinforced with headed-end FRP bars embedded in fibrous concrete. Therefore, a new model was proposed to account for the effect of incorporating different types of discrete fibers into specimens reinforced with headed-end bars. The proposed model produced good predictions for FRP-FRC specimens with a mean P_{exp}/P_{pred} 1.09 ± 0.19 , a CoV of 18%, and R^2 of 0.95.

CHAPTER 7: STRUCTURAL BEHAVIOUR OF FRCC LAYERED DEEP BEAMS REINFORCED WITH GFRP HEADED-END BARS

Authors and Affiliation:

- Ahmed G. Bediwy, PhD Candidate, Department of Civil Engineering, University of Manitoba.
- Karam Mahmoud, Post-Doctoral Fellow, Department of Civil Engineering, University of Manitoba, Lecturer, Department of Civil Engineering, Assiut University, Egypt.
- Ehab F. El-Salakawy, Professor, Department of Civil Engineering, University of Manitoba

Journal and Status:

Elsevier, Journal of Engineering Structures, accepted for publication on February 2021.

Reference:

Bediwy, A., Mahmoud, K., and El-Salakawy, E. “Structural behaviour of FRCC layered deep beams reinforced with GFRP headed-end bars.” *Engineering Structures*, in press.

Note:

The manuscript had been slightly altered from the original paper by renumbering the tables and figures to include the chapter number. In addition, the reference list and list of notations have been moved to the appropriate sections in the thesis as indicated in the table of contents.

Abstract:

In this study, seven concrete deep beams reinforced with glass fiber reinforced polymer (GFRP) headed-end bars were constructed and tested to failure. The beams had a rectangular section of 250 mm in width and 590 mm in depth with overall span of 1,390 mm and were tested under three-point bending loading. The main test variables were the longitudinal reinforcement ratio and the incorporation of fiber-reinforced cementitious composite material in the tie zone. The arch action mechanism developed in all specimens as substantiated by the measured strains along the tie length. In addition, analysis of test results showed that the incorporation of basalt fiber pellets or steel fibers in the tie zone of the beam improved the behaviour including the ductility and the load carrying capacity. It was also found out that the provisions for strut-and-tie model in the Canadian codes for FRP-RC structures and the American code for steel-RC structures yielded reasonable predictions to the load capacity of deep beams.

Keywords: Deep beams, fiber-reinforced cementitious composites, glass fiber-reinforced polymer reinforcement, headed-end bars, shear capacity.

7.1 Introduction

Infrastructure deterioration induced by steel reinforcement corrosion is one of the major challenges facing the industry in North America due to the large amounts of de-icing salts used during winter seasons. In recent years, the non-corrodible glass fiber-reinforced polymer (GFRP) reinforcement has been established as a realistic alternative in order to overcome the costly rehabilitation associated with the corrosion of steel reinforcement (ACI 2015). In addition, concrete structures in such aggressive environments are prime examples for the use of fiber-reinforced composites (FRCs) due to their capability to increase the energy-absorbing capacity and deformation.

Reinforced concrete (RC) deep beams are common structural elements in bridges because of their ability to support high concentrated loads and tremendous bearing capacity. Deep beams have various structural applications, e.g. transfer girders, pile caps, foundation, and transverse bridge girders (Mohammadhassani et al. 2012). Deep beams are structural members characterized with relatively small shear span-to-depth ratio ($a/d < 2.5$) in which arch action is the main load transfer mechanism, unlike the beam action in slender beams (ASCE-ACI Committee 426 1973, ASCE-ACI Committee 445 1999; Wight and MacGregor 2009). The arching action mechanism involves the transmission of the vertical loads to the supports through the concrete compression struts while the reinforcement acts as a tie.

Due to their geometrical dimensions, strength of RC deep beam is usually controlled by shear rather than flexural. Shear failure is relatively brittle and can occur without warning. Using plain high-performance concrete, without fibers, in deep beams will contribute to its bearing capacity; however, it would fail to overcome of the brittle nature of concrete (Liu and Xu 2013). Therefore, some researchers have employed discrete fibers into cementitious materials/concrete aiming to enhance the overall structural performance (Song and Hwand 2004, Xu et al. 2012, Iyer et al. 2015,

Corinaldesi and Nardinocchi 2016). Furthermore, the presence of fibers significantly enhanced the flexural toughness of the cementitious composites, which in turn contributed to improving the capacity and ductility of structural elements. In this context, the incorporation of fibers in the entire beam showed a significant effect on enhancing the load carrying capacity of deep beams because of the capability of fibers to bridge the concrete cracks (Mohammadhassani et al. 2012, Liu and Xu 2013).

Various commercially available fibers can be used to make fiber-reinforced cementitious composites (FRCC), such as steel, synthetic, organic and inorganic fibers. However, a relatively new type of fibers manufactured from basalt rocks is progressively immersing in civil engineering research, including a special type of basalt fiber pellets (BF), which is made of basalt fibers encapsulated by polyamide or other resins. Basalt fibers have high tensile strength, and they are not vulnerable to corrosion contrary to steel fibers that corrode resulting in irregular/rough surfaces, e.g. slab on ground, bridge decks and pavements (Iyer et al. 2015; Arslan 2016; Ayub et al. 2016; Ghazy et al. 2016; Mahmoud et al. 2017).

In addition, the strength of deep beams is strongly affected by the detailing of their support zones where high-tension forces develop in the longitudinal bars over the entire shear span. As such, it requires longer development length beyond the support (over-hang part) compared to slender beams. This can be satisfied by anchoring the reinforcement using hooks or headed-end bars and/or using a high performance cementitious composite reinforced with fibers at this location, which would shorten the required development length considerably. Benmokrane et al. (2016) concluded that headed-end GFRP bars yielded 90% higher pullout capacity with respect to their straight counterpart bars.

The Canadian codes for FRP-RC building structures, CSA/S806-12 (CSA 2017) and the bridge code, CSA/S6-19 (CSA 2019a) included provisions for the strut-and tie model (STM) for FRP-RC deep beams, which are based on those specified in the CSA/A23.3-19 (CSA 2019c). The strut capacity in these Canadian codes depends on the concrete compressive strength and the strains developed in the tie, and consequently the type of reinforcement of the tie. On the other hand, the current American guidelines for FRP-RC members, ACI 440.1R-15 (ACI 2015), do not provide any provisions for the design of deep beams. However, in the ACI 318-19 code for steel-RC structures (ACI 2019), the design provisions for the strut account for the concrete compressive strength and strut geometry through strut coefficients. In FRP-RC deep beams, the load capacity was governed by the compression strut capacity not the capacity of the node or the tie. Therefore, the ACI 318 design provisions can be applied to the FRP-RC deep beams. Table 7.1 lists the STM design equations in the Canadian and American codes.

To date, limited research has been carried out to investigate the behaviour of steel-FRC simply supported deep beams ((Mohammadhassani et al. 2012, Liu and Xu 2013, Campione 2012, Shah and Modhera 2012, Kumar and Mahendran 2016). In addition, up to the authors' knowledge, there is no experimental data on the behaviour of simply supported FRP-RC deep beam with a layer of FRCC in the tie zone. This paper is a part of an ongoing research program at the University of Manitoba to study the behaviour of RC deep beams (Mohamed et al. 2020). This study examines the effect of the reinforcement ratio and the addition of basalt FRCC layer in the tie zone on the behaviour and ductility of simply supported GFRP-RC deep beams.

Table 7.1: Design code provisions for STM

STM Component	CSA S6-19	ACI 318-14	ACI 318-19
Strut	<p>Compressive force in the strut $= \phi_c f_{cu} A_{cs}$ f_{cu} is the limiting compressive stress, $f_{cu} = \frac{f_c'}{0.8+170\varepsilon_1}$ where, $\varepsilon_1 = \varepsilon_f + (\varepsilon_f + 0.002) \cot^2 \theta_s$ f_c' = concrete strength ε_1 = transverse tensile strain ε_f = tensile strain in the tie θ_s = the smallest angle between the strut and the adjoining ties</p>	<p>Strength of struts = $F_{ns} = f_{ce} A_{cs}$ f_{ce} is effective compressive strength of concrete in a strut $f_{ce} = 0.85\beta_s f_c'$ where β_s is strut coefficient: <ul style="list-style-type: none"> • $\beta_s = 1.0$, for struts with uniform cross-sectional area along the length • $\beta_s = 0.75$ or 0.6, based on satisfying web reinforcement equation $\sum \frac{A_{si}}{b_s s_i} \sin \alpha_i \geq 0.003$ </p>	<p>Strength of struts = $F_{ns} = f_{ce} A_{cs}$ $f_{ce} = 0.85\beta_s \beta_c f_c'$ where, <ul style="list-style-type: none"> • β_s is strut coefficient = 1.0 for boundary struts, 0.75 for interior struts satisfying one of the following equations $\frac{0.0025}{\sin^2 \alpha_1}$ & $V_u \leq \phi 5 \tan \phi \lambda \lambda_s \sqrt{f_c'} b_w d$ and 0.4 for other cases • β_c is Strut confinement factor, which is the lesser of $\sqrt{\frac{A_2}{A_1}}$ or 2.0, where A_1 is the loaded area and A_2 is the area of the lower base of the largest frustum of a pyramid, cone, or tapered wedge contained wholly within the support and having its upper base equal to the loaded area </p>
Tie	<p>Tensile force in the tie $\leq 0.65\phi_F A_{FT} f_{FU}$</p>	<p>The nominal tensile strength of a tie, F_{nt}, shall be calculated by $F_{nt} = A_{st} f_y$</p>	
Node	<p>Compressive stress in the node regions $\leq 0.85\phi_c m f_c'$ in node regions bounded by struts and bearing areas, $0.75\phi_c m f_c'$ in node regions anchoring a tie in only one direction and $0.65\phi_c m f_c'$ in node regions anchoring ties in more than one direction</p>	<p>The nominal compressive strength of a nodal zone, F_{nm}, is calculated by $F_{nm} = f_{ce} A_{nz}$ where $f_{ce} = 0.85\beta_n f_c'$ (ACI 2014) $f_{ce} = 0.85\beta_n \beta_c f_c'$ (ACI 2019) β_n is Nodal zone coefficient <ul style="list-style-type: none"> • $\beta_n = 1.0$, nodal zones bounded by struts and bearing areas or both • $\beta_n = 0.8$, nodal zones anchoring one tie • $\beta_n = 0.6$, nodal zones anchoring two or more ties. </p>	

The strut coefficient β_s was set as 0.6 and 0.4 for the ACI 318-14 and ACI 318-19, respectively.

7.2 Experimental Program

7.2.1 Test specimens

Seven reinforced concrete simply supported deep beams were constructed and tested to failure under monotonic loading. The beams represent a half scale of a typical cross girder in a bridge with a rectangular cross-section measuring 500 mm in width by 1,200 mm in height over a span of 2,780 mm with a longitudinal reinforcement ratio of 0.63%. Therefore, the deep beams in this study had a rectangular cross section of 250-mm width by 590-mm height and a total length of 2,100 mm over a simply supported span of 1,390 mm. The beams had a shear span-to-depth ratio (a/d) of 1.18. In all beams, the reinforcement consisted of GFRP headed-end bars with a development/anchorage length of 280 mm. All beams had no web reinforcement. Three control beams without fibers were cast for comparative purposes, while four beams had FRCC layer that is reinforced with either BP (two specimens) or steel fibers (two specimens) in the tie zone only. The inclusion of the FRCC layer is expected to be effective in enhancing the behaviour of the beams while it is more economical in practice. The ACI 544.4R (2018) recommended a dosage of steel fibers higher than 0.5% by volume to provide flexural toughness after cracking. In addition, earlier version of the same document (ACI 544.4R (1988)) recommended a dosage between 0.5 and 1.5% if it is mixed and placed with conventional equipment. Thus, a dosage of 1% of steel fiber was selected. In case of the BP, a dosage of 2.5% was used, which is corresponding to 1% by volume of basalt fiber, as the fibers represents 40% of the pellets by volume. The test variables were the longitudinal reinforcement ratio (ρ), which ranged between 0.6 and 1.4%, and the incorporation of an FRCC layer, with different types of fibers (BP and steel fibers) in the tie zone. In all beams, 200- and 150-mm wide plates were used at loading point and supports, respectively.

The designation of the beams consists of two characters. The first character describes the presence of the layer and type of fibers (X for no layer, B for layer with basalt fiber pellets, S for layer with steel fibers, and the second character is a number indicating the flexural reinforcement ratio in percentage. For example, B-1.0 denotes a beam having a layer reinforced with basalt fiber pellets and a longitudinal reinforcement ratio of 1.0%. The details of the beams are listed in Table 7.2 and the reinforcement configurations for all specimens are shown in Figure 7.1.

Table 7.2: Details of test beams

Specimen	Fiber type	Fiber dosage (%)	Reinforcement ratio, ρ (%)	f'_c (MPa)	
				Tie layer	Rest of the beam
X-0.6	N/A	N/A	0.6	N/A	45±0.54
X-1.0	N/A	N/A	1.0	N/A	47±0.63
X-1.4	N/A	N/A	1.4	N/A	46±0.78
B-0.6	Basalt	2.5	0.6	81±1.21	47±0.42
B-1.0	Basalt	2.5	1.0	79±1.12	48±0.55
S-0.6	Steel	1.0	0.6	90±0.98	46±0.37
S-1.0	Steel	1.0	1.0	89±1.06	45±0.89

7.2.2 Materials

Except for the bottom FRCC layer where applicable, normal-weight, normal strength, ready-mix concrete with a target compressive strength (f'_c) of 40 MPa at 28 days and a target slump of 120 mm was used. The actual compressive strength of concrete was determined by testing standard cylinders (100 × 200 mm) on the day of testing according to CSA A23.1-19/A23.2-19 (CSA 2019b) as listed in Table 7.2. For the FRCC layer, the cementitious composite was prepared at the laboratory using general use (GU) cement and a constant dosage of slag as well as Nano-silica (6% by mass of the binder). The water-to-binder ratio (w/b) was kept constant at 0.30. The cementitious composite was reinforced with either BP or steel fibers (Figure 7.2). The BF pellets were made of 16-micron basalt roving encapsulated by polyamide resin, in which the BF represented 60% of the

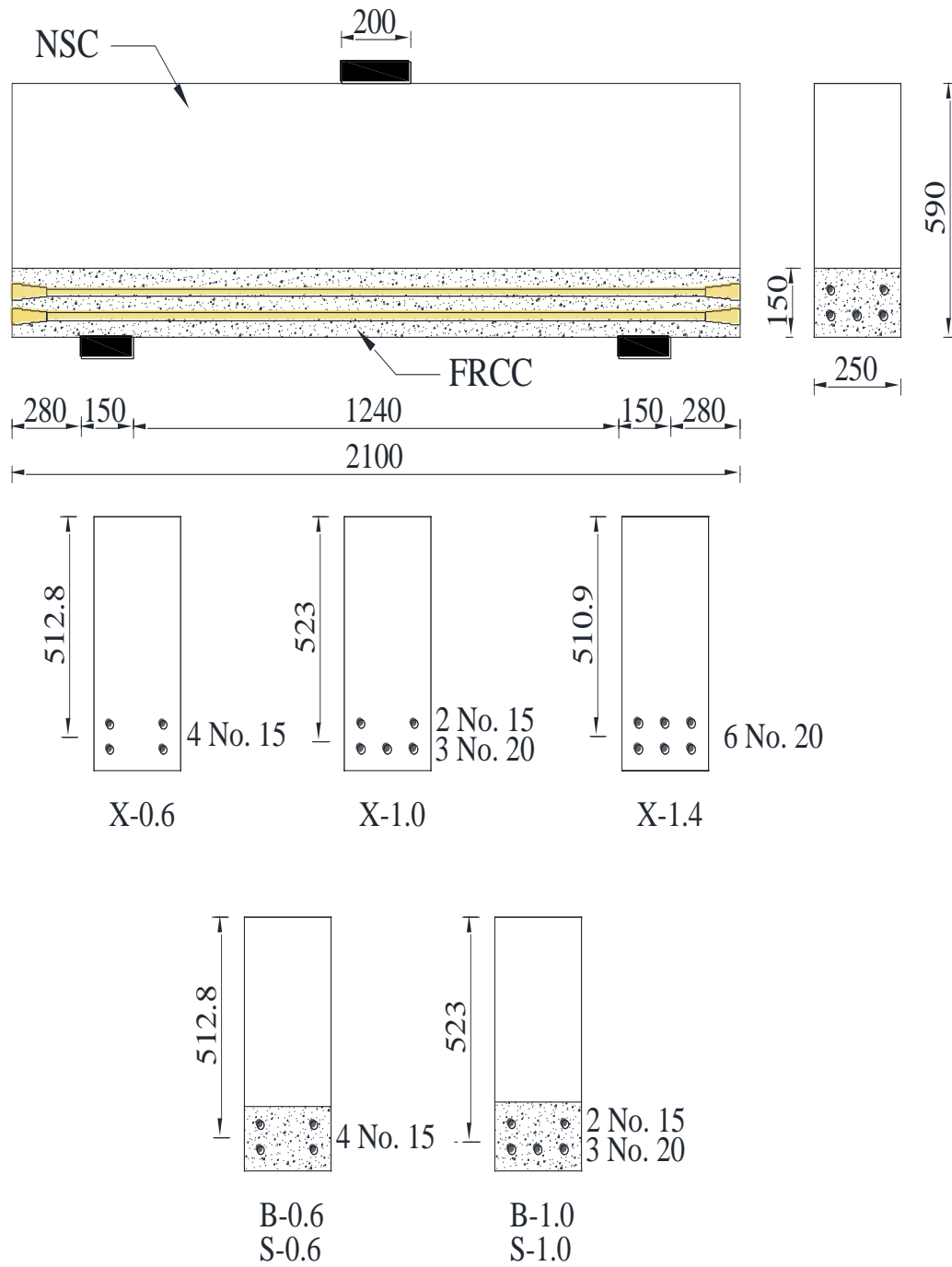


Figure 7.1: Details of specimens (all dimensions in mm)

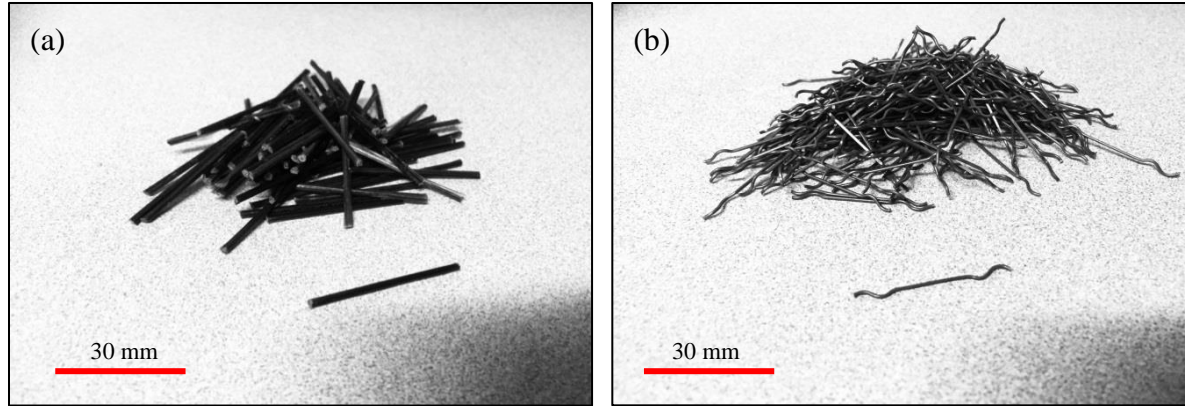


Figure 7.2: Reinforcing fibers: (a) basalt fibers pellets, and (b) steel fibers

pellet by weight. The BP were 36 mm long with a diameter of 1.8 mm. Hooked-end steel fibers with a diameter of 0.5 mm and a length of 30 mm was also used. The properties of the BP and the steel fibers are listed in Table 7.3. Further description of the components and the mixing procedures can be found elsewhere (Mahmoud et al. 2017). In addition, it is worth noting that the FRCC layer on the tie zone was cast first, and then an hour later, the NSC was cast to improve the integrity and bond between the two layers.

Table 7.3: Properties of fibers

Properties	Properties of fibers	
	BP	Hooked steel
Length (mm)	36	30
Diameter/dimensions (mm)	1.80	0.65
Aspect ratio	20	45
Specific gravity	1.74	7.70
Tensile strength (MPa)	2,300	1,200
Elastic modulus (GPa)	65	200

The authors selected 1-hour gap between casting the bottom and top layers based on pilot experimental trials conducted on small-scale specimens prior to casting the test deep beams. Concrete slabs of 300×400 mm surface area and 140 mm thickness were used as concrete substrate; subsequently, the fibrous composites were placed on the top surface with a thickness of 80 mm.

The top layer was cast 1, 2.5, and 4 hrs after casting the base to evaluate how long gap is required between the two pours allowing the assembly to behave as an integral element. After casting, the slabs were demolded and moist cured for 28 days in the curing room, then the slabs were partially cored to determine the pull-off strength according to ASTM C1583 (2020c). The slabs with 1-hr gap yielded the best results. Leaving 2.5 and 4-hrs gap between castings resulted in failure at the interface between the FRCC layer and the substrate concrete (reflecting some level of incompatibility, Figure 7.3. The failure was shifted toward the substrate concrete, when 1-hr gap was left between the two castings; confirming that the assembly behaved as an integral system with a high degree of compatibility. In addition, during the compaction process of the NSC layer in the deep beam specimens, appropriate precautions were taken to ensure that the vibrator tip did not reach the level of the fibrous layer to avoid any adverse effect on the bond between GFRP bars and the FRCC layer.



Figure 7.3: Pull-off test, (a) slab specimens, and (b) mode of failure

Two different diameters (No. 15 and No. 20) of sand-coated GFRP bars with headed ends were used as main longitudinal reinforcement. The mechanical properties of the GFRP bars, listed in Table 7.4, were obtained through standard test carried out according to ASTM D7205-06 (ASTM

2016). The headed ends were made of thermoplastic matrix reinforced with short glass fiber, cast at the end of bars at high temperature. The head is approximately 100 mm in length with a maximum outer diameter of 50 mm at the end as shown in Figure 7.4. Benmokrane et al. (2016)[16] and Mahmoud et al. (2017) reported significant increase in the bond strength between the headed-end bar and concrete. Therefore, in this study, the provided development length was less than that required by design. The required development length for each beam was calculated based on the Canadian standard CSA/S6-19 (CSA 2019a) and it ranged between 430 mm to 610 mm.

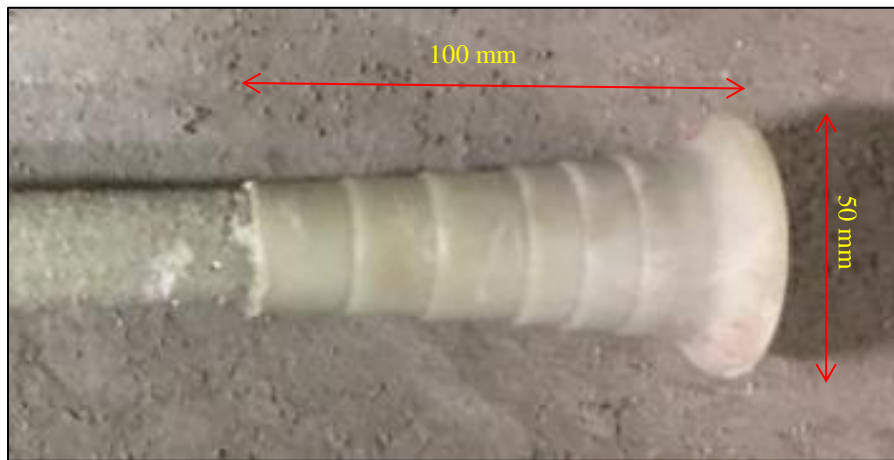


Figure 7.4: Configuration of the head

Table 7.4: GFRP Reinforcement properties

Bar size	Nominal diameter (mm)	Area (mm ²)		Tensile strength (MPa)	Modulus of elasticity (GPa)	Ultimate strain (%)
		Nominal	CSA/S806-12 Annex A			
No. 15	15.9	198	291	1,184	62.6	1.89
No. 20	19.0	285	394	1,105	63.7	1.73

7.2.3 Test setup

Figure 7.5 shows a schematic drawing of the test setup. The beams were supported on a hinged support at one end and a roller support on the other. The beams were tested under three-point bending configuration. The vertical concentrated load was applied through a 5000-kN MTS machine using a load-controlled rate of 10 kN/min.

Both internal and external instrumentation were used to provide a real-time monitoring of the behaviour of the beams during the test (Figure 7.5). All instrumentation was connected to a computerized data acquisition system (DAQ) to record the readings during the test. To measure deflection, linear variable displacement transducers (LVDTs) were installed at three different locations; at mid-span and at the two mid-shear spans. In addition, two high-accuracy LVDTs (± 0.001 mm) were used to monitor the slip at the end of one bottom reinforcing bar to evaluate the anchorage behaviour of the headed-end. Electrical-resistance strain gauges (ESG) were attached to longitudinal reinforcement at critical locations in the vicinity of the loading and supporting points, the mid-span, and the middle of each shear span. Three 200-mm long PI gauges were attached to the concrete surface to measure crack width; two for the diagonal cracks in the shear spans between the loading and the supporting points, and one at the mid-span for the flexural crack.

7.3 Test Results and Discussion

7.3.1 Crack pattern and mode of failure

The cracks pattern was closely monitored and carefully marked on the concrete surface. Figure 7.6 shows the cracks pattern for all specimens at failure. The initial crack was predominantly vertical and formed at the soffit of the beam directly under the loading point and propagated vertically up to approximately 80-90% of the beam depth. With the increasing load, additional flexural cracks were developed close to the first one, and new flexural cracks were formed on the shear span

between the loading point and the support. With further increase of the load, flexural-shear cracks developed in the shear span and propagated towards the loading point, parallel to the compression strut. Within the range of 33-44% of the ultimate load, the main diagonal crack formed, defining the direction and location of the main concrete strut. After a load level

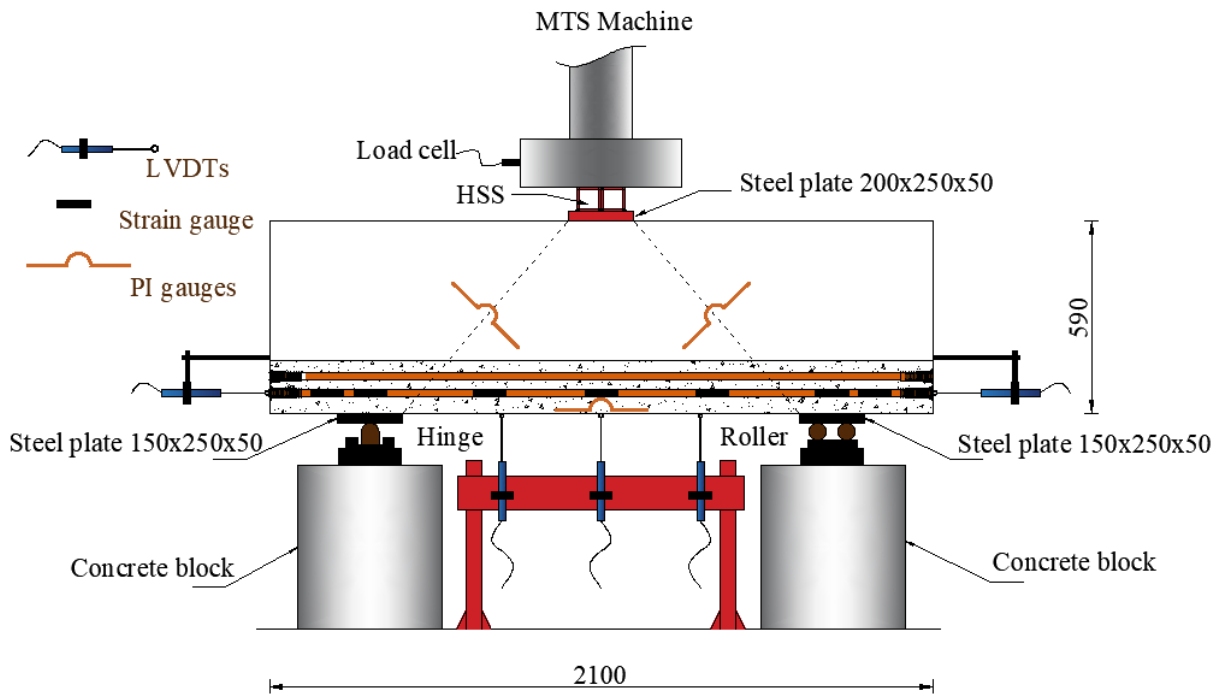


Figure 7.5: Schematic drawing of the test setup (dimensions are in mm)

corresponding to about 70% of ultimate load was attained, no more cracks appeared and only widening of the existing diagonal cracks was observed until the specimens failed.

Beams X-0.6 and X-1.0 experienced brittle failure. This failure was sudden and associated with an abrupt sound of the concrete crushing. On the other hand, Beam X-1.4 experienced a local failure at the loading point. As the failure of this beam was at the node not the strut, it was not expected to gain any additional load by incorporating the FRCC layer in specimens with 1.4% reinforcement ratio. On the other hand, B-0.6, B-1.0, S-0.6, and S-1.0 showed significantly less brittleness with

no loud “bang” at failure, as the FRCC layer (either with steel or basalt pellets) maintained the integrity of the beam.

Four types of failure were observed in this study: strut failure, node failure, shear-compression failure, and diagonal-splitting failure. Failure of strut in the region between loading and supporting plates occurred in X-0.6 and X-1.0. This mode of failure is defined by the crushing of concrete along the crack due to compression stresses in the strut (ASCE-ACI Committee 426 1973, Whight and MacGregor 2009). Beam X-1.4 failed due crushing of concrete at the loading plate (node failure). Shear compression failure occurred in S-0.6 and S-1.0. This failure is defined by crushing of concrete in the flexural compression zone at the tip of the main diagonal crack. The diagonal splitting failure took place in B-0.6 and B-1.0, which is characterized by a critical diagonal crack joining the loading point and the support. Such a splitting shear failure takes place because of the transverse tensile stresses perpendicular to the diagonal strut. El Sayed et al. (2012) reported similar mode of failure for simply supported FRP deep beams with an a/d ratio of 0.92. Figure 7.7 shows the mode of failure for all beams. No sign of end-anchorage failure or slippage of the bottom reinforcement was observed in all beams. The maximum measured slip value was approximately 0.001 mm. This shows that the headed-end bars used in this study with only 280 mm overhang length were effective in anchoring the tie reinforcement in such deep beams.

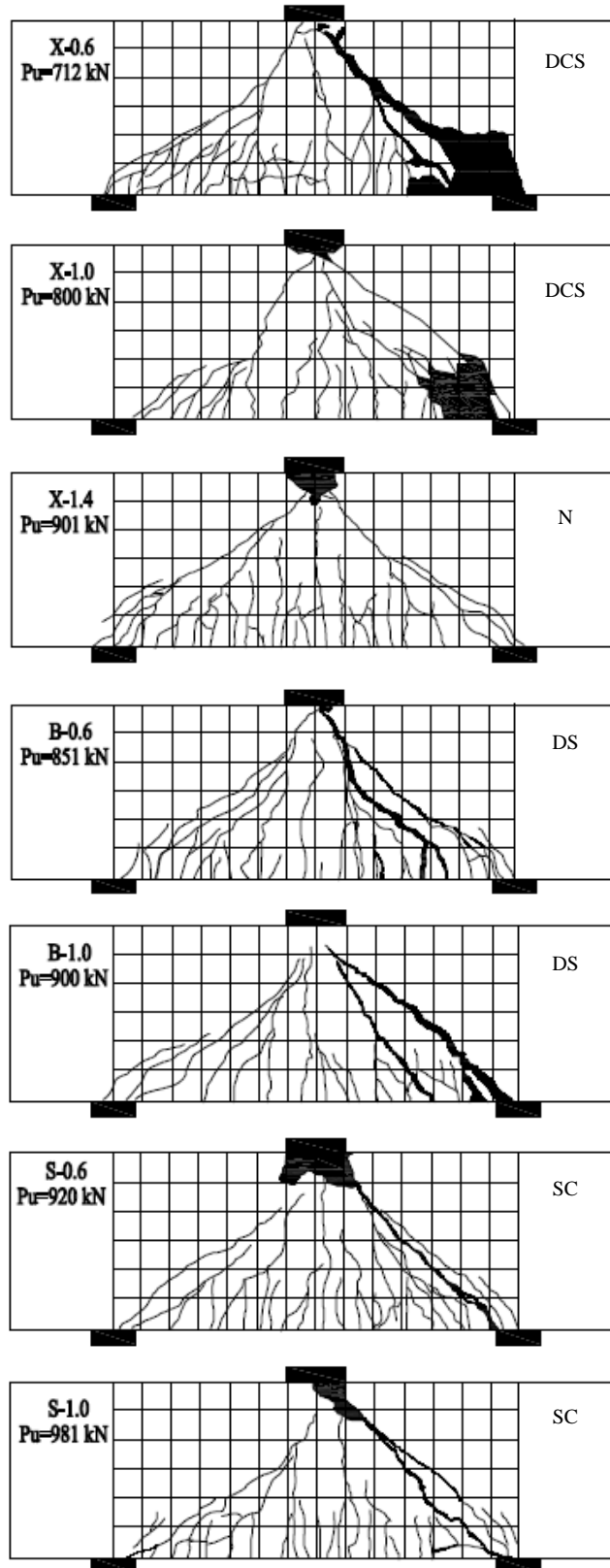
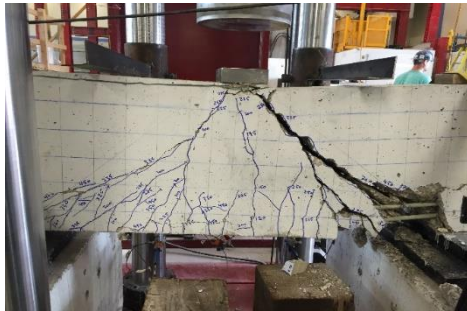


Figure 7.6: Cracking pattern at failure of beams

7.3.2 Cracking load and ultimate capacity

Table 7.5 summarizes the experimental results for test beams at different loading stages. For the control beams X-0.6, X-1.0, and X-1.4, the first flexural crack appeared at a load of 133, 140, and 122 kN, respectively. The experimental cracking loads were comparable to those calculated according to CSA/S6-19 (CSA 2019a), which was 113 kN for an average concrete strength of 46 MPa. On the other hand, the incorporation of the fibrous layer, either BFRCC or SFRCC, delayed the initiation of the first crack. In beams with a reinforcement ratio of 0.6%, the cracking load increased by 59 or 20% when the beam had the SFRCC or BFRCC layer, respectively. Similarly, compared to beam X-1.0, the addition of the BFRCC and SFRCC layer to the beam with same reinforcement ratio (B-1.0 and S-1.0) led to a significant increase in the flexural cracking load by 43 and 47%, respectively. As expected, increasing the reinforcement ratio had no effect on the initial flexural and shear cracking loads. The results showed that all beams had comparable diagonal cracking loads, which agrees with the findings of Farghaly and Benmokrane (2013) and Mohamed et al. (2017). This could be due to that all beams had similar concrete strength at the mid-height of the beam.

On the other hand, the reinforcement ratio had a clear effect on the ultimate capacity of the deep beams. Increasing the reinforcement ratio enhanced the diagonal strut strength, which, in turn, increased the transferred shear forces through the arch action, as shown in Figure 7.8.



X-0.6



X-1.0



X-1.4



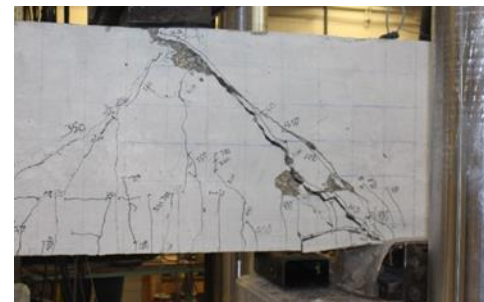
B-0.6



B-1.0



S-0.6



S-1.0

Figure 7.7: Mode of failure of test beams

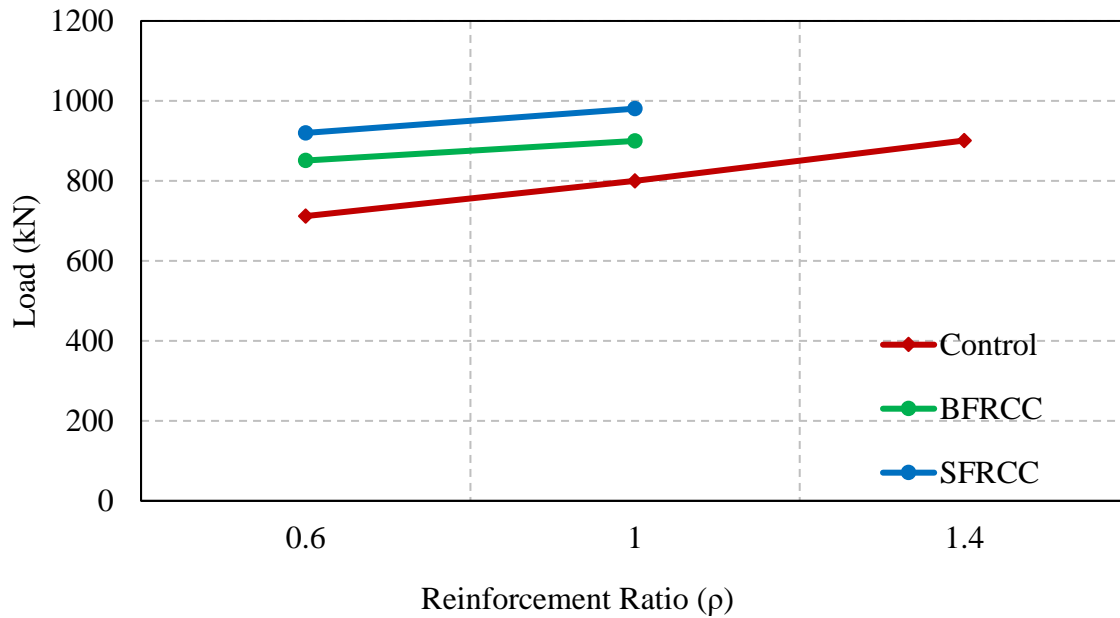


Figure 7.8: Effect of reinforcement ratio on the ultimate load capacity

Increasing the reinforcement ratio by 67%, from 0.6 to 1.0%, showed an improvement in the ultimate capacity of about 12%. Further increasing the reinforcement ratio to 1.4% resulted in 26% increase in the ultimate load. Moreover, the incorporation of fibers in the tie zone, regardless of the type of fibers, had a notable effect on enhancing the ultimate capacity. Compared to control beam X-1.0, the incorporation of BFRCC or SFRCC layers yielded an increase in the ultimate capacity of 12.5 and 23%, respectively. Similarly, in beams with reinforcement ratio of 0.6%, the ultimate capacity increased by 19 and 28% when the BFRCC or SFRCC layer was added to the beam, respectively. In addition, it seems that changing the type of fibers in the FRRC layer had a direct effect on the ultimate capacity. For instance, replacing the BP with steel fibers for the beams sharing the same reinforcement ratio of 1.0% (B-1.0 and S-1.0) led to an increase in the ultimate capacity of approximately 9%. This might be attributed to the small dosage of the BP, in addition to the superior properties of steel fibers with respect to the BP.

7.3.3 Load-deflection response

Figure 7.9 illustrates the load-deflection relationship at mid-span. All specimens exhibited similar overall behaviour before the formation of the flexural cracks where the deflection was of very small values. The behaviour of beams, before the ultimate load, was characterized by a nearly bilinear response. After cracking, a reduction in the flexural stiffness of the specimens was observed but with different tendencies, which is attributed to the different reinforcement ratio of each specimen. As the amount of reinforcement increased, the post-cracking flexural stiffness increased. In addition, the increased stiffness that occurred in control beams during the post-cracking stage could occur in deep beams, where the arching action (or strut-and-tie model) starts to develop with the initiation of diagonal cracks. During that early stage, the beam stiffness decreases due to cracking. However, once the full arching action develops or establishes, the load-transfer mechanism changes, to be mainly through the compression strut, leading to enhanced stiffness.

As expected, no beams without FRCC layer showed any residual strength after the peak load. On the other hand, all FRCC layered deep beams, irrespective of the type of fibers added to the tie zone, exhibited a post-peak behaviour due to bridging mechanism of the BP and the steel fibers. As for the SFRCC layered beams, after reaching the maximum load, the beams did not fail suddenly but it continued to carry gradually decreasing load showing a distinctive deflection softening behaviour. On the other hand, beams with BFRCC layer experienced a significant drop in the load carrying capacity by 63 and 78% for B-0.6 and B-1.0 beams, respectively. This could be attributed to the small dosage of the BP; therefore, a future investigation is recommended to investigate higher dosages of BP.

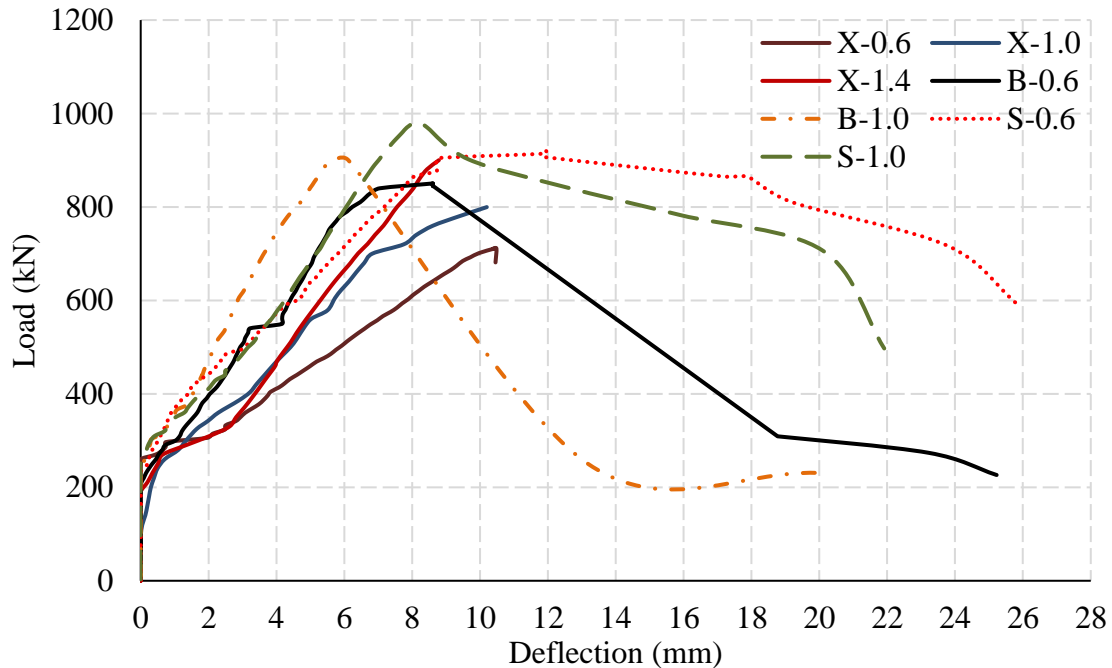


Figure 7.9: Load-deflection relationship for beams

The latter behaviour was substantiated by calculating the flexural toughness, which is commonly defined as the area under the load-deflection curve; referred to as the total energy absorbed by structural elements until failure (Bentur and Mindess 2007). In computing the toughness, it was assumed that the failure point is the point where the applied load dropped to 80% of its ultimate value (Naaman and Jeong 1995; Alsayed and Alhozaimy 1999). Table 7.5 gives the absorbed energy for all beams. It indicates that as the reinforcement ratio increased, the energy absorption capacity decreased because beams with high reinforcement ratio had a stiffer load-deflection response (Figure 7.9). For example, increasing the reinforcement ratio from 0.6 to 1.0 and further to 1.4%, decreased the toughness by 6 and 16%, respectively. Similarly, for BFRCC and SFRCC layered beams, increasing the reinforcement ratio from 0.6 to 1.0%, led to 10 and 35% reduction in the energy absorption capacity, respectively. Generally, the presence of the fibers (BP or SF) had a significant effect on the toughness of deep beams. For instance, adding the BFRCC or

SFRCC layers in the tie zone of specimens with a reinforcement ratio of 0.6% led to 84 and 262% increase in the toughness of specimens, respectively, compared to that of the counterpart control beams made without fibers. Similar trend was observed for the beams with a reinforcement ratio of 1.0, as the incorporation of BP and SF in the tie zone led to 76 and 148% increase in the absorbed energy with respect to the control beam X-1.0.

Table 7.5: Summary of test results

Specimen	$P_{c,exp}$ (kN)	P_{cr} (kN)	P_u (kN)	ϵ_{max} ($\mu\epsilon$)	δ_{max} (mm)	Mode of failure	Toughness/absorbed energy (kN.mm)
X-0.6	133	310	716	11,280	10.5	DCS	4,968
X-1.0	140	340	800	8,410	10.1	DCS	4,679
X-1.4	122	300	900	7,150	8.70	N	4,199
B-0.6	160	320	851	11,230	25.2	DS	9,125
B-1.0	200	310	900	7,940	19.9	DS	8,245
S-0.6	212	350	920	16,100	25.9	SC	17,970
S-1.0	205	320	981	10,300	21.9	SC	11,633

Note: P_c = first flexural-cracking load; P_{cr} = main diagonal cracking load; P_u = ultimate load; ϵ_{max} = reinforcement strain at failure at mid-span; δ_{max} = mid-span deflection at failure; DCS is diagonal concrete strut failure; SC is shear compression failure; DS is diagonal splitting failure; N is node failure.

7.3.4 Crack width

Figure 7.10 shows the monitored flexural and diagonal crack width. The measured flexural crack width at the soffit of the deep beams supported the role of the fibers in enhancing the behaviour of the tested deep beam. It is worth mentioning that the equivalent service load was taken as 50% of the peak load (Andermatt and Lubell 2013). As expected, increasing the reinforcement ratio of the longitudinal bars had a significant effect on controlling the crack width. At service load, the crack width for the control beams X-0.6 and X-1.0 was 1.2 and 0.71 mm, respectively, which

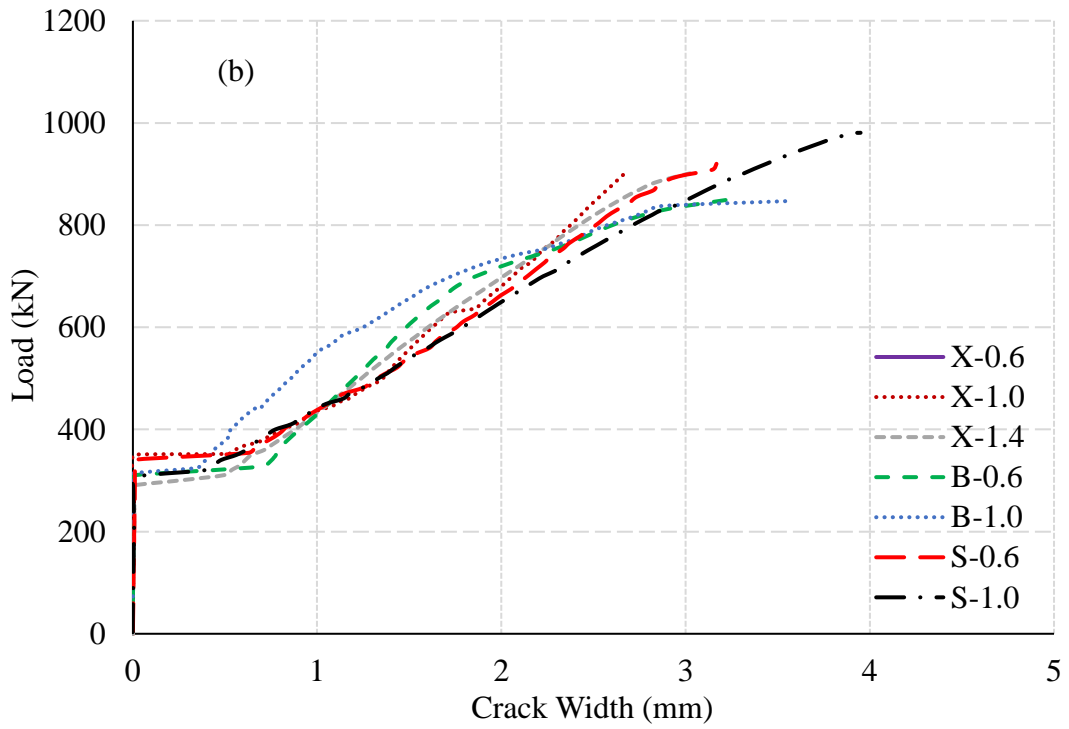
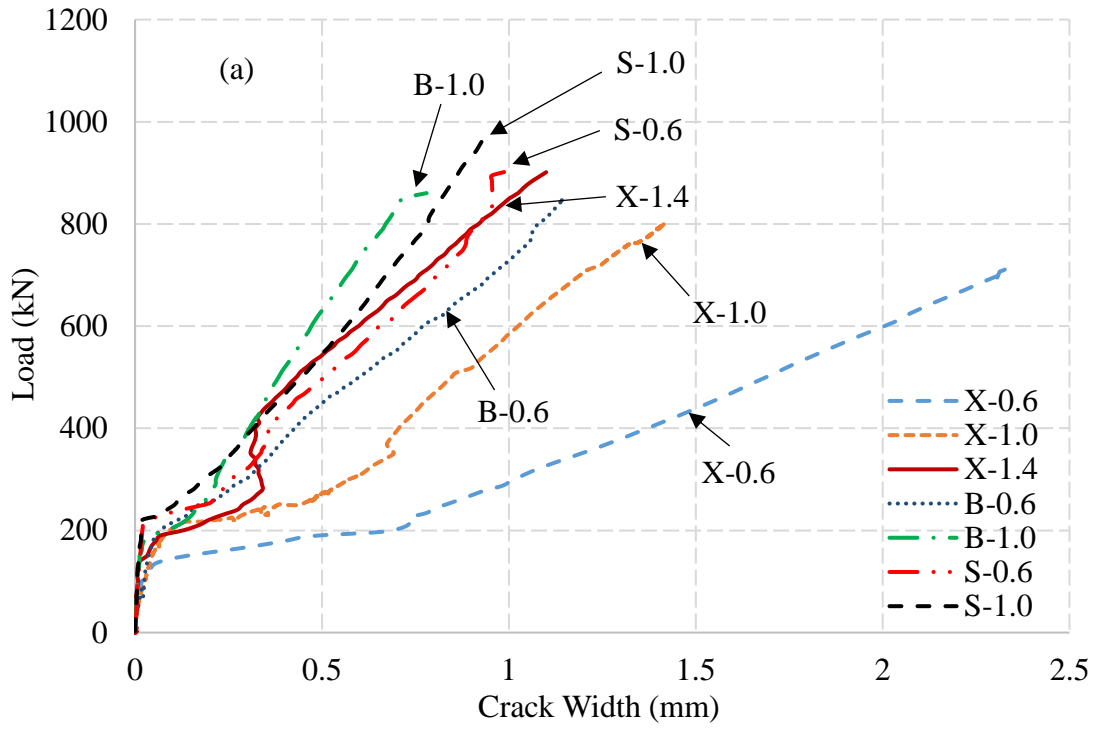


Figure 7.10: Crack width for a) the flexural crack, and b) the diagonal crack

exceeded the maximum crack width of 0.5 mm specified by CSA S6-19 (CSA 2019a). However, for beam X-1.4, this value was 0.38 mm, which is below the crack width limit. In addition, with increasing the reinforcement ratio from 0.6 to 1.0 and further to 1.4%, the crack width significantly decreased by 40 and 53%, respectively, at the failure load level of beam X-0.6.

In general, regardless of the type of fibers, the incorporation of FRCC layer in the tie zone showed smaller crack width compared to their counterparts without FRCC layer. This is mainly attributed to the bridging effect that enabled forces to be redistributed from one zone to the next. At service load level, the inclusion of FRCC showed a crack width of 0.45, 0.33, 0.45, and 0.44 mm, for beams B-0.6, B-1.0, S-0.6, S-1.0 respectively, which satisfied the crack width limit at service. Similarly, at the ultimate load level of beam X-0.6, adding BFRCC and SFRCC layers led to 58 and 76%, reduction in the crack width, respectively. Consistently, the crack width values for the beams containing BFRCC and SFRCC layers (B-1.0 and S-1.0) were 0.67 and 0.78 mm, respectively, at the ultimate load level of beam X-1.0, which had a crack width of 1.4 mm.

On the other hand, Figure 7.10b shows the load versus the diagonal crack width. There is no clear effect of the test parameters on the diagonal crack width as all the beams showed similar crack widths. At the service load level, the diagonal crack width ranged between 0.65 and 0.8 mm. In addition, the crack width ranged between 2.7 and 3.9 mm at the ultimate load. These findings are in a good agreement with the crack width ranges reported by Amdermatt and Lubell (2013) at both stages.

7.3.5 Strain in reinforcement and strain profile

Figure 7.11 shows the load versus measured mid-span strains in reinforcement for the tested beams. The load-strain plots for all beams of this study exhibited similar characteristics. It can be noted that the strains after cracking varied in approximately linear manner with the increased load

up to failure. In addition, the results showed that increasing the reinforcement ratio decreased the strains in the bars measured at the same load level. Similar trend was observed when the FRCC layer was incorporated in the beams irrespective of the type of the fibers. For instance, at the ultimate load level of beam X-0.6, incorporating the BFRCC or SFRCC layers in the beams with reinforcement ratio of 0.6 led to 10 and 19% reduction in the measured strains compared to that of the counterpart control beam without the FRCC layer. Similarly, at the ultimate load level of beam X-1.0, the strains reduced by 22 and 3% when the beam had a layer of BFRCC or SFRCC, respectively. In addition, the shear stress required to cause failure increased as tensile strain in the longitudinal reinforcement decreased, which is known as transverse strain effect. This was illustrated by the modified compression field theory (Vecchio and Collins 1986), for members with longitudinal reinforcement only. The theory predicts that failure occurs when the shear stress at the crack faces, required for equilibrium, reaches the maximum shear stress that can be transmitted by aggregate interlock. The predicted failure shear stress decreases as the predicted width of the inclined crack increases. In addition, the incorporation of FRCC layer enhanced the bond within the anchorage zones, where high tensile stresses developed.

The maximum measured tensile strains in the FRP bars at failure ranged between 60, 48 and 41% of the ultimate strain of the FRP bars for beams with reinforcement ratio of 0.6, 1.0 and 1.4%, respectively. In addition, the strain at ultimate load in B-0.6 and S-0.6 was 11,230 and 16,100 $\mu\epsilon$, while it was 7,940 and 10,300 $\mu\epsilon$ in B-1.0 and S-1.0, respectively. Table 7.5 lists the measured tensile strains in the reinforcement at failure for each beam.

The nearly uniform distribution of strains along the main tensile reinforcement between the two supports indicates the formation of the tied arch action. This agrees with the findings of El-Sayed et al. (2012), Mohamed et al. (2017) and Mohamed et al. (2020). The development of the arching

behaviour in the beams was verified by measuring the strains along the bottom layer of the longitudinal reinforcement at five points along the span. Figures 7.12 and 7.13 shows the typical strain profiles at various stages of loading for all specimens. It can be noticed that the strains were distributed in a manner similar to the bending moment prior to the formation of the inclined cracks. Strains along the longitudinal reinforcement were similar after the formation of the diagonal shear crack with uniform increase in the strains.

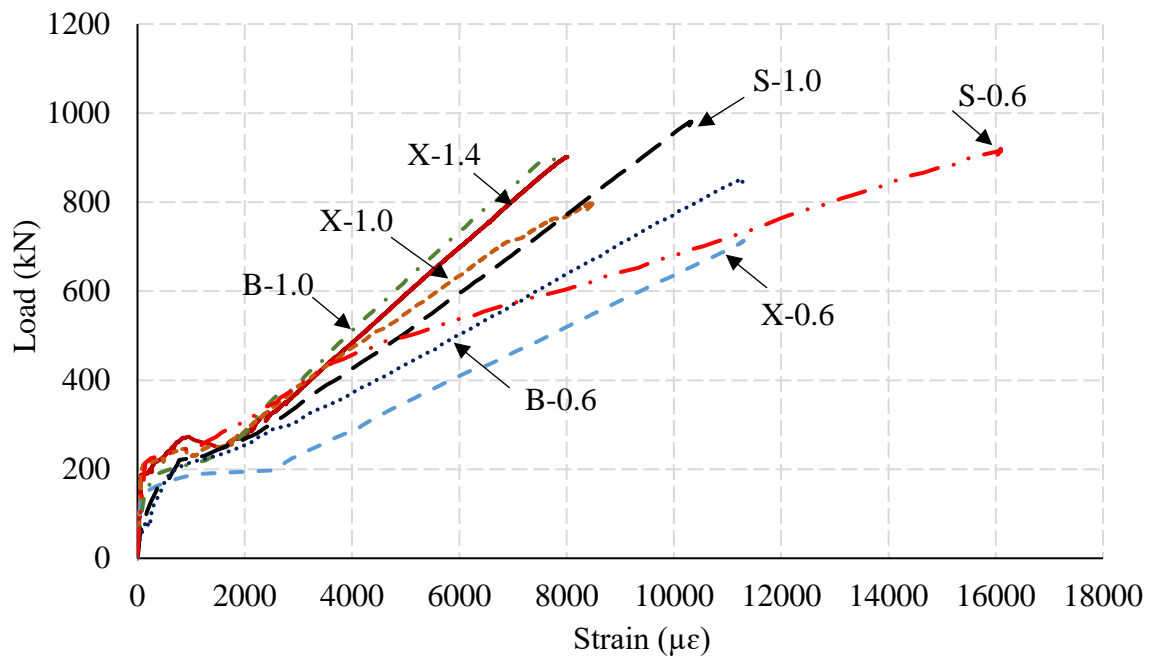


Figure 7.11: Strains at mid-span section in tested deep beams

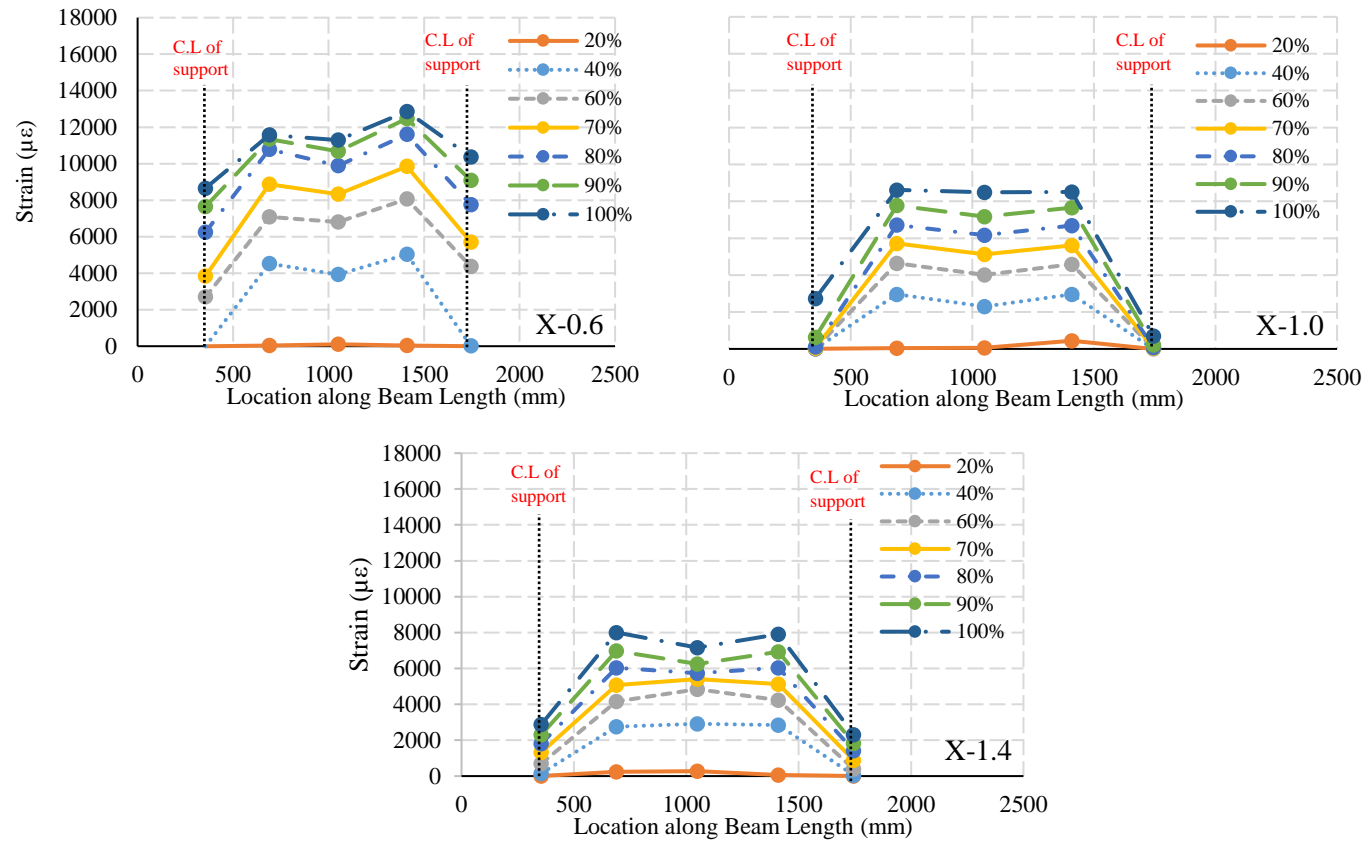


Figure 7.12: Strain profile in deep beams without FRRC layer

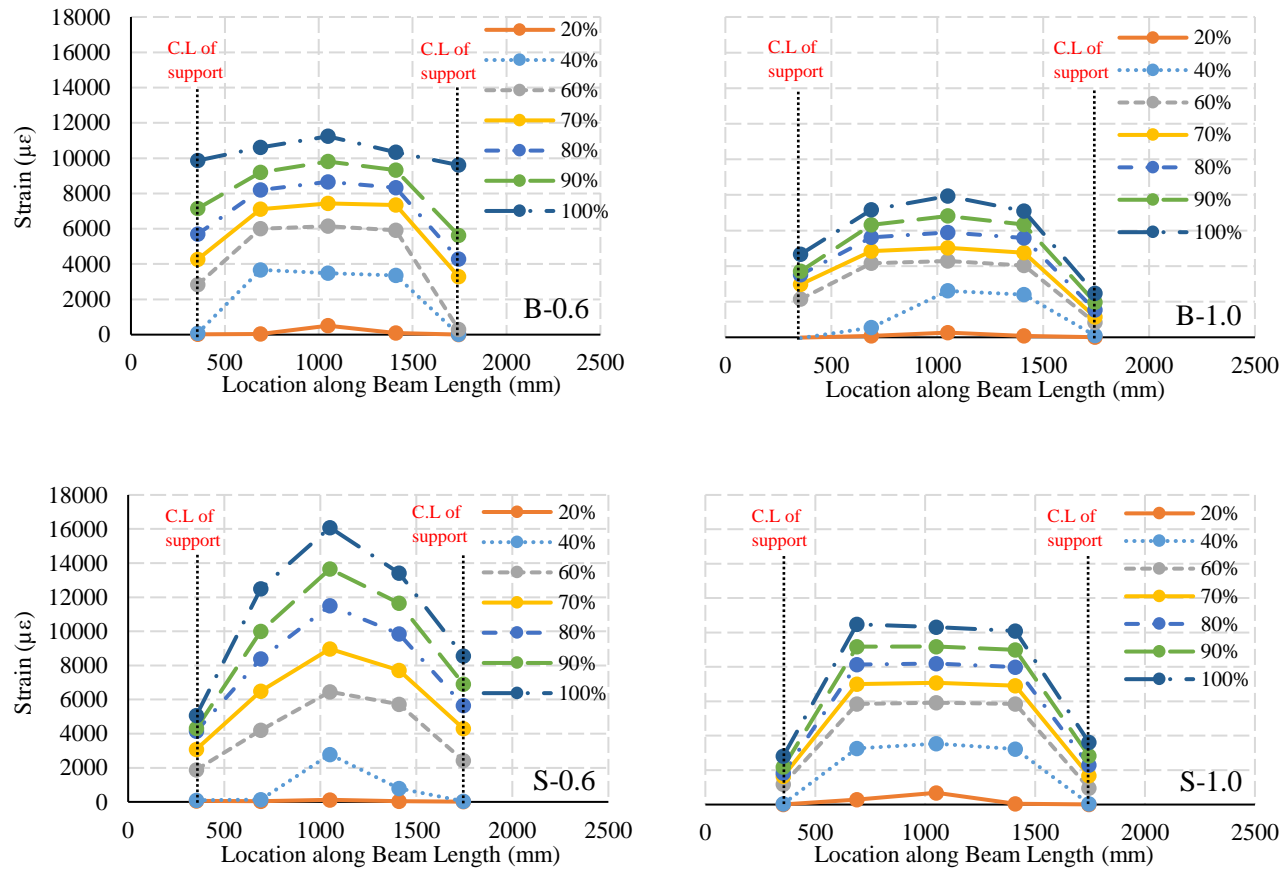


Figure 7.13: Strain profile in deep beams with FRRC layer

7.3.6 Comparison between experimental and code predicted load

The load capacity of the tested deep beams was calculated using the STM provisions in the CSA/S6-19 (CSA 2019a), ACI 318-14 (ACI 2014) and the recent version of ACI 318-19 (ACI 2019). The strength reduction factors, and the material resistance factors, ϕ , in the code equations were set to unity. A single-panel STM was used to analyze the test specimens as illustrated in Figure 7.14. For the ACI 318-19, the strut coefficient was taken as 0.4, while the strut confinement modification factor was set to unity (Tuchscherer et al. 2010). It should be noted that the design provisions of the ACI 318 code relate the capacity of the strut to the concrete compressive strength and strut geometry, while the capacity of the strut in the CSA/S6-19 depends on concrete compressive strength and the strains developed in the tie and consequently the tie material.

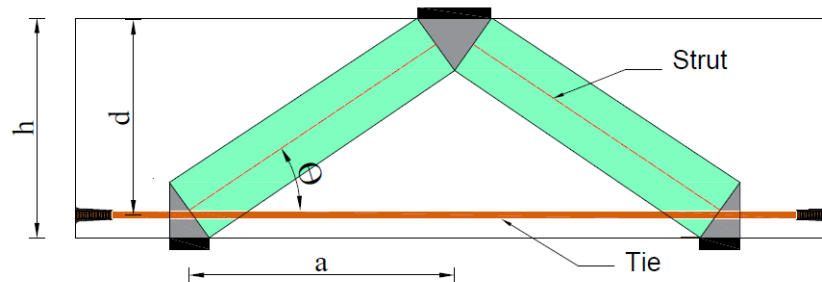


Figure 7.14: Strut-and-tie model (STM) for simply supported deep beams

Table 7.6 shows comparisons between the experimental load capacity and the code predicted capacity of the test beams. The STM based on CSA/S6-19 (CSA 2019a) yielded reasonable prediction of the ultimate loads compared to the experimental results with an average value of P_{pre}/P_{exp} of 1.33 and a coefficient of variation (CoV) of 13%, yet these predictions seem to be consistent for beams with different reinforcement ratios. On the other hand, the ACI 318-14 (ACI 2014) overestimated the experimental loads with a mean value of P_{pre}/P_{exp} of 0.61 and CoV of 5%.

The latest version of the ACI code (ACI 2019) that included a modification to the strut coefficients yielded better prediction with a mean value of P_{pre}/P_{exp} of 1.06 and a CoV of 12%.

Table 7.6: Comparison between the experimental and predicted failure loads

Beam	P_{exp} (kN)	Strut-and-tie model					
		CSA/S6-19		ACI 318-14		ACI 318-19	
		P_{CSA} (kN)	$P_{exp/CSA}$	P_{ACI} (kN)	$P_{exp/ACI}$	P_{ACI} (kN)	$P_{exp/ACI}$
X-0.6	716	571	1.25	1,229	0.58	819	0.87
X-1.0	800	683	1.17	1,198	0.67	799	1.00
X-1.4	900	807	0.12	1,270	0.71	846	1.06
B-0.6	851	585	1.45	1,283	0.66	855	1.00
B-1.0	900	693	1.30	1,224	0.74	816	1.10
S-0.6	920	581	1.58	1,256	0.73	837	1.10
S-1.0	981	665	1.47	1,147	0.86	765	1.28
Mean			1.33		0.71		1.06
*CoV			0.13		0.12		0.12

*CoV = coefficient of variation

7.4 Conclusions

The main objective of the current study was to investigate the behavior of GFRP-RC deep beams, emphasizing the effect of adding a layer of FRCC in the tie zone of such structural element. Seven large-scale GFRP-RC deep beam with a/d ratio equal to 1.18 and with different reinforcement ratio were tested to failure. Based on the test results, the main findings of this study can be summarized as follow:

1. The development of the arching action in the tested FRP-RC deep beams was substantiated by the essentially uniform strain distribution in the bottom reinforcement. After the formation of the main diagonal crack, significant reserve capacity was available, indicating the formation of an arch action mechanism.
2. Unlike control specimens, beams with an FRCC layer exhibited a deflection softening behavior, which was characterized by a gradual decrease in the load carrying capacity up to

failure. In addition, the failure of FRP-RC deep beams with an FRCC layer in the tie zone changed from brittle and sudden to a more ductile failure, particularly for those reinforced with steel fibers.

3. The reinforcement ratio had no effect on the cracking load, either for initial flexural or shear cracks; however, it clearly affected the ultimate load capacity of the deep beam. The presence of FRCC in the tie zone had a notable effect on the cracking load and ultimate capacity.
4. The ACI 318-14 (ACI 2014) STM yielded unconservative predictions of the ultimate capacity of deep beams (strut failure), since this strut capacity is based only on the concrete compressive strength without considering the effect of the longitudinal reinforcement. However, the ACI 318-19 gave better predictions with an average experimental-to-predicted load of 1.06. On the other hand, the STM provision in the CSA/S6-19 (CSA 2019a) yielded reasonable prediction of the ultimate capacity for the tested deep beams with an average experimental-to-predicted load capacity of 1.33.

CHAPTER 8: DUCTILITY AND PERFORMANCE ASSESSMENT OF GFRP-RC DEEP BEAMS INCORPORATING BFRCC

Authors and Affiliation:

- Ahmed G. Bediwy, PhD Candidate, Department of Civil Engineering, University of Manitoba
- Ehab F. El-Salakawy, Professor, Department of Civil Engineering, University of Manitoba

Journal and Status:

American Concrete Institute (ACI) Structural Journal, in press, accepted on December 04, 2020.

Reference:

Bediwy, A., and El-Salakawy, E. “Ductility and Performance Assessment of GFRP-RC deep beams incorporating BFRCC.” *ACI Structural Journal*, in press.

Note:

The manuscript had been slightly altered from the original paper by renumbering the tables and figures to include the chapter number. In addition, the reference list and list of notations have been moved to the appropriate sections in the thesis as indicated in the table of contents.

Abstract

The purpose of this study is to assess the feasibility of using a non-metallic basalt fiber (BF) pellets to enhance the ductility of glass fiber-reinforced polymer (GFRP)-reinforced concrete deep beams. In addition, the ability of BP to supplant conventional web reinforcement was evaluated. To achieve the goals of this study, seven large-scale concrete deep beams reinforced with GFRP headed-end bars were constructed and tested to failure under three-point loading over a span of 1,390 mm. The beams had a rectangular section of 250 by 590 mm with overall length of 2,100 mm. Experimental variables included the volumetric percentage of BP and transverse web reinforcement. The addition of fibers improved the post-peak behaviour by increasing the ductility index by more than 50%, when compared to the counterpart control beam. The results provide support for replacing conventional web reinforcement in deep beams with a layer containing BP in the tie zone.

Keywords: glass fiber reinforced polymer; deep Beams; basalt fiber pellets; ductility.

8.1 Introduction

The shear strength of reinforced concrete (RC) beams is affected significantly by the shear span-to-depth ratio, a/d . Based on this ratio, the RC beams are generally divided into two categories with different shear behaviour and strength: slender and deep. The particular interest of this study is the shear behaviour of deep beams. An RC deep beam is a structural member with an a/d ratio less than 2.0 such that the behaviour is shear dominated, as stipulated in the ACI 318-19 (ACI 2019) and CSA/A23.3-19 (CSA 2019c) codes. Deep beams are dominated by a disturbed region (D-region) where the conventional elastic beam theory is not applicable to predict its behaviour due to the non-linear strain distribution across the deep beam section (Joint ACI-ASCE Committee 445 1998; Wight and MacGregor 2009). Accordingly, codes allow using the strut-and-tie model (STM) to assess the shear strength of deep beams. An STM idealizes the complex flow of stresses in a structural member by aligning uniaxial truss elements. The applied load is transmitted directly to the support by in-plane compression through an inclined concrete strut and constant tension in the reinforcement. The point of intersection of struts, ties, or a combination of both forms a node. Struts, ties, and nodes are the three elements that shape an STM and they must be proportioned to resist the applied forces.

Reinforced concrete deep beams have a wide range of applications in structural engineering, such as pile caps, foundation, offshore structures, and transfer girders, which might be exposed to extreme weather conditions and the application of deicing salts. Therefore, the use of concrete structures reinforced with glass fiber-reinforced polymer (GFRP) has gained significant acceptance in the construction field to overcome the problems caused by corrosion of steel reinforcement. The non-corrodible nature of GFRP bars along with their high tensile strength, light weight and ease of installation made it a realistic and cost-effective reinforcing alternative to steel

especially for concrete structures under aggressive environment. However, GFRP reinforcement has relatively low elastic modulus and linear-elastic stress-strain relationship, which cause FRP-RC flexural members exhibit less ductility (Naaman and Jeong 1995; Jaeger et al. 1995). In addition, those members designed based on STM generally have limited post-peak ductility (Brena and Morrison 2007; Kuchma et al. 2008; Moradi and Esfahani 2017).

The brittle behaviour of structural members reinforced with GFRP bars is a prominent concern for many researchers (Naaman and Jeong 1995; Jager et al. 1997; Harris et al. 1998; Wang and Belarbi 2011). To benefit from the little nonlinearity of concrete, GFRP-RC structures are often over-reinforced in such a way that concrete crushing governs the failure mode (ACI 2015). Thus, many investigations have been performed to enhance the ductility of GFRP-RC members through improving the compressive strain properties of concrete (Alsayed and Alhozaimy 1999; Wang and Belarbi 2011; El Refai et al. 2015; Abed and Alhafiz 2019). One of the promising solutions to enhance the deformability of such members is incorporating randomly disturbed discrete fibers into the concrete mix (Wang and Belarbi 2011; Issa et al. 2011; Sahoo et al. 2012; Balgude 2014). Fiber-reinforced cementitious composite (FRCC) is widely adopted in civil engineering construction, such as bridge deck slabs, industrial floors and precast concrete products (Sorelli et al. 2006). Incorporating discrete fibers into any cementitious composite is capable of reducing bleeding, controlling shrinkage cracking, and improving impact resistance. Furthermore, the most pronounced advantages of using fibers in cementitious composites are increasing their energy absorbing capacity (toughness), deformation capability, and load-carrying capacity after cracking (Bentur and Mindess 2007). Various commercially available fibers can be used to produce FRCC, such as steel, synthetic, organic and inorganic fibers. In this context, steel fiber reinforced concrete (SFRC) has gained increased popularity in construction industries in recent years, as these fibers

had the capability to reduce the crack propagation in the concrete members due to fiber bridging action. However, the long-term performance of FRCC could be jeopardized with the presence of steel fibers (SF), as they are vulnerable to corrosion resulting in irregular and rough surfaces reducing the quality and functionality of structures, e.g. slab-on-ground, and bridge decks. Thus, a relatively new type of fibers manufactured from basalt rocks is progressively immersing in civil engineering research, including a newly-developed type of basalt fiber pellets (BP), which is made of basalt fibers with a polyamide or other resin protective coating. The production process of basalt fibers is more environment friendly, and it is cheaper with respect to the other types of fibers such as glass fibers. In addition to their high tensile strength, basalt fibers, unlike steel fibers, do not corrode, which makes them perfectly appropriate for reinforcing concrete structures in harsh environments (Iyer et al. 2015; Arslan 2016; Ayub et al. 2016; Ghazy et al. 2016; Mahmoud et al. 2017).

Shear reinforcement restrains the growth of inclined cracks, which improves the ductility of the RC member and provides a warning of failure; however, reducing the amount of required shear reinforcement can reduce the congestion of reinforcing bars and the construction cost. Therefore, the ACI 318-19 (ACI 2019) recommends the use of deformed SF as a partial replacement to the shear reinforcement for the fiber amount greater than 59 kg/m^3 or 0.75% of the volume. In addition, one of the main modes of failure in deep beams is end anchorage failure, which is attributed to the high tensile stresses that develop in the longitudinal reinforcement (tie) after the formation of the STM. This requires a longer development length or a mechanical anchorage at beam ends. This would be satisfied by anchoring the reinforcement using hooks or headed-end bars and/or adding fibers at this location (the tie zone). The headed-end improves the mechanical interlock to the bar surface, which results in the development of higher tensile strength compared to straight end bars.

Moreover, headed-end GFRP bars showed higher pull-out capacity compared to straight counterpart bars in specimens made of different concrete types (Benmokrane et al. 2016; Mahmoud et al. 2017).

In the past years, several experimental studies have been carried out to investigate the shear behaviour of SFRC beams reinforced longitudinally with conventional steel reinforcement (Mansur and Ong 1991; Madan et al. 2007; Sahoo et al. 2012; Tuchscherer and Quesada 2015; Moradi and Esfahani 2017). In these studies, the incorporation of SF in such members showed a significant improvement of the load carrying capacity and the ductility of the beams. On the other hand, to the authors' knowledge, there is a dearth of research data on the shear behaviour of deep beams reinforced with FRP bars and discontinuous non-metallic fibers such as BP. This paper is a part of an ongoing research program at the University of Manitoba to investigate the behaviour of cementitious composites reinforced with BP (BFRCC). The first phase of this program included bending tests on small prisms and compressive tests on concrete cylinders (Mahmoud et al. 2017). Compared to plain cementitious composites, these tests showed superior load carrying capacity exhibiting a deflection hardening process, as it behaved similar to cementitious composites reinforced with ductile fibers (e.g., SF). Thus, it has promising potential for structural application. This study, which is part of phase two of the program, investigates the effect of the addition of BP to the cementitious composites on the shear behaviour of deep beams reinforced longitudinally with GFRP headed-end bars. In this context, the authors believe that the use of BFRCC can be effective and more economical in practice, if it is particularly incorporated as a layer in the tie zone. Discussions regarding the ductility evaluation for the GFRP-RC members and the ability of BP to supplant shear reinforcement are also provided.

8.2 Research Significance

Due to their geometrical dimensions, deep beams usually fail in shear, which is relatively brittle and can occur without warning. Past experimental investigations have highlighted that the incorporation of SF into concrete matrix significantly enhance the shear strength, ductility and energy absorbing capacity of SFRC deep beams. However, SF are vulnerable to corrosion in aggressive environments, and it was arbitrary established that if low modulus fibers are used in the concrete matrix, a sudden drop in the post-peak strength of the FRC members is expected. Therefore, this research program is designed to assess the effectiveness of using BP in improving the ductility and post-peak behaviour of concrete deep beams reinforced with GFRP bars.

8.3 Experimental Procedure

8.3.1 Test specimens

Seven simply supported RC deep beams were constructed and tested to failure under gravity loads. The test specimens were modeled assuming a prototype structure that consisted of a typical bridge in the City of Winnipeg, MB, Canada. The design was conducted using the strut-and-tie model in which a single strut is assumed between the loading point and the support. With this configuration, the design was carried out according to Chapter 16 of the Canadian Highway Bridge Design Code, CSA S6-19 (CSA 2019a) and the CSA/S806-12 (CSA 2017) for FRP-RC structures, where applicable. The resulting deep beam was 4,200-mm long and have a cross-section of 1,200-mm high by 500-mm wide with a bottom longitudinal reinforcement ratio of 1.0%. However, the test beam in this study represented a half-scale model of the prototype beam. Therefore, all test specimens had a 250-mm wide by 590-mm high rectangular cross section with a total length of 2,100 mm.

The beams had a shear span-to-depth ratio (a/d) of 1.18. In all beams, the reinforcement consisted of GFRP headed-end bars with an anchorage length overhang of 280 mm while the reinforcement ratio was kept constant at 1.0%.

Two control beams without discrete fibers were constructed; one with minimum and one without web reinforcement. The minimum web reinforcement was chosen to satisfy the crack control reinforcement specified in CSA/S806-12 (CSA 2017). Accordingly, 2-branch, No.13 GFRP stirrups spaced at 200 mm were used. The BP or SF were incorporated as a FRCC layer with different dosages in four specimens. In addition, one specimen was entirely cast with the BFRCC. In all beams, 200 and 150-mm wide plates were used at loading point and supports, respectively. The designation of the beams consists of three characters. The first character is referring to the FRCC layer; X for beams with normal concrete (no fibers), L for beams with a fibrous layer in the tie zone, and A for the beam with FRCC over the whole depth. The second character describes the type of fibers; X for no fibers, B for BP, and S for SF, while the third character indicates the dosage of fibers in percentage. It is worth noting that the specimen with web reinforcement had an extra character (W). For example, L-B-2.5 denotes a beam with BFRCC layer in the tie zone and with a BP dosage of 2.5%. The beams were divided into two series. Series I, which includes X-X-0, L-B-2.5, L-B-4.5, L-B-6.9, L-S-1.0, to study the effect of incorporating a layer of BP in the tie zone, and Series II, which includes X-X-0, X-X-0-W, L-B-4.5, A-B-4.5, to investigate the effect of replacing the web reinforcement with FRCC material. The details of the beams are listed in Table 8.1 and the reinforcement configuration for all specimens is shown in Figure 8.1.

Table 8.1: Details of test beams

Series	Specimen	Fiber type	Discrete fiber dosage (%)	Web reinforcement		f'_c (MPa)	
				ρ_v (%)	s (mm)	Bottom layer	Top layer
Series I	X-X-0*	N/A	N/A	N/A-	N/A	47±0.63	47±0.63
	L-B-2.5	Basalt	2.5	N/A	N/A	79±1.12	48±0.55
	L-B-4.5*	Basalt	4.5	N/A	N/A	70±1.42	46±0.21
	L-B-6.9	Basalt	6.9	N/A	N/A	65±0.82	46±0.36
	L-S-1.0	Steel	1.0	N/A	N/A	89±1.06	45±0.89
Series II	X-X-0*	N/A	N/A	N/A-	N/A	47±0.63	47±0.63
	X-X-0-W	N/A	N/A	0.52	200	48±0.56	48±0.56
	L-B-4.5*	Basalt	4.5	N/A	N/A	70±1.42	46±0.21
	A-B-4.5	Steel	4.5	N/A	N/A	71±0.86	71±0.86

*Beams X-X-0 and L-B-4.5 are common between the two series.

ρ_v is the ratio of vertical reinforcement-to-effective area ($A/b s$)

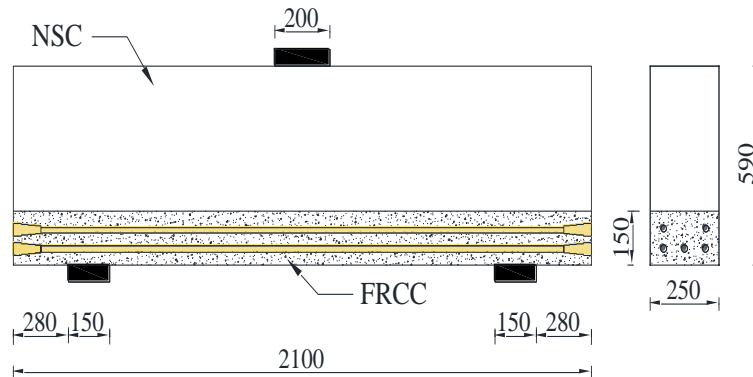


Figure 8.1: Details of specimens (all dimensions in mm)

7.3.2 Materials

For the control beams, a ready-mix, normal-weight, normal strength concrete (NSC) with a target 28-day compressive strength (f'_c) of 40 MPa and a target slump of 120 mm that was measured according to ASTM C143 (2020) was used. However, the actual compressive strength of concrete was assessed by testing standard cylinders (100 × 200 mm) on the day of testing according to CSA A23.1-19/A23.2-19 (CSA 2019b).

As for the beams cast with FRCC either as a layer or over the whole depth, the cementitious composite was prepared with general use (GU) Portland cement as specified by ASTM C1157 (2020), and a constant dosage of slag (280 kg/m^3), representing 40% replacement by mass of the binder (700 kg/m^3 comprising GU cement and slag). In addition, the nano-silica was added at a dosage of 6% by mass of the binder. Fine sand, having a specific properties of fineness modulus of 2.9 and a gradation less than $600 \mu\text{m}$, according to ASTM C136 (2019a), was adopted to cast the composites. The absorption and specific gravity of the sand were 1.5% and 26, respectively, according to ASTM C128 (2015). The water-to-binder ratio (w/b) was kept constant at 0.30. A high-range water-reducing admixture (HRWRA) complying with ASTM C494 Type F (2019b) was added to maintain a target flow of $150 \pm 15 \text{ mm}$, which was measured using a truncated cone and flow table method according to ASTM C230 (2014) and ASTM C1437 (2020b). The cementitious composite was reinforced with either BP or SF (Figure 8.2). The BP were made of 16-micron basalt roving coated with polyamide resin. The BP were 36-mm long with a diameter of 1.8 mm. Hooked-end SF of diameter 0.5 mm and 30-mm length was also used. The properties of the BP and the SF are listed in Table 8.2. The BP were added to the mixtures at different dosages of 2.5%, 4.5 % and 6.9 % by volume, corresponding to 1.0%, 1.85% and 2.75%, respectively, as the fibers itself represents 40% of the pellets by volume, whereas in the case of SF, it was 1%. Two rational approaches were adopted to select the range of dosages of BP, when compared to SF: using either the same volume or the same stiffness (multiply the fiber volume by the modular ratio defined as the ratio of modulus of elasticity of SF to that of BP) constant. Further description of the components and the mixing procedures can be found elsewhere (Mahmoud et al. 2017). In addition, it is worth noting that the FRCC layer on the tie zone was cast first, and then an hour later, the NSC was cast to improve the integrity and bond between the two layers.

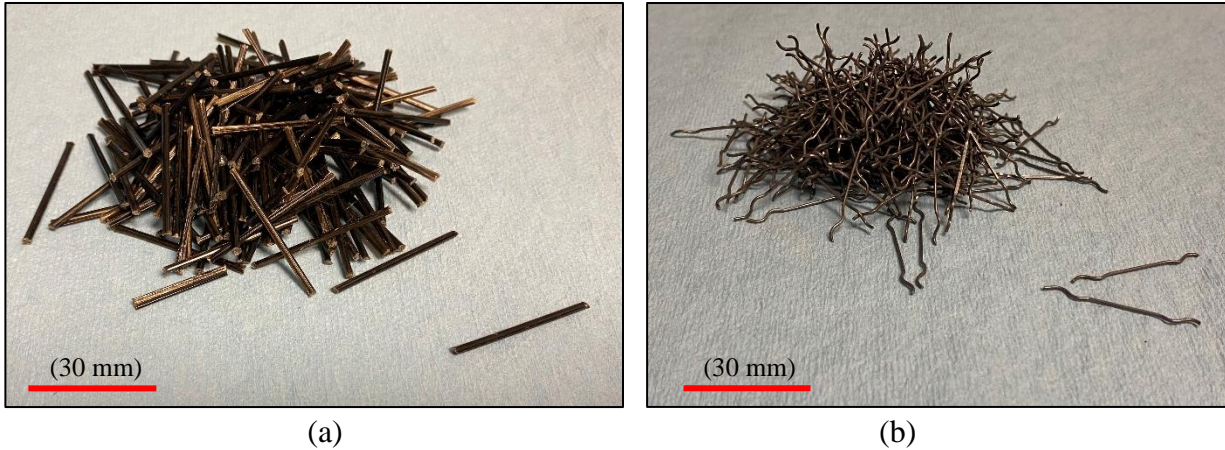


Figure 8.2: Reinforcing fibers, (a) basalt fiber pellets, and (b) steel fibers

Table 8.2: Properties of fibers

Properties	Properties of fibers	
	BP	Hooked steel
Length (mm)	36	30
Diameter/dimensions (mm)	1.80	0.65
Aspect ratio	20	45
Specific gravity	1.74	7.70
Tensile strength (MPa)	2,300	1,200
Elastic modulus (GPa)	65	200

Size No. 15 and No. 20 Sand-coated, headed-end GFRP bars were used as main longitudinal reinforcement. The headed-ends were made of thermoplastic matrix reinforced with short glass fiber, cast at the end of bars at high temperature. Irrespective of the bar size, the head was approximately 100 mm in length with a maximum outer diameter of 50 mm at the end as shown in Figure 8.3. The mechanical properties of the GFRP bars were obtained through standard tests carried out according to CSA/S806-12 (CSA 2017), as listed in Table 8.3. In this study, the provided development length was less than that required by design. The required development length for each beam was calculated based on the Canadian standard CSA/S806-12 (CSA 2017) and it ranged between 430 mm to 610 mm.

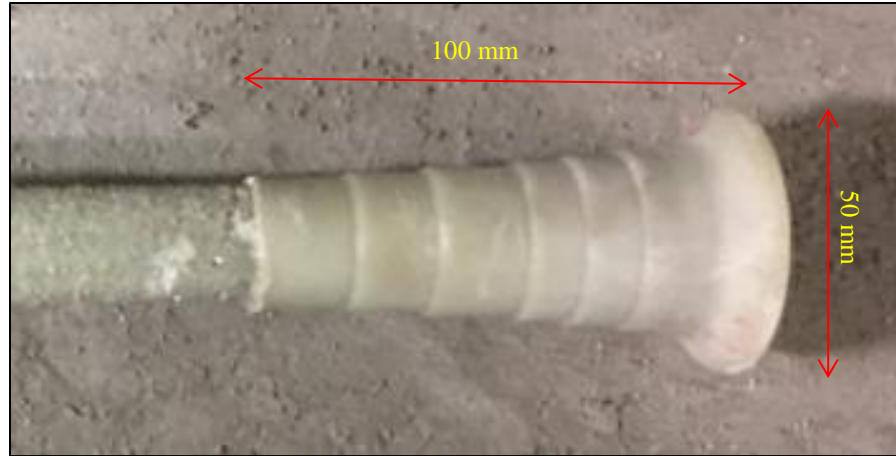


Figure 8.3: Configuration of the head of GFRP bar

Table 8.3: GFRP reinforcement properties

Bar size	Nominal diameter (mm)	Area (mm ²)		Tensile strength (MPa)	Modulus of elasticity (GPa)	Ultimate strain (%)
		Nominal	CSA/S806-12 Annex A			
No. 15	15.9	198	291	1,184	62.6	1.89
No. 20	19.0	285	394	1,105	63.7	1.73

7.3.3 Test setup

Specimens were tested in a 5,000-kN capacity MTS testing machine. The beams were tested under three-point bending setup over a simply supported span of 1,390 mm. Each specimen was supported on a roller support at one end and a hinged support on the other. Figure 8.4 depicts the test setup details. The load was applied at a loading rate of 10 kN/min until failure. The tested deep beams were instrumented with linear variable displacement transducers (LVDTs) to monitor deflection during the test. Three additional LVDTs were attached at mid-span and the two mid-shear spans of the beam. In addition, two high-accuracy (± 0.001 mm) LVDTs were used to monitor the slip at the end of one bottom reinforcing bar to evaluate the ability of the headed-end

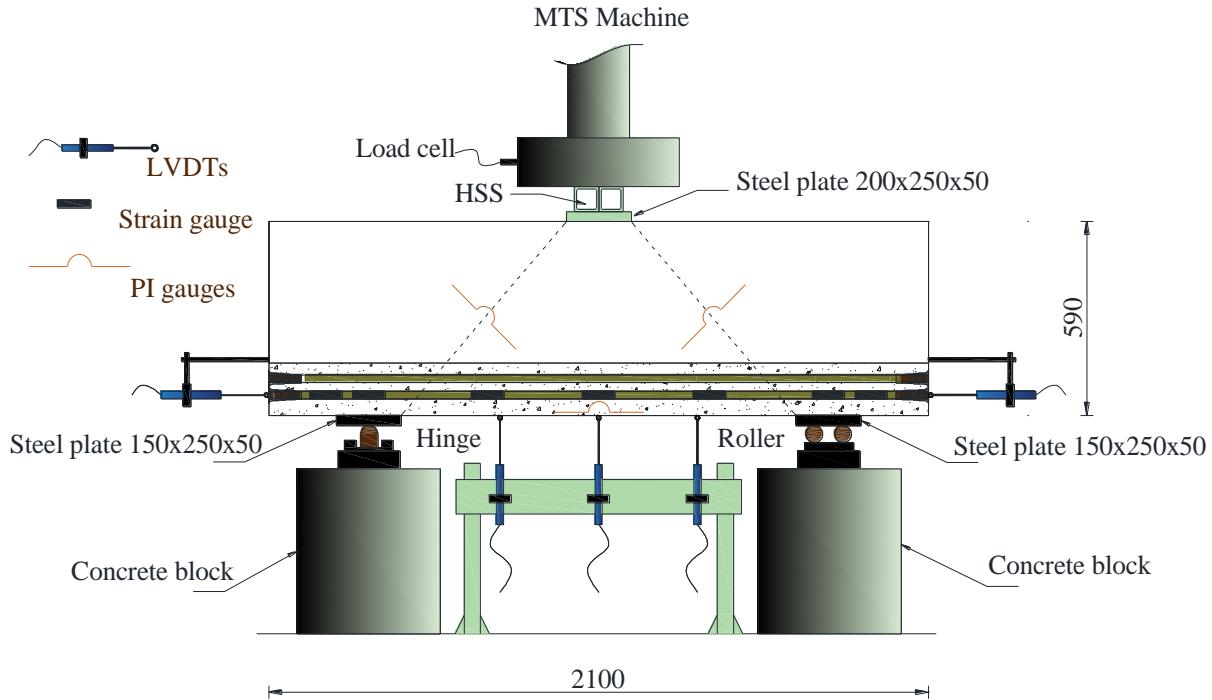


Figure 8.4: Schematic drawing of the test setup (all dimensions in mm)

to provide adequate anchorage. Seven strain gauges were attached to the longitudinal reinforcement in order to measure the strain profile in the longitudinal GFRP bars, as shown in Figure 8.4. Three 200-mm long PI gauges were attached to the concrete surface to measure the width of the diagonal cracks in the shear spans between the loading and the supporting plates and at the mid-span to monitor the flexural crack width. A data-acquisition system monitored by a computer was used to record the readings of the LVDTs, strain gauges, and PI gauges.

8.4 Experimental Results and Discussion

8.4.1 Modes of failure and crack pattern

The experimental results for all test specimens at different loading stages are summarized in Table 8.4. For all beams, no local bearing failure at loading or supporting plates was observed. Different

modes of failure were identified, i.e. shear-compression, crushing of compression strut, and diagonal-splitting failures. Shear-compression failure was the most common mode of failure, occurring in four specimens (X-X-0-W, L-S-1.0, L-B-4.5, and L-B-6.9). This failure was identified by an inclined crack parallel to the main strut followed by crushing of the concrete in the flexural compression zone above the upper end of the diagonal crack. Crushing of strut failure, occurred in X-X-0 and A-4.5-1.0, is characterized by multiple inclined cracks with the concrete between these cracks forming the concrete strut (ASCE-ACI Committee 426 1973). The diagonal-splitting failure, occurred in L-B-2.5, is identified by an inclined crack joining the outside edge of the loading plate and the inside edge of the support plate. In addition, the authors believe that the 2.5% of BF was presumably insufficient to act as a web reinforcement in the beam. Figure 8.5 shows the mode of failure for all beams.

It is worth mentioning that upon failure, the two reference beams (X-X-0 and X-X-0-W) experienced brittle failure, which was sudden and associated with abrupt sound of the concrete crushing. On the other hand, the beams reinforced with fibers, regardless of the type of the fibers, showed ductile failure, as no explosive sound was heard. This behaviour was substantiated by the load-deflection response discussed in the next section. No sign of end-anchorage failure nor slip of the tension reinforcement were observed in all beams. The failure modes of the 7 specimens are listed in Table 8.4. After the formation of the first crack, the propagation of cracks was monitored and marked at 50 kN intervals. In the early stages of loading within the range of 14-22% of the ultimate load, a flexural crack started from the bottom of the mid-span, just below the loading point, and propagated vertically upward; however, it did not penetrate into the compression zone.

Table 8.4: Summary of test results

Series	Specimen	$P_{c,exp}$ (kN)	$P_{c,CSA}$ (kN)	P_{cr} (kN)	P_u (kN)	ϵ_{max} ($\mu\epsilon$)	δ_{max} (mm)	Mode of failure	Ductility index
Series I	X-X-0*	140	172	320	800	8,410	10.2	DCS	1.14
	L-B-2.5	200	223	310	900	7,940	19.95	DS	1.70
	L-B-4.5*	182	209	350	1,005	7,310	30.9	SC	2.48
	L-B-6.9	170	202	380	1,096	8,040	27.4	SC	1.99
	L-S-1.0	205	236	320	980	10,320	21.9	SC	1.70
Series II	X-X-0*	140	172	320	800	8,410	10.2	DCS	1.14
	X-X-0-W	145	173	315	1,011	9,900	13.9	SC	1.59
	L-B-4.5*	182	209	350	1,005	7,310	30.9	SC	2.48
	A-B-4.5	179	211	410	1,238	11,000	41.8	DCS	4.43

*Beams X-X-0 and L-B-4.5 are common between the two series.

Note: $P_{c,exp}$ = first experimental flexural-cracking load; $P_{c,CSA}$ = first flexural-cracking load calculated according to the CSA S806 (CSA 2017); P_{cr} = main diagonal cracking load; P_u = ultimate load; ϵ_{max} = reinforcement strain at failure at mid-span; δ_{max} = Mid-span deflection at failure; DCS is diagonal concrete-strut failure; SC is shear-compression failure; DS is diagonal-splitting failure

It is worth mentioning that the experimental flexural cracking loads were comparable to those calculated according to CSA/S806-12 (CSA 2017), as listed in Table 8.4. The incorporation of fibers either as a layer in the tie zone, or in the whole depth, delayed the onset of cracks, which significantly contributed to the enhancement in the shear capacity of the specimens. For instance, compared to X-X-0, where the first crack appeared at a load of 140 kN, adding BFRCC layer in the tie zone with different dosages in L-B-2.5, L-B-4.5, and L-B-6.9 increased the flexural cracking load by 43, 30, and 21%, respectively. However, the increase in the cracking load was inversely proportioned to the BF dosage due to the reduction in concrete strength with the increase of the BF dosage. This reduction in strength was attributed to that the incorporation of discrete fibers formed interfacial transitional zones (ITZs) in the matrix and reduced the workability, which, in turn, increased entrapped air in the cementitious matrix and reduced the strength. Similar trend was reported by Bediwy et al. (2018).

With further increase in the load, more flexural cracks were initiated in the shear span, such cracks turned into diagonal and propagated towards the central zone, due to shear stresses in these regions. Suddenly, within the range of 32-40% of the ultimate load, a major diagonal crack was formed between the loading point and the support. At a load level of about 60-70% of the ultimate load, no new major cracks were formed; however, the major diagonal cracks kept widening up to failure. Figure 8.6 shows the crack pattern for all specimens at failure.

8.4.2 Cracking load and ultimate capacity

The flexural cracking load did not depend on the presence or type of fibers but rather on the strength properties of the cementitious matrix. For example, increasing the dosage of the BP from 2.5 (L-B-2.5) to 6.9% (L-B-6.9) showed a 17 % reduction in the flexural cracking load (from 200 kN to 170 kN, respectively). This was attributed to the difference in the compressive strength between both beams, which were 79 and 65 MPa, respectively, as explained above.

Similarly, the incorporation of conventional web reinforcement did not show any significant difference in terms of the flexural cracking load. For instance, X-X-0-W experienced a flexural cracking load of 145 kN compared to the control specimen without stirrups (X-X-0), which had a flexural cracking load of 140 kN. The results showed that all the beams had comparable diagonal cracking load within 25% variation. Conversely, the ultimate capacity of the deep beams was considerably affected when the BFRCC layer was incorporated in the tie zone, as depicted in Figure 8.7a. Compared to X-X-0, which had an ultimate load of 800 kN, adding the BFRCC layer in the tie zone at dosages of 2.5, 4.5, and 6.9% increased the load carrying capacity by 13, 26, and 37%, respectively. Similar increase in the capacity (approximately 26.4%) was observed when the beam was reinforced with stirrups (X-X-0-W with a capacity of 1,011 kN), with respect to the control beam without web reinforcement (X-X-0).

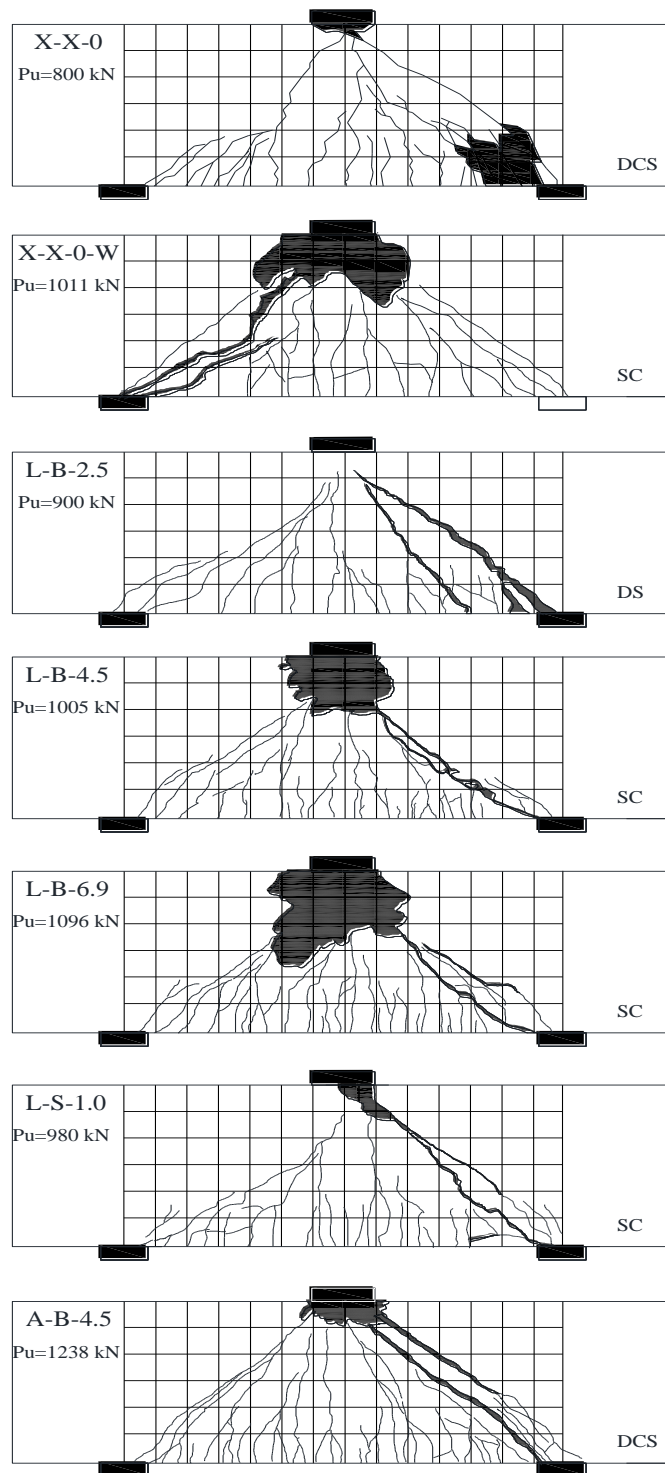
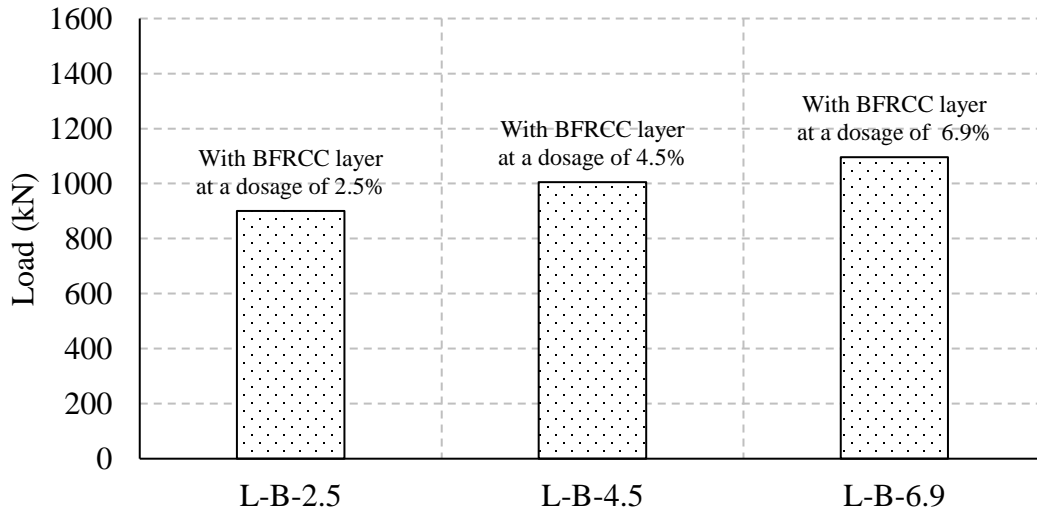


Figure 8.6: Cracking patterns at failure

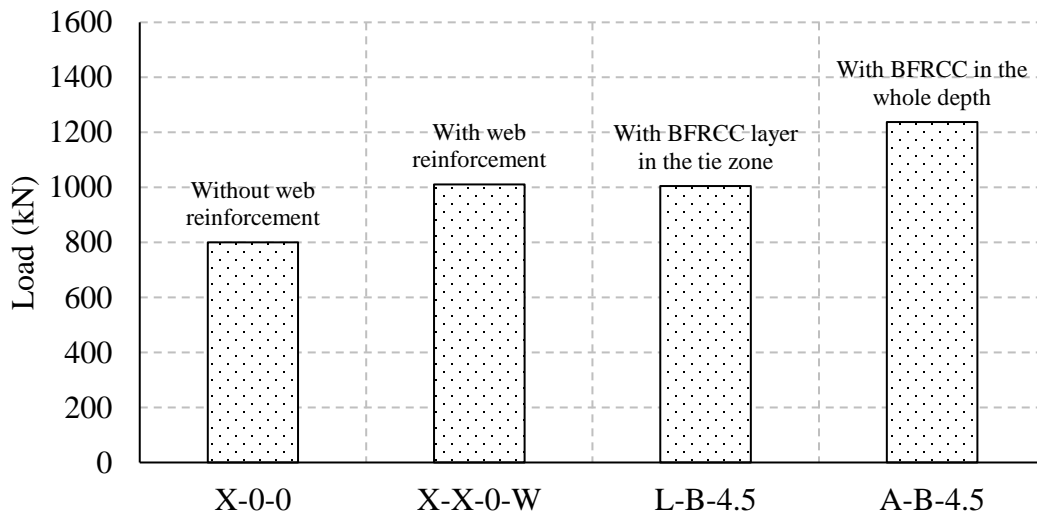
Moreover, these results support the use of BP, whether it was incorporated as a layer in the tie zone or over the whole depth, as an alternative to web reinforcement. This is evident since the ultimate capacity of the BFRCC layered beam with a dosage of 4.5% (1,005 kN) was quite close to that of the control beam reinforced with stirrups (approximately 1,011 kN). In addition, when the entire beam was made of BFRCC, the ultimate load carrying capacity was significantly increased by 23% (up to 1,238 kN), as shown in Figure 8.7b.

8.4.3 Load-deflection response

For all beams, the load deflection response was approximately bilinear up to the peak load as shown in Figure 8.8. The specimens with a layer of BFRCC had similar stiffness up to the initial flexural crack, followed by a reduction in stiffness for all beams but with different tendencies, which is attributed to the difference in dosage. As expected, the control beam without web reinforcement (X-X-0) failed suddenly in a brittle manner after reaching the peak load, and it did not exhibit any post-peak behaviour. Whereas, all beams with FRCC layer, irrespective of the type of fibers, showed an improved post-peak behaviour (Figure 8.8a). After reaching the peak, the layered beams (L-B-4.5, L-B-6.9, and L-S-1.0) did not fail rather it continued to carry decreasing load. This indicated the significant contribution of the fibers to the residual strength of the specimens. For example, the behaviour of L-B-4.5 and L-B-6.9 was associated with a gradual post-peak descending branch. This behaviour might be attributed to the adequate distribution of BP over the cross section of the layer and the intensity of fibers in case of the high dosage of fibers, which enhanced their efficacy in restraining the cracks in the matrix. On the other hand, specimen L-B-2.5 did not fail; however, the post-peak behaviour was associated with steep descending branch owing to the low volume fraction of the BP in the tie zone. Interestingly, a non-metallic

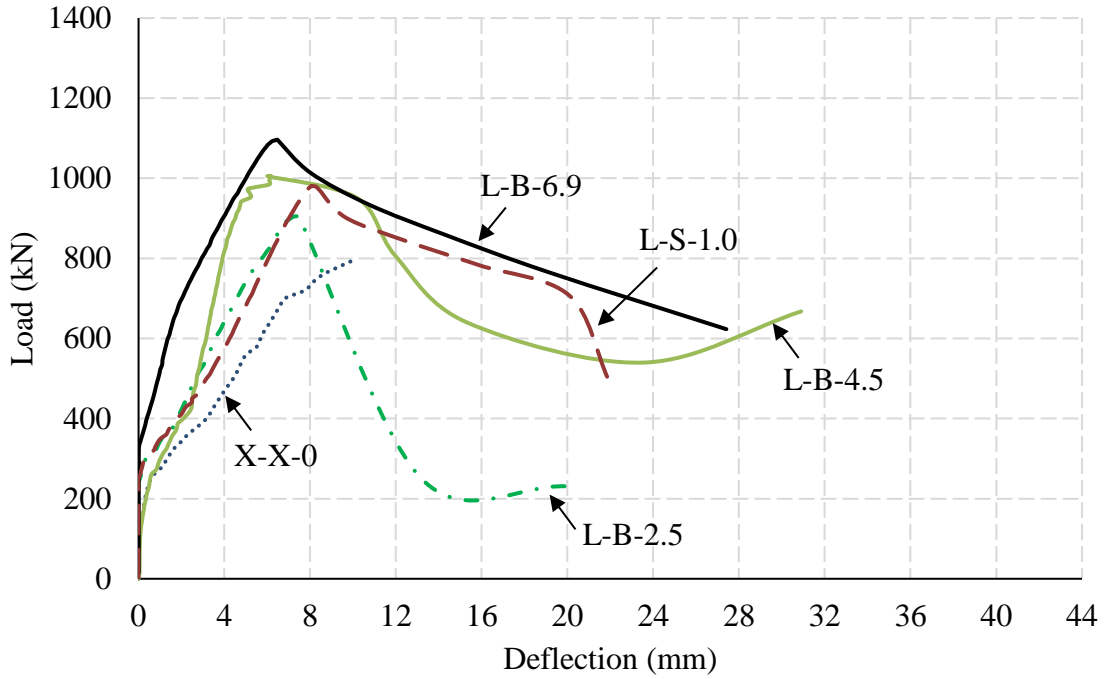


(a) Series I (Layer of FRCC in tie-zone)

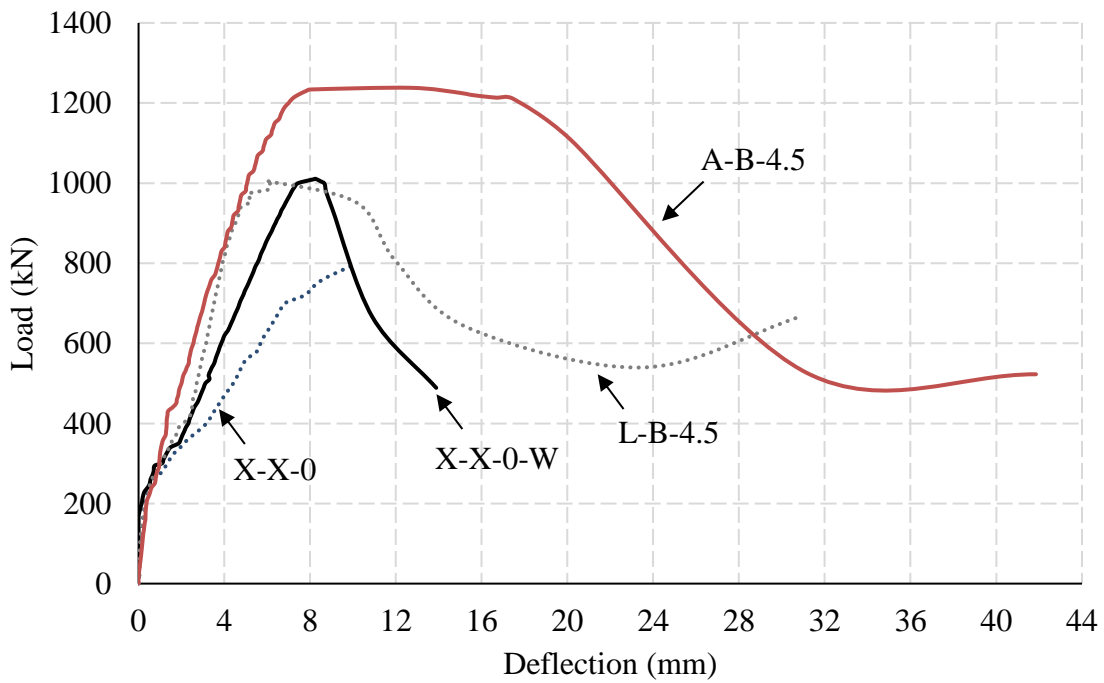


(b) Series II (web reinforcement replaced with FRCC)

Figure 8.7: Ultimate capacity of test beams



(a) Series I (Layer of FRCC in tie-zone)



(b) Series II (web reinforcement replaced with FRCC)

Figure 8.8: Load-deflection relationship for beams

BF pellet, which had a lower modulus of elasticity and aspect ratio with respect to SF, behaved as a ductile material showing a comparable post-peak behaviour as that of SF. When the BP were incorporated in the tie zone, it behaved as micro reinforcement and significantly boosted the strength of the specimens. It played a vital role in delaying the expansion of micro-cracks through the pullout-resisting mechanisms that is achieved from fibers bridging the cracks, which accordingly resulted in an increase in the load-carrying capacity and the energy dissipation (ductility).

In addition, adding the BP as a layer in the tie zone, or over the whole depth, had the capability to resist and control the flexural crack initiation and propagation that appeared at beam soffit. Consequently, both specimens L-B-4.5 and A-B-4.5 showed a gradual post peak behaviour, as the fibrous composite showed a comparable post-peak descending branch, when compared to the control beam with web reinforcement (see Figure 8.8b).

8.4.4 Ductility

In order to support the aforementioned discussion, the ductility of all tested beams was evaluated. The conventional definitions of the ductility were formulated based on steel reinforcement, where there is a clear plastic deformation of steel at yield. These definitions were expressed in the form of a ratio called ductility index or ductility factor between the ultimate deformation and the deformation at yield, thus the yield point is usually needed as the reference base. However, since FRP reinforcement shows linear stress-strain relationship up to failure with no yielding, the conventional definition is not applicable.

The ductility index (μ_E) approach, adopted in this study to assess the ductility of the beams reinforced with GFRP, was proposed by Naaman and Jeong (1995) as shown in Equation 8.1.

$$\mu_E = \frac{1}{2} \left(\frac{E_{tot}}{E_{el}} + 1 \right) \quad \text{Equation 8.1}$$

where E_{tot} is the total energy computed as the area under the load deflection curve up to failure and E_{el} is the elastic energy. The latter can be calculated as the triangle formed at failure load by the line S that having the weighted average slope of the two initial straight lines of the load deflection curve, as shown in Figure 8.9. It is worth mentioning that Naaman and Jeong (1995) defined the failure load to be, either the maximum load for specimens without post-peak behaviour, or 80% of the maximum load on the descending branch of the load-deflection response. Table 8.4 summarizes the computed values of the ductility index of the test specimens. Significantly higher ductility index was obtained due to the addition of fibers. Compared to the control beam X-X-0, adding the BFRCC layer in the tie zone with dosages of 2.5, 4.5, and 6.9% increased the ductility indices markedly by 50, 118, and 76%, respectively. The specimen with 6.9% BP content showed a slightly smaller value of the ductility compared with the specimens with the fiber content of 4.5%, this can be attributed to the reduced workability due to the clustering of the fibers when a high dosage was used (6.9% of BP). In addition, one of the limitations of the approach adopted herein is that the failure load is defined to be 80% of the maximum load on the descending branch of the load-deflection response. As such, the whole area under the curve was not calculated, just up to 80% of the maximum load. From Figure 8.8a, it can be noticed that beam L-B-4.5 showed a plateau after reaching the maximum load leading to a high ductility index. On the other hand, although specimen L-B-6.9 had higher maximum load, the slope of the descending branch after the maximum load became steeper when it is compared with specimen L-B-4.5, leading to less ductility index.

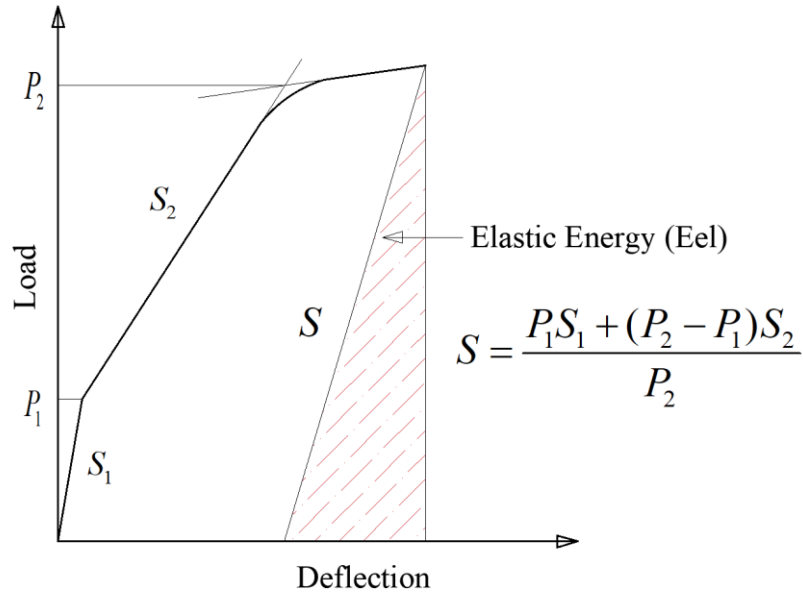


Figure 8.9: Definition of ductility index and line S

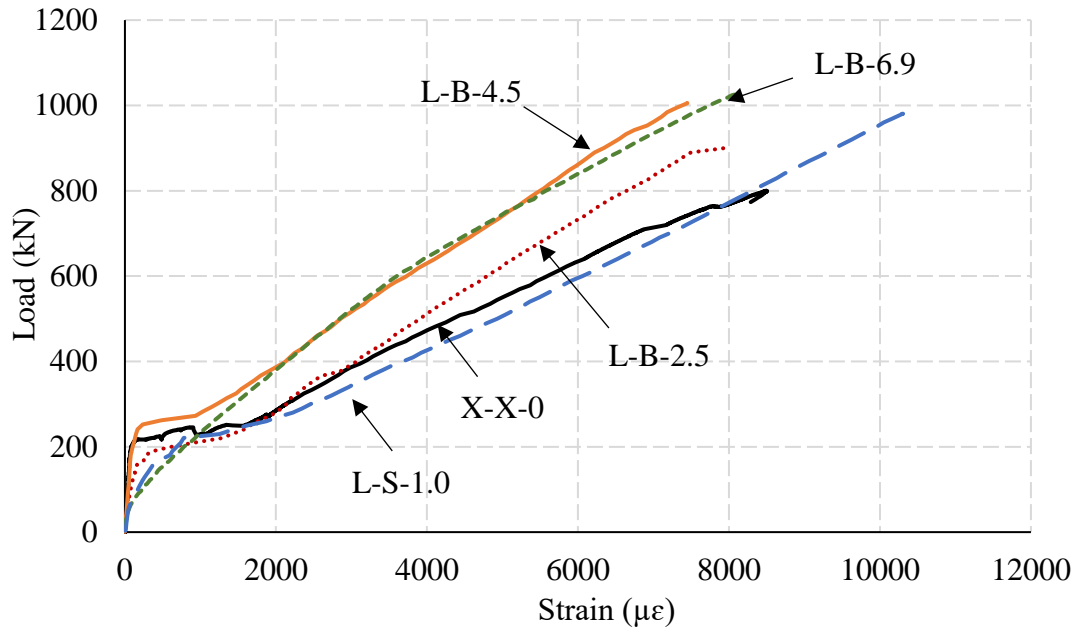
Moreover, in case of keeping the ratio of volume of BP to SF equal to the modular ratio, the ductility index was increased. For instance, replacing 1% SFRCC layer with 6.9% BFRCC layer led to 18% increase in the ductility index (from 1.70 to 1.99 for L-S-1.0 and L-B-6.9, respectively). Surprisingly, when the volume of both fibers was kept constant, taking into consideration the superior properties of SF with respect to the BP, the ductility was quite comparable, as listed in Table 8.4. Such distinctive behaviour beyond the peak load substantiates the notion that BP could be incorporated to substitute the conventional web reinforcement. For example, a threefold increase in the ductility index was observed when the web reinforcement in beam X-X-0-W was replaced with BP over the whole cross section with a dosage of 4.5% (A-B-4.5).

8.4.5 Load-longitudinal reinforcement strain relationship

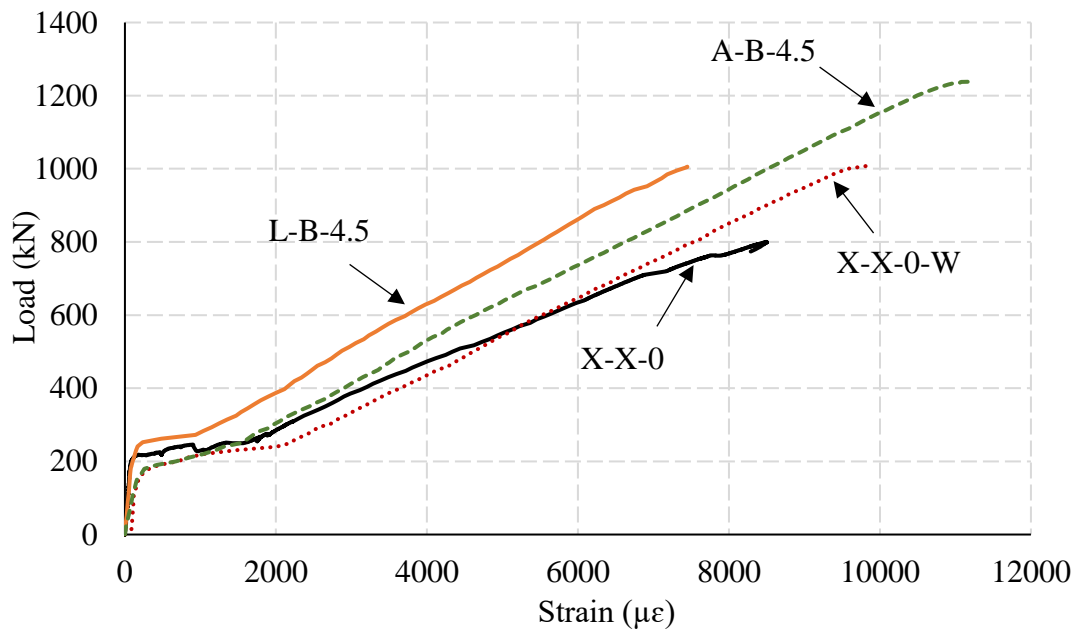
Figure 8.10 shows the relationship between the applied load and the measured strain developed in the longitudinal reinforcement at the mid-span for the tested beams. In addition, the measured mid-

span strain at failure is presented in Table 8.4. For all beams, the strain in longitudinal reinforcement did not reach 65% of the ultimate tensile strain of the GFRP bars throughout the tests. The load-strain graphs for all beams of this study exhibited similar characteristics, as the strains after cracking varied almost linearly with the increased load up to failure. It can be noticed that, for the FRCC layered beams, increasing the dosage of fibers was followed with a reduction in the measured strain in the reinforcement at the same load level. For example, at the ultimate load level of X-X-0, increasing the BP from 2.5 to 4.5 and further to 6.9% in L-B-2.5, L-B-4.5 and L-B-6.9 yielded 20, 34 and 33% reduction in the measured strains. Similarly, reinforcing the beam with stirrups or incorporating BP over the whole depth in X-X-0-W and A-B-4.5 decreased the measured strains by 15 and 20%, respectively, compared to X-X-0 at its ultimate load level. In general, the addition of stirrups controls the diagonal crack width and propagation, which resulted in lowering the strains along the longitudinal reinforcement (Wight and MacGregor 2009). In addition, the beams with BP, whether it was incorporated as a layer or over the whole depth, had less transverse strains, which is directly proportionate to the strains developed within the longitudinal reinforcement (Vecchio and Collins 1986). In addition, the incorporation of BP improved the longitudinal tensile strength of fibrous specimens along with the GFRP bars leading to better uniform distribution of tensile stresses over the length of the beam. The latter observations were among the reasons behind improving the strength of the diagonal strut and the load carrying capacity.

To examine whether and to what extent the arch action formed in the test beams, the strain distribution along the bottom layer of the longitudinal reinforcement was measured at five different locations along the beam span. In a fully developed arch action, the strain profile in the longitudinal



(a) Series I (Layer of FRCC in tie-zone)

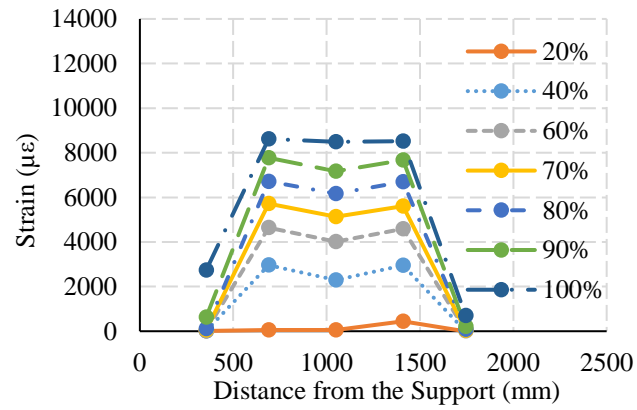


(b) Series II (web reinforcement replaced with FRCC)

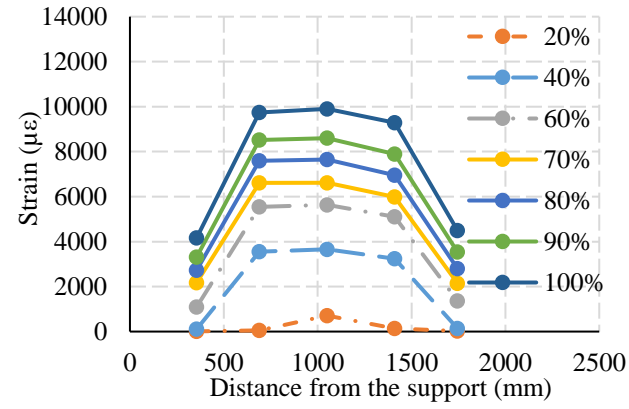
Figure 8.10: Strains at mid-span section in tested deep beams

reinforcement is expected to be approximately uniform, since the main longitudinal reinforcement serves as a tie for the arch. The strain profiles at different stages of loading for all specimens are presented in Figure 8.11. It was observed that the strains were distributed in a manner similar to the bending moment prior to the formation of the inclined cracks, where the elastic analysis (beam action) is still applicable. Between 40-60% of the ultimate load capacity, strains in the longitudinal reinforcement were very similar after the formation of the main diagonal shear crack with uniform increase in the strains confirming the formation of the arch action.

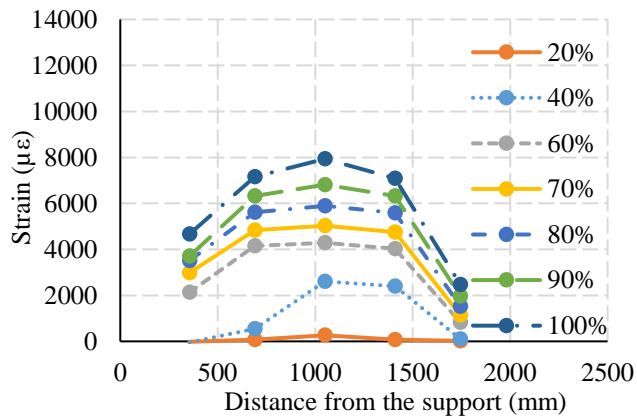
It was found out that the STM is more appropriate to design deep beams rather than the traditional sectional shear analysis. Another approach to confirm the development of the tied-arch mechanism, is by calculating the predicted ultimate load using the average of the measured strains, the axial stiffness of the GFRP longitudinal bars, and the angle between the strut and tie, and compare it to the experimental ultimate load. The ratio between the experimental ultimate-to-predicted load ranged from 70 to 98% (with a mean value of 80%), confirming that the strut and tie model is applicable for the tested deep beams.



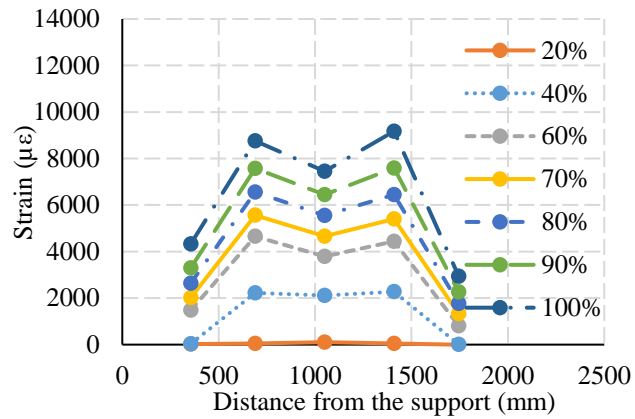
(a) X-X-0



(b) X-X-0-W

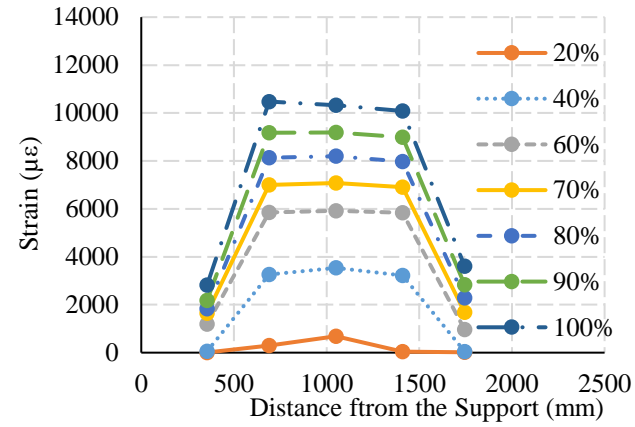
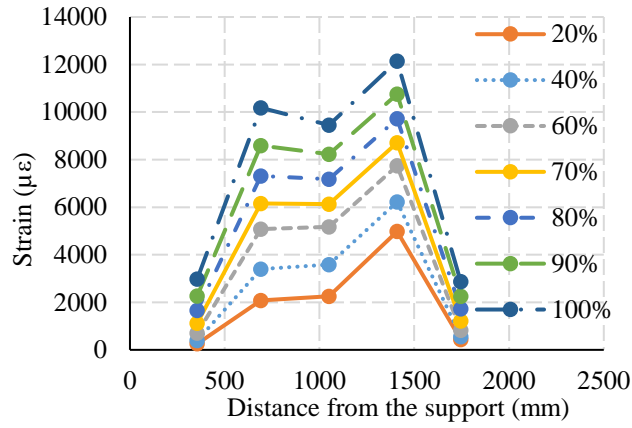


(c) L-B-2.5



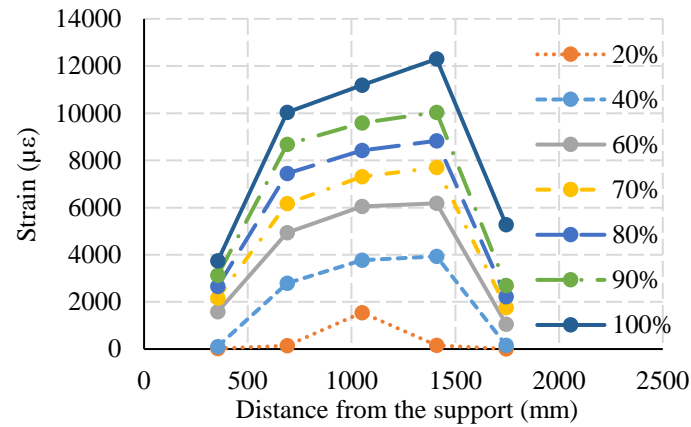
(d) L-B-4.5

Figure 8.11: Strain profile in deep beams



(e) L-B-6.9

(f) L-S-1.0



(g) A-B-4.5

Figure 7.11: Strain profile in deep beams

8.4.6 Evaluation of code provisions for strut and tie models

The STM adopted by the CSA/S806-12 (CSA 2017), the ACI 318-19 (ACI 2019), and the Eurocode 2 (EN 1992-1-1:2004) were examined in this study to check their applicability to predict the ultimate shear capacity of FRP-RC deep beams, as listed in Table 8.5. All the resistance factors, ϕ , for both concrete and reinforcing bars were taken as unity. A single-panel STM was used to analyze the test specimens as illustrated in Figure 8.12. It is worth mentioning that the CSA/S806-12 (CSA 2017) included provision for STM for FRP-RC deep beams, while the American guidelines for FRP-RC members, ACI 440.1R-15 (ACI 2015), do not provide any provisions for the design of deep beams. However, the design provisions in the ACI 318-19 code and the Eurocode 2 for steel-RC structures can be applied to the FRP-RC deep beams because the load capacity was governed by the compression strut capacity for all specimens rather than the capacity of the node or the tie. The STM in the CSA/S806-12 depends mainly on the concrete compressive strength and the strains developed in the tie, while the ACI 318-19 and Eurocode 2 related the capacity of the strut to the concrete compressive strength.

Table 8.6 shows comparisons between the experimental load capacity and the code predicted capacity of the tested beams. The results showed that the Eurocode 2 overestimated the failure load with a mean ratio of predicted-to-experimental, P_{exp}/P_{pre} , of 0.84 and CoV of 0.11. This might be attributed to that the Eurocode 2 neglected the effect of concrete softening in the diagonal strut resulting from the high longitudinal strains permitted by the GFRP longitudinal reinforcement.

On the other hand, the CSA/S806-12 and ACI 318-19 underestimated the capacity of FRP-RC deep beams with a mean value of P_{exp}/P_{pre} ratio of 1.39 and 1.11 and CoV of 0.11 and 0.22, respectively. This was attributed to that the capacity of the compression strut in the CSA/S806 is

Table 8.5: Code design provisions for STM

STM Component	CSA S806-12	Eurocode 2	ACI 318-19
Strut	<p>Compressive force in the strut = $\phi_c f_{cu} A_{cs}$</p> <p>f_{cu} is the limiting compressive stress</p> <p>$f_{cu} = \frac{f'_c}{0.8 + 170\varepsilon_1}$ where,</p> <p>$\varepsilon_1 = \varepsilon_f + (\varepsilon_f + 0.002) \cot^2 \theta_s$</p> <p>$f'_c$ = concrete strength ε_1 = transverse tensile strain ε_f = tensile strain in the tie θ_s = the smallest angle between the strut and the adjoining ties</p>	<p>The allowable compressive stress of struts = $\sigma_{Rd,max} = 0.6\nu f_{cd}$</p> <p>$f_{cd}$ is design value of concrete compressive strength</p> <p>ν is reduction factor concrete and it equals to $(1 - f_{ck} / 250)$ where f_{ck} is characteristic compressive cylinder strength of concrete at 28 days</p>	<p>Strength of struts = $F_{ns} = f_{ce} A_{cs}$ and</p> <p>$f_{ce} = 0.85\beta_s\beta_c f'_c$ where</p> <ul style="list-style-type: none"> β_s is strut coefficient = 1.0 for boundary struts, 0.75 for interior struts satisfying one of the following equations $\frac{0.0025}{\sin^2 \alpha_1} & V_u \leq \phi 5 \tan \phi \lambda \lambda_s \sqrt{f'_c} b_w d$ and 0.4 for other cases β_c is strut confinement factor, which is the lesser of: $\sqrt{\frac{A_2}{A_1}}$ or 2.0, where A_1 is the loaded area and A_2 is the area of the lower base of the largest frustum of a pyramid, cone, or tapered wedge contained wholly within the support and having its upper base equal to the loaded area
Tie	<p>Tensile force in the tie $\leq 0.65\phi_F A_{FT} f_{FU}$</p> <p>$\phi_F$ = resistance factor for FRP A_{FT} = area of reinforcement f_{FU} = ultimate strength of the bar</p>	<p>The nominal tensile strength of a tie, F_{nt}, shall be calculated by $F_{nt} = A_{st} f_y$</p> <p>A_{st} = area of steel reinforcement f_y = yield strength of steel reinforcement</p>	
Node	<p>Compressive stress in the node regions $\leq 0.85\phi_c m f'_c$ in node regions bounded by struts and bearing areas, $0.75\phi_c m f'_c$ in node regions anchoring a tie in only one direction and $0.65\phi_c m f'_c$ in node regions anchoring ties in more than one direction</p>	<p>Compressive stress in the node regions $\leq \nu f_{cd}$ in node regions bounded by struts and bearing areas, $0.85 \nu f_{cd}$ in node regions anchoring a tie in only one direction and $0.75 \nu f_{cd}$ in node regions anchoring ties in more than one direction</p>	<p>The nominal compressive strength of a nodal zone, F_{mn}, is calculated by $F_{mn} = f_{ce} A_{nz}$</p> <p>where $f_{ce} = 0.85\beta_n f'_c$</p> <p>$\beta_n$ is nodal zone coefficient</p> <ul style="list-style-type: none"> $\beta_n = 1.0$, nodal zones bounded by struts and bearing areas or both $\beta_n = 0.8$, nodal zones anchoring one tie $\beta_n = 0.6$, nodal zones anchoring two or more ties.

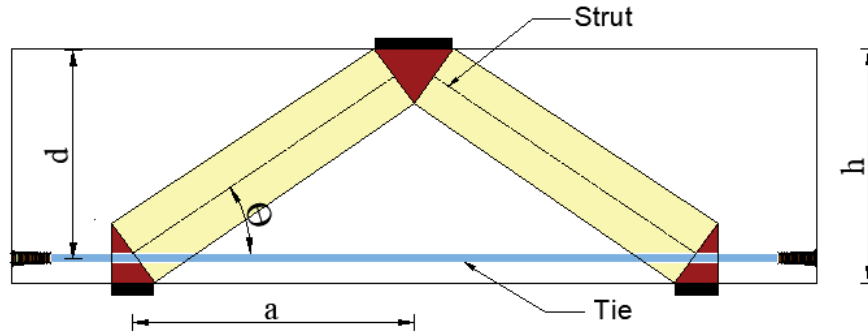


Figure 8.12: Strut-and-tie model (STM) for simply supported deep beams

adversely affected by the amount of longitudinal strain (ϵ_l) that could reach 0.01 or more in GFRP-RC beams bars, which leads to significantly conservative predictions. For the ACI 318-19, neglecting the effect of the longitudinal reinforcement ratio along with providing a reduced value of the coefficient β_s led to a conservative estimation of the beam capacity.

Table 8.6: Comparison between the experimental and predicted failure loads

Series	Specimen	Experimental load, P_{exp} (kN)	Strut-and-tie model					
			CSA S806-12		Eurocode 2		ACI 318-19	
			P_{CSA} (kN)	$P_{exp/CSA}$	P_{Ecode} (kN)	$P_{exp/Ecode}$	P_{ACI} (kN)	$P_{exp/ACI}$
Series I	X-X-0*	800	683	1.17	1,144	0.70	799	1.00
	L-B-2.5	900	693	1.30	1,163	0.77	816	1.10
	L-B-4.5*	1,005	675	1.49	1,126	0.89	782	1.29
	L-B-6.9	1,096	679	1.61	1,126	0.97	782	1.40
	L-S-1.0	980	664	1.48	1,107	0.89	765	1.28
Series II	X-X-0*	800	683	1.17	1,144	0.70	799	1.00
	X-X-0-W	1,011	816	1.24	1,163	0.87	1529	0.66
	L-B-4.5*	1,005	675	1.49	1,126	0.89	782	1.29
	A-B-4.5	1,238	875	1.41	1,524	0.81	1,207	1.03
	Mean			1.39		0.84		1.11
	**CoV			0.11		0.11		0.22

*Beams X-X-0 and L-B-4.5 are common between the two series.

**CoV = coefficient of variation.

8.5 Conclusions

Seven large-scale deep beam with a/d ratio equal to 1.18 were tested to failure to investigate the feasibility of using a steel-free reinforcement system for concrete deep beams by combining FRP reinforcement with BF pellets. The structural behavior in terms of the ultimate load carrying capacity, deflection, ductility, and failure mode was evaluated. The following conclusions were drawn from the results of this research:

- The formation of the arch action was confirmed by the nearly uniform strain distribution along the longitudinal reinforcement. In addition, the applicability of strut-and-tie model for the tested deep beams was confirmed by using the model to predict the ultimate capacity, which yields an average P_{pre}/P_{exp} ratio of 0.8.
- Three different modes of failure were observed in this study; shear-compression, crushing of strut, and diagonal-splitting failures. All specimens failed after the development of a major diagonal shear crack extending from the inside edge of the support plate toward the loading plate.
- The beneficial effect of BFRCC on the various aspects of structural behavior of FRP-RC deep beams is pronounced. The inclusion of FRCC layer in the tie zone played an important role in delaying the initiation of the first crack, which in turn enhanced the load carrying capacity of the specimens with respect to that of the control counterparts without fibers.
- The results of the experimental tests indicate that the brittle behavior of FRP-RC deep beams can be highly improved by the inclusion of BF pellets in the tie zone, as reflected by the deflection softening behavior, which was characterized by a gradual decrease in the ultimate load up to failure.
- Adding fibers has been proved as an effective way to enhance the ductility of FRP-RC deep beams. The ductility indices increased by 50, 118, and 76% with the addition of 2.5, 4.5, and 6.9% BF pellets in the tie zone compared to the counterpart beam without fibers. In addition, despite the superior properties of SF with respect to the BF pellets, keeping the volume of BF pellets and SF constant (L-B-2.5 vs L-S-1.0) showed comparable ductility indices.

- The inclusion of BFRCC with a dosage of 4.5% in the whole depth was an effective substitution to conventional web reinforcement in deep beams. However, from the direct cost perspective, adding the BF pellets as a layer with a dosage of 4.5% will reduce costs and achieve an acceptable level of performance in terms of strength and ductility.
- The STM proposed by the CSA/S806-12 and the ACI 318-19 underestimated the ultimate capacity of FRP-RC beams by as much as 39 and 11%, respectively. On the other hand, the Eurocode 2 overestimated the ultimate capacity, which could lead to higher failure risk than other codes. Moreover, provisions of STM available in current codes need to be revised to better predict the capacity of FRP-FRCC deep beams.

CHAPTER 9: ASSESSMENT OF SHEAR STRENGTH DESIGN MODELS FOR FIBER-REINFORCED CONCRETE DEEP BEAMS

Authors and Affiliation:

- Ahmed G. Bediwy, PhD Candidate, Department of Civil Engineering, University of Manitoba
- Ehab F. El-Salakawy, Professor, Department of Civil Engineering, University of Manitoba

Journal and Status:

American Concrete Institute (ACI) special publication, submitted on January 08, 2021.

Reference:

Bediwy, A. and El-Salakawy, E. “Assessment of shear strength design models for fiber-reinforced concrete deep beams.” in “Development and Applications of FRP Reinforcements.” *ACI Special Publication*, under review.

Note:

The manuscript had been slightly altered from the original paper by renumbering the tables and figures to include the chapter number. In addition, the reference list and list of notations have been moved to the appropriate sections in the thesis as indicated in the table of contents.

Abstract

Deep beams are common elements in concrete structures such as bridges, water tanks and parking garages, which are usually exposed to harsh environments. To mitigate corrosion-induced damage in these structures, steel reinforcement is replaced by fiber-reinforced polymers (FRPs). Several attempts have been made during the last decade to introduce empirical models to estimate the shear strength of FRP-reinforced concrete (RC) deep beams. In this study, the applicability of these models to predict the capacity of simply supported deep beams with and without web reinforcement was assessed. Test results of 54 FRP-RC deep beams and 31 steel/FRP-FRC deep beams were used to evaluate the available models. In addition, a proposed model to predict the shear strength of FRP-FRC deep beams was introduced. The model was calibrated against experiments conducted previously by the authors on FRP-FRC deep beams under gravity load. The model was capable of predicting the ultimate capacity with a mean experimental-to-predicted value of 1.04 and a standard deviation of 0.14.

Keywords: empirical models, database, FRP, FRC, shear strength, deep beams.

9.1 Introduction

Reinforced concrete (RC) deep beams have been extensively employed in many structural applications such as pile caps, foundation, offshore structures, and transfer girders. Deep beams are dominated by a disturbed region (D-region) where the Bernoulli hypothesis of strain distribution is no longer valid to predict its behaviour due to the non-linear strain distribution across the deep beam section (Joint ACI-ASCE Committee 445 1998; Wight and MacGregor 2009). Accordingly, codes of practice divided the shear behaviour of concrete beams based on the shear span to depth ratio (a/d), where RC deep beam was defined as a structural member with an a/d ratio less than 2.0 such that the behaviour is shear dominated, as stipulated in the ACI 318-19 (ACI 2019) and CSA/A23.3-19 (CSA 2019c) codes. These codes allow using the strut-and-tie model (STM) to assess the shear strength of deep beams, where the applied load is transmitted directly to the support by in-plane compression through an inclined concrete strut and constant tension in the reinforcement (tie). The point of intersection of struts, ties, or a combination of both forms a node, as shown in Figure 9.1. The STM follows the lower-bound theorem of plasticity, where the computed failure based on the STM is less than or equal to the actual collapse load for the structure. To provide a safe distribution of stresses for a structural member, the struts, ties, and nodes, the three elements that shape an STM, must be proportioned in a way to maintain equilibrium and to exhibit sufficient deformation capacity. When fiber-reinforced polymer (FRP) reinforcement is used, it is expected that such deformation capacity is reduced due to the linear-elastic behaviour and low elastic modulus of the GFRP material (Naaman and Jeong 1995; Jaeger et al. 1995).

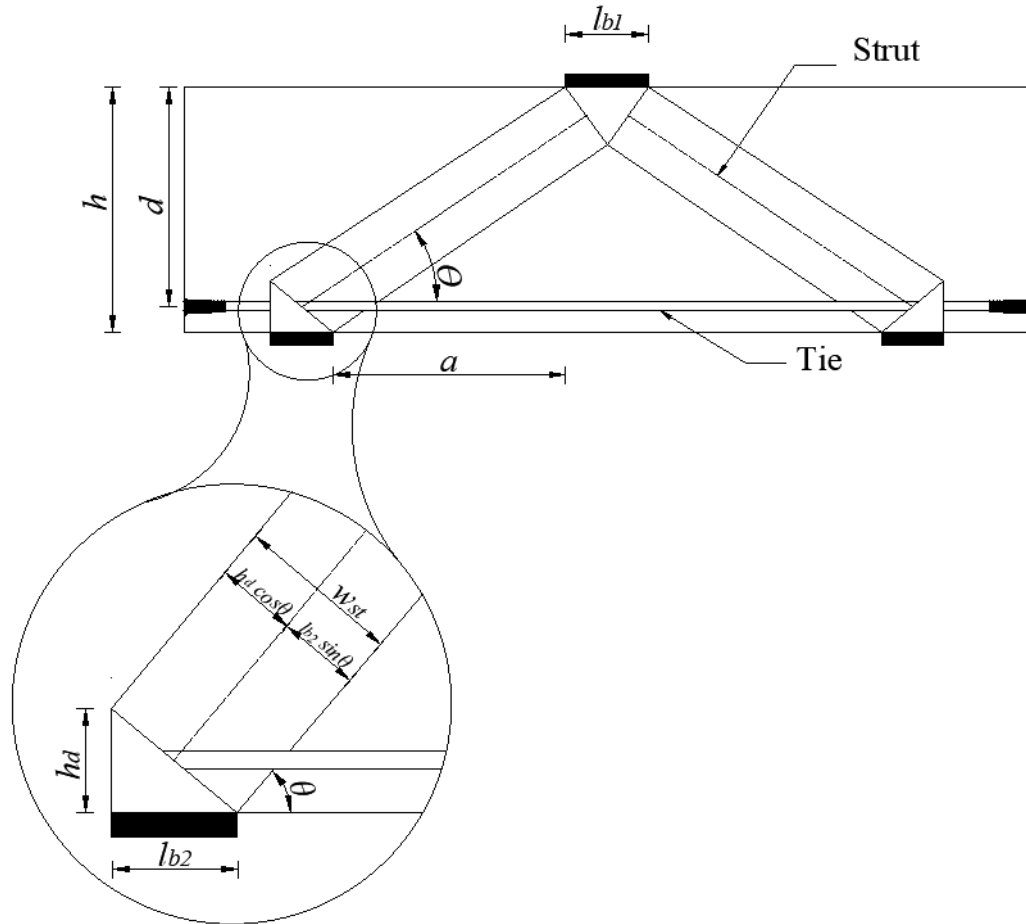


Figure 9.1: Strut-and-tie model (STM) for simply supported deep beams

Several experimental studies have been carried out to investigate the behaviour of FRP-RC deep beams (Nehdi et al. 2008; Andermatt and Lubell 2013; Farghaly and Benmokrane 2013; Mohamed et al. 2017; Mohamed et al. 2020). The authors found that an arch-action mechanism was formed in the tested beams. However, only the Canadian codes for FRP-RC building structures, CSA/S806-12 (CSA 2017) and the highway bridge design code, CSA/S6-19 (CSA 2019a) included provisions for the strut-and tie model (STM) for FRP-RC deep beams, which is the same model specified in CSA/A23.3-19 (CSA 2019c) for steel-RC deep beams with replacing the yield strength of steel by the strength of FRP bars.

The use of discrete fibers to produce fiber reinforced concrete (FRC) has gained significant acceptance in the construction field to alleviate the concerns associated with the brittleness of shear-critical concrete members such as deep beams. At the material level, the incorporation of randomly distributed fibers had the capability of reducing bleeding, controlling shrinkage cracking, and improving impact resistance. Furthermore, at the structural performance level, the most pronounced advantages of using fibers in cementitious composites are increasing their energy absorbing capacity (toughness), deformation capability, and load-carrying capacity due to fiber bridging action (Bentur and Mindess 2007). Steel fibers reinforced concrete (SFRC) has gained popularity in construction industries in recent years. There are several experimental studies focused on using SFRC in deep beam reinforced longitudinally with steel bars. Mansur and Ong (1991), Fang and Wu (1994), Campione (2012), Sahoo et al. (2012), Tuchscherer and Quesada (2015); Moradi and Esfahani (2017) tested large scale deep beams with a/d varying between 0.5 and 1.7 and reinforced with longitudinal steel bars. The tested beams contained hooked-end steel fibers (SF) ranged between 0.5 and 1.5% by volume. All researchers unanimously concluded that the utilization of SF increased the strength and ductility of beams, since it served as a vehicle to allow for significant internal plastic stress redistribution. However, up to the authors' knowledge, there is no experimental data on the behaviour of simply supported FRP-FRC deep beams.

The main objectives of the current study are to evaluate the STM specified in the current codes and guidelines (ACI 318 [ACI 2019], Eurocode 2 [2004], AASHTO-LRFD [2014], and JSCE [2007] for steel-RC deep beams and CSA/S806-12 [CSA 2017] and CSA/S6-19 [CSA 2019a] for FRP-RC deep beams), as well as the models developed by different researchers in order to evaluate the key parameters affecting such models. The applicability of these models on steel-FRC and FRP-FRC deep beams subjected to gravity load was investigated. In addition, a new model was

proposed to better predict the shear capacity of fibrous deep beams, which was then validated against the test results of FRP-FRC beams that were conducted by the authors.

9.2 Research Significance

Despite the abundance of literature data that focused solely on the shear response of steel-FRC deep beams or FRP-RC deep beams, all the available codes and guidelines, except for the Canadian codes CSA/S806-12 and CSA/S6-19, did not include any guidance regarding the design of FRP deep beams using the strut-and-tie design model. Conversely, the research studies pertaining to FRP-FRC deep beams were very scanty, except for the only data point that conducted by the authors. Therefore, the STM provided in all available codes either for steel- or FRP-RC structures were found to be unsatisfactory because of neglecting the major contribution of discrete fibers. Thus, a new model was proposed and validated to predict the strength of FRC deep beams reinforced longitudinally with FRP bars.

9.3 Summary of Experimental Results

Ten GFRP-RC simply supported deep beams were constructed and tested to failure under monotonic loading (Bediwy and El-Salakawy forthcoming b & c), as listed in Table 9.1. The deep beams in that study had a rectangular cross section of 250-mm width by 590-mm height and a total length of 2,100 mm over a simply supported span of 1,390 mm. The beams had a shear span-to-depth ratio (a/d) of 1.18. In all beams, the reinforcement consisted of GFRP headed-end bars with an anchorage length of 280 mm. All beams had no web reinforcement, while the longitudinal reinforcement ratio (ρ) ranged between 0.6 and 1.4%. Figure 9.2 shows the reinforcement details of the tested specimens, while Figure 9.3 provides the loading setup.

Three control beams without fibers were cast for comparative analysis, while six beams had FRC layer that is additionally reinforced with basalt fiber pellets (BF) [four specimens] with different dosage ranged between 2.5 and 6.9% and steel fibers (SF) [two specimens] in the tie zone only. In

Table 9.1: Details of test beams

Specimen ID	Fiber type	Discrete fiber dosage (%)	Reinforcement ratio, ρ (%)	f'_c (MPa)	
				Bottom layer	Top layer
X-X-0.0-0.6	N/A	N/A	0.6	47±0.63	47±0.63
X-X-0.0-1.0	N/A	N/A	1.0	47±0.63	47±0.63
X-X-0.0-1.4	N/A	N/A	1.4	47±0.63	47±0.63
L-B-2.5-0.6	Basalt	2.5	0.6	81±1.21	47±0.42
L-B-2.5-1.0	Basalt	2.5	1.0	79±1.12	48±0.55
L-B-4.5-1.0	Basalt	4.5	1.0	70±1.42	46±0.21
L-B-6.9-1.0	Basalt	6.9	1.0	65±0.82	46±0.36
L-S-1.0-0.6	Steel	1.0	0.6	90±0.98	46±0.37
L-S-1.0-1.0	Steel	1.0	1.0	89±1.06	45±0.89
A-B-4.5-1.0*	Basalt	4.5	1.0	71±0.86	71±0.86

*The fibers were incorporated entirely over the whole depth

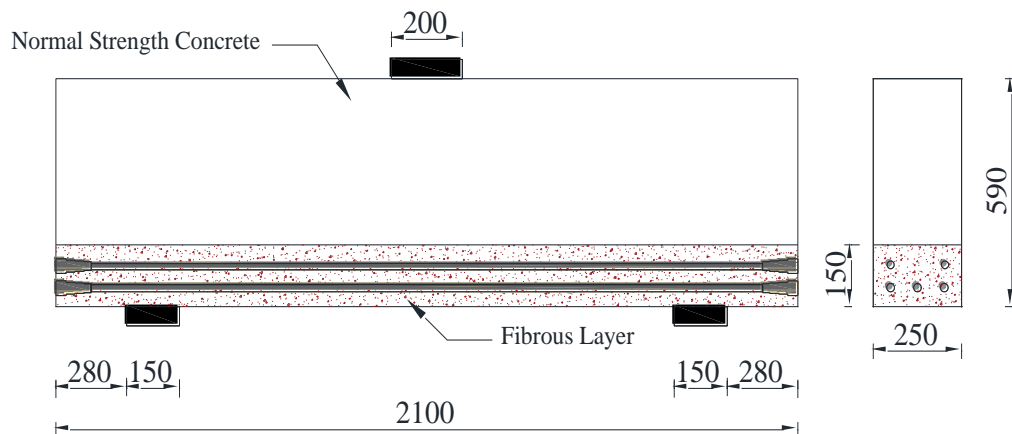


Figure 9.2: Details of specimens (all dimensions in mm)

addition, one specimen was entirely cast with the FRC. The properties of GFRP bars and discrete fibers are listed in Table 9.2 and 9.3, respectively. Crushing of diagonal strut was the dominant mode of failure for all specimens (Figure 9.4), except for beams with ρ of 1.4, which experienced

a local failure at the loading plate. The plain beams without fibers showed sudden failure that was associated with an abrupt sound of the concrete crushing.

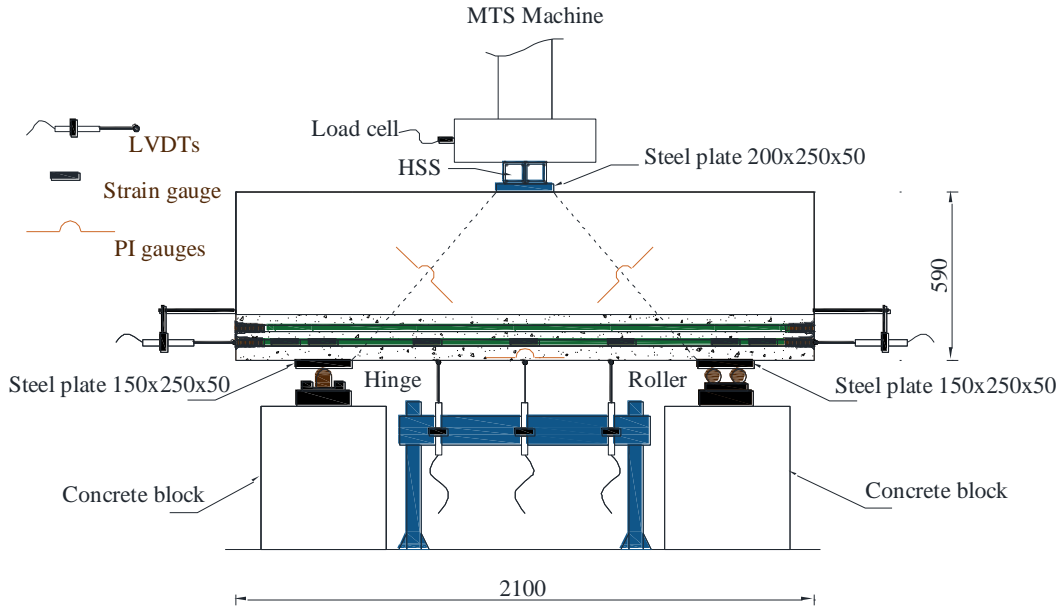


Figure 9.3: Schematic drawing of the test setup (all dimensions in mm)

Table 9.2: Properties of fibers

Properties	Properties of fibers	
	BP	Hooked steel
Length (mm)	36	30
Diameter/dimensions (mm)	1.80	0.65
Aspect ratio	20	45
Specific gravity	1.74	7.70
Tensile strength (MPa)	2,300	1,200
Elastic modulus (GPa)	65	200

Table 9.3: GFRP reinforcement properties

Bar size	Nominal diameter (mm)	Area (mm ²)		Tensile strength (MPa)	Modulus of elasticity (GPa)	Ultimate strain (%)
		Nominal	CSA/S806-12 Annex A			
No. 15	15.9	198	291	1,184	62.6	1.89
No. 20	19.0	285	394	1,105	63.7	1.73



Figure 9.4: Typical crushing of strut failure mode (A-B-4.5-1.0)

On the other hand, the fibrous beams showed significantly less brittleness with no loud “bang” at failure. The incorporation of fibers enhanced the overall performance of the tested beams in terms of the maximum capacity, and the post-peak response. The development of the arching action in the tested FRP-FRC deep beams was substantiated by the essentially uniform strain distribution in the bottom reinforcement, as shown in Figure 9.5. More details on this series of tests can be found elsewhere (Bediwy and El-Salakawy forthcoming b & c). The test results were used to assess the STMs in the available codes and guidelines, as well as the proposed models in the literature.

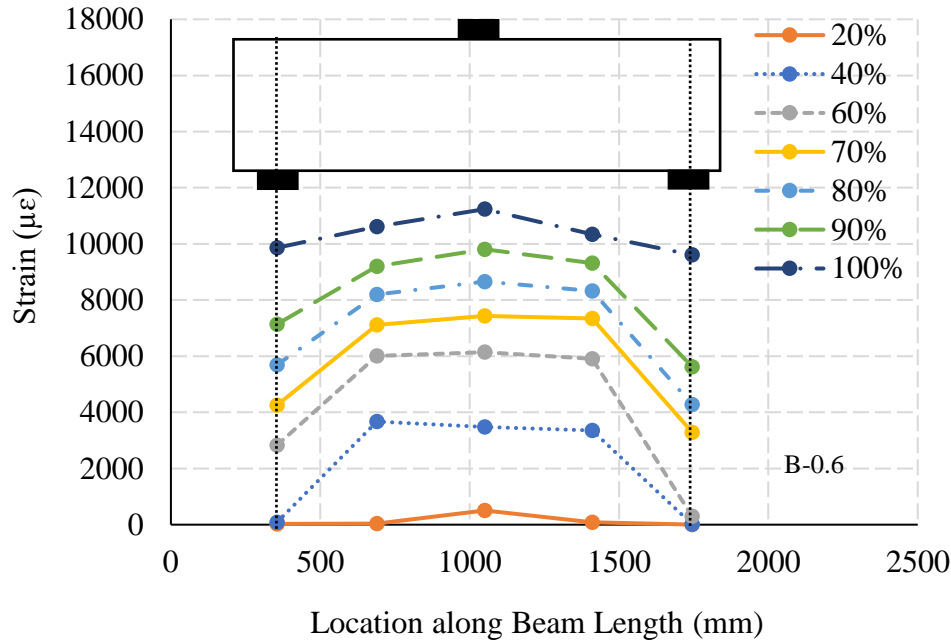


Figure 9.5: Typical Strain profile in deep beams (L-B-2.5-1.0)

9.4 Experimental Database

Recently, the shear strength of FRP-RC deep beams subjected to gravity load has gained considerable attention (Nehdi et al. 2008; Andermatt and Lubell 2013; Farghaly and Benmokrane 2013; Kim et al. 2014; Mohamed et al. 2017; Mohamed et al. 2020). All beams had a rectangular cross section and were tested under three- or four-point bending. Table 9.4 lists data for a total of 54 FRP-RC deep beams with and without web reinforcement collected from 6 investigations available in the literature. These 54 specimens covered a large spectrum of materials and geometrical properties with a wide range of shear span-to-depth ratio, a/d (0.83 to 2.1), support and loading plate width (50 to 330 mm), beam height (200 to 1,200 mm), effective depth of beam (150 to 1,111 mm), concrete strength (26.1 to 68.5 MPa), average longitudinal reinforcement ratio (0.26 to 2.3%), average modulus of elasticity for FRP reinforcement (37.9 to 144 GPa), and different types of FRP bars (AFRP, CFRP, and GFRP).

In addition, the applicability of the available STMs to predict the capacity of FRC deep beams reinforced with FRP bars was evaluated. However, due to the dearth of literature on the shear behaviour of FRP-FRC deep beam except for those tested by the authors, the authors collected data for a total of 31 specimens reported in the literature including 24 steel-FRC specimens and 7 FRP-FRC specimens, as listed in Table 9.5. The later data covered a wide range of design parameters similar to those mentioned previously in addition to parameters associated to the properties of discrete fibers such as the length of fibers (30 to 60 mm), the diameter of fibers (0.5 to 1.8 mm), the dosage of fibers (0.5 to 6.9%), and different types of discrete fibers (hooked-end steel fibers and basalt fibers).

Table 9.4: Test data for FRP-RC deep beams

Specimen ID	Beam Details						FRP Details			P_{exp} (kN)	ASSHTO-14	ACI 318-19	Eurocode 2	JSCE 07	Model I	Model II
	b (mm)	d (mm)	a/d	l_{b1} (mm)	l_{b2} (mm)	f_c' (MPa)	Type	A_{frp} (mm ²)	E_{frp} (GPa)		CSA S6-19					
											CSA S806-12					
											P_{exp}/P_{pre}					
Mohamed et al. (2017)																
G1.47	300	1,088	1.47	228	203	38.7	GFRP	4,048	62.4	1,849	2.48	0.98	1.01	1.12	1.08	0.99
G1.47H	300	1,088	1.47	228	203	45.4	GFRP	4,048	62.4	1,695	2.05	0.64	0.56	0.45	1.10	0.95
G1.47V	300	1,088	1.47	228	203	45.4	GFRP	4,048	62.4	2,650	1.15	1.01	0.92	0.70	1.04	0.97
G1.13	300	1,088	1.13	228	203	37.0	GFRP	4,048	62.4	2,687	2.35	1.22	1.12	1.43	1.05	1.05
G1.13H	300	1,088	1.13	228	203	44.6	GFRP	4,048	62.4	2,533	1.97	0.78	0.69	0.64	0.98	1.15
G1.13V	300	1,088	1.13	228	203	44.6	GFRP	4,048	62.4	3,236	1.45	1.23	0.78	0.82	1.15	1.25
G1.13VH	300	1,088	1.13	228	203	37.0	GFRP	4,048	62.4	2,904	1.45	0.94	0.82	0.88	1.00	1.22
G0.83	300	1,088	0.83	228	203	38.7	GFRP	4,048	62.4	3,000	1.59	1.24	1.16	1.30	1.44	1.09
G0.83H	300	1,088	0.83	228	203	43.6	GFRP	4,048	62.4	3,166	1.56	0.78	0.82	0.78	1.05	1.14
G0.83V	300	1,088	0.83	228	203	43.6	GFRP	4,048	62.4	3,387	1.67	0.83	0.78	0.83	1.08	1.25
Farghaly and benmokrane (2013)																
G8N6	300	1,097	1.14	228	130	49.3	GFRP	2,280	47.6	1,477	1.96	1.12	1.16	0.91	0.98	0.96
G8N8	300	1,088	1.15	228	130	49.3	GFRP	4,054	51.9	1,906	1.95	1.59	1.60	1.10	1.15	0.95
C12N3	300	1,111	1.13	228	130	38.7	CFRP	856	120.0	1,191	1.79	1.10	1.12	0.93	1.08	0.94
C12N4	300	1,106	1.13	228	130	38.7	CFRP	1,521	144.0	1,601	1.81	1.55	1.60	1.21	1.16	0.94
Andermatt and Lubell (2013)																
A1N	310	257	1.07	100	100	40.2	GFRP	1,188	41.1	814	1.68	1.02	1.09	0.81	1.23	0.71
A2N	310	261	1.44	100	100	45.4	GFRP	1,188	41.1	472	1.57	0.68	0.72	0.52	1.31	0.90
A3N	310	261	2.02	100	100	41.3	GFRP	1,188	41.1	244	1.97	0.57	0.62	0.41	1.65	0.92
A4N	310	261	2.02	100	100	64.6	GFRP	1,188	41.1	192	1.21	0.32	0.35	0.18	1.14	0.94
B1N	300	503	1.08	200	200	40.5	GFRP	2,576	37.9	1,274	1.48	0.79	0.82	0.62	1.00	0.91
B2N	300	501	1.48	200	200	39.9	GFRP	2,576	37.9	800	1.64	0.67	0.78	0.49	1.26	0.91

Specimen ID	Beam Details						FRP Details			P_{exp} (kN)	ASSHTO-14	ACI 318-19	Eurocode 2	JSCE 07	Model I	Model II
	b (mm)	d (mm)	a/d	l_{b1} (mm)	l_{b2} (mm)	f_c' (MPa)	Type	A_{frp} (mm ²)	E_{frp} (GPa)		CSA S6-19					
											CSA S806-12					
											P_{exp}/P_{pre}					
B3N	300	502	2.07	200	200	41.2	GFRP	2,576	37.9	432	1.81	0.52	0.49	0.33	1.61	0.95
B4N	300	496	1.48	200	200	40.7	GFRP	3,168	41.1	830	1.52	0.62	0.63	0.62	1.19	0.99
B5H	300	497	1.48	200	200	66.4	GFRP	3,168	41.1	1,062	1.38	0.49	0.52	0.52	1.32	1.17
B6H	300	505	2.06	200	200	68.5	GFRP	2,576	37.9	376	1.12	0.32	0.43	0.22	1.18	1.21
C1N	301	889	1.10	330	330	51.6	GFRP	4,224	42.3	2,270	1.21	0.65	0.78	0.52	0.99	0.89
C2N	304	891	1.49	330	330	50.7	GFRP	4,224	42.3	1,324	1.25	0.51	0.49	0.51	1.15	0.96
Nehdi et al. (2008)																
CF-B-1	150	150	1.55	50	50	34.7	CFRP	254	134.0	185	1.96	0.21	1.13	0.98	0.62	0.77
CF-B-1.5	150	150	1.83	50	50	38.9	CFRP	254	134.0	154	2.48	0.97	0.63	0.82	0.78	0.77
CF-pl-1.5	150	150	1.83	50	50	37.4	CFRP	383	134.0	162	1.78	0.32	0.98	1.10	1.35	0.80
CF-pl-2.0	150	150	1.83	50	50	39.6	CFRP	509	134.0	185	1.65	0.94	1.43	0.93	1.21	0.78
CF-d-250	150	250	1.41	50	50	41.7	CFRP	506	134.0	298	2.20	0.81	1.62	1.32	0.77	0.83
CF-fc-60	150	150	1.36	50	50	63.1	CFRP	254	134.0	227	2.12	0.99	0.89	0.87	0.92	0.83
F-B-1	150	150	1.55	50	50	35.5	GFRP	290	40.8	135	1.98	1.01	1.05	0.54	1.12	0.90
F-B-1.5	150	150	1.83	50	50	48.0	GFRP	290	40.8	122	1.50	0.14	0.76	0.92	1.21	1.18
F-pl-1.5	150	150	1.83	50	50	48.0	GFRP	385	40.8	147	1.69	0.69	0.69	1.22	1.32	0.98
F-pl-2.0	150	150	1.83	50	50	35.2	GFRP	520	40.8	122	1.32	0.98	0.71	0.63	1.22	0.87
F-d-250	150	150	1.41	50	50	42.0	GFRP	313	40.8	243	2.70	0.62	1.38	1.01	0.80	0.68
Bediwy et al. (forthcoming a and b)																
X-X-0.0-0.6	250	512.8	1.18	200	150	45.0	GFRP	770	63.2	716	1.25	0.58	0.70	0.84	1.34	0.81
X-X-0.0-1.0	250	521.3	1.18	200	150	47.0	GFRP	1,268	63.2	800	1.17	0.67	0.65	0.72	1.41	0.85
X-X-0.0-1.4	250	509.3	1.18	200	150	48.0	GFRP	1,783	63.2	900	1.11	0.71	0.76	0.81	1.44	0.91
Kim et al (2014)																
A3D9M-1.4	200	250	1.40	100	100	26.1	AFRP	190	80.7	136	1.32	0.50	0.41	0.36	1.06	1.05

Specimen ID	Beam Details						FRP Details			P_{exp} (kN)	ASSHTO-14	ACI 318-19	Eurocode 2	JSCE 07	Model I	Model II
	b (mm)	d (mm)	a/d	l_{b1} (mm)	l_{b2} (mm)	f_c' (MPa)	Type	A_{frp} (mm ²)	E_{frp} (GPa)		CSA S6-19					
											CSA S806-12					
											P_{exp}/P_{pre}	P_{exp}/P_{pre}	P_{exp}/P_{pre}	P_{exp}/P_{pre}	P_{exp}/P_{pre}	P_{exp}/P_{pre}
A3D9M-1.7	200	250	1.70	100	100	26.1	AFRP	190	80.7	99	1.43	0.46	0.52	0.34	1.22	1.22
A3D9M-2.1	200	250	2.10	100	100	26.1	AFRP	190	80.7	88	2.10	0.51	0.32	0.38	1.24	1.06
A4D9M-1.7	200	250	1.70	100	100	26.1	AFRP	255	80.7	121	1.56	0.55	0.51	0.41	0.91	1.00
A5D9M-1.7	200	250	1.70	100	100	26.1	AFRP	320	80.7	134	1.58	0.59	0.48	0.45	1.40	0.91
A3D9S-1.7	200	190	1.70	100	100	26.1	AFRP	190	80.7	110	1.35	0.48	0.46	0.42	1.32	1.08
A5D9L-1.7	200	310	1.70	100	100	26.1	AFRP	316	80.7	134	1.64	0.58	0.29	0.38	1.47	0.93
C3D9M-1.4	200	250	1.40	100	100	26.1	CFRP	190	120.2	169	1.38	0.62	0.51	0.48	1.10	0.96
C3D9M-1.7	200	250	1.70	100	100	26.1	CFRP	190	120.2	107	1.32	0.49	0.42	0.36	1.12	1.13
C3D9M-2.1	200	250	2.10	100	100	26.1	CFRP	190	120.2	53	1.10	0.31	0.32	0.23	1.00	1.14
C4D9M-1.7	200	250	1.70	100	100	26.1	CFRP	255	120.2	96	1.21	0.42	0.28	0.33	0.95	1.35
C5D9M-1.7	200	250	1.70	100	100	26.1	CFRP	320	120.2	151	1.52	0.68	0.52	0.51	1.23	0.92
C3D9S-1.7	200	190	1.70	100	100	26.1	CFRP	190	120.2	105	1.48	0.42	0.41	0.32	1.22	1.13
C5D9L-1.7	200	310	1.70	100	100	26.1	CFRP	316	120.2	146	1.13	0.62	0.32	0.29	1.01	0.98
Mean											1.63	0.72	0.75	0.68	1.18	0.98
SD											0.38	0.31	0.35	0.31	0.21	0.09
CoV (%)											23.2	43.1	46.3	46.5	17.5	9.30
R ²											0.96	0.92	0.92	0.90	0.98	0.95

b = beam width; d = effective depth; l_{b1} = loading plate width; l_{b2} = supporting plate width; f_c' = concrete compressive strength; A_{frp} = area of reinforcement; E_{frp} = modulus of elasticity of longitudinal bar; P_{exp} = ultimate capacity of the beam

Table 9.5: Test data for steel-FRC deep beams

Specimen ID	Beam						Reinforcement			Fiber					P_{exp} (kN)	ASSHTO-14	ACI 318-19	Eurocode 2	JSCE 07	Model III	Model IV
	b (mm)	d (mm)	a/d	l_{b1} (mm)	l_{b2} (mm)	f_c (MPa)	Type	Area(mm ²)	E (GPa)	L (mm)	D (mm)	V_f (%)	Type	E (GPa)		CSA S6-19					
																CSA S806-12					
																P_{exp}/P_{pre}	P_{exp}/P_{pre}	P_{exp}/P_{pre}	P_{exp}/P_{pre}	P_{exp}/P_{pre}	P_{exp}/P_{pre}
Campione (2012)																					
1	100	700.0	1.30	218	218	48.0	Steel	1,050	200	-	-	0.00	-	-	960	2.29	2.91	2.04	2.14	-	-
2	100	700.0	1.30	218	218	48.0	Steel	1,050	200	30	0.50	1.00	Steel	200	1,160	2.77	3.52	2.46	2.59	2.60	1.98
Tuchscherer and Quesada (2015)																					
00-03	300	435.0	1.40	75	75	29.4	Steel	1,256	200	-	-	0.00	-	-	672	2.53	1.48	1.79	1.53	-	-
00-02	300	435.0	1.40	75	75	29.8	Steel	1,256	200	-	-	0.00	-	-	784	2.94	1.73	2.09	1.79	-	-
00-00	300	435.0	1.40	75	75	29.8	Steel	1,256	200	-	-	0.00	-	-	864	3.24	3.57	2.30	2.63	-	-
05-03	300	435.0	1.40	75	75	30.5	Steel	1,256	200	50	1.0	0.50	Steel	200	828	3.04	1.77	2.15	1.84	1.92	1.12
05-02	300	435.0	1.40	75	75	30.5	Steel	1,256	200	50	1.0	0.50	Steel	200	734	2.70	1.57	1.90	1.63	1.71	1.21
05-00	300	435.0	1.40	75	75	30.5	Steel	1,256	200	50	1.0	0.50	Steel	200	934	3.43	3.75	2.42	2.76	2.17	1.14
10-03	300	435.0	1.40	75	75	31.3	Steel	1,256	200	50	1.0	1.00	Steel	200	738	2.59	1.49	1.82	1.54	1.29	1.65
10-02	300	435.0	1.40	75	75	32.3	Steel	1,256	200	50	1.0	1.00	Steel	200	832	2.92	1.68	2.05	1.74	1.45	1.22
10-00	300	435.0	1.40	75	75	32.3	Steel	1,256	200	50	1.0	1.00	Steel	200	938	3.29	3.55	2.31	2.62	1.63	0.88
Adebar et al. (1997)																					
FC1	150	558.0	1.35	75	75	60.0	Steel	1,800	200	-	-	0.00	-	-	298	0.62	0.76	0.57	0.56	-	-
FC2	150	558.0	1.35	75	75	60.0	Steel	1,800	200	30	0.50	0.75	Steel	200	552	1.14	1.41	1.05	1.04	1.06	1.12
FC3	150	558.0	1.35	75	75	60.0	Steel	1,800	200	30	0.50	1.50	Steel	200	648	1.34	1.66	1.24	1.22	0.91	1.24
FC5	150	558.0	1.35	75	75	60.0	Steel	1,800	200	30	0.50	0.75	Steel	200	474	0.98	1.21	0.90	0.89	0.91	1.06
FC6	150	558.0	1.35	75	75	60.0	Steel	1,800	200	30	0.50	1.50	Steel	200	556	1.15	1.42	1.06	1.05	0.78	1.14
FC7	150	558.0	1.35	75	75	57.0	Steel	1,800	200	-	-	0.00	-	-	244	0.52	0.66	0.48	0.48	-	-
FC8	150	558.0	1.35	75	75	57.0	Steel	1,800	200	30	0.50	0.40	Steel	200	408	0.88	1.10	0.81	0.81	0.97	0.98
FC9	150	558.0	1.35	75	75	57.0	Steel	1,800	200	30	0.50	0.60	Steel	200	464	1.00	1.25	0.92	0.92	0.98	1.08

Specimen ID	Beam						Reinforcement			Fiber					P_{exp} (kN)	ASSHTO-14	ACI 318-19	Eurocode 2	JSCE 07	Model III	Model IV
	b (mm)	d (mm)	a/d	l_{b1} (mm)	l_{b2} (mm)	f_c (MPa)	Type	Area(mm ²)	E (GPa)	L (mm)	D (mm)	V_f (%)	Type	E (GPa)		CSA S6-19					
																CSA S806-12					
																P_{exp}/P_{pre}	P_{exp}/P_{pre}	P_{exp}/P_{pre}	P_{exp}/P_{pre}	P_{exp}/P_{pre}	P_{exp}/P_{pre}
FC10	150	558.0	1.35	75	75	57.0	Steel	1,800	200	50	0.50	0.40	Steel	200	494	1.06	1.33	0.98	0.98	1.00	1.02
FC11	150	558.0	1.35	75	75	57.0	Steel	1,800	200	50	0.50	0.60	Steel	200	474	1.02	1.28	0.94	0.94	0.82	0.98
Ashour et al. (1992)																					
B-1-0.5-A	125	215.0	1.18	75	75	99.0	Steel	764	200	60	0.80	0.50	Steel	200	264	0.77	0.64	0.60	0.47	0.94	1.17
B-1-1.0-A	125	215.0	1.18	75	75	95.3	Steel	764	200	60	0.80	1.00	Steel	200	411	1.23	1.04	0.95	0.77	1.15	1.32
B-1-1.5-A	125	215.0	1.18	75	75	96.4	Steel	764	200	60	0.80	1.50	Steel	200	435	1.29	1.09	1.00	0.80	0.99	1.44
Mean																1.87	1.74	1.45	1.41	1.32	1.19
SD																1.00	0.95	0.67	0.72	0.52	0.26
CoV (%)																53.8	54.9	45.9	51.5	39.8	21.8
R ²																0.49	0.23	0.52	0.75	0.79	0.88

b = beam width; d = effective depth; l_{b1} = loading plate width; l_{b2} = supporting plate width; f_c' = concrete compressive strength; A_{frp} = area of reinforcement; E = modulus of elasticity of longitudinal bar; P_{exp} = ultimate capacity of the beam; L = discrete fiber length; D = discrete fiber diameter; V_f = dosage of discrete fibers

9.5 Review of Current Code Provisions for STM

9.5.1 The CSA codes provisions (CSA S806-12 and CSA S6-19) for STM

The Canadian standards for FRP-RC structures, CSA/S806-12 (CSA 2017) and highway bridges, CSA/S6-19 (CSA 2019a) have permitted the use of STM for the design of FRP-RC deep beams.

It stated that the compressive strength of any concrete strut shall not exceed $\phi_c f_{cu} A_{cs}$, where ϕ_c is strength reduction factor of concrete, and A_{cs} is the cross-sectional area of the strut.

The limiting compressive stress of a concrete strut crossed by a tension tie was computed based on the modified compression field theory that predicts that failure occurs when the shear stress at the crack faces, required for equilibrium, reaches the maximum shear stress that can be transmitted by aggregate interlock. It was firstly introduced by Vecchiano and Collins (1986), and later adopted by the Canadian standard associations (CSA), and is calculated by:

$$f_{cu} = \frac{f'_c}{0.8 + 170\varepsilon_1} \leq 0.85 f'_c \quad \text{Equation 9.1}$$

where ε_1 represents the transverse tensile strain within the inclined concrete strut and it is given as $\varepsilon_1 = \varepsilon_f + (\varepsilon_f + 0.002) \cot^2 \theta$, where θ is the angle between the concrete strut and the FRP tie, while ε_f is the tensile strain developed in the FRP tension tie crossing the strut.

The tensile force in the tie shall not exceed $0.65 \phi_F F_{FU} A_{FT}$ where F_{FU} and A_{FT} are the ultimate strength of the bar and the area of reinforcement, respectively. For the nodal zones, the allowable stress developed in the node regions bounded by struts and bearing areas (CCC node), anchoring a tie in only one direction (CCT node), or anchoring ties in more than one direction (CTT node) shall not exceed $0.85 \phi_c f'_c$, $0.85 \phi_c f'_c$, and $0.85 \phi_c f'_c$, respectively, unless a special confinement is adopted.

9.5.2 AASHTO-LRFD code provisions (AASHTO LRFD-14) for STM

The AASHTO LRFD bridge design specifications referred to using the STM for the design of D-regions. The AASHTO approach for the allowable stress in the strut is also based on the modified compression field theory. Thus, the compressive strength of the strut f_{cu} calculated using the same equation of the CSA codes (Equation 9.1). For the nodal stress limits, the AASHTO-LRFD (2014) also specified factors based on the type of node similar to the factors stipulated in the Canadian codes.

9.5.3 ACI code provisions (ACI 318-19) for STM

The ACI 440.1R-15 (ACI 2015) has not yet considered the use of strut-and-tie models (STMs) for the design of FRP-RC deep beams. However, ACI 318-19 (ACI 2019) provides clear guidance regarding the use of STMs for the design of steel-RC deep beams.

The effective compressive strength of the concrete strut shall be taken as:

$$f_{ce} = 0.85\beta_c\beta_s f'_c \quad \text{Equation 9.2}$$

where β_s is a reduction factor, which accounts for the efficiency of the concrete strut. It depends on several factors such as the stress condition within the strut and the location of the strut, which ranged from 0.4 to 1.0, while β_c is taking into account the effect of concrete confinement on the compressive strength of a strut. The nominal tensile strength of a tie F_{nt} shall be calculated by $A_{st} f_y$. For nodal zones, when no confining reinforcement is provided, ACI 318-19 (ACI 2019) limits the compressive stress on the face of a nodal zone to:

$$f_{ce} = 0.85\beta_n\beta_c f'_c \quad \text{Equation 9.3}$$

β_n shall be taken as 1.0, 0.8, or 0.6 in case of CCC, CCT, or CTT nodes.

9.5.4 Eurocode 2 code provisions (BS EN 1992-1-1-2004) for STM

The Eurocode 2 included provisions for the design of deep beams using STM without any specifics for FRP-RC members. The suitability of these provisions to predict the shear capacity of FRP-RC deep beams was investigated by Mohamed Dharir (2017), who concluded that Eurocode 2 overestimated the shear strength and provided arbitrary and inconsistent results.

The design strength for concrete strut in a region with transverse compressive stress can be computed using the equation:

$$\sigma_{Rd,max} = f_{cd} \quad \text{Equation 9.4}$$

where f_{cd} is design value of concrete compressive strength. On the other hand, if concrete strut is prone to transverse tensile stresses, the allowable compressive stress is given by:

$$\sigma_{Rd,max} = 0.6v' f_{cd} \quad \text{Equation 9.5}$$

where v' is a reduction factor for concrete cracked in shear and it equals to $(1 - f_{ck}/250)$, where f_{ck} is characteristic compressive cylinder strength of concrete at 28 days. The nominal tensile strength of a tie F_{nt} shall be calculated by $A_{st} f_y$. For nodal zones, Eurocode 2 limits the compressive stress on the face of a nodal zone to:

$$\sigma_{Rd,max} = k_1 v' f_{cd} \quad \text{Equation 9.6}$$

where k_1 shall be taken as 1.0, 0.85, or 0.75 in case of CCC, CCT, or CTT nodes.

9.5.5 JSCE code provisions (JSCE 2007) for STM

The Japanese recommendations for design and construction of concrete structures using continuous fibre reinforcing materials (JSCE 1997) did not permit the use of STM for the design of deep beams. Conversely, JSCE (2007) for steel-RC structures has specified the strength of

concrete strut by $f'_{cd,eff} A_c / \gamma_b$, where $f'_{cd,eff}$ is the effective strength of concrete, and it is calculated by:

$$f'_{cd,eff} = v_1 v_2 f'_{cd} \quad \text{Equation 9.7}$$

where v_1 is a reduction factor to consider the difference between the compressive strength of concrete cast in the field and the strength obtained in controlled environment such as laboratory, and v_2 is a reduction factor to take into account the effect of transverse reinforcement.

The strength of tie shall be obtained by multiplying the cross-sectional area of the reinforcement by the design yield strength. For nodal zones, the compressive stress on the face of a nodal zone equals to the effective strength of concrete $f'_{cd,eff}$ for all types of nodes (CCC, CCT, and CTT).

9.6 Review of Models Proposed in the Literature

9.6.1 Model I (Mohamed et al. 2017)

Mohamed et al. (2017) proposed a simple model to calculate the strut efficiency (reduction) factor (β_s) of the ACI-318 model in order to predict the shear capacity of simply supported deep beams reinforced with FRP bars. This model [Equation 9.8] considered the effect of different parameters such as concrete compressive strength (f'_c), shear span-to-depth ratio (a/d), and strain of longitudinal reinforcement ε_l , which were neglected in the ACI 318 provisions. In addition, using the efficiency factor provided by the CSA provisions led to un-necessarily underestimated capacity of the deep beam.

$$\beta_s = 0.5 \frac{1}{\sqrt{f'_c}} \frac{1}{(a/d)^{0.8}} \frac{1}{\sqrt{\varepsilon_l}} \quad \text{Equation 9.8}$$

where ε_l is given by $\varepsilon_l = \varepsilon_f + (\varepsilon_f + 0.002) \cot^2 \theta$, and a/d is limited to unity for specimens having a a/d of less than 1.0, to prevent over-stressing the strut.

9.6.2 Model II (Dharir 2017)

This model was proposed based on the model provided by Sagasetta (2008) to estimate the shear strength of steel-RC deep beams. However, for FRP-RC deep beams, the inclined concrete strut is expected to be heavily cracked near the bottom node, due to the high transverse tensile strain caused by the relatively low modulus of elasticity of FRPs. In addition, it does not account for neither the a/d ratio nor the axial rigidity of the longitudinal FRP reinforcement, which is essential when assessing the shear strength of FRP-RC deep beams. In this model, the shear capacity of the beam is predicted through iteration process by the assuming the angle θ and then using the following equations:

$$P = 4 \tan \theta \left[d - \left(a - \frac{\ell_t (2 - n_{1p})}{4} \right) \tan \theta \right] b v f_{cd} \quad \text{Equation 9.9}$$

Where P is the total load, ℓ_t is the length of top bearing plate, n_{1p} is the number of loading points (one or two), θ and f_{cd} were previously defined.

$$\varepsilon_1 = \frac{P}{2A_f E_f \tan \theta} + \left(0.002 + \frac{P}{2A_f E_f \tan \theta} \right) \cot^2 \theta \quad \text{Equation 9.10}$$

where A_f is the area of longitudinal FRP reinforcement, and E_f is the modulus of elasticity of FRPs.

$$P = \frac{2(l_b \sin^2 \theta + c \sin 2\theta) b f_{cd}}{0.8 + 170\varepsilon_1} \quad \text{Equation 9.11}$$

where l_b is the length of bottom bearing plate, and c is the concrete cover.

9.6.3 Model III (Ashour et al. 1992)

Ashour et al. (1992) proposed an empirical equation to predict the shear strength of steel-FRC deep beams. Based on 18 tests conducted on deep beams, the following equation, which is a revised version of Zsutty's equation (1968) to include the contribution of the steel fibers, was introduced:

$$P_u = \left[2.5 \frac{d}{a} \left(2.11 \sqrt[3]{f'_c} + 7.F \right) \left(\rho_s \frac{d}{a} \right)^{0.333} + 1.7F \left(2.5 - \frac{a}{d} \right) \right] bd \quad \text{Equation 9.12}$$

$$F = \frac{V_f \ell_f}{d_f}$$

where P_u is the ultimate strength of the beam in N, f'_c is the compressive strength of concrete in MPa, ρ_s is the longitudinal reinforcement ratio, V_f is the fiber volume ratio, ℓ_f is the fiber length in mm, d_f is the fiber diameter in mm, b is the cross-sectional width in mm, and d is the effective depth in mm.

9.6.4 Model IV (Shahnewaz and Alam 2014)

A database of 358 beams were collected and divided into two groups of deep beams and slender beams based on a/d . Half of the data from each group was selected randomly from the database and used to develop Equation 9.13. A factorial design was used to identify the parameters that significantly affected the shear strength of SFRC beams. From the factorial analysis, it was observed that a/d , f'_c , ρ , ℓ_f/d_f , and V_f are the most significant parameters that affect the shear strength of fibrous deep beams; therefore, the following equation was proposed:

$$P_u = \left[\begin{array}{l} 0.2 + 0.034 f'_c + 19 \rho^{0.087} - 5.8 \left(\frac{a}{d} \right)^{1/2} + 3.4 V_f^{0.4} - 800 \left(\frac{\ell_f}{d_f} \right)^{-1.6} \\ -12 \left(\left(\frac{a}{d} \right) V_f \right)^{0.05} - 197 \left(\left(\frac{a}{d} \right) \left(\frac{\ell_f}{d_f} \right) \right)^{-1.4} + 105 \left(V_f \left(\frac{\ell_f}{d_f} \right) \right)^{-2.12} \end{array} \right] bd \quad \text{Equation 9.13}$$

where P_u , f'_c , ρ_s , V_f , ℓ_f , d_f , b , and d were previously defined in *Model III*.

9.7 Assessment of Current Design Models

Table 9.4 lists comparisons between the experimental and predicted shear capacity of the simply supported FRP-RC deep beams. The predicted values for all beams were calculated while all strength and material factors were set to 1.0. As mentioned above, the CSA/S806-12 (CSA 2017) included provision for STM for FRP-RC deep beams, while the American guidelines for FRP-RC members, ACI 440.1R-15 (ACI 2015), do not provide any provisions for the design of deep beams. However, the design provisions in the ACI 318-19 code, the Eurocode 2, and JSCE for steel-RC structures can be applied to the FRP-RC deep beams because the beam capacity was governed by the strength of the compression strut for all specimens rather than the capacity of the node or the tie. As can be noticed in Figure 9.6, in general, the results of the predicted capacities for all codes were either above or under the line of equality, confirming that each provision had shortcomings. The CSA/S806-12 (CSA 2017), CSA/S6-19 (CSA 2019a), and AASHTO LRFD-14 (AASHTO 2014) highly underestimate the capacity of the beams. These codes adopted the same model to estimate the shear strength of deep beams. Therefore, these models predicted the capacity with a mean P_{exp}/P_{pred} , coefficient of variation (CoV) and coefficient of determination (R^2) of 1.63 ± 0.38 , 23.2% and 0.96, respectively. This was attributed to that the capacity of the compression strut in the CSA/S806 is adversely affected by the amount of longitudinal strain (ϵ_l) that could reach 0.01 or more in GFRP-RC beams bars owing to the low modulus of elasticity of the bars, which leads to significantly conservative predictions.

On the other hand, the ACI 318-19 (2019) model highly overestimated the strength with a mean P_{exp}/P_{pred} , CoV and R^2 of 0.72 ± 0.31 , 43.1%, and 0.92, respectively. Similarly, for the Eurocode 2 (2004), these values were 0.75 ± 0.35 , 46.3%, and 0.92, respectively. The JSCE (2007) was also

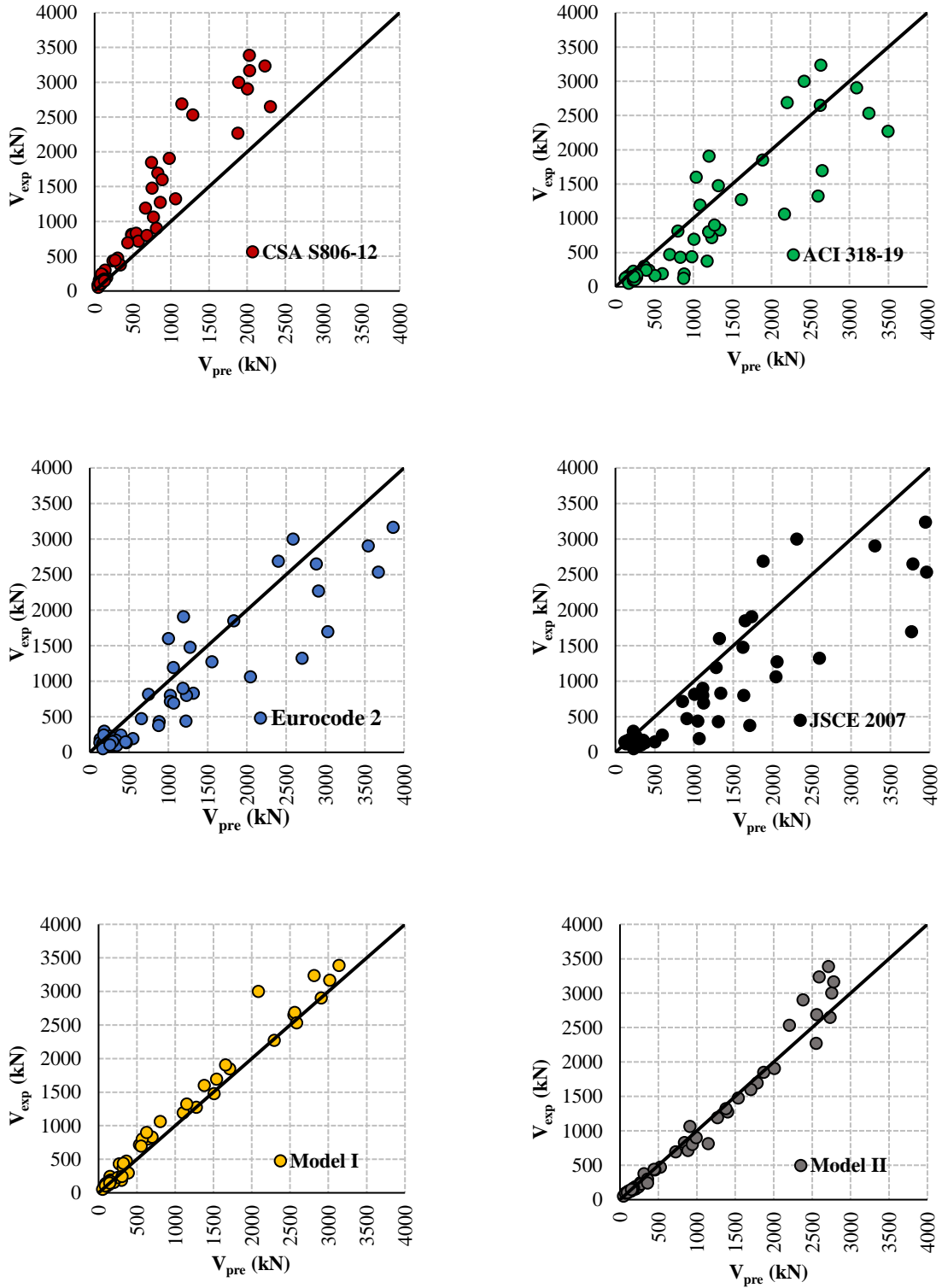


Figure 9.6: Prediction of available models for FRP-RC deep beams

unable to accurately predict the capacity of the FRP-RC deep beams with a mean experimental-to-predicted value of 0.68 ± 0.31 , 46.5%, and 0.90, respectively. This may be attributed to neglecting the effect of concrete softening in the inclined strut imparted by the high tensile strains in the FRP reinforcement. Furthermore, such provisions do not take into account the key factor of shear span-to-depth ratio in calculating the capacity of the beams, in addition to using constant values for the efficiency factor that only varies with the presence of transverse reinforcement led to unsafe scattered estimation of the capacity.

Similarly, Table 9.5 lists comparisons between the experimental and predicted shear capacity of simply supported steel-FRC deep beams. The STM provisions stated in the previously mentioned codes failed to accurately predict the experimental capacity of the fibrous deep beams reinforced with steel bars. This deficiency was more evident in the case of incorporating discrete fibers. Consequently, it can be concluded that the STMs stipulated in the CSA/S806-12, CSA/S6-19, ASHTO LRFD-14, ACI 318-19, Eurocode 2, and JSCE did not show reasonable prediction of the capacity of FRP-RC or steel/FRP-FRC deep beams, and therefore, the model must be modified.

Considering the previous deficiencies in the STMs reported in the codes, Mohamed et al. 2017 and Dharir (2017) proposed their STMs to mitigate these weaknesses and to reasonably predict the shear capacity of FRP deep beams. Thus, these models were evaluated against the results of FRP-RC or FRP-FRC deep beams. *Model I*, proposed by Mohamed et al. (2017), provided reasonable estimates for FRP-RC deep beams with a mean P_{exp}/P_{pred} , CoV and R^2 of 1.18 ± 0.21 , 17.5% and 0.98, respectively. This is a better mean than that of the STM provisions provided by the codes herein with a comparable R^2 value. Out of all models, *Model II* (Dharir 2017) produced the best estimates with a mean P_{exp}/P_{pred} , CoV and R^2 of 0.98 ± 0.09 , 9.3% and 0.95, respectively, it provides the least scattered results and best fit for FRP-RC deep beams.

On the other hand, since *Model III* (Ashour et al. 1992) and *Model IV* (Shahnewaz and Allam 2014) were mainly developed to predict the shear strength of FRC deep beams, these models were evaluated against the results of steel-FRC deep beams (see Table 9.5). *Model III* gave slightly conservative estimates, since the mean P_{exp}/P_{pred} , CoV and R^2 were 1.32 ± 0.52 , 39.8%, and 0.79, respectively, which may be attributed to the small number of specimens used to validate the model (18 specimens that were conducted by the authors). Conversely, *Model IV* provided reasonable prediction for steel-FRC deep beams with a mean P_{exp}/P_{pred} , CoV and R^2 were 1.19 ± 0.26 , 21.8%, and 0.88, respectively, as a wide population of more than 180 specimens, reinforced with discrete steel fibers and longitudinal steel bars, were utilized to develop and validate this equation.

9.8 Proposed Equation and Verification

Model I (Mohamed et al. 2017) and *Model II* (Dharir 2017) provide consistent and reasonable predictions for simply supported FRP-RC deep beams, which indicates that their equation fits well with the experimental results. However, such models are not applicable for FRP beams poured with FRC (see Table 9.6 and Figure 9.7), since the mean P_{exp}/P_{pred} and CoV for *Model I* and *Model II* were 1.6 ± 0.14 and 9%, and 1.4 ± 0.3 and 22%, respectively, which was attributed to that both models neglected the effect of adding fibers in enhancing the capacity of the beams. Consistently, *Model III* and *Model IV* reasonably predicted the shear strength for steel-FRC deep beams; however, when those models were employed to predict the shear strength of fibrous beams reinforced longitudinally with FRP bars, *Model III* gave conservative estimates with a mean P_{exp}/P_{pred} , CoV and R^2 of 1.36 ± 0.42 , 31.2%, and 0.72, respectively, and *Model IV* gave negative shear strength values of the beams reinforced with discrete fibers other than steel (e.g. basalt fiber pellets).

Table 9.6: Test data for FRP-FRC deep beams

Specimen ID	Beam						Reinforcement			Fiber					P_{exp} (kN)	ASSHTO-14	ACI 318-19	Eurocode 2	JSCE 07	Model I	Model II	Model III	Model IV	Proposed model								
	b (mm)	d (mm)	a/d	l_{b1} (mm)	l_{b2} (mm)	f_c (MPa)	Type	Area(mm ²)	E (GPa)	L (mm)	D (mm)	V_f (%)	Type	E (GPa)		CSA S6-19									CSA S806-12							
																P_{exp}/P_{pre}									P_{exp}/P_{pre}							
																P_{exp}/P_{pre}									P_{exp}/P_{pre}							
Bediwy et al. (forthcoming)																																
L-B-2.5-0.6	250	521.3	1.18	200	150	47.0	GFRP	770	63.2	36	1.80	2.50	Basalt	65	851	1.45	1.00	0.70	0.72	1.38	1.20	1.45	N/A	1.10								
L-B-2.5-1.0	250	512.8	1.18	200	150	48.0	GFRP	1,268	63.2	36	1.80	2.50	Basalt	65	900	1.30	1.10	0.77	0.81	1.44	1.24	1.15	N/A	0.97								
L-S-1.0-0.6	250	512.8	1.18	200	150	46.0	GFRP	770	63.2	30	0.65	1.00	Steel	200	920	1.58	1.10	0.76	0.83	1.49	1.19	0.87	1.81	1.26								
L-S-1.0-1.0	250	521.3	1.18	200	150	45.0	GFRP	1,268	63.2	30	0.65	1.00	Steel	200	981	1.48	1.28	0.89	0.94	1.57	1.48	0.78	1.45	1.10								
Bediwy and El-Salakawy (forthcoming)																																
L-B-4.5-1.0	250	521.3	1.18	200	150	46.0	GFRP	1,268	63.2	36	1.80	4.50	Basalt	65	1,005	1.49	1.29	0.89	0.83	1.61	1.35	1.72	N/A	1.03								
L-B-6.9-1.0	250	521.3	1.18	200	150	46.0	GFRP	1,268	63.2	36	1.80	6.90	Basalt	65	1,096	1.61	1.40	0.97	0.91	1.75	1.42	1.62	N/A	1.02								
A-B-4.5-1.0	250	521.3	1.18	200	150	71.0	GFRP	1,268	63.2	36	1.80	4.50	Basalt	65	1,238	1.41	1.03	0.81	0.72	1.74	2.10	1.85	N/A	0.86								
Mean																1.47	1.21	0.83	0.83	1.60	1.40	1.36	1.63	1.04								
SD																0.10	0.15	0.09	0.08	0.14	0.30	0.42	0.25	0.12								
CoV (%)																7.10	12.9	11.3	10.3	9.00	22.0	31.2	15.6	11.2								
R ²																0.87	0.68	0.63	0.82	0.84	0.54	0.72	-	0.94								

b = beam width; d = effective depth; l_{b1} = loading plate width; l_{b2} = supporting plate width; f_c' = concrete compressive strength; A_{frp} = area of reinforcement; E = modulus of elasticity of longitudinal bar; P_{exp} = ultimate capacity of the beam; L = discrete fiber length; D = discrete fiber diameter; V_f = dosage of discrete fibers

Therefore, the authors conducted this research program to test FRC-deep beams reinforced with FRP bars in order to develop a model (Equation 9.14) for accurately capturing the shear capacity of GFRP-FRC deep beams. The equation was proposed through linear regression analysis of the present experimental results of FRP beams containing BF pellets with a dosage range between 2.5 and 6.9% or SF with a dosage of 1%, reinforcement ratio of 0.6 to 1%, and compressive strength of 45-70 MPa.

$$P_{tot} = \left[0.255 f'_c \frac{d}{a} (F_1)^{0.4} + .015 \left(f'_c \frac{a}{d} \right)^{0.05} (F_2)^{0.1} (F_3 - 1) \right] bd \quad \text{Equation 9.14}$$

$$F_1 = \rho_f \frac{E_f}{E_s} \quad \text{Equation 9.14a}$$

$$F_2 = \frac{E_{BF}}{E_{SF}} \frac{X_a}{H} \quad \text{Equation 9.14b}$$

$$F_3 = \frac{V_f l_f}{d_f} \quad \text{Equation 9.14c}$$

where P_{tot} is the total capacity of the beam in N, ρ_f the longitudinal reinforcement ratio in percent, E_f the modulus of elasticity of the FRP bar in GPa, E_s the modulus of elasticity steel bar (200 GPa), E_{BF} the modulus of elasticity of basalt fiber pellets in GPa, E_{SF} the modulus of elasticity of steel fibers in GPa, X_a is the height of the fibrous layer in mm, H is the total height of the specimen, V_f the fiber volume ratio in percent, l_f the fiber length in mm, d_f the fiber diameter in mm, b the cross-sectional width in mm, and d the effective depth in mm.

The test-to-predicted ratios using the proposed *Model* are listed in Table 9.6 and shown in Figure 9.7. This equation produced good predictions with a mean P_{exp}/P_{pred} of 1.04 ± 0.12 , a CoV of 11%, and R^2 of 0.94. Furthermore, the value for the coefficient of determination of 0.94 close to unity, indicating a strong association between the actual and predicted capacities. In addition, this model

explains all the variability factors of the FRP-FRC deep beams with a reasonable degree of accuracy.

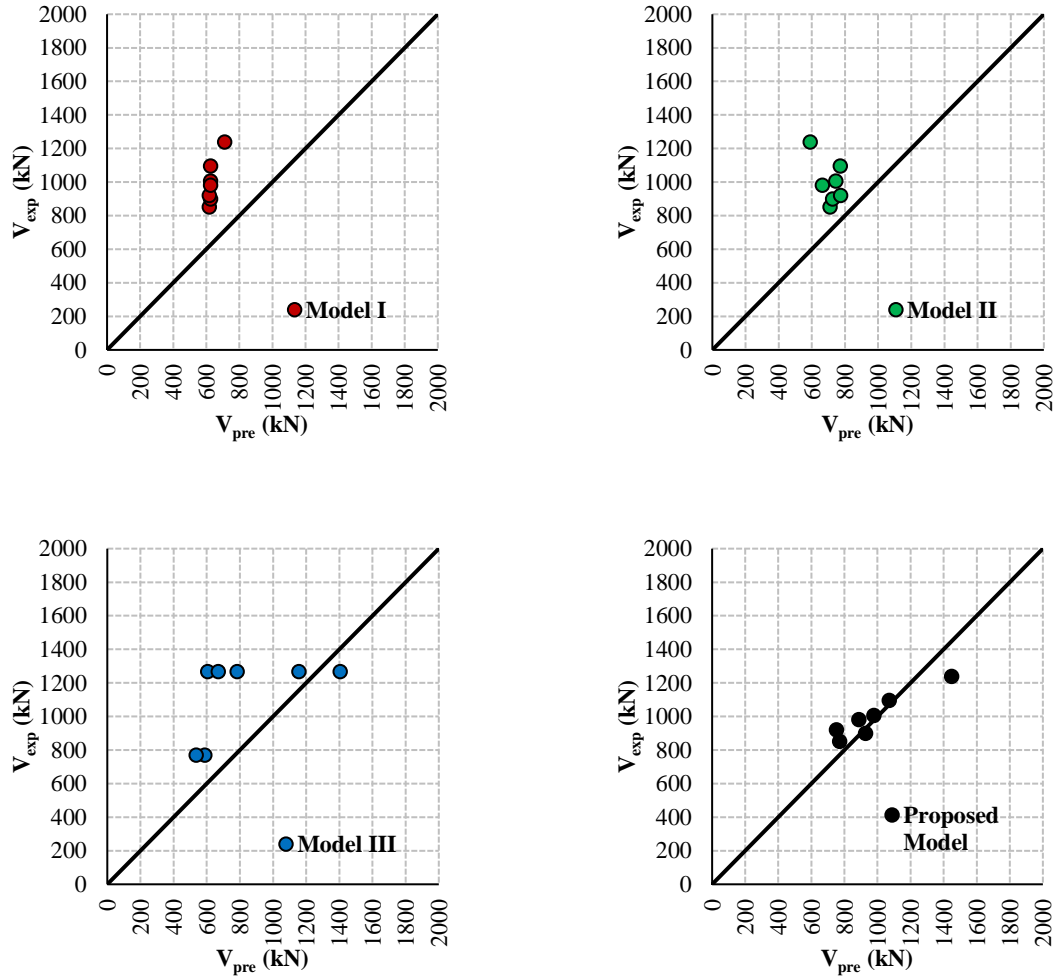


Figure 9.7: Prediction of available models for FRP-FRC deep beams

9.9 Conclusions

Based on the experimental and analytical investigations, the following conclusions can be drawn:

- The STMs in different design provisions was assessed. The CSA S806-12 (CSA 2017), CSA S6-19 (CSA 2019a), and AASHTO LRFD-14 (AASHTO 2014) underestimated the ultimate capacity of FRP-RC deep beams with a mean P_{exp}/P_{pred} of 1.63 ± 0.38 , which

could lead to uneconomic design. On the other hand, the ACI 318-19 (ACI 2019), Eurocode 2 (2004), and JSCE (2007) highly overestimated the capacity with a mean P_{exp}/P_{pred} of 0.72 ± 0.31 , 0.75 ± 0.35 , and 0.68 ± 0.31 , respectively, owing to neglecting the effects of major parameters such as the concrete softening of the inclined strut and the shear span-to-depth ratio.

- Two models were proposed by Mohamed et al. (2017), *Model I*, and Dharir (2017), *Model II*, to mitigate the deficiencies in the STMs stipulated by the design codes. *Model I* provided reasonable predictions of FRP-RC deep beams with a mean P_{exp}/P_{pred} , CoV, and R^2 of 1.18 ± 0.21 , 17.5% and 0.98, respectively. For *Model II* (Dharir 2017), these values were 0.98 ± 0.09 , 9.3% and 0.95, respectively. In addition, *Model III* and *Model IV*, proposed by Ashour et al. (1992) and Shahnewaz and Alam (2014), gave consistent and reasonable predictions of SFRC-deep beams reinforced longitudinally with steel bars with the mean P_{exp}/P_{pred} , CoV, and R^2 for both models were 1.32 ± 0.52 , 39.8%, and 0.79, and 1.19 ± 0.26 , 21.8%, and 0.88, respectively. On the other hand, all models *Model I*, *Model II*, *Model III* and *Model IV* underestimated the capacity of FRP deep beams poured with discrete fibers, since the mean P_{exp}/P_{pred} and CoV for *Model I*, *Model II* and *Model III* were 1.6 ± 0.14 and 9%, 1.4 ± 0.3 and 22%, and 1.35 ± 0.42 and 31.2%, respectively. Therefore, a new model was proposed to account for the effect of incorporating different types of discrete fibers into the beam either as a layer in the tie zone or entirely over the whole depth. The proposed model produced good predictions for FRP-FRC deep beams with a mean P_{exp}/P_{pred} and R^2 of 1.04 ± 0.12 and 0.94, respectively.

CHAPTER 10: CONCLUSIONS AND FUTURE WORK

10.1 Summary

This pioneer research study investigated the behaviour of high-strength nano-modified cementitious composites (BFRCC) incorporating 40% slag and reinforced with BP under ambient and severe environmental conditions, and the feasibility of implementing the BFRCC in large-scale structural elements. The study consisted of three main phases: Phase *I* that focused on experimentally assessing the mechanical performance of BFRCC small-scale specimens before and after exposure to consecutive freeze-thaw and wet-dry cycles simulating consecutive winter and summer seasons in cold regions, phase *II* that investigated in more depth the pull-out capacity of GFRP bars embedded in BFRCC with different dosages of BP compared to SF under harsh environmental conditions that include repetitive freeze-thaw and wet-dry cycles. A total of 180 specimens consisting of 200 mm concrete cubes were cast and tested according to the guidelines of Annex G of the CSA/S806-12 (CSA 2017). In addition to the concrete type, the test variables include the type of the FRP bar, and the type of the GFRP bar end (straight or headed-end bars), the type and the dosage of discrete fibers in the matrix.

Phase *III* consisted of two parts: an experimental part and an analytical part. The experimental part comprised the construction and testing of eleven simply-supported deep beams under one-point loading. All beams had a rectangular cross section with a width of 250 mm and a height of 590 mm, and length of 2100 mm. The test parameters included the type of the fibers (steel or BP), the dosage of the BP, the web reinforcement, and the longitudinal reinforcement ratio. On the other hand, the analytical phase involved the assessment of current shear design models for FRP-RC and FRP-FRC deep beams and the introduction of new models.

10.2 Conclusions

Based on the results of the results of experimental and analytical studies, the following conclusions can be drawn:

10.2.1 Conclusions from phase I

1. The synergistic effects of Ns and slag in refining and densifying the pore structure of the matrix in the H composites led to higher residual compressive and flexural strengths as well as relative dynamic modulus of elasticity, compared to that of counterpart N composites without SCMs.
2. The presence of BP in the cementitious composites effectively discounted the rate of deterioration, resulting in lower reductions in compressive and flexural capacity as well as toughness. The presence of BP impeded the damage imparted by the tensile stress induced by the combined exposure, especially due to the efficient bonding with matrix (deposition of hydration products in microgrooves).
3. The layered prisms cast with the H composite comprising high dosages of BP (H-B-4.5 and H-B-6.9) achieved superior post-cracking (deflection-hardening) behaviour after the combined exposure, as the residual strengths at a deflection of 0.5 mm (span/600) were approximately 32 and 27%, respectively higher than their first-crack strengths, and their residual toughness was comparable to that of their initial values before exposure. In addition, BPRCC specimens containing high volume (4.5% and 6.9%) of BP yielded the lowest reduction in stiffness after the F/T portion of the exposure, due to the increased air content associated with the foaming action during mixing.
4. All the N and H composites, reinforced with either BP or SF, showed high compatibility with the base concrete. There was no relative shrinkage cracking during curing and

exposure to hot/arid conditions. Correspondingly, the substrate failure was the dominant mode of failure in the pull-off bond test, with marginal reductions of the bond strength after exposure to consecutive F/T and W/D cycles. This implies that all the BPRCC and SFRCC produced herein has enhanced dimensional stability relative to normal concrete, when they are cast within a short period of time (one hour) forming a layered system.

10.2.2 Conclusions from phase II

10.2.2.1 For unexposed specimens

1. Compared to the control mixtures, mixtures with fibers yielded lower compressive strength, especially with higher dosages of BP with statistical insignificance; however, the mode of failure considerably changed from brittle to ductile.
2. Four modes of failure for specimens cast without fibers were observed; pure pullout, partial pullout, splitting of concrete, and concrete crushing followed by splitting of the head. On the other hand, three modes of failure were noticed for fibrous specimens; partial pullout, cracking of concrete, and cracking of concrete followed by bar slippage. It is worth mentioning that the presence of fibers, in general, managed to keep the concrete block as one unit, even for specimens with headed-end bars.
3. Adding 40% of slag as a partial replacement of cement in addition to 6% of nano silica (HP-X-15-S vs NP-X-15-S) significantly increased the failure load by approximately 19% due to the synergistic effects of nano-silica and slag resulting in densification of microstructure.
4. The embedment length, transverse contraction strain (Poisson effect), and shear lag are the main reasons behind the lower bond strength for larger bar diameter. In addition, using

headed-end bar in fibrous specimens, irrespective of the bar diameter, showed a tremendous increase in the failure pullout load compared to straight bars.

5. The Canadian standards (CSA 2017 and 2019) and the American guidelines (ACI 2015) for GFRP bars were too conservative in predicting the ultimate bond strength. Therefore, the provisions of bond strength in current FRP design codes and guidelines need to be revised to better predict the bond strength of fibrous concrete reinforced with straight or headed-end GFRP bars.
6. The bond stress equations in different design provisions were assessed. The CSA/S806-12 (CSA 2017), CSA/S6-19 (CSA 2019), and JSCE-97 (JSCE 1997) highly underestimate the capacity of the specimens reinforced with straight FRP bars embedded in plain concrete without fibers with a mean P_{exp}/P_{pred} , coefficient of variation (CoV) and coefficient of determination (R^2) of 3.65 ± 1.1 , 30% and 0.37, 2.25 ± 0.7 , 29% and 0.41, 3.02 ± 0.8 , 27% and 0.48, respectively. This was attributed to neglecting major factors that directly affect the bond performance. On the other hand, the ACI 440.1R-15 equation overestimated the bond stress with a mean P_{exp}/P_{pred} , (CoV) and (R^2) of 0.83 ± 0.26 , 31% and 0.35, respectively.
7. Four models from literature (Krem 2013; Quayyum and Rteil 2011; Newman et al. 2010; Basaran and KalKan 2020) were introduced to mitigate the deficiencies in the bond strength equations stipulated by the design codes. However, all models, except *Model IV*, highly underestimate test results, due to the limited number of specimens used to develop these models. On the other hand, *Model IV* provided better prediction for straight FRP bars embedded in plain concrete with a mean P_{exp}/P_{pred} , CoV and R^2 were 1.28 ± 0.42 , 32%, and 0.52. This prediction of bond strength of straight FRP/plain concrete specimens might

be attributed to the wide population of specimens used in that study (180 test specimens), which covered all the parameters and mitigated all the deficiencies in the other models.

8. *Model V*, which was particularly developed to predict the bond strength of headed-end FRP bars embedded in plain concrete, yielded reasonable, yet conservative, predictions compared to other models reviewed in this study, with a mean P_{exp}/P_{pred} , CoV and R^2 were 1.62 ± 0.44 , 27%, and 0.30, respectively.
9. Out of all models, *Model IV* (Basaran and Kalkan 2020) produced the best estimates for specimens reinforced with straight FRP bars embedded in fibrous concrete (FRC), with a mean P_{exp}/P_{pred} , CoV and R^2 of 1.27 ± 0.42 , 33% and 0.52, respectively. It provides the least scattered results and best fit for specimens reinforced with straight FRP bars embedded in FRC.
10. All current models failed in providing reasonable predictions of the bond strength when it was applied to specimens reinforced with headed-end FRP bars embedded in fibrous concrete. Therefore, a new model was proposed to account for the effect of incorporating different types of discrete fibers into specimens reinforced with headed-end bars. The proposed model produced good predictions for FRP-FRC specimens with a mean P_{exp}/P_{pred} 1.09 ± 0.19 , a CoV of 18%, and R^2 of 0.95.

10.2.2.2 For exposed specimens

1. Based on the visual analysis, the control specimens without any fibers suffered from severe damage that was reflected by wide web cracks located at the surface. On the other hand, fibrous specimens seem to be immune to the environmental exposure.
2. The compressive strength was decreased for all specimens after the cyclic conditioning regime adopted in this study due to the formation of internal microcrack. Nevertheless, the

synergistic effect of nano silica and slag refined the pore structure of the matrix, which accordingly controlled the reduction rate in compressive strength. Similarly, the incorporation of fibers effectively mitigated the rate of deterioration to the extent that the fibrous mixtures exceeded the compressive strength of their counterpart mixtures cast without fibers.

3. All the FRCC specimens yielded the lowest stiffness degradation, in particular the composites containing BP. This is mainly linked to the increased air content associated with the use of high dosages of BP (e.g. 4.5 %), so it can be said that better F/T and W/D durability was attained without the inclusion of intentional entrained air.
4. Four modes of failure for specimens cast without fibers were observed; pure pullout, partial pullout, splitting of concrete, and splitting of both concrete and the head of the bar. On the other hand, the dominant mode of failure for fibrous specimens was partial pullout for straight bars, and cracking of concrete for headed-end bars. It is worth mentioning that the presence of fibers, in general, managed to keep the concrete cube as one unit, even for specimens with headed-end bars.
5. The bond durability markedly enhanced for fibrous specimens due to the restriction of the crack propagation at the bar/matrix interface. The loss of pullout capacity of GFRP bar embedded in plain composite was found to be 22%, whereas only 8% reduction, on average, was obtained for the FRCC specimens.

10.2.3 Conclusions from phase III

10.2.3.1 For the experimental part

1. The development of the arching action in the tested FRP-RC deep beams was substantiated by the essentially uniform strain distribution in the bottom reinforcement. After the

formation of the main diagonal crack, significant reserve capacity was available, indicating the formation of an arch action mechanism.

2. Unlike control specimens, beams with an FRCC layer exhibited a deflection softening behaviour, which was characterized by a gradual decrease in the load carrying capacity up to failure. In addition, the failure of FRP-RC deep beams with an FRCC layer in the tie zone changed from brittle and sudden to a more ductile failure, particularly for those reinforced with steel fibers.
3. The reinforcement ratio had no effect on the cracking load, either for initial flexural or shear cracks; however, it clearly affected the ultimate load capacity of the deep beam. The presence of FRCC in the tie zone had a notable effect on the cracking load and ultimate capacity.
4. The ACI 318-14 STM yielded unconservative predictions of the ultimate capacity of deep beams (strut failure), since this strut-capacity is based only on the concrete compressive strength without considering the effect of the longitudinal reinforcement. However, the ACI 318-19 gave better predictions with an average experimental-to-predicted load of 1.06. On the other hand, the STM provision in the CSA/S6-19 yielded reasonable prediction of the ultimate capacity for the tested deep beams with an average experimental-to-predicted load capacity of 1.33
5. Adding fibers has been proved as an effective way to enhance the ductility of FRP-RC deep beams. The ductility indices increased by 50, 118, and 76% with the addition of 2.5, 4.5, and 6.9% BP in the tie zone compared to the counterpart beam without fibers. In addition, despite the superior properties of SF with respect to the BP, keeping the volume of BP and SF constant (L-B-2.5 vs L-S-1.0) showed comparable ductility indices.

6. The inclusion of BFRCC with a dosage of 4.5% in the whole depth was an effective substitution to conventional web reinforcement in deep beams. However, from the direct cost perspective, adding the BP as a layer with a dosage of 4.5% will reduce costs and achieve an acceptable level of performance in terms of strength and ductility.

10.2.3.2 For the analytical part

1. The STMs in different design provisions was assessed. The CSA S806-12 (CSA 2017), CSA S6-19 (CSA 2019a), and AASHTO LRFD-14 (AASHTO 2014) underestimated the ultimate capacity of FRP-RC deep beams with a mean P_{exp}/P_{pred} of 1.63 ± 0.38 , which could lead to uneconomic design. On the other hand, the ACI 318-19 (ACI 2019), Eurocode 2 (2004), and JSCE (2007) highly overestimated the capacity with a mean P_{exp}/P_{pred} of 0.72 ± 0.31 , 0.75 ± 0.35 , and 0.68 ± 0.31 , respectively, owing to neglecting the effects of major parameters such as the concrete softening of the inclined strut and the shear span-to-depth ratio.
2. Two models were proposed by Mohamed et al. (2017), *Model I*, and Dharir (2017), *Model II*, to mitigate the deficiencies in the STMs stipulated by the design codes. *Model I* provided reasonable predictions of FRP-RC deep beams with a mean P_{exp}/P_{pred} , CoV, and R^2 of 1.18 ± 0.21 , 17.5% and 0.98, respectively. For *Model II* (Dharir 2017), these values were 0.98 ± 0.09 , 9.3% and 0.95, respectively. In addition, *Model III* and *Model IV*, proposed by Ashour et al. (1992) and Shahnewaz and Alam (2014), gave consistent and reasonable predictions of SFRC-deep beams reinforced longitudinally with steel bars with the mean P_{exp}/P_{pred} , CoV, and R^2 for both models were 1.32 ± 0.52 , 39.8%, and 0.79, and 1.19 ± 0.26 , 21.8%, and 0.88, respectively. On the other hand, all models *Model I*, *Model II*, *Model III* and *Model IV* underestimated the capacity of FRP deep beams poured with discrete fibers,

since the mean P_{exp}/P_{pred} and CoV for *Model I*, *Model II* and *Model III* were 1.6 ± 0.14 and 9%, 1.4 ± 0.3 and 22%, and 1.35 ± 0.42 and 31.2%, respectively. Therefore, a new model was proposed to account for the effect of incorporating different types of discrete fibers into the beam either as a layer in the tie zone or entirely over the whole depth. The proposed model produced good predictions for FRP-FRC deep beams with a mean P_{exp}/P_{pred} and R^2 of 1.04 ± 0.12 and 0.94, respectively.

10.3 Recommendations for Future Work

The results and discussion presented in this thesis provide useful insights for the extension of this research work. The following are recommendations for further investigations:

1. The overall results show that the nano-modified slag-based cementitious composites are suitable for new construction applications vulnerable to freeze–thaw and wet-dry environments. Yet, field trials are recommended for future research to verify these laboratory trends, and further aspects should be considered to enhance the trends of Phase *I* such as including other supplementary cementitious materials (e.g. fly ash or metakaolin), and/or including the concept of hybrid fibers. In addition, for rehabilitation applications, more investigations on the interfacial bond mechanics to understand what governs this new composite's bond to hardened concrete.
2. The bond interaction between GFRP bars and BFRCC was evaluated under consecutive freeze/thaw and wet/dry cycles in Phase *II*. Additional experimental studies on FRP/FRC interactions employing the same environmental exposure, yet with using saline solution. The implementation of loading conditions such as sustained or fatigue loads, and the use of other types of fibers (carbon or basalt), or bar surface patterns (wrapped, deformed, wrapped with sand-coating) would enhance and confirm the obtained findings.

3. Throughout this research program, some of the STM design methods suggested by the Canadian code for design of FRP-RC/FRC structures (CSA 2017) has been used in the design of the test specimens in Phase *III* with the primary goal of evaluating its sufficiency. However, studies on the efficiency of code provisions remains necessary. More investigations on the transverse reinforcement detailing such as stirrup spacing, and the type of discrete fibers in the deep beams are recommended. In addition, the application of nano-modified BFRCC in concrete structures that require a certain level of ductility and deformability (e.g. beam-column joints).
4. One further step is to examine the resisting mechanism of FRP-reinforced deep beams subjected to reversed cyclic loads. This issue is relevant to ensure adequate design of FRP-reinforced deep beams located in seismic zones

REFERENCES

- 1 AASHTO (2014), "AASHTO LRFD bridge design specifications." 7th Edition, *American*
2 *Association of State Highway and Transportation Officials*, (AASHTO), Washington.
- 3 Abed, F., and Alhafiz, A. R. (2019). "Effect of basalt fibers on the flexural behaviour of concrete
4 beams reinforced with BFRP bars." *Composite Structures*, 215: 23-34.
- 5 Achillides, Z., and Pilakoutas, K. (2004). "Bond behaviour of fiber reinforced polymer bars under
6 direct pullout conditions." *Journal of Composites for construction*, 8(2): 173-181.
- 7 ACI (1988). "Design consideration for steel fiber reinforced concrete, ACI 544.4R." *American*
8 *Concrete Institute*, Detroit, MI.
- 9 ACI (2015). "Guide for the design and construction of structural concrete reinforced with FRP
10 bars." ACI 440.1R-15, *American Concrete Institute*, Detroit, MI.
- 11 ACI (2018) "Guide to design with fibre-reinforced concrete, ACI 544.4R." *American Concrete*
12 *Institute*, Detroit, MI
- 13 ACI (2019). "Building code requirements for structural concrete (ACI 318-19) and commentary
14 (ACI 318R-19)" *American Concrete Institute*, Detroit, MI.
- 15 ACI. (2002). "State-of-the-art report on fiber reinforced concrete." ACI 544.1R-96, *American*
16 *Concrete Institute*, Detroit, MI.
- 17 ACI. (2014). "Building code requirements for structural concrete (ACI 318-14) and commentary
18 (ACI 318R-14)." *American Concrete Institute* Detroit, MI.
- 19 ACI. (2015). "Guide for the design and construction of structural concrete reinforced with FRP
20 bars." ACI 440.1R-15, *American Concrete Institute*, Detroit, MI, 1-88.
- 21 ACI-ASCE Committee 445. (1998). "Recent approaches to shear design of structural concrete."

- 22 *Journal of Structural Engineering*, ASCE, 124 (12): 1375-1417.
- 23 Adebar, P., Mindess, S., Pierre, D. S., and Olund, B. (1997). "Shear tests of fiber concrete beams
24 without stirrups." *ACI Structural Journal*, 94(1): 68-76.
- 25 Afroughsabet, V., and Ozbakkaloglu, T. (2015). "Mechanical and durability properties of high-
26 strength concrete containing steel and polypropylene fibers." *Construction and Building*
27 *Materials*, 94: 73–82.
- 28 Alsaif, A., Bernal, S. A., Guadagnini, M. and Pilakoutas, K. (2019). "Freeze-thaw resistance of
29 steel fibre reinforced rubberised concrete." *Construction and Building Materials*, 195: 450-
30 458.
- 31 Alsaif, A., Koutas, L., Bernal, S. A., Guadagnini, M. and Pilakoutas, K. (2018). "Mechanical
32 performance of steel fibre reinforced rubberised concrete for flexible concrete pavements."
33 *Construction and Building Materials*, 172: 533-543.
- 34 Alsayed, S. and Alhozaimy, A. (1999). "Ductility of concrete beams reinforced with FRP bars and
35 steel fibers." ASCE, *Journal of Composite Material*, 33(19): 1792–804.
- 36 Altalmas, A., El Refai, A., and Abed, F. (2015). "Bond degradation of basalt fiber-reinforced
37 polymer (BFRP) bars exposed to accelerated aging conditions." *Construction and Building*
38 *Materials*, 81: 162-171.
- 39 Alves, J., El-Ragaby, A., and El-Salakawy, E. (2011). "Durability of GFRP bars' bond to concrete
40 under different loading and environmental conditions." *Journal of Composites for*
41 *Construction*, ASCE, 15(3): 249-262.
- 42 Andermatt, M. F., Lubell A. S. (2013). "Behaviour of concrete deep beams reinforced with internal
43 fiber-reinforced polymer—experimental study." *ACI Structural Journal*, 110(4): 585-594.
- 44 Arslan, M. E. (2016). "Effects of basalt and glass chopped fibers addition on fracture energy and

- 45 mechanical properties of ordinary concrete: CMOD measurement." *Construction and*
46 *Building Materials*, 114: 383–391.
- 47 ASCE-ACI Committee 426. (1973). "Shear and diagonal tension." *Journal of Structure Division*,
48 ASCE, (6): 1091–1187.
- 49 Ashour, S. A., Hasanain, G. S., and Wafa, F. F. (1992). "Shear behaviour of high-strength fiber
50 reinforced concrete beams." *ACI Structural Journal*, 89(2): 176-184.
- 51 ASTM. (2012). "Standard test method for scaling resistance of concrete surfaces exposed to
52 deicing chemicals." C672, West Conshohocken, PA,
- 53 ASTM. (2014). "Standard specification for flow table for use in tests of hydraulic cement." ASTM
54 C230, West Conshohocken, PA.
- 55 ASTM. (2015). "Standard test method for relative density (specific gravity) and absorption of fine
56 aggregate." C128, West Conshohocken, PA.
- 57 ASTM. (2016). "Standard test method for tensile properties of fiber reinforced polymer matrix
58 composite bars." D7205, West Conshohocken, PA.
- 59 ASTM. (2017). "Standard test method for air content of freshly mixed concrete by the pressure
60 method." C231, West Conshohocken, PA.
- 61 ASTM. (2019a). "Standard test method for sieve analysis of fine and coarse aggregates." C 136,
62 West Conshohocken, PA.
- 63 ASTM. (2019b). "Standard specification for chemical admixtures for concrete." C494, West
64 Conshohocken, PA.
- 65 ASTM. (2019c). "Standard test method for resistance of concrete to rapid freezing and thawing."
66 C666, West Conshohocken, PA.
- 67 ASTM. (2019d). "Standard test method for flexural performance of fiber- reinforced concrete

- 68 (using beam with third-point loading).” C1609, West Conshohocken, PA.
- 69 ASTM. (2019e). “Standard test method for fundamental transverse, longitudinal, and torsional
70 resonant frequencies of concrete specimens.” C215, West Conshohocken, PA.
- 71 ASTM. (2020). “Standard performance specification for hydraulic cement.” ASTM C1157, West
72 Conshohocken, PA.
- 73 ASTM. (2020a). “Standard test method for compressive strength of cylindrical concrete
74 specimens.” C39, West Conshohocken, PA.
- 75 ASTM. (2020b). “Standard test method for slump of hydraulic-cement concrete.” ASTM C1437,
76 West Conshohocken, PA.
- 77 ASTM. (2020c). “Standard test method for tensile strength of concrete surfaces and the bond
78 strength or tensile strength of concrete repair and overlay materials by direct tension (pull-
79 off method).” C1583, West Conshohocken, PA.
- 80 Ayub, T., Shafiq, N., and Khan, S. (2016). "Compressive stress-strain behaviour of HSFRC
81 reinforced with basalt fibers." *Journal of Materials in Civil Engineering*, ASCE, 28(4):
82 06015014.
- 83 Azzam, A., Bassuoni, M. T. and Shalaby, A. (2019). “Properties of high-volume fly ash and slag
84 cementitious composites incorporating nanosilica and basalt fiber pellets.” *Advances in Civil
85 Engineering Materials*, 8(3): 255-274.
- 86 Baena, M., Torres, L., Turon, A., and Barris, C. (2009). “Experimental study of bond behaviour
87 between concrete and FRP bars using a pull-out test.” *Composites Part B: Engineering*,
88 40(8): 784-797.
- 89 Balgude, M. V. (2014). “Experimental study on crimped steel fiber reinforced concrete deep beam
90 in shear.” *IOSR Journal of Mechanical and Civil Engineering*, 11(2): 24-39.

- 91 Banthia, N., Zanotti, C., Sappakittipakorn, M. (2014). "Sustainable fiber reinforced concrete for
92 repair applications." *Construction and Building Materials*, 67: 405–412.
- 93 Basaran, B., and Kalkan, I. (2020). "Development length and bond strength equations for FRP bars
94 embedded in concrete." *Composite Structures*, 251: 112662.
- 95 Bassuoni, M. T., and Rahman, M. M. (2016). "Response of concrete to accelerated physical salt
96 attack exposure." *Cement and concrete research*, 79: 395-408.
- 97 Bediwy, A. and El-Salakawy, E.F. (Forthcoming). "Bond behavior of straight and headed-end
98 GFRP bars embedded in basalt fiber pellets cementitious composites." *ASCE, Journal of*
99 *Composites for Construction*, in press.
- 100 Bediwy, A. Mahmoud, K., and El-Salakawy, E.F. (Forthcoming a). "Structural behaviour of FRCC
101 layered deep beams reinforced with GFRP headed-end bars." *Engineering Structures*, in
102 press.
- 103 Bediwy, A. and El-Salakawy, E.F. (Forthcoming b). "Ductility and performance assessment of
104 basalt fiber-reinforced cementitious composite layered deep beams." *ACI Structural*
105 *Journal*, in press.
- 106 Bediwy, A., Bassuoni, M. T. and El-Salakawy, E. F. (2018). "Post-cracking behaviour of
107 cementitious composite incorporating nano-silica and basalt fiber pellets." *Sixth*
108 *International Conference on Durability of Concrete Structures*, University of Leeds, Leeds,
109 West Yorkshire, United Kingdom.
- 110 Belarbi, A., and Wang, H. (2012). "Bond durability of FRP bars embedded in fiber-reinforced
111 concrete." *Journal of composites for construction*, 16(4): 371-380.
- 112 Benmokrane, B., Mohamed, H. M., Manalo, A., and Cousin, P. (2016). "Evaluation of physical
113 and durability characteristics of new headed glass fiber – reinforced polymer bars for

- 114 concrete structures.” *Journal of Composites for Construction*, ASCE, 21 (2): 04016081.
- 115 Benmokrane, B., Tighiouart, B. and Chaallal, O. (1996). "Bond strength and load distribution of
116 composite GFRP reinforcing bars in concrete." *ACI Materials Journal*, 93(3): 246-253.
- 117 Bentur, A. and Mindess, S. (2007). "Fiber reinforced cementitious composites." 2nd Ed., *E and FN*
118 *Spon*, New York.
- 119 Branston, J., Das, S., Kenno, S. Y. and Taylor, C. (2016). "Mechanical behaviour of basalt fibre
120 reinforced concrete.” *Construction and Building Materials*, 124: 878–886.
- 121 Brena, S. F. and Morrison, M. C. (2007). "Factors affecting strength of elements designed using
122 strut-and-tie models.” *ACI Structural Journal*, 104: 267–277.
- 123 Brown, M. D. and Bayrak, O. (2007). "Investigation of deep beams with various load
124 configurations." *ACI Structural Journal*, 104(5): 611-620.
- 125 Calvet, V., Valcuende, M., Benlloch, J., and Cánoves, J. (2015). "Influence of moderate
126 temperatures on the bond between carbon fibre reinforced polymer bars (CFRP) and
127 concrete.” *Construction and Building Materials*, 94: 589-604.
- 128 Campione, G. (2012). "Flexural behaviour of steel fibrous reinforced concrete deep beams." *Journal of Structural Engineering*, ASCE, 138(2): 235-246.
- 129
- 130 Çavdar, A. (2014). "Investigation of freeze–thaw effects on mechanical properties of fiber
131 reinforced cement mortars.” *Composites Part B: Engineering*, 58: 463-472.
- 132 Chu, S. H., and Kwan, A. K. H. (2019). "A new bond model for reinforcing bars in steel fibre
133 reinforced concrete.” *Cement and Concrete Composites*, 104: 103405.
- 134 Collins, M. P. and Mitchell, D. (1997). "Prestressed concrete structures." *Response Publications*,
135 Toronto, Ontario, Canada.
- 136 Corinaldesi, V., and Nardinocchi, A. (2016). "Influence of type of fibers on the properties of high

- 137 performance cement-based composites.” *Construction and Building Materials*, 107: 321-
138 331.
- 139 Cosenza, E., Manfredi, G., and Realfonzo, R. (1997). “Behaviour and modeling of bond of FRP
140 rebars to concrete.” *Journal of Composites for Construction*, 1(2): 40-51.
- 141 CSA. (2017). “Design and construction of building structures with fibre-reinforced polymer.”
142 CSA/S806-12 (R2017). *Canadian Standard Association (CSA)*, Toronto, ON, Canada.
- 143 CSA. (2018). “Cementitious materials for use in concrete.” CSA-A3001-13, *Canadian Standards*
144 *Association (CSA)*, Toronto, ON, Canada.
- 145 CSA. (2019a). "Canadian highway bridge design code and commentary." CSA S6-19, *Canadian*
146 *Standard Association (CSA)*, Toronto, ON, Canada.
- 147 CSA. (2019b). "Concrete materials and methods of concrete construction / test methods and
148 standard practices for concrete." CSA A23.1-19/A23.2-19, *Canadian Standard Association*
149 *(CSA)*, Toronto, ON, Canada.
- 150 CSA. (2019c). “Design of concrete structures.” CSA/A23.3-19, *Canadian Standard Association*
151 *(CSA)*, Toronto, ON, Canada.
- 152 Dancygier, A. N., Katz, A., and Wexler, U. (2010). “Bond between deformed reinforcement and
153 normal and high-strength concrete with and without fibers.” *Materials and Structures*, 43(6):
154 839-856.
- 155 Daniali, S. (1992). “Development length for fiber-reinforced plastic bars.” In *Advanced Composite*
156 *Materials in Bridges and Structures*, Sherbrooke, Canada, 179-188.
- 157 Davalos, J. F., Chen, Y., and Ray, I. (2008). “Effect of FRP bar degradation on interface bond with
158 high strength concrete.” *Cement and Concrete Composites*, 30(8): 722-730.
- 159 Deitz, D. H., Harik, I. E., and Gesund, H. (2003). "Physical properties of glass fiber reinforced

- 160 polymer rebars in compression." *Journal of Composites for Construction*, ASCE, 7(4): 363–
161 366.
- 162 Dhahir, M. K. (2017). "Shear strength of FRP reinforced deep beams without web reinforcement."
163 *Composite Structures*, 165: 223-232.
- 164 El Refai, A., Abed, F.H., and Al-Rahmani, A. (2015). "Structural performance and serviceability
165 of concrete beams reinforced with hybrid (GFRP and steel) bars." *Construction and Building*
166 *Materials*, 96: 518–29.
- 167 El-Sayed, A. K., El-Salakawy, E. F., and Benmokrane, B. (2012). "Shear strength of fibre-
168 reinforced polymer reinforced concrete deep beams without web reinforcement." *Canadian*
169 *Journal in Civil Engineering*, 39(5): 546-555.
- 170 EN 1992-1-1:2004. (2004). "Eurocode 2: Design of Concrete Structures Part 1-1: General Rules
171 and Rules for Buildings," *British Standards Institution*, London.
- 172 Ezeldin, A., and Balaguru, P. (1989). "Bond behaviour of normal and high-strength fiber
173 reinforced concrete." *Materials Journal*, 86(5): 515-524.
- 174 Fang, I. K., and Wu, J. Y. (1994). "Shear behaviour of fiber-reinforced HPC deep beams." *ACI*
175 *Special Publication*, 149: 523-544.
- 176 Farghaly, A. S., and Benmokrane, B. (2013). "Shear behaviour of FRP-reinforced concrete deep
177 beams without web reinforcement." *Journal of Composites for Construction*, 17(6):
178 04013015.
- 179 Ghazy, A., Bassuoni, M.T., Maguire, E. and O’Loan, M. (2016). "Properties of fiber-reinforced
180 mortars incorporating nano-silica." *Fibers*, 4(6): 1-16.
- 181 Gravina, R. J., Li, J., Smith, S. T., and Visintin, P. (2020). "Environmental durability of FRP bar-
182 to-concrete bond: critical review." *Journal of Composites for Construction*, 24(4):

- 183 03120001.
- 184 Harajli, M., and Abouniaj, M. (2010). "Bond performance of GFRP bars in tension: Experimental
185 evaluation and assessment of ACI 440 guidelines." *Journal of Composites for
186 Construction*, 14(6): 659-668.
- 187 Harris, H. G., Somboonsong, W., and Ko, F. K. (1998). "New ductile hybrid FRP reinforcing bar
188 for concrete structures." *Journal of Composites for Construction*, 2(1): 28-37.
- 189 Hossain, K. M. A., Ametrano, D., and Lachemi, M. (2014). "Bond strength of standard and high-
190 modulus GFRP bars in high-strength concrete." ASCE, *Journal of Materials in Civil
191 Engineering*, 26(3): 449-456.
- 192 Hou, L., Liu, H., Xu, S., Zhuang, N., and Chen, D. (2017). "Effect of corrosion on bond behaviours
193 of rebar embedded in ultra-high toughness cementitious composite." *Construction and
194 Building Materials*, 138: 141-150.
- 195 Islam, S., Afefy, H. M., Sennah, K., and Azimi, H. (2015). "Bond characteristics of straight-and
196 headed-end, ribbed-surface, GFRP bars embedded in high-strength concrete." *Construction
197 and Building Materials*, 83: 283-298.
- 198 Issa, M. S., Metwally, I. M., and Elzeiny, S. M. (2011). "Influence of fibers on flexural behaviour
199 and ductility of concrete beams reinforced with GFRP rebars." *Engineering Structures*,
200 33(5): 1754-1763.
- 201 Iyer, P., Kenno, S. Y., and Das, S. (2015). "Mechanical properties of fiber reinforced concrete
202 made with basalt filament fibers." *Journal of Materials in Civil Eng.*, ASCE, 27(11):
203 04015015.
- 204 Jaeger G. L., Tadros G., and Mufti A. A. (1995). "Balanced section, ductility, and deformability
205 in concrete with FRP reinforcement." Research report no. 2-1995. Halifax (NS, Canada):

- 206 *Industry Center for Computer-Aided Engineering*, Technical University of Nova Scotia.
- 207 Japan Society of Civil Engineering. (1997). "Recommendation for design and construction of
208 concrete structures using continuous fibre reinforcing materials." *Concrete Engineering*
209 *Series 23*, Tokyo, Japan, 325.
- 210 Japan Society of Civil Engineering. (2007). "Standard specifications for concrete structures."
211 Tokyo, Japan, 469.
- 212 Kim, B., Doh, J. H., Yi, C. K., and Lee, J. Y. (2013). "Effects of structural fibers on bonding
213 mechanism changes in interface between GFRP bar and concrete." *Composites Part B:*
214 *Engineering*, 45(1): 768-779.
- 215 Kim, D. J., Lee, J., and Lee, Y. H. (2014). "Effectiveness factor of strut-and-tie model for concrete
216 deep beams reinforced with FRP rebars." *Composites Part B: Engineering*, 56: 117-125.
- 217 Kong, D., Xiangfei, D., Wei, S., Zhang, H., Yang, Y., and Shah, S. P. (2012). "Influence of nano-
218 silica agglomeration on microstructure and properties of the hardened cement-based
219 materials." *Construction and Building Materials*, 37: 707–715.
- 220 Krem S. (2013). "Bond and Flexural Behaviour of Self Consolidating Concrete Beams Reinforced
221 and Prestressed with FRP Bars." Doctoral dissertation, University of Waterloo, Waterloo,
222 ON, Canada.
- 223 Kuchma D., Yindeesuk S., Nagle T., Hart J., and Lee H. H. (2008) "Experimental validation of
224 strut-and-tie method for complex regions. " *ACI Structural Journal*, 105: 578–589.
- 225 Kumar, K., and Mahendran, N. (2016). "Structural behaviour of deep beam using SCC with
226 chopped strands and polypropylene fibre." *Journal of Intelligent and Fuzzy Systems*, 30(2):
227 1219-1229.
- 228 Larralde, J. and Silva-Rodriguez (1993). "Bond and slip of FRP rebars in concrete." ASCE,

- 229 *Journal of Materials in Civil Engineering*, 5(1): 30-40.
- 230 Lee, J. Y., Kim, T. Y., Kim, T. J., Yi, C. K., Park, J. S., You, Y. C., and Park, Y. H. (2008).
231 “Interfacial bond strength of glass fiber reinforced polymer bars in high-strength concrete.”
232 *Composites Part B: Engineering*, 39(2): 258-270.
- 233 Li, C., Gao, D., Wang, Y., and Tang, J. (2017). “Effect of high temperature on the bond
234 performance between basalt fibre reinforced polymer (BFRP) bars and
235 concrete.” *Construction and Building Materials*, 141: 44-51.
- 236 Li, H., Xiao, H. G., Yuan, J. and Ou, J. (2004). “Microstructure of cement mortar with nano-
237 particles.” *Composites part B: Engineering*, 35(2): 185-189.
- 238 Liu, S. B., and Xu, L. H. (2013). “Ductility and deformation performance of hybrid fiber reinforced
239 high performance concrete shear deep beams.” in *Applied Mechanics and Materials*, 357:
240 858-862.
- 241 Madan, S. K., Rajesh, K. G., and Singh, S. P. (2007). “Steel fibers as replacement of web
242 reinforcement for RCC deep beams in shear.” *Asian Journal of Civil Engineering (Building
243 and Housing)*, 8(5): 479-489.
- 244 Madani, H., Bagheri, A. and Parhizkar, T. (2012). “The pozzolanic reactivity of monodispersed
245 nano-silica hydrosols and their influence on the hydration characteristics of Portland
246 cement.” *Cement and Concrete Research*, 42(12): 1563–1570.
- 247 Mahmoud, K., Ghazy, A., Bassuoni, M.T., and El-Salakawy, E. (2017). "Properties of
248 nanomodified fiber-reinforced cementitious composites." *Journal of Materials in Civil
249 Engineering*, ASCE, 29(10): 04017173.
- 250 Malhotra, V. M., Zhang, M. H., Read, P. H., and Ryell, J. (2000). "Long term mechanical
251 properties and durability characteristics of high-strength/ high-performance concrete

- 252 incorporating supplementary cementing materials under outdoor exposure conditions." *ACI*
253 *Materials Journal*, 97(5): 518–525.
- 254 Mansur, M. A., and Ong, K. C. G. (1991). "Behaviour of reinforced fiber concrete deep beams in
255 shear." *Structural Journal*, 88(1): 98-105.
- 256 Maranan, G. B., Manalo, A. C., Karunasena, W., and Benmokrane, B. (2015). "Pullout behaviour
257 of GFRP bars with anchor head in geopolymer concrete." *Composite Structures*, 132: 1113-
258 1121.
- 259 Mohamed, A., Mahmoud, K. and El-Salakawy, E. (2020). "Behaviour of simply supported and
260 continuous concrete deep beams reinforced with GFRP bars." *Journal of Composites for*
261 *Construction*, ASCE, 24(7): 04020032.
- 262 Mohamed, K., Farghaly, A.S. and Benmokrane, B. (2017). "Effect of vertical and horizontal web
263 reinforcement on the strength and deformation of concrete deep beams reinforced with
264 GFRP bars." *Journal of Structural Engineering*, ASCE, 143 (8): 04017079.
- 265 Mohamed, K. (2015). "Performance and strut efficiency factor of concrete deep beams reinforced
266 with GFRP bar." *PhD. Thesis*, University of Sherbrooke, Quebec, Canada.
- 267 Mohammadhassani, M., Jumaat, M. Z., Jameel, M., Badiie, H., and Arumugam, A. M. (2012).
268 "Ductility and performance assessment of high strength self compacting concrete (HSSCC)
269 deep beams: An experimental investigation." *Nuclear engineering and design.*, 250: 116-
270 124.
- 271 Montgomery, D. C. (2017). "Design and analysis of experiments." Wiley, New York.
- 272 Moradi, M. and Esfahani, M. R. (2017). "Application of the strut-and-tie method for steel fiber
273 reinforced concrete deep beams." *Construction and Building Materials*, 131: 423-437.

- 274 Muhammad, N. Z., Keyvanfar, A., Majid, M. Z. A., Shafaghat, A. and Mirza, J. (2015).
275 “Waterproof performance of concrete: A critical review on implemented approaches.”
276 *Construction and Building Materials*, 101: 80-90.
- 277 Naaman A. E. and Jeong S. M. (1995). “Structural ductility of concrete beams prestressed with
278 FRP tendons.” In: Proceedings, 2nd int. RILEM symp. FRPRXS-2. Non-metric (FRP)
279 reinforcement for concrete structures. RILEM, London: E and FN Spon, 379–86.
- 280 Nehdi, M., Omeman, Z., and El-Chabib, H. (2008). “Optimal efficiency factor in strut-and-tie
281 model for FRP-reinforced concrete short beams with $(1.5 < a/d < 2.5)$.” *Materials and*
282 *structures*, 41(10): 1713-1727.
- 283 Nes, L. G., and Øverli, J. A. (2015). “Structural behaviour of layered beams with fibre-reinforced
284 LWAC and normal density concrete.” *Materials and Structures*, 49(2): 689–703.
- 285 Newman, N., Ayoub, A., and Belarbi, A. (2010). “Development length of straight FRP composite
286 bars embedded in concrete.” *Journal of Reinforced Plastics and Composites*, 29(4): 571-589.
- 287 Omeman, Z., Nehdi, M., and El-Chabib, H. (2008). "Experimental study on shear behaviour of
288 carbon-fiber-reinforced polymer reinforced concrete short beams without web
289 reinforcement." *Canadian Journal of Civil Engineering*, 35: 1-10.
- 290 Özbay, E., Karahan, O., Lachemi, M., Hossain, K. M., and Atis, C. D. (2013). “Dual effectiveness
291 of freezing–thawing and sulfate attack on high-volume slag-incorporated ECC.” *Composites*
292 *Part B: Engineering*, 45(1): 1384-1390.
- 293 Puertas, F., Amat, T., Fernández-Jiménez, A. and Vázquez, T. (2003). “Mechanical and durable
294 behaviour of alkaline cement mortars reinforced with polypropylene fibres.” *Cement and*
295 *Concrete Research*, 33(12): 2031-2036.

- 296 Qing, Y., Zenan, Z., Deyu, K. and Rongshen, C. (2007). "Influence of nano-SiO₂ addition on
297 properties of hardened cement paste as compared with silica fume." *Construction and*
298 *Building Materials*, 21(3): 539-545.
- 299 Quayyum, S. (2010). "Bond behaviour of fibre reinforced polymer (FRP) rebars in concrete."
300 Doctoral dissertation, University of British Columbia, Vancouver, BC, Canada.
- 301 Sagaseta J. (2008). "The influence of aggregate fracture on the shear strength of reinforced
302 concrete beams." *PhD thesis*, Imperial Collage London, 2008.
- 303 Sahoo, D. R., Flores, C. A., and Chao, S. H. (2012). "Behaviour of steel fiber-reinforced concrete
304 deep beams with large opening. *ACI Structural Journal*, 109(2).
- 305 Said, A. M., Zeidan, M. S., Bassuoni, M. T., and Tian, Y. (2012). "Properties of concrete
306 incorporating nano-silica." *Construction and Building Materials*, 36: 838–844.
- 307 Saleh, N., Ashour, A., and Sheehan, T. (2019). "Bond between glass fibre reinforced polymer bars
308 and high-strength concrete." In *Structures*, 22: 139-153.
- 309 Salemi, N. and Behfarnia, K. (2013). "Effect of nano-particles on durability of fiber-reinforced
310 concrete pavement." *Construction and Building Materials*, 48: 934-941.
- 311 Shah, D. L., and Modhera, C. D. (2012). "Evaluation of shear strength in self-compacting fibre-
312 reinforced concrete and conventional concrete deep beams." *Magazine of concrete research*,
313 64(6): 527-537.
- 314 Shahnewaz, M., and Alam, M. S. (2014). "Improved shear equations for steel fiber-reinforced
315 concrete deep and slender beams." *ACI Structural Journal*, 111(4): 551-860.
- 316 Song, P. S., and Hwang, S. (2004). "Mechanical properties of high-strength steel fiber-reinforced
317 concrete." *Construction and Building Materials*, 18(9): 669-673.
- 318 Sorelli, L. G., Meda, A., and Plizzari, G. A. (2006). "Steel fiber concrete slabs on ground: a

- 319 structural matter.” *ACI Structural Journal*, 103(4): 551.
- 320 Soylev, T.A., Ozturan, T. (2014). "Durability, physical and mechanical properties of fiber-
- 321 reinforced concretes at low-volume fraction." *Construction and Building Materials*, 73: 67–
- 322 75.
- 323 Tastani, S., Pantazopoulou, S., and Karvounis, P. (1984). "Local bond-slip characteristics of GFRP
- 324 bar." *ACI Structural Journal*, 2(230): 1481–1496.
- 325 Tuchscherer, R. G., and Quesada, A. (2015). “Replacement of deformed side-face steel
- 326 reinforcement in deep beams with steel fibers.” in *Structures*, 3: 130-136.
- 327 Tuchscherer, R., Birrcher, D., Huizinga, M., and Bayrak, O. (2010). “Confinement of deep beam
- 328 nodal regions.” *ACI Structural Journal*, 107(6): 709.
- 329 Vasanelli, E., Micelli, F., Aiello, M. A. and Plizzari, G. (2013). “Crack width prediction of FRC
- 330 beams in short and long term bending condition.” *Materials and Structures*, 47(2): 39–54.
- 331 Vecchio FJ, Collins MP. (1986) “The modified compression-field theory for reinforced concrete
- 332 elements subjected to shear.” *ACI Structural Journal*, 83(2): 219–31.
- 333 Veljkovic, A., Carvelli, V., Haffke, M. M., and Pahn, M. (2017). “Concrete cover effect on the
- 334 bond of GFRP bar and concrete under static loading.” *Composites Part B: Engineering*, 124:
- 335 40-53.
- 336 Wambeke, B. W., and Shield, C. K. (2006). “Development length of glass fiber-reinforced polymer
- 337 bars in concrete.” *ACI Materials Journal*, 103(1): 11.
- 338 Wang, H. and Belarbi A. (2011). “Ductility characteristics of fiber-reinforced-concrete beams
- 339 reinforced with FRP rebars.” *Construction and Building Materials*, 25(5): 2391–401.
- 340 Wight, J. K. and MacGregor, J. G. (2009). “Reinforced concrete: mechanics and design.” (6th
- 341 edition), *Pearson Prentice Hall*, Upper Saddle River, New Jersey: 1-1157.

- 342 Wille, K., Naaman, A. E., El-Tawil, S. and Parra-Montesinos, G. J. (2012). "Ultra-high
343 performance concrete and fiber reinforced concrete: achieving strength and ductility without
344 heat curing." *Materials and structures*, 45(3): 309-324.
- 345 Xu, S. L., Wang, N., and Zhang, X. F. (2012). "Flexural behaviour of plain concrete beams
346 strengthened with ultra high toughness cementitious composites layer." *Materials and*
347 *Structures*, 45(6): 851-859.
- 348 Yan, F., and Lin, Z. (2017). "Bond durability assessment and long-term degradation prediction for
349 GFRP bars to fiber-reinforced concrete under saline solutions." *Composite Structures*, 161:
350 393-406.
- 351 Yan, F., Lin, Z., and Yang, M. (2016). "Bond mechanism and bond strength of GFRP bars to
352 concrete: A review." *Composites Part B: Engineering*, 98: 56-69.
- 353 Zhang, M., Islam, J., and Peethamparan, S. (2012). "Use of nano-silica to increase early strength
354 and reduce setting time of concretes with high volumes of slag." *Cement and Concrete*
355 *Composites*. 34(5): 650–662.
- 356 Zhang, Z. H., Yao, X., Zhu, H. J., Hua, S. D. and Chen, Y. (2009). "Preparation and mechanical
357 properties of polypropylene fiber reinforced calcined kaolin-fly ash based geopolymer."
358 *Journal of Central South University of Technology*, 16(1): 49-52.
- 359 Zheng, X.G., Liu, J., Li, S.M., Zeng, Z., Weng, Z.C., Yang, D.J. (2015) "Effect of polypropylene
360 fiber and silica fume on mechanical properties and durability improvement of high
361 performance concrete." Kao, J., Sung, C., and Ren. C. (Eds.), CRC Press, Taylor and Francis
362 Group, London: UK: 333–342.
- 363 Zsutty, T. C. (1968). "Beam shear strength prediction by analysis of existing data." *ACI Journal*
364 *Proceedings*, 65(11): 943-951.